The timing, dynamics and palaeoclimatic significance of ice sheet deglaciation in central Patagonia, southern South America

Jacob Martin Bendle

Department of Geography

Royal Holloway, University of London

Thesis submitted for the degree of Doctor of Philosophy (PhD), Royal Holloway, University of London

September, 2017

Declaration

I, Jacob Martin Bendle, hereby declare that this thesis and the work presented in it are entirely my own unless otherwise stated. Chapters 3-7 of this thesis form a series of research papers, which are either published, accepted or prepared for publication. I am responsible for all data collection, analysis, and primary authorship of Chapters 3, 5, 6 and 7. For Chapter 4, I contributed datasets, and co-authored the paper, which was led by Thorndycraft. Detailed statements of contribution are given in Chapter 1 of this thesis, for each research paper. I wrote the introductory (Chapters 1 and 2), synthesis (Chapter 8) and concluding (Chapter 9) chapters of the thesis.

Signed: ..... Date:.....
(Candidate)

Signed: ..... Date:.....
(Supervisor)

Acknowledgements

First and foremost, I am very grateful to my supervisors Varyl Thorndycraft, Adrian Palmer, and Ian Matthews, whose tireless support, guidance and, most of all, enthusiasm, have made this project great fun. Through their company in the field they have contributed greatly to this thesis, and provided much needed humour along the way. For always giving me the freedom to explore, but wisely guiding me when required, I am very thankful.

I am indebted to my brother, Aaron Bendle, who helped me for five weeks as a field assistant in Patagonia, and who tirelessly, and without complaint, dug hundreds of sections – thank you for your hard work and great company. Chris Hayward and Christina Manning helped me analyse tephra samples, and Andy Breckenridge gave up much of his time responding to email queries about lake reconstruction in ArcGIS. A huge thank you is also owed to the Royal Holloway technical staff, Katy Flowers, Iñaki Valcarcel, Jenny Kynaston, Raymond Aung, and Marta Perez-Fernandez, who have always been approachable and helpful, and have solved more than a few issues.

Many of the Department of Geography staff and PhD community have made the last four years so enjoyable. There are too many people to name individually, but a special mention goes to Paul Lincoln, Jenni Sherriff, Rhys Timms, Ash Abrook, Angharad Jones, Rachel Squire and Dan Webb, who were there throughout, and all helped, listened and provided a steady, and much needed flow of humour. And to those who came later, Julian, Nicola, and the other Quaternarists, your company in the office has made the whole process bearable, and even quite enjoyable!

Finally, to my family – Mum, Dad, Aaron and Gus – thank you for your endless encouragement and for always believing in me. Last, and by no means least, Helen, your positivity, motivation and unwavering support has kept me going – I wouldn't have got through it without you.

This thesis was supported by a Natural Environment Research Council (NERC) studentship [grant number: NE/L501803/1]. In addition, several other funding bodies supported fieldwork and/or laboratory costs, namely: an Explorers Club Exploration Grant; a Quaternary Research Association (QRA) New Research Workers' Award; and a University of London PGR Grant.

The timing, dynamics and palaeoclimatic significance of ice sheet deglaciation in central Patagonia, southern South America

Jacob Martin Bendle

Abstract

Robust reconstructions of glacial retreat are required to elucidate controls on ice-sheet deglaciation and (a)synchronicity in the climate system. Such reconstructions can be derived through detailed geological investigations of glacial landforms and sediments. Patagonia, in southern South America, contains a well-preserved glacial record and occupies an important location regarding major Southern Hemisphere climate systems. However, resolving the history of ice-sheet deglaciation has proven problematic, owing to generally low-resolution geomorphological mapping, and a paucity of high-precision dating control. This thesis explores the deglacial history of the Lago General Carrera–Buenos Aires (LGC–BA) and Lago Cochrane–Pueyrredón (LC–P) ice lobes (46–48°S) of the former Patagonian Ice Sheet (PIS). The region is chosen because there are uncertainties associated with: (i) the deglacial configuration and evolution of retreating ice lobes and proglacial lake systems; and (ii) the sub-millennial timing of deglacial events.

A new glacial geomorphological map is produced to reconstruct the spatio-temporal evolution of ice lobes and proglacial lakes. The elevation(s) of relict lake shorelines are examined to quantify glacio-isostatic adjustment and accurately assign former lake levels, lake outflows, and ice-margin positions, through the last deglaciation. These new reconstructions are used to target sites for high-resolution dating. A ~1000-year varve chronology is developed at LGC–BA after examining the sedimentary properties of laminated glaciolacustrine sequences. Tephrochronology anchors this record to the calendar-year timescale. The chronology indicates that PIS retreat commenced at 18,086 ± 214 cal a BP, and accelerated from 5 to 18 m yr^{-1} over the next ~1000 years. The new timing for deglaciation at LGC–BA allows an exploration of climate forcing mechanisms. Comparisons with palaeoclimatic records reveal a hemisphere-wide warming influence on LGC–BA deglaciation. Moreover, spectral analyses of varve thickness time-series demonstrate a likely teleconnection with tropical Pacific climate oscillations, and PIS sensitivity to short-term variations in melt-season temperature.

Contents

List of figures

List of tables

Chapter 1. Introduction

1.1. Rationale

Southern South America is influenced by dynamic climatic systems that operate on hemispheric and global scales, and with origins rooted in the tropics and high polar latitudes. While ideally located to reconstruct Southern Hemisphere climate changes over the Quaternary, the extent and timing of mid-latitude glacial fluctuations are still uncertain in many areas, and the demise of the last major ice masses remains poorly constrained. Improved understanding of the deglaciation of the Last Glacial Maximum (LGM) Patagonian Ice Sheet may generate new insights into global ocean-atmosphere variability and glacial dynamics through an interval of dramatic natural climate reorganisation.

Due to the absence of land between 40–60°S, the Southern Hemisphere mid-latitudes are dominated by zonal circulation patterns (Figure 1.1). Most important is the Southern Westerly Wind (SWW) system, which exerts strong control over mid-latitude air temperatures and the distribution of precipitation (Garreaud, 2007). Moreover, the location and strength of the SWWs play a major role in global climate (Kohfeld et al., 2013; Sime et al., 2013) by influencing upwelling within the Antarctic Circumpolar Current (ACC) and, by extension, glacial-interglacial CO_2 ventilation from the deep Southern Ocean (Toggweiler et al., 2006, 2009; Anderson et al., 2009). Moreover, the SWWs modulate the latitude of oceanic fronts, such as the Sub-Tropical Front (STF e.g. Sikes et al., 2009; 2013), and latitudinal movements of the SWWs can, for example, alter the strength of ocean currents and even the connection between marine basins (e.g. so-called 'Agulhas leakage'; Bard and Rickaby, 2009). Together with these dominant, wind-driven circumpolar systems, southern South America between the latitudes 40–50°S, is uniquely sensitive to both tropical ocean-atmosphere variability, such as El Niño–Southern Oscillation (ENSO; Schneider and Gies, 2004; Killan and Lamy, 2012), and high-latitude changes in the Southern Annular Mode (SAM; Villalba et al., 2012). Determining how these globally-important ocean-atmosphere systems have changed in the past, and their impact on terrestrial environments is, therefore, fundamental for improved understanding of late Quaternary palaeoclimate.

Widespread terrestrial and marine changes occurred during Earth's transition out of the global Last Glacial Maximum (gLGM) – often referred to as the last glacial termination (LGT) – between ~20,000 and 7,000 years ago (cf. Denton et al., 2010). Although the exact sequence of events that instigated the LGT remain highly contentious (e.g. Stott

et al., 2007; Wolff et al., 2009; Denton et al., 2010), Southern Hemisphere oceans (e.g. ACC; Caniupán et al., 2011; De Deckker et al., 2012 Lamy et al., 2007; 2015), atmosphere (e.g. SWWs; Kohfeld et al., 2013; Sime et al., 2013) and cryosphere (Denton et al., 1999; Putnam et al., 2013a; 2013b; Moreno et al., 2015) underwent major changes during this period. Discussion on the mechanisms behind such pervasive environmental changes have relied largely on the phasing of events recorded in the polar ice-cores (EPICA Members, 2006; Lemieux-Dudon et al., 2010; Parrenin et al., 2013; WAIS Members, 2013; 2015; Markle et al., 2016). To what extent the events detailed in these records are representative of changes in the extra-polar regions of the Southern Hemisphere, however, remains poorly understood.

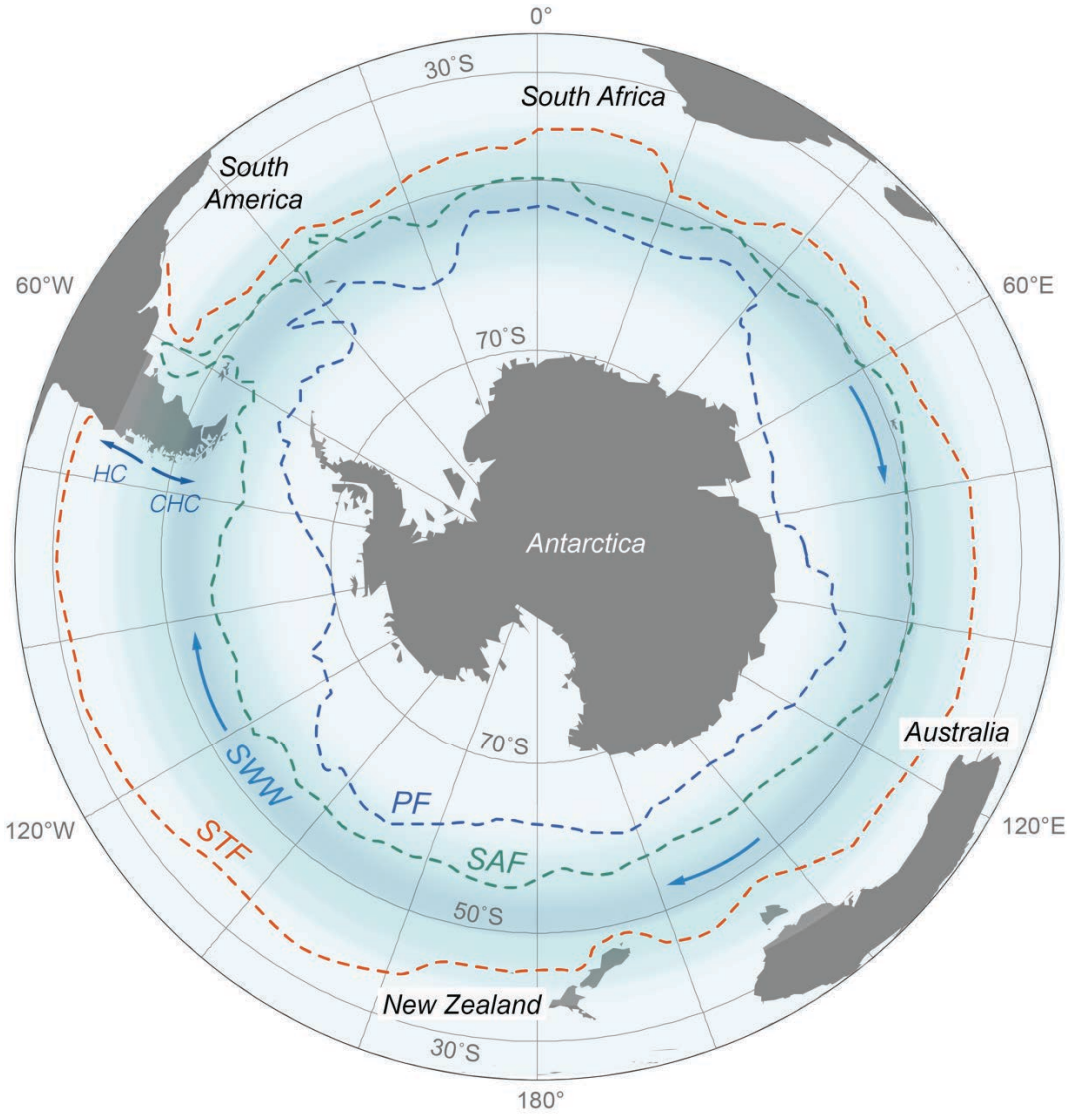

Figure 1.1. Schematic illustration of modern surface ocean fronts (cf. Orsi et al., 1995; Carter et al., 2008) and the Southern Westerly Wind (SWW) system in the Southern Hemisphere middle to high latitudes. STF = Sub-Tropical Front; SAF = Sub-Antarctic Front; PF = Polar Front; HC = Humboldt Current; CHC = Cape Horn Current.

In this context, Patagonia, situated between 40–56°S and adjacent to the South Pacific, South Atlantic, and Southern Oceans, is ideally located to test hypotheses of intra- and inter-hemispheric climate and glacial (a)synchronicity (Denton et al., 1999; Sugden et al., 2005; Moreno et al., 2015). The terrestrial geological record of the former Patagonian Ice Sheet represents one of the longest and most complete in the world (Clapperton, 1993; Coronato and Rabassa, 2011). However, many areas are unmapped, and few records resolve the detailed pattern of deglaciation throughout the LGT. This incorporates the growth and evolution of proglacial lakes (Caldenius, 1932; Turner et al., 2005) that have the capacity to modulate glacial dynamics (Porter et al., 1992; Carrivick and Tweed, 2013) and may have impacted regional climates through the sudden release of freshwater to the Pacific Ocean (Glasser et al., 2016). However, much of our current understanding is based on the chronology of maximum glacial advances (Kaplan et al., 2004; Hein et al., 2010; Boex et al., 2013), while the precise timing, nature and rates of post-LGM Patagonian Ice Sheet deglaciation are poorly constrained. This problem is made more salient by recent developments of high-resolution climate records from Antarctic ice-cores (WAIS Members, 2013; 2015; Marcott et al., 2014; Markle et al., 2016), that cannot be fully exploited through comparisons with terrestrial mid-latitude glacial changes, because the latter generally lack equivalent temporal resolution and/or firm dating control.

This thesis targets the deglacial history of two major ice lobes in the central sector of the former Patagonian Ice Sheet: the Lago General Carrera–Buenos Aires (LGC–BA) and the Lago Cochrane–Pueyrredón (LC–P) lobes. The thesis focuses on constraining the timing and nature of post–LGM evolution of ice lobes and glacial lakes.

1.2. Study area

1.2.1 Central Patagonian Andes

This thesis focuses on the region occupied by the Lago General Carrera–Buenos Aires (LGC–BA) and the Lago Cochrane–Pueyrredón (LC–P) ice lobes of the former Patagonian Ice Sheet (Figure 1.2), between around 45–48°S (Figure 1.3). The western sector of the study area along the Pacific coastline features many fjords, islands and archipelagos (Glasser and Ghiglione, 2009). The central sector is characterised by complicated relief that comprises the Patagonian Andes with summits surpassing 4000 m asl, many surrounding lake-filled valleys incised to below present sea level, and active volcanoes, such as Hudson, Macá, Cay, Mentolat and Melimoyu (Naranjo and Stern, 1998; 2004; Stern, 2004; Fontijn et al., 2014, 2016). East of the highest mountains, the landscape is dominated by two large, broadly west-east trending valleys that contain the

transnational lakes of Lago General Carrera (Chile)–Buenos Aires (Argentina) in the north, and Lago Cochrane (Chile)–Pueyrredón (Argentina) in the south (Figure 1.3), with maximum lake depths of ~600 m and ~500 m respectively (Murdie et al., 1999). These basins extend beyond the Patagonian mountain front, where the landscape transitions into semi-arid extra-Andean plains that are interspersed with basaltic upland plateaus, termed mesetas, of Miocene to Pleistocene age (Gorring et al., 2003; Guivel et al., 2006).

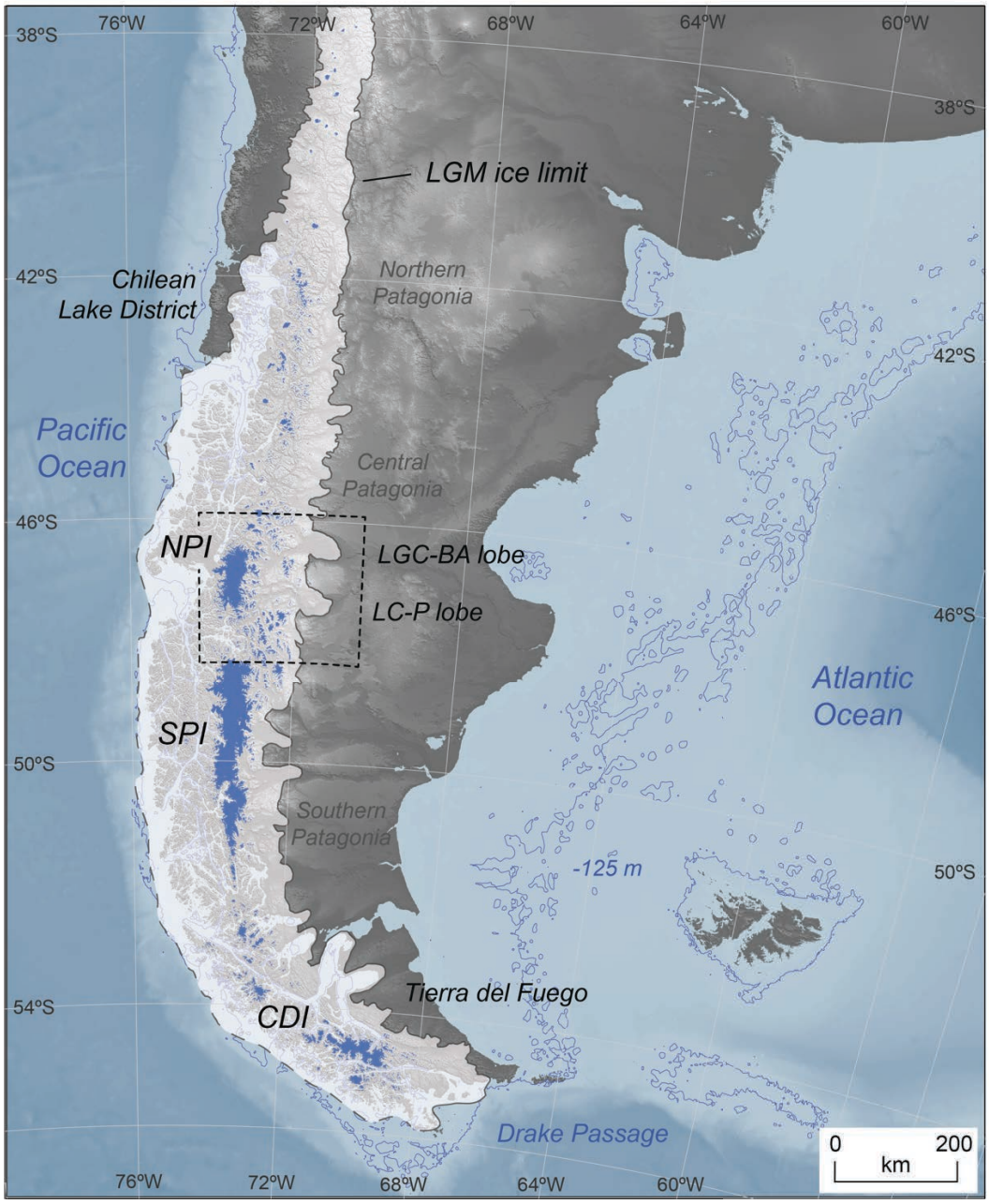

Figure 1.2. The location of the study area in central Patagonia (dashed black box). Present day icefield and glacier extents (shown in blue) are taken from the Randolph Glacier Inventory (cf. Pffefer et al., 2014). The hypothesised extent of the Patagonian Ice Sheet and the gLGM, adapted from: Singer et al. (2004) and Coronato and Rabassa (2011). The -125 m contour provides an indication of the approximate sea-level reduction at the gLGM (cf. Yokoyama et al., 2001; Lambeck et al., 2014). NPI = North Patagonian Icefield; SPI = South Patagonian Icefield; CDI = Cordillera Darwin Icefield.

At present, the glacierized portion of the study area incorporates the North Patagonian Icefield (NPI) and many smaller satellite icefields including Monte San Lorenzo (Figure 1.3). During Quaternary glaciations, NPI outlet glaciers advanced eastwards, coalesced with glaciers from the Southern Patagonian Icefield (SPI), and formed the LGC–BA and LC–P lobes of the Patagonian Ice Sheet (Figure 1.2; Glasser and Jansson, 2005; Glasser et al., 2008; Hein et al., 2010). This ice sheet blocked the drainage of rivers toward the Pacific Ocean and shifted the continental drainage divide ~200 km further east of its interglacial positon over the Andean Cordillera (Turner et al., 2005; Figure 1.3).

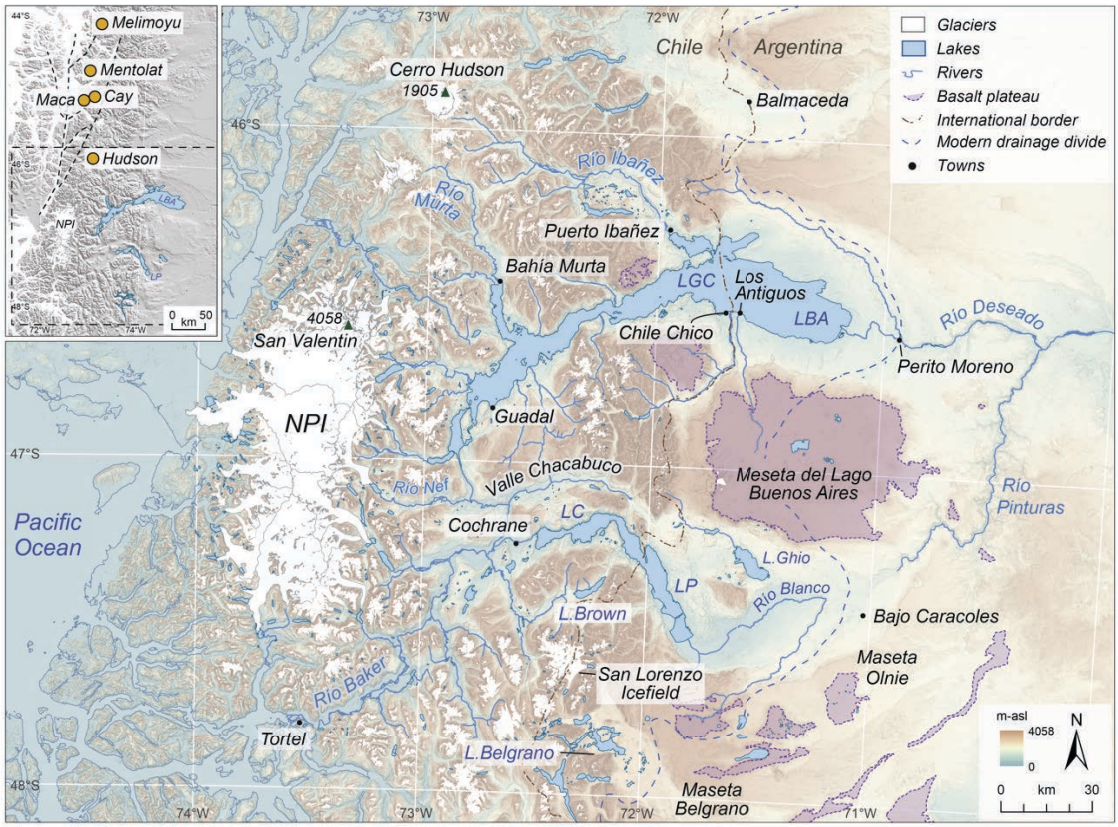

Figure 1.3. Map of the study area in the vicinity of the North Patagonian Icefield (NPI), with major place names or features labelled. Inset shows location of major regional volcanic centres.

1.2.2 Río Fenix Chico valley

Within the wider central Patagonian region (Figure 1.3), much of the new research presented in this thesis results from investigations in the Río Fenix Chico valley (Figure 1.4; 46.58°S, 71.07°W). The ~10 km long, broadly east-west trending valley lies at the eastern end of LGC–BA. The valley is situated on the distal rising side of the glacially overdeepened LGC–BA basin (Kaplan et al., 2009), and drops from ~400 m asl at the inner limit of the local LGM Fenix moraine complex, to 200 m asl where the modern Río Fenix Chico enters LGC–BA (Figure 1.4). The valley itself comprises a narrow gorge

incised through glacigenic deposits (Caldenius, 1932). Glaciolacustrine sediments record the development of a proglacial lake during deglaciation, and are thought to be annually-laminated, i.e. varved (Caldenius, 1932; Sylwan, 1989). If annual in nature, these laminations could offer precise chronological control on the timing of deglaciation, and dating of ice lobe retreat activity (e.g. Ridge et al., 2012). However, these sequences have not been studied in detail to confirm a varve origin, and robust independent dating control is absent.

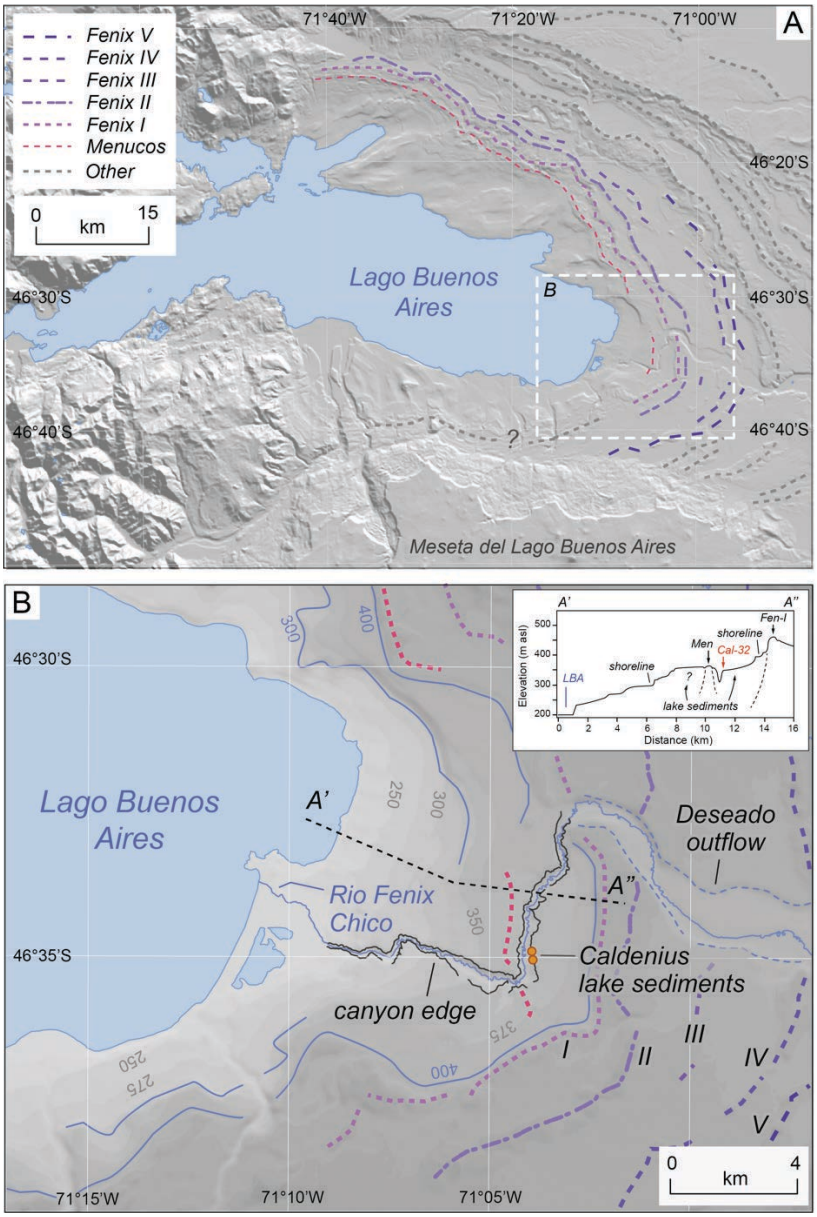

Figure 1.4. (A) Map of the Lago Buenos Aires basin east of the Patagonian mountain front. Major LGM moraines after Singer et al. (2004) and Douglass et al. (2006). Older moraine complexes shown with dashed grey lines (cf. Singer et al., 2004). Location of the Río Fenix Chico valley is indicated. (B) Map of Rio Fenix Chico valley with major LGM-aged geomorphological features, and location of sites studied by Caldenius (1932). Major proglacial lake levels at ~400 and ~300 m asl (blue lines) after Caldenius (1932), Hein et al. (2010) and Glasser et al. (2016), with Deseado outflow (the eastwards-draining outflow of the 400 m asl lake to the Atlantic Ocean) indicated by blue dashed lines. Inset diagram shows surface elevation profile of A'–A'' transect.

1.3 Previous work

The history of Quaternary glaciations has previously been synthesised at the ice sheet scale in several comprehensive reviews (e.g. Rabassa and Clapperton, 1990; Rabassa et al., 2011; Coronato et al., 2004; Glasser et al., 2008; Kaplan et al., 2008; Rabassa et al., 2008; Rodbell et al., 2009; Coronato and Rabassa, 2011; Mendelova et al., 2017). However, a critical review of the evidence from the central Patagonian region is required to identify issues with previous reconstructions of the deglacial history of the LGC–BA and LC–P ice lobes (see also reviews in Hein, 2009 and Boex, 2011), and possible targets for improvement that are addressed by this thesis.

1.3.1 Glacial extent

The maximum extent of Quaternary glacial advances has received most attention. Caldenius (1932) made the first observations of glacial deposits in central Patagonia, and defined four major nested glacial limits (Figure 1.5) that he correlated across Patagonia. Based on their state of preservation, he argued that these moraine systems were relatively young. Identifying parallels with the Weichselian glaciation moraine systems of northern Europe and Scandinavia, Caldenius (1932) named the four Patagonian limits accordingly, and in descending order: the Initioglacial, Daniglacial, Gotiglacial and Finiglacial limits (Figure 1.5; Table 1.1). Subsequent dating (section 1.3.2; Table 1.1) has shown that these limits formed over multiple glaciations (Mörner and Sylwan, 1987; 1989; Sylwan et al., 1991; Ton-That et al., 1999; Singer et al., 2004; Hein et al., 2011; 2017). More recent studies have built upon the framework developed by Caldenius (1932) and other early works (Feruglio, 1950; Fidalgo and Riggi, 1965) to constrain, in greater detail, the configuration of former glacial limits, using both field and remotely sensed mapping techniques (Figure 1.6; Singer et al., 2004; Kaplan et al., 2004; Douglass et al., 2006; Glasser and Jansson, 2008; Hein et al., 2009; 2010; 2011).

However, ice lobe extents have proven more difficult to constrain through the last deglaciation. Moraine ridges and ice-contact landforms are best developed close to the modern NPI (Turner et al., 2005; Glasser et al., 2006; 2009; 2012; Nimick et al., 2016) and record the temporary stabilisation or re-advance of NPI outlet glaciers. However, between these limits and the maximum advance moraines on the Argentine plains, former ice lobe positions are largely unconstrained. For instance, the LGM Fenix moraines at LGC–BA (Table 1.1) occur ~150 km further east of the next deglacial moraine sets identified by Glasser et al. (2012). This gap in the geomorphological record relates to the presence of large lakes in the LGC–BA and LC–P basins, which potentially conceal geomorphological evidence of former ice-margins. Moreover, glaciolacustrine,

rather than ice-marginal, landforms dominate west of the mountain front (Turner et al., 2005; Bell et al., 2008; Bourgois et al., 2016; Glasser et al., 2016) because of proglacial lake growth during deglaciation (section 1.3.3). Interestingly, the spatial extent of palaeolake evidence (e.g. shorelines) has the potential to constrain ice-margin position at various stages, but remains underutilised for this purpose.

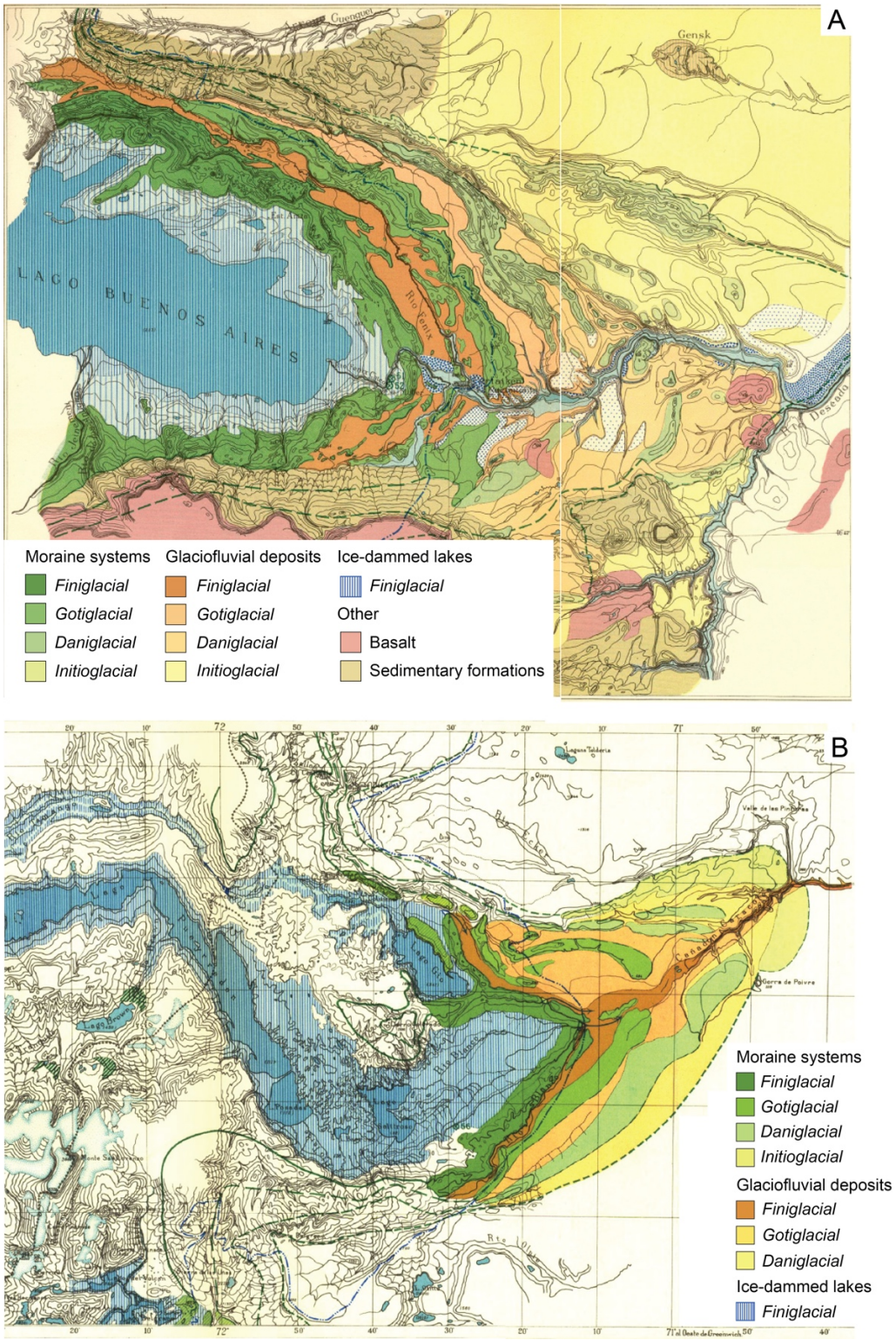

Figure 1.5. Caldenius' (1932) original mapping at (A) Lago General Carrera–Buenos Aires; and (B) Lago Cochrane–Pueyrredón, with proposed glacial stages.

Table 1.1. Names (cf. Caldenius, 1932) and ages of maximum ice lobe moraine complexes. Limits (n) refer to minimum number of former ice-margin positions identified within a given moraine complex. Original dating evidence is reported in the following publications: Singer et al. (2004); Kaplan et al. (2004); Douglass et al. (2006); Hein et al. (2009, 2010, 2011, 2017); Smedley et al. (2016). Ticks indicate a moraine limit dated by $^{40}Ar/^{39}Ar$, cosmogenic nuclide exposure dating (CND), or luminescence dating (Lum). Marine Isotope Stages (MIS) reflect the chronological range of available dating evidence.

	Moraine complex			Dating			
Valley	Local name	Limits (*n*)	Caldenius (1932)	$^{40}Ar/^{39}Ar$	CND	Lum.	Marine Isotope Stage (MIS)
LGC–BA	Telken	7	Initioglacial	✓	✓		MIS 30-34
	Deseado	3	Daniglacial		✓	✓	MIS 10-18
	Moreno	3	Gotiglacial		✓	✓	MIS 6-8
	Fenix	5	Finiglacial		✓	✓	MIS 2-3
LC–P	Gorra de Poivre	?	Initioglacial		✓		MIS 30-34
	Cañadon de Caracoles	≥3	Daniglacial		✓		MIS 10-18
	Hatcher	≥2	Gotiglacial		✓		MIS 6-8
	Río Blanco	4	Finiglacial		✓		MIS 2

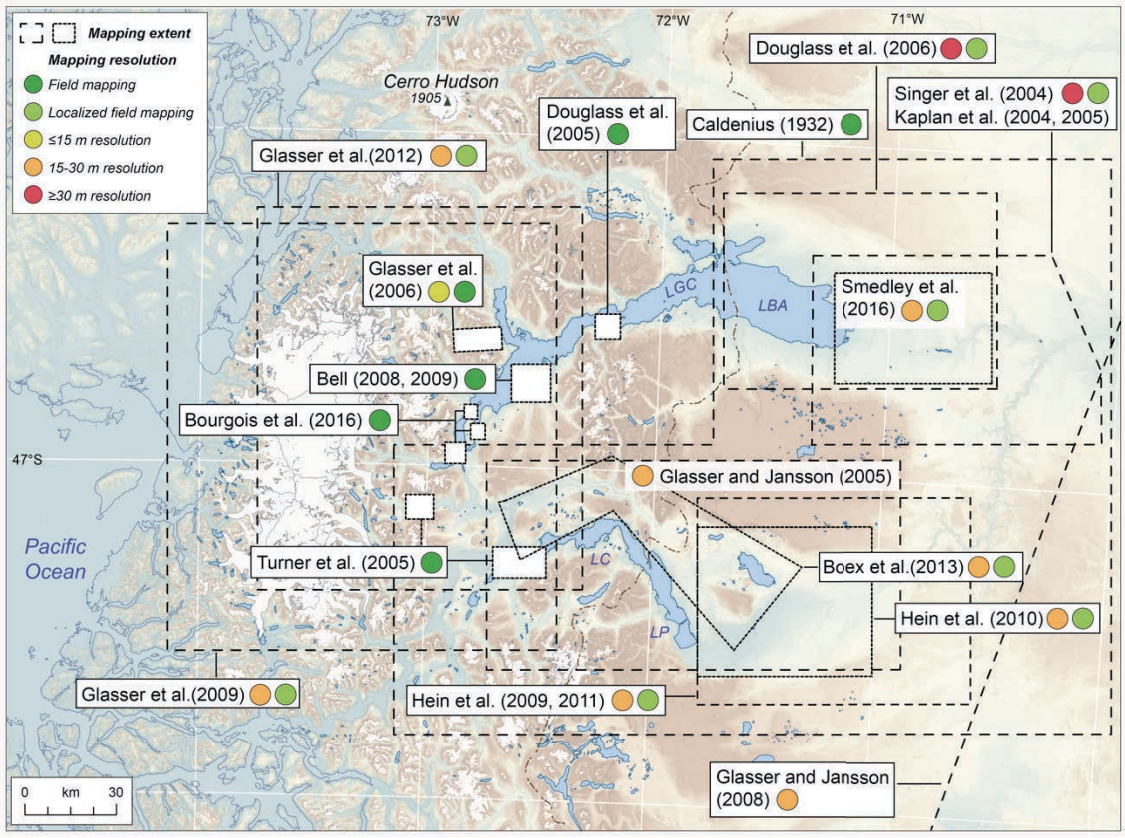

Figure 1.6. Extent and resolution of previous glacial geomorphological mapping in the vicinity of the North Patagonian Icefield (NPI).

Much progress on the configuration of former ice lobes has been made since the early work of Caldenius (1932), particularly west of the mountain front (Figure 1.6), with a greater appreciation of the variety and distribution of glacial landforms (Glasser and

Jansson, 2008; Glaser et al., 2008). However, only select areas have been mapped in detail, from high-resolution imagery (<15 m) or in the field (Figure 1.6). At the ice lobe-scale, previous work has relied on coarse resolution (~30 m) imagery, such that subtle or complex geomorphology may be overlooked. Higher resolution mapping may offer additional information on ice position(s) during the last deglaciation.

1.3.2 Glacial chronology

A range of dating techniques have been applied in the study area to constrain the timing of ice lobe advances (Figure 1.7; Table 1.1), with most attention given to the nested latero-frontal moraine belts first mapped by Caldenius (1932). Magnetic polarity studies were the first to question the chronological framework proposed by Caldenius (1932), demonstrating that some of the outer moraines at LGC–BA (Mörner and Slywan, 1987; 1989) and LC–P (Sylwan et al., 1991) formed during the Matuyama Reversed Chron over ~780 ka ago. The evidence for older advances has subsequently been supported by $^{40}Ar/^{39}Ar$ dating of basaltic lava flows found interbedded with glacial deposits (Ton-That et al., 1999; Singer et al., 2004). At LGC–BA, this analysis dated the outermost Telken complex to between ~1016 ka and ~760 ka, and the Deseado I–III and Moreno I–III deposits to ~760 ka to ~109 ka (Table 1.1). Direct dating of glacial deposits has since refined the timing of maximum ice lobe advances. Cosmogenic nuclide exposure dating of moraine boulders (Kaplan et al., 2004; 2005; Douglass et al., 2006; Hein et al., 2010) and outwash cobbles (Hein et al., 2009; 2011; 2017), and luminescence dating of outwash sands (Smedley et al., 2016), has provided evidence for ice lobe advances in Marine Isotope Stage (MIS) 2, 3, 6, and 8 (Figure 1.7). Together these efforts have yielded one of the longest and most comprehensive ice sheet chronologies in the world.

The onset of deglaciation in central Patagonia is constrained by the culmination of local-LGM advances (Figure 1.8) that are dated by (i) moraine boulder ages at LGC–BA and LC–P (Kaplan et al., 2004; Douglass et al., 2006; Hein et al., 2010); (ii) luminescence ages at LGC–BA (Smedley et al., 2016); and (iii) cosmogenic nuclide exposure ages derived from ice-scoured bedrock outcrops and erratic boulders on a mountain ridge above Valle Chacabucco, and which provide constraints on ice sheet surface elevation and thickness (Boex et al., 2013). Dates for the broad timing of deglaciation range from 18.7 ± 1.7 ka based on moraine boulder ages (weighted mean and standard deviation derived from recalculated ages; Kaplan et al., 2011), to as young as 14.7 ± 2.1 ka based on luminescence dating (Smedley et al., 2016). Boex et al. (2013) constrain a phase of ice sheet thinning between ~18–15 ka.

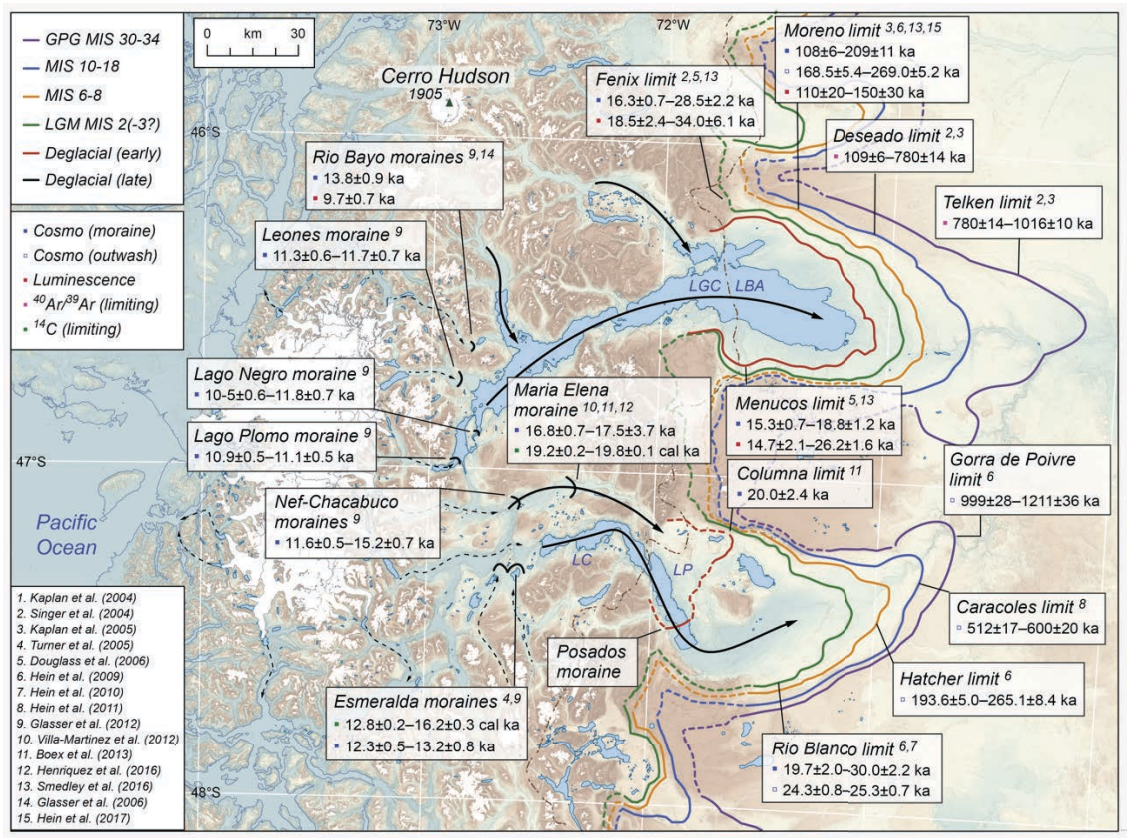

Figure 1.7. Major glacier limits and summary of associated dating evidence based on previous studies. Cosmogenic nuclide exposure ages are presented as detailed in original publications, except where original dates have been recalculated with Southern Hemisphere production rates (see Kaplan et al., 2011). Luminescence ages are reported as in original publications. Radiocarbon (^{14}C) ages have been recalibrated in Oxcal v4.3 (Bronk Ramsey, 2009) using the SHCal13 calibration curve of Hogg et al. (2013). Arrows represent major ice lobe flow trajectories cf. Glasser and Jansson (2005).

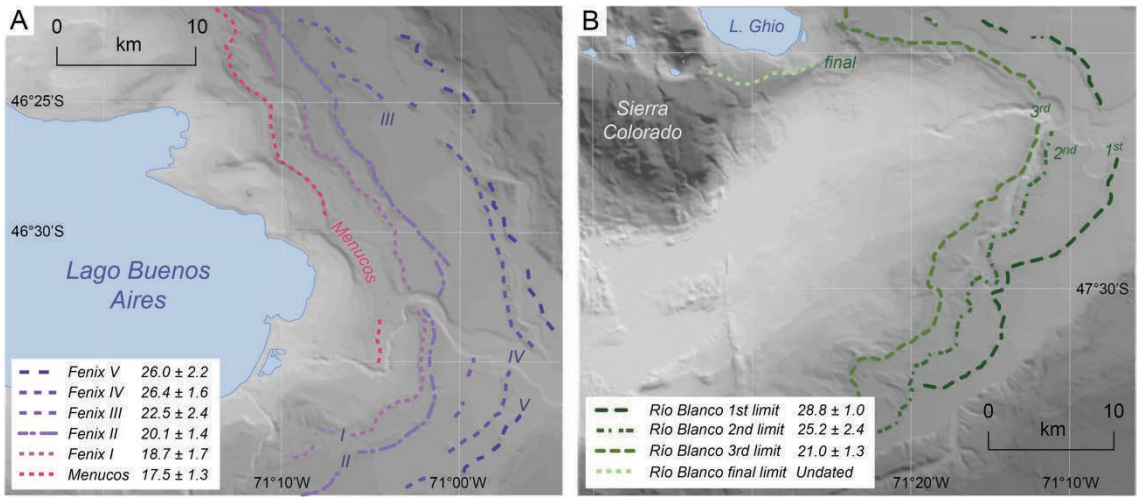

Figure 1.8. Distribution and age of LGM moraine complexes at (A) Lago Buenos Aires; and (B) Lago Pueyrredón. Ages are weighted mean and standard deviations derived from recalculated cosmogenic nuclide exposure ages, using the time-dependent scaling scheme (Lm) of Lal (1991) and Stone (2000) at 0 cm-yr^{-1} erosion rate, and the Lago Argentino (50°S) production rate of Kaplan et al. (2011). Original data from Kaplan et al. (2004), Douglass et al. (2006), and Hein et al. (2010).

These ages are hampered by relatively low chronological precision. Existing chronological constraints afford limited comparisons of deglacial activity and higher resolution climate records, such as the Antarctic ice cores that resolve abrupt (sub-millennial) climate changes (WAIS Members, 2013; 2015). As such, knowledge on the local to hemispheric controls on Patagonian Ice Sheet deglaciation remain poorly understood (Moreno et al., 2015). The purported, though unproven, varves at Río Fenix Chico (cf. Caldenius, 1932; section 1.2.2; Figure 1.3 and 1.4) have the potential to provide high-precision dating of deglaciation at LGC–BA. Varve records have been developed for the former Scandinavian (De Geer, 1912, 1940; Wolhfarth et al., 1997) and Laurentide (Antevs, 1922, 1928; Breckenridge, 2007; Breckenridge et al., 2011; Ridge et al., 2012) ice sheets, although their potential is unexplored in Patagonia.

Other chronological issues arise from landform evidence preserved in the main valleys close to the modern NPI, which delimit stabilisation positions of waning ice lobes during the last deglaciation (Figure 1.7; Turner et al., 2005; Glasser et al., 2006; 2012; Bourgois et al., 2016; Nimick et al., 2016). Based on comparable cosmogenic nuclide exposure dates from four separate valleys, Glasser et al. (2012) argue for a regional advance of NPI outlet glaciers at the time of the European Younger Dryas, between ~12.8–11 ka (Figure 1.7). In contrast, Nimick et al. (2016) date moraine ridges from an expanded Colonia glacier that exhibit similar morphostratigraphic position, but coincide in timing with the Antarctic Cold Reversal. These differences may represent variable glacier responses to climatic fluctuations, or result from currently unidentified methodological issues.

There is also disagreement between moraine boulder ages, luminescence ages from glaciolacustrine landforms, and basal radiocarbon ages sampled from lake basins that were exposed subaerially after ice lobe retreat (Villa-Martinez et al., 2012; Henríquez et al., 2017). One example is Valle Chacabuco, where boulders on the Maria Elena moraine (Figure 1.7) yield an age of ~17.1 ka (Boex et al., 2013) whereas organic remains deposited immediately behind the moraine yield ages of ~19.8 cal ka (Villa-Martinez et al., 2012). Glasser et al. (2016) derived luminescence ages from relict lake shorelines, deltas, and capping aeolian sediments that indirectly date ice lobe extents, based on inferred relationships between proglacial lake extent and ice-margin position (see section 1.3.3). However, the youngest of these ages are ~4–5 ka younger than radiocarbon dating evidence for lake drainage (Turner et al., 2005), whilst the spatial relationship between lake level and ice-dams remains poorly constrained by geomorphological evidence (section 1.3.3).

In summary, the greatest ambiguity is associated with the exact timing of ice lobe positions or configurations during the last deglaciation, owing to a combination of relatively low dating resolution and uncertainties around the spatial relationships between glacial landform assemblages. This problem requires more comprehensive mapping to constrain the relative order of events. Palaeolake evidence may prove essential in this goal, as lake extent is intrinsically related to the location of ice-dams.

1.3.3 Proglacial lakes

The growth and evolution of proglacial lakes represents a major component of deglaciation in central Patagonia. The evidence for these lakes includes raised shorelines and terraces, lacustrine deltas, beaches, and lake sediments (Caldenius, 1932; McCulloch et al., 2005; Turner et al., 2005; Bell et al., 2008; 2009; Hein et al., 2010; Villa-Martinez et al., 2012; Bourgois et al., 2016; Glasser et al., 2016; Martinod et al., 2016; Henríquez et al., 2017). Previous work has focused on the elevation of palaeolake indicators to establish a sequence of proglacial lake levels, ice-dam positions, and lake drainage events (Bell, 2008; Turner et al., 2005; Bourgois et al., 2016; Glasser et al., 2016). This work has been conducted at a range of scales and using a variety of techniques (Table 1.2), leading to contradictory reconstructions in places. However, all models portray an inter-basin lake system (Figure 1.9), often termed the 'united' lake (cf. Turner et al., 2005; Hein et al., 2010), which initially drained eastwards to the Atlantic (Figure 1.9). The exact sequence and level(s) of palaeolakes, and the timing and route of westwards drainage to the Pacific Ocean, however, remains ambiguous (Figure 1.9).

This uncertainty results from two main issues. First, previous shoreline mapping has been generally limited in spatial coverage and/or resolution (Figure Table 1.2; Figure 1.6). Second, lake level reconstructions have failed to adequately explain spatial trends in shoreline elevation. For instance, while Glasser et al. (2016) map regional shoreline distributions, they employ a pixel-counting method to define former water levels (Table 1.2) that fails to account for shoreline tilt due to post-glacial isostatic rebound. These issues have prevented robust quantification of isostatic adjustment, based on shoreline tilt datasets, which are fundamental to accurate definition of palaeolake levels and outflows (e.g. Breckenridge, 2013; 2015). Robust constraints on palaeolake extent and elevation are also critical to the interpretation of existing cosmogenic nuclide exposure dates (e.g. Glasser et al., 2006; 2012; Bourgois et al., 2016; Boex et al., 2013) because moraine boulders submerged beneath lake waters would be shielded from incoming

cosmogenic rays until exposed by lake-level drop (Hein et al., 2010) and, therefore, yield erroneous ages for glacial limits.

Table 1.2. Summary of methods used in palaeolake reconstruction studies. Isostasy column refers to method used to quantify shoreline tilt. In chronology column, 'direct' refers to dating of shoreline features; 'indirect' refers to dating of other features (e.g. moraine boulders); CND = cosmogenic nuclide exposure dating; OSL = optically stimulated luminescence dating.

	Geomorphology (shorelines)				Chronology
Study	Mapping	Elevation	Coverage	Isostasy	
Turner et al. 2005	Field	GPS	Local	Linear	^{14}C (limiting)
Bell, 2008	Field	GPS	Local	n/a	n/a
Hein et al. 2010	Field/satellite	n/a	Local	n/a	CND (indirect)
Borgois et al. 2016	Field	GPS	Local	n/a	CND (indirect)
Glasser et al. 2016	Field/satellite	DEM (30m)	Regional	n/a	OSL (direct); CND
Martinod et al. 2016	Field	GPS	Local	Linear	n/a

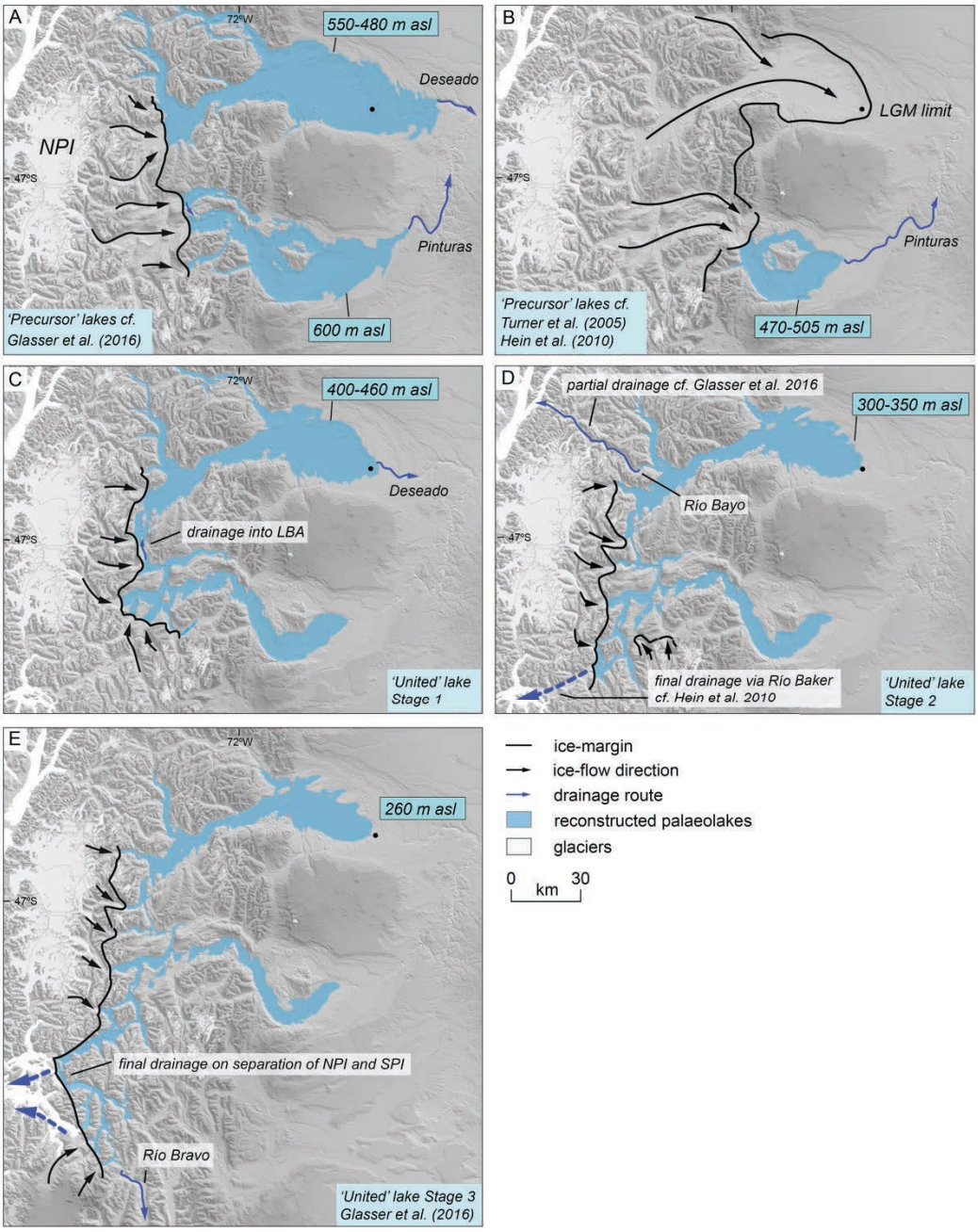

Figure. 1.9. Summary of main proglacial lake levels during the last deglaciation of the Patagonian Ice Sheet (cf. Turner et al., 2005; Hein et al., 2010; Glasser et al., 2016). The location of the Río Fenix Chico valley is indicated by the filled black circle. Stages (A) and (B) represent competing models for the configuration of precursor lake levels, which existed prior to the unification of lakes between the LGC–BA and LC–P basins. (A) Glasser et al. (2016) reconstruct a 550–480 m asl lake system in LGC–BA, which overtops the LGM-age Fenix moraine complex, based on the existence of high-level raised deltas in tributary valleys west of the mountain front. (B) Hein et al. (2010) reconstruct a 505–470 m precursor lake system in LC–P, but no corresponding lake system in LGC–BA, based on the elevation of the highest shorelines east of the mountain front, which are cut into the late LGM-age Fenix I moraine at ~400 m asl. (C) Ice lobe retreat exposes a linking valley at Lago Bertrand and allows a unified glacial lake system to develop at ~400–460 m asl (Turner et al., 2005; Bell, 2008; Hein et al., 2010). This lake system drained to the Atlantic via the Río Deseado at LGC–BA. (D) Glacier retreat in the Río Bayo valley opens a drainage route to the Pacific Ocean, and causes a lake level drop to 300–350 m asl (Glasser et al., 2016). This drainage reversal represents the likely mechanism for the formation of the Río Fenix Chico gorge, and subaerial exposure of glaciolacustrine sediments. Hein et al. (2010) argue that final lake drainage (dashed blue arrow) to the Pacific occurred at ~12.8 ka (cf. Turner et al., 2005) as the Río Baker valley became ice free. (E) In contrast, Glasser et al. (2016) reconstruct a 260 m asl level that drained southwards into Lago O'Higgins via Río Bravo, before draining to the Pacific on separation of the NPI and SPI.

1.3.4 Glacial dynamics

There has been limited work on the nature of glacial dynamics in central Patagonia. Over glacial–interglacial timescales, Kaplan et al. (2009) noted a trend of decreasing ice extent since the 'Greatest Patagonian Glaciation' (cf. Mercer, 1976) and cited the potential impact of erosional feedbacks on ice lobe dynamics, where subglacial erosion can limit the extent of ice in subsequent glacial cycles through mass-balance and mass flux changes. This process may have caused overdeepening of the LGC–BA and LC–P basins (Kaplan et al., 2009), which may also influence glacial dynamics (cf. Barr and Lovell, 2014; see discussion below).

Glasser and Jansson (2005) mapped inferred LGM features consistent with landscape modification by fast ice-flow and sustained warmed-based conditions, and suggest that topographically-controlled ice-streaming may have decoupled the ice lobes from climate-driven changes in extent and thickness. Moreover, Glasser and Jansson (2005) argue that fast-flow dynamics may explain discrepancies between empirical LGM limits and those simulated in ice sheet-scale numerical models (Hulton et al., 1994; 2002).

Two additional, but largely unconsidered factors, require further attention. First, the formation and growth of ice-contact palaeolakes in LGC–BA and LC–P (section 1.3.3) could have influenced ice lobe dynamics, as retreat into deep basins often triggers enhanced calving and accelerated recession (Benn et al., 2007). This, in turn, can induce a positive feedback effect, where lake expansion causes further calving and retreat

(Carrivick and Tweed, 2013). Such mechanisms are suggested to cause rapid disintegration (Warren et al., 1995; Boyce et al., 2007), or rapid surges due to low effective pressures at the ice margin (e.g. Stokes and Clark, 2003). Calving dynamics strongly affect the behaviour of modern lake-terminating glaciers of the Patagonian icefields (e.g. Warren and Aniya, 1999; Sugiyama et al., 2011), and has been suggested from palaeo-records in southernmost Patagonia (Porter et al., 1992; Lovell et al., 2012). The overdeepened nature of the LGC–BA and LC–P basins (Murdie et al., 1999; Kaplan et al., 2009) would suggest that such processes were also likely important during the last deglaciation in central Patagonia.

Second, and intrinsically associated with calving dynamics, basin topography can be important in lake-terminating environments (Barr and Lovell, 2014). Across the study area, bed topography varies significantly, however, reverse-bed gradients are common (Scalabrino et al., 2010). Such zones often experience faster retreat rates due to greater water depths and enhanced calving (e.g. Boyce et al., 2007), as described above. Around the modern NPI, changes in valley width or depth are also common (Figure 1.3). Zones of valley narrowing or shallowing could have acted as topographic pinning points that promoted ice-margin stability through enhanced basal drag, lateral drag and backstress (O'Neel et al., 2005; Benn et al., 2007), causing local differences in ice lobe retreat dynamics.

The factors outlined above require greater consideration to help separate climatic from internal controls on deglaciation in central Patagonia. These could be tested with the geomorphological record. For example, in some systems ice-marginal landforms, such as moraines or grounding-line fans, concentrate at topographic pinning-points where valley width or depth is reduced (Barr and Lovell, 2014).

1.3.5 Numerical modelling

Several studies have attempted to simulate the maximum extent and deglaciation of the LGM Patagonian Ice Sheet. Hulton et al. (1994; 2002) used a coupled ice sheet–climate model to simulate the entire Patagonian Ice Sheet at the LGM and during several retreat stages (Figure 1.10). The LGM simulation is achieved using a stepped 6°C temperature decrease and a constant wind field, and illustrates a highly dynamic western maritime margin driven by high precipitation and positive mass balance (Hulton et al., 2002). The eastern continental margin also experiences positive mass balance, but at an order of magnitude lower. Nonetheless, east of the NPI, the simulated LGM margin overestimates the empirical record by ~150 km. Using a stepped temperature increase of 6°C, Hulton et al. (2002) simulated rapid deglaciation of the LGM ice sheet (Figure

1.11). In northern Patagonia, ice diminished extensively in <1000 model years. Between ~45–51°S, however, the ice sheet survived for longer, but had separated into the Northern and Southern Patagonian Icefields by ~5000 years of modelled deglaciation.

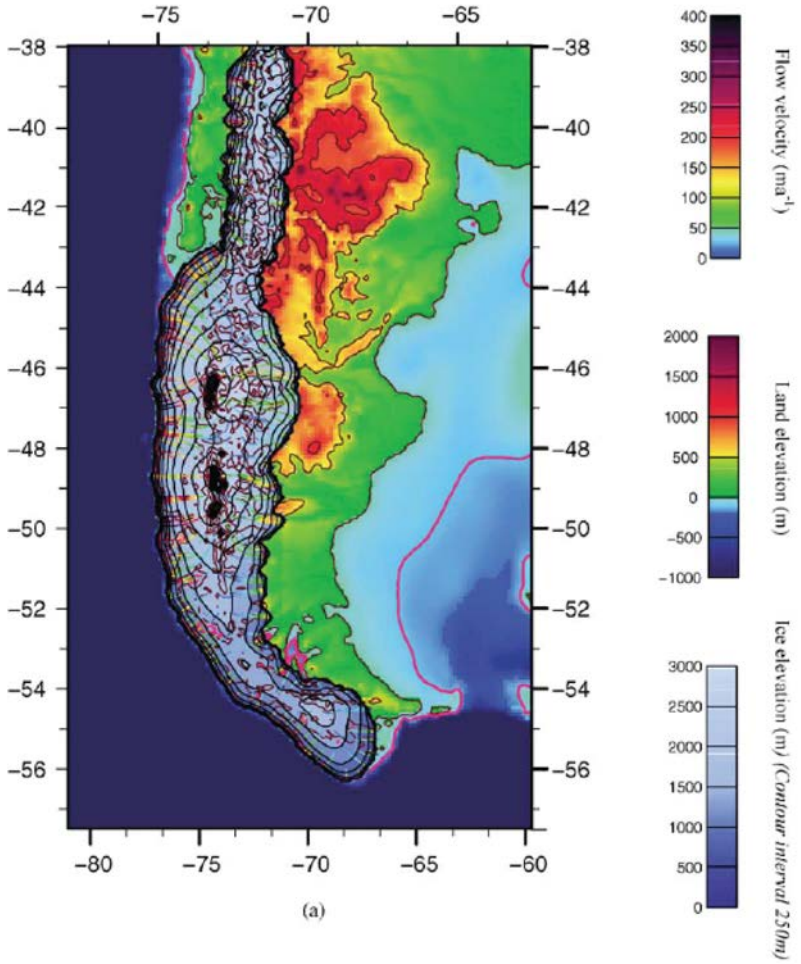

Figure. 1.10. Modelled extent of the Patagonian Ice Sheet at the Last Glacial Maximum cf. Hulton et al. (2002). Note the overestimation of ice extent east of the NPI.

To address the problem of model overestimation east of the Andes (Hulton et al., 1994; 2002), Hubbard et al. (2005) used a finer resolution model to investigate the dynamics of the LGC–BA and LC–P lobes (Figure 1.12). The time-dependent model used a 2-km grid to better capture relief changes, and allowed ice thickness, isostatic bed adjustment, and ice flow to freely interact. The model also enabled basal sliding and, importantly, calving (see section 1.3.3 and 1.3.4). Hubbard et al. (2005) simulated an ice limit at the Fenix I–V complex (cf. Caldenius, 1932; Table 1.1) through an ELA lowering of 750–950 m, which yielded highly-dynamic, low gradient ice lobes with regions of fast flow. In this model, the LGC–BA and LC–P lobes drain the ice sheet interior and prevent excessive ice build-up and eastward expansion through draw-down of the main accumulation areas (Hubbard et al., 2005).

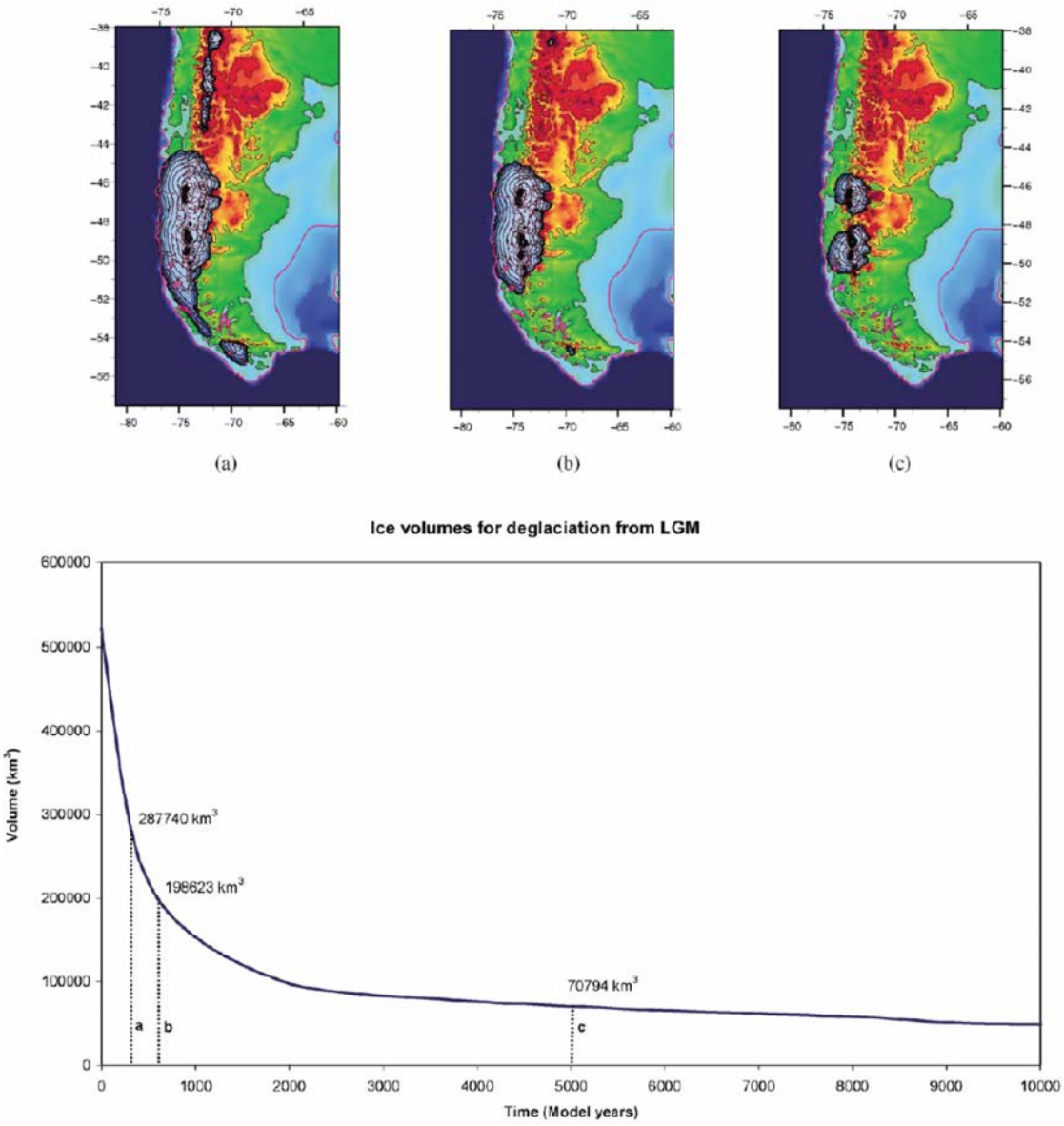

Figure 1.11. Time-slices of Patagonian Ice Sheet deglaciation simulated by Hulton et al. (2002) following abrupt 6°C warming after (a) 300; (b) 600; and (c) 5000 modelled years. Lower graph depicts ice-volume reduction through simulated deglaciation.

Deglaciation was forced using a re-scaled Vostok ice-core record (Petit et al., 1999), and illustrates gradual shrinkage (<10% volume) before ~16 ka, followed by rapid collapse. Interestingly, the model predicts ice-margin stabilisation at ~13.5 ka, coincident with the ACR (Figure 1.12e). This opposes recent evidence for glacier re-advance during the Younger Dryas interval (Glasser et al., 2012; see section 1.3.1). This issue remains contentious in central and northern Patagonia, as while proxy records indicate cooler and wetter conditions during ACR (e.g. Villa-Martinez et al., 2012; Moreno et al., 2015), evidence for renewed glacial activity is currently limited (Nimick et al., 2016), unlike in southeastern Patagonia (e.g. Moreno et al., 2009; Strelin et al., 2011; García et al., 2012).

Ice sheet modelling offers the potential to gain significant insights into ice lobe dynamics and climate during deglaciation. At present, however, there are few empirical constraints on ice lobe position, and where available, mapped and dated moraine limits close to contemporary icefield limits have yielded contradictory ages (e.g. Turner et al., 2005; Glasser et al., 2012; Villa-Martinez et al., 2012; see section 1.3.2). Improved constraints on ice lobe configuration and timing are, therefore, essential requirements to further test modelling capabilities, and require more detailed interrogation of the geomorphological record.

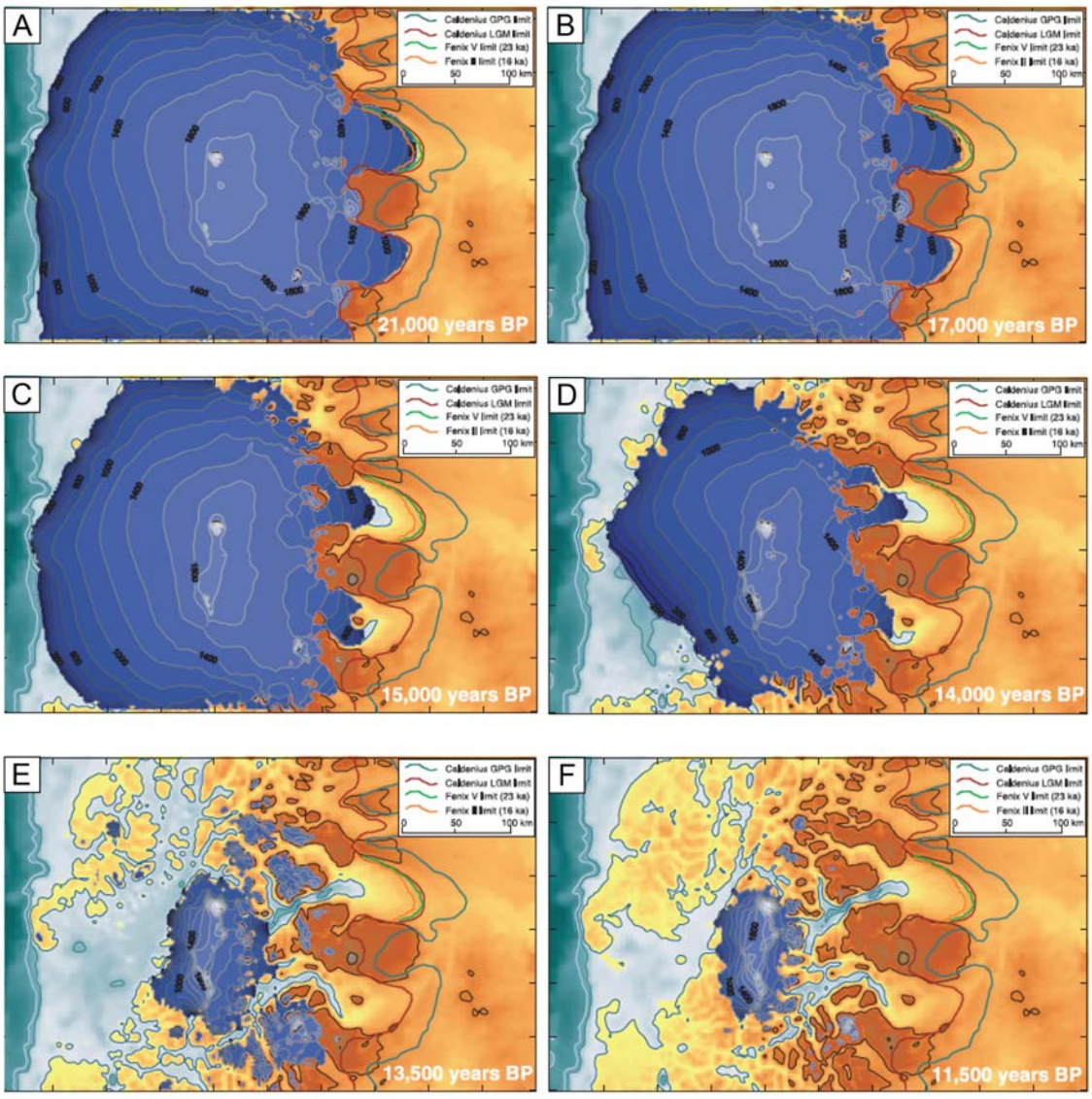

Figure. 1.12. Time-slices of deglaciation simulated by Hubbard et al. (2005) using a time-dependent three-dimensional ice-flow model. The model depicts ice sheet surface elevation and isostatic adjustment. Ice sheet extent at (A) 21,000 yrs BP; (B) 17,000 yrs BP; (C) 15,000 yrs BP; (D) 14,000 yrs BP; (E) 13,500 yrs, BP, where outlet glaciers stabilise during the Antarctic Cold Reversal (ACR); and (F) 11,500 yrs BP.

1.3.6 Summary

Previous work on the glacial history of central Patagonia has focused primarily on maximum ice lobe advances, which are the most comprehensively mapped (section 1.3.1) and dated (section 1.3.2). However, there are several issues that require further investigation to better characterise the nature of the last deglaciation.

1) There is significant uncertainty in the long-term deglacial history of ice lobes and proglacial lakes, from the LGM to early Holocene. There are few firm constraints on ice-margin position through time, whilst the dating of mapped limits has yielded inconsistent results (Turner et al., 2005; Glasser et al., 2012; Villa-Martinez et al., 2012; Henríquez et al., 2017). Moreover, relationships between ice lobe position and palaeolake extent(s) are spatially poorly constrained. This is highlighted by the current range of competing palaeolake models, with major differences in lake configuration, the phasing of lake level changes, and the route and timing of lake drainage events (Turner et al., 2005; Bell et al., 2008; Hein et al., 2010; Bourgois et al., 2016; Glasser et al., 2016; Table 1.2; Figure 1.9). As proglacial lakes formed an integral part of deglaciation in central Patagonia, further constraint on their configuration and timing may help resolve current uncertainties. Robust isostatic adjustment data is needed to accurately correlate regional lake levels and identify outflows (e.g. Breckenridge et al., 2013; 2015). Such information may circumvent current discrepancies around chronological studies, by testing whether dated moraine boulders were submerged beneath palaeolakes, and therefore shielded (Hein et al., 2010). Systematic, high-resolution mapping conducted at the ice lobe-scale is therefore a fundamental first step to resolving the long-term deglacial history of central Patagonia.

2) The precise timing of ice sheet deglaciation is blurred by chronological uncertainties, and differences between dating techniques (e.g. cosmogenic nuclide exposure dating: Kaplan et al., 2004; Douglass et al., 2006; and OSL: Smedley et al., 2016). Cosmogenic nuclide exposure dating of moraine boulders has revolutionised the chronology of the major ice lobe advances in central Patagonia, securely dating them to the gLGM (Kaplan et al., 2004; Douglass et al., 2006; Hein et al., 2010). However, such approaches rarely yield sub-millennial dating precision (Figure 1.8), and are not ideally suited to constraining the precise timing of deglaciation, being inherently biased towards ice lobe advance and temporary ice sheet stability. As previously mentioned (section 1.3.1), there are also major geomorphological gaps between the LGM limits and recessional limits dated to ~11–13 ka, during which the dynamics and rates of ice lobe deglaciation are unknown. OSL dating of raised shoreline deposits (e.g. Glasser et al., 2016) may help

bridge this gap, however, these techniques are limited by large chronological uncertainties, and ice–lake spatial relationships are not yet sufficiently constrained.

3) The issues raised in (1) and (2) have important implications for understanding the potential climatic controls on the last deglaciation in central Patagonia. Over multi-millennial timescales, the timing of major changes in ice lobe or palaeolake configuration cannot be securely compared with climatic records, because a reconstruction that reconciles the available geomorphological and chronological data has yet to be achieved. Moreover, the role of internal processes (e.g. calving) and topography are not yet well understood from either empirical datasets (Glasser and Jansson, 2005; Kaplan et al., 2009) or modelling simulations (Hubbard et al., 2005), although these factors require further constraint before secure climatic interpretations are made.

Over sub-millennial timescales, the absence of precise chronological control on ice lobe deglaciation has prevented detailed comparisons with high-resolution climate records (e.g. Antarctic ice-cores), and the identification of climatic forcing factors. This problem is becoming increasingly important as new, higher resolution ice cores reveal abrupt (e.g. decadal) climate changes during the last deglaciation over the Southern Hemisphere high-latitudes (WAIS Members, 2013; 2015; Marcott et al., 2014; Markle et al., 2017). To what extent these changes impacted mid-latitude deglaciation is, however, largely unknown, due to a paucity of glacial (and other palaeoenvironmental) records with high temporal resolution and firm dating control. Previous work has largely overlooked sedimentary archives. Proglacial lake basins are excellent sediment sinks (see Carrivick and Tweed, 2013 for review) that effectively restrict the passage of glacial meltwater and entrained sediments to the proglacial zone, leading to sediment storage. Such basins often accumulate long, continuous records of temporal changes in sediment delivery (Carrivick and Tweed, 2013), and owing to typical high sedimentation rates in proglacial environments (e.g. Gustavson, 1975), these records tend to offer high, and sometimes annual, temporal resolution (e.g. Ashley, 1975; Ridge et al., 2012). Proglacial sediment sequences are, therefore, capable of bridging gaps in the regional geomorphological and chronological record and, given reports of varved sequences (cf. Caldenius, 1932), may provide high-resolution chronological control on ice lobe deglaciation.

The three main issues raised above provide the motivation for this thesis, and the intention to improve the spatial and temporal constraints on regional ice sheet deglaciation. Addressing these issues is essential to future calibration of modelling studies on former glacial and climate dynamics, which ultimately have the potential to predict future climate changes.

1.4 Aims and objectives

1.4.1 Aims

1. To reconstruct the evolution of proglacial lake systems through the last deglaciation in central Patagonia, to establish former lake extents, levels, and drainage routes; and interactions with the LGC–BA and LC–P ice lobes.

2. To provide precise chronological control on the timing, rates and dynamics of ice lobe deglaciation.

3. To use this new chronology to investigate the potential climatic controls on Patagonian Ice Sheet deglaciation in southern South America.

1.4.2 Objectives

To achieve these aims, this thesis will complete seven main objectives:

1. Map the glacial geomorphology of the LGC–BA and LC–P ice lobes from high-resolution remotely-sensed imagery and field-checking.

2. Use this new mapping to reconstruct palaeolake history, by modelling regional isostatic adjustment patterns and correlating former lake levels.

3. Conduct detailed sedimentological analyses of reported varve sediments at LGC–BA (cf. Caldenius, 1932), to evaluate whether they can be used to produce an annually-resolved chronology for the last deglaciation.

4. Develop an absolutely-dated varve chronology through varve counting and tephrochronology.

5. Refine the timing and dynamics of initial Patagonian Ice Sheet deglaciation at LGC–BA through the integration of the new varve chronology and existing geochronological data using Bayesian age modelling.

6. Undertake time-series analysis of varve thickness trends to elucidate annual–decadal climatic influences on Patagonian Ice Sheet deglaciation.

7. Compare the annual varve thickness record with Southern Hemisphere palaeoclimate records, to explore the sensitivity of the Patagonian Ice Sheet to regional, hemispheric, and inter-hemispheric forcing.

1.5 Thesis structure and results

Chapter 2 describes the methods used in this thesis. Following this, Chapters 3–7 comprise a series of research papers that have been published (Chapter 3), accepted (Chapter 5), or prepared (Chapters 4, 6 and 7) for peer-reviewed journals. These papers present analytical results and discussion of major findings. Chapter 8 synthesises the major outcomes of Chapters 3–7, provides a critical evaluation of the new research, and considers directions for future research. Chapter 9 presents the main conclusions.

1.5.1 Chapter 3

Bendle, J.M., Thorndycraft, V.R., Palmer, A.P. 2017. The glacial geomorphology of the Lago Buenos Aires and Lago Pueyrredón ice lobes of central Patagonia. *Journal of Maps* 13, 654–673.

This paper describes the results of high-resolution geomorphological mapping for the LGC-BA and LC-P ice lobes of the former Patagonian Ice Sheet. The paper presents a new map of glacial landforms, several of which have not previously been identified (e.g. hummocky terrain, eskers, till eskers, iceberg wallow pits and craters). The map highlights the existence of distinct landform assemblages that formed (i) as ice lobes occupied their maximal positions on the Argentine steppe (e.g. moraines, outwash plains, eskers); and (ii) as ice lobes retreated into bedrock valleys during deglaciation (e.g. ice-contact fans, lacustrine shorelines, raised deltas). The map also provides the basis for more detailed analysis in subsequent chapters: allowing quantification of shoreline elevation(s), post-glacial isostasy, and former lake levels in Chapter 4; (ii) contextualising the field mapping and stratigraphic analysis undertaken in Chapters 4 and 5; and (iii) allowing targeted sampling of glaciolacustrine varve sequences in Chapter 5.

In this paper, I carried out the mapping, wrote the manuscript and drew the figures. All authors assisted with fieldwork, contributed ideas and edited the manuscript. The paper has been published in *Journal of Maps*.

1.5.2 Chapter 4

Thorndycraft, V.R. Bendle, J.M., Benito, G., Sancho, C., Palmer, A.P., Davies, B.J., Martin, J., Medealdea, A. (in prep) A new reconstruction of glacial lake evolution and multiple Atlantic–Pacific drainage reversals during the deglaciation of the Patagonian Ice Sheet (46–48°S). *Geomorphology*

The configuration, timing, and drainage of former glacial lakes is a critical component in models of regional deglaciation. Previous palaeolake reconstructions are, however,

contradictory, mapping over a variety of scales and using a range of lake reconstruction approaches. This paper provides the first systematic mapping and quantification of post-glacial isostasy and former lake levels. The reconstruction depicts new ice-dam positions, drainage routes and previously unidentified lake-level phases. The isostatic evidence contradicts the hypothesis of Younger Dryas-aged glacier advances, as many boulders dated using cosmogenic nuclide exposure methods were shielded under lake water.

In this paper, I (i) undertook the remotely sensed mapping of glacial and palaeolake geomorphology (Chapter 3); (ii) performed the reconstruction of post-glacial isostasy, histogram analysis of palaeolake levels, and lake-level correlations, (iii) recalibrated published boulder ages and radiocarbon dates; (iv) wrote sections of the manuscript (4.3.1; 4.3.2; 4.4.2); (v) drew Figures 4.6, 4.11, and 4.12, and edited all remaining Figures; (vi) edited the manuscript and supplementary materials. Thorndycraft (i) led the field mapping; (ii) carried out the regional topographic analysis; (iii) undertook the altitudinal-based review of recalibrated geochronology; and (iv) wrote all remaining sections of the manuscript and drew remaining figures. Medealdea carried out the OSL dating at the University of Seville. All other authors contributed to fieldwork campaigns and/or added ideas to the manuscript. The paper has been prepared for *Geomorphology*.

1.5.3 Chapter 5

Bendle, J.M., Palmer, A.P., Thorndycraft, V.R., Matthews, I.P. 2017. High-resolution chronology for deglaciation of the Patagonian Ice Sheet at Lago Buenos Aires (46.5°S) revealed through varve chronology and Bayesian age modelling. *Quaternary Science Reviews*.

The paper provides high-resolution age constraints for the timing of deglaciation at LGC–BA, and overcomes the typical resolution limitations of boulder dating chronologies. We interpret laminated sediments as varves and, using varve counting and tephrochronology, develop the first annually-resolved, calendar-year chronology for ice sheet deglaciation in Patagonia. We integrate the new varve chronology with existing geochronological datasets using Bayesian statistics, and constrain the onset of deglaciation to 18,086 ± 214 cal a BP. We show that ice remained in eastern Lago Buenos Aires until at least 16,934 ± 116 cal a BP. During this ~1000-year time-window, ice-margin retreat rates progressively accelerated, likely partly influenced by calving in the latter part of the record.

In this paper, I conducted (i) fieldwork: i.e. stratigraphic analysis, varve counts and thickness measurements, and sampling; (ii) the laboratory production and microscopic analysis of thin sections; (iii) developed the site and composite varve chronologies; (iv) the geochemical analysis of tephra layers; and (v) Bayesian age modelling. I wrote the manuscript and drew the figures. Thorndycraft and Palmer assisted in fieldwork. Palmer undertook repeat varve counts, helped with stratigraphic analysis, and helped produce and analyse petrographic thin sections. Matthews assisted with tephra analysis and Bayesian age modelling. All authors contributed to ideas and edited the paper.

1.5.4 Chapter 6

Bendle, J.M., Palmer, A.P., Thorndycraft, V.T. Matthews, I.P. (in prep) Sensitivity of the Patagonian Ice Sheet to sub-decadal tropical climate variability between ~18–17 ka derived from a glaciolacustrine varve record at Lago Buenos Aires, Argentina. *Earth and Planetary Science Letters*

Chapter 5 produced a chronology for the onset of deglaciation at LGC–BA. In this paper, we investigate the role of short-term climatic variability on Patagonian Ice Sheet deglaciation through spectral analysis of varve thickness datasets. The analysed intervals display inter-annual (2–8) and decadal (20–30 and 40–60 year) cycles that match the periodic features of well-studied modes of contemporary ocean-atmosphere variability. We suggest that tropical Pacific forcing factors, such as El Niño–Southern Oscillation (ENSO), had a strong influence on regional temperatures and ice sheet ablation rates, providing empirical evidence in support of climate model simulations that predict enhanced ENSO variability during the last deglaciation. The amplitude of ENSO variance appears to change through time, indicative of either non-stationarity in tropical–extra-tropical climate teleconnections or signal dampening due to ice lobe retreat.

In this paper, I carried out the spectral analysis, wrote the manuscript and drew the figures. All authors contributed ideas and edited the manuscript. This paper has been prepared for *Earth and Planetary Science Letters*.

1.5.5 Chapter 7

Bendle, J.M., Palmer, A.P., Thorndycraft, V.T. Matthews, I.P. (in prep) Near-synchronous southern hemisphere warming and mid-latitude ice sheet response during Heinrich Stadial 1. *Nature Geoscience*

Chapter 6 demonstrated the potential influence of tropical Pacific climate variability on regional temperatures and annual/decadal ice sheet ablation patterns. In this paper, we

used the LGC–BA varve thickness record to determine the timing of major changes in ice lobe retreat dynamics, and compared these changes with regional palaeoclimate records. This enabled discussion on the possible forcing factors behind mid-latitude deglaciation and an assessment of intra- and inter-hemispheric phasing of climate and glacial changes following the gLGM. The comparison suggests that the middle and high southern latitudes warmed synchronously (within dating uncertainties) after ~18 ka, and that the Patagonian Ice Sheet responded rapidly to these atmospheric changes. We suggest that Northern Hemisphere cooling during Heinrich Stadial-1 may have triggered mid-latitude deglaciation by forcing southwards migration of the Intertropical Convergence Zone (ITCZ) and, subsequently, the coupled ocean-atmosphere fronts of the Southern Hemisphere, which in doing so contributed to the release of heat from the Southern Ocean that initiated hemispheric warming.

In this paper, I compiled the palaeoclimate records and undertook the comparison with the LGC–BA varve record, wrote the manuscript and drew the figures. All authors contributed ideas and edited the manuscript. This paper has been prepared for *Nature Geoscience*.

Chapter 2. Methods

2.1 Research framework

This chapter details the methods used to address the research aims and objectives outlined in Chapter 1. While analytical methods are described in the papers presented in Chapters 3–7, this chapter provides a rationale for the selection of research methods and outlines their practical application. This thesis utilises high-resolution geomorphological (spatial) and chronological (temporal) approaches to refine the understanding of regional ice sheet deglaciation. The work was undertaken in four phases:

1. The glacial geomorphology of the LGC–BA and LC–P ice lobes was mapped in detail from high-resolution (<15 m) remotely-sensed imagery and localised field checking.
2. Regional post-glacial isostasy was reconstructed from the new geomorphological dataset, and used a Geographic Information System (GIS)-based approach to quantify the distribution and elevation of former lake level indicators (e.g. shorelines). Together, Phases (1) and (2) were used to target key sediment sequences for chronological analyses.
3. (a) The sedimentology of laminated glaciolacustrine deposits was examined in detail to evaluate potential annual (varve) structure; (b) an annually-resolved (varve) chronology was developed through layer counting and inter-site correlation; (c) the absolute age of the floating varve chronology was assessed using tephrochronology; and (d) a model for ice lobe retreat was established using Bayesian modelling of available geochronological data.
4. Inter-annual to decadal cycles in the thickness of glaciolacustrine varves were statistically examined using spectral analysis techniques, and compared with Southern Hemisphere palaeoclimate records.

2.2 Phase 1: Mapping the glacial geomorphology of the LGC–BA and LC–P ice lobes

2.2.1 Rationale

As detailed in Chapter 1, previous mapping has been conducted at local to regional scales (Figure 1.6). The most detailed maps have been based on remote sensing and field investigations from individual valleys (e.g. Glasser et al., 2006; Bell, 2008; Nimick et al., 2016) or moraine belts (e.g. Hein et al., 2010), and are restricted in spatial

coverage. Glasser and Jansson (2008) provide the only geomorphological map covering the entire study area, as part of an ice-sheet scale study extending from 38–56°S. Mapping over such a large area, however, incorporating >60 former ice lobes (Glasser et al., 2008), required coarse (30 m) mapping resolution (Figure 2.1) and the generalisation of subtle and/or complex geomorphology. High-resolution (<15 m) mapping at the ice lobe-scale is, therefore, essential to: (i) characterise the detailed nature and distribution of glacial landform assemblages formed by the LGC–BA and LC–P ice lobes; (ii) provide a basis for glacial reconstructions; and (iii) select key field sites for detailed investigation, including the identification of laminated (varved) glaciolacustrine deposits for Phase 3.

2.2.2 Glacial geomorphological mapping

The glacial geomorphology of the LGC-BA and LC-P basins was characterised through satellite image interpretation and field verification. Mapped features were stored as vector shapefiles within a GIS. A GIS-based approach allows for coherent, systematic and efficient mapping over wide areas (e.g. Clark et al., 2004; Smith et al., 2006; Glasser and Jansson, 2008; Hughes et al., 2010), and benefits from the existence of standard mapping practices. Features were digitised in ArcGIS (v10.3) at imaging scales ranging from 1:8,000 to 1:50,000. The mapping procedure utilised standard practices and conceptual frameworks (e.g. an inversion scheme, cf. Kleman and Borgstrom, 1996; Kleman et al., 2006) for the genetic interpretation of landforms.

The primary datasets used for mapping were 2.5 m resolution SPOT-5 and ~1–2 m resolution DigitalGlobe (GeoEye-1, IKONOS) images, freely available through the ESRI™ 'World Imagery' service (Figure 2.1). Areas of poor image quality (e.g. obscured by clouds) were examined in GoogleEarthPro™ (v7.1), which also offers SPOT-5 and DigitalGlobe images across the study area. These image sources were used in preference to lower resolution satellite scenes (e.g. Landsat: 30 m; Glasser and Jansson, 2008) as they allowed a greater diversity of features to be mapped (Figure 2.1c), and provided clarity in the identification of previously un-recorded, and subtle landform types. To provide topographic context for landform identification, both relief-shaded ('hillshade') and slope gradient-shaded models were created from a mosaic of ASTER G-DEM tiles (30 m cell-size). Relief-shaded models were created following procedures outlined in Smith and Clark (2005), i.e. using multiple azimuths (southwest, northwest, southeast, northeast) and low illumination values (20-30°) to reduce the effects of azimuth biasing (Smith and Clark, 2005; Smith and Wise, 2007).

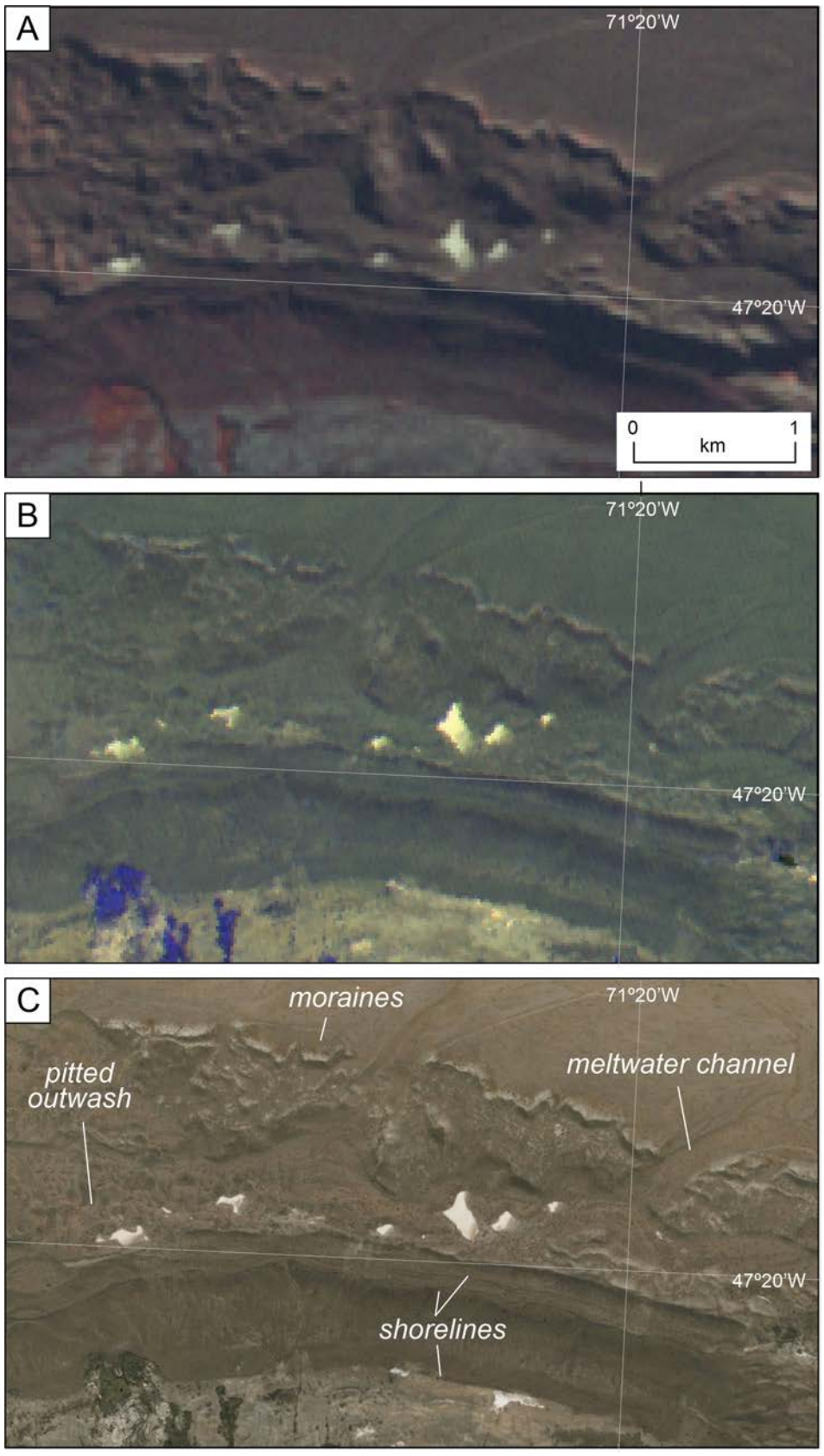

Figure 2.1. Examples of different imaging sources used in previous mapping and this thesis. Previous mapping (see Figure 1.6) has used: (A) Landsat 7 ETM+ (30 m resolution); and (B) ASTER (15 m) images. This thesis uses: (C) DigitalGlobe (or SPOT-5) images accessed through the ESRI™ 'World Imagery' service (1–2 m) and GoogleEarthPro™. Subtle landform types, such as pitted outwash, are only confidently discernible in high-resolution imagery.

Despite this, gradient-shaded models were consulted preferentially as they do not necessitate illumination to create terrain representations, so are unbiased by azimuth (Smith and Clark, 2005). To further aid landform identification, semi-transparent satellite images were draped over the various terrain models. Additionally, GoogleEarthPro™ was used to produce oblique three-dimensional views of the landscape. This technique was advantageous as the image manipulation capabilities in GoogleEarthPro™ allowed an unlimited number of viewing angles to be explored quickly and efficiently, with terrain representations overlain by high-resolution imagery. Three-dimensional GoogleEarthPro™ scenes were especially useful in areas where field verification was not possible. In practice, all model types were consulted when mapping to ensure robust interpretation of landforms.

Field mapping was used to check the accuracy of digital mapping and inspect smaller (e.g. landforms with <5 m relief) or more complex landform assemblages in detail. Given the size of the study area, field mapping was limited to key areas. Where sections exposed the internal sedimentary architecture of mapped landforms, their sedimentology was inspected to help assign landform origins.

2.2.3 Glacial sedimentology and stratigraphy

In some instances (see Chapter 4 and 5), the sedimentology of mapped landforms was examined to aid landform identification. However, such analyses were limited by field time, accessibility, and the availability of open exposures. Sedimentary exposures through landforms of interest were documented using field sketches, vertical sedimentary logs and digital image mosaics (Evans and Benn, 2004). In Río Fenix Chico, at the eastern end of LGC—BA (Figure 1.4), the sedimentology and stratigraphic architecture of more extensive sedimentary accumulations was recorded (Chapter 5). Sediment sequences were logged from natural (e.g. river cuttings) and man-made (e.g. road cuttings, quarries) exposures. Vertically continuous exposures were sought to limit the need for composite logs. In all situations, sediment grain-size, sorting, structure, texture, bed geometry, contacts, and deformation structures were recorded to identify *lithofacies* (LF) units. This thesis uses the lithofacies codes of Evans and Benn (2004). *Lithofacies* (LFs) units were grouped into *lithofacies associations* (LFAs) based on common sedimentological characteristics. All assessments of sediment properties (e.g. grain-size, sorting, texture) were made in the field.

2.3 Phase 2: Reconstructing glacio-isostatic rebound and proglacial lakes

2.3.1 Rationale

The formation and drainage of proglacial lakes is a fundamental element of ice sheet deglaciation in central Patagonia (Caldenius, 1932; Turner et al., 2005; Glasser et al., 2016). These lakes imparted a strong geomorphological signature, which offers the potential to reconstruct both lake and ice lobe history. However, this record has not been fully exploited, because previous reconstructions have used fragmentary shoreline datasets (e.g. Turner et al., 2005; Bell, 2008; Hein et al., 2010; Bourgois et al., 2016; Martinod et al., 2016) or fail to adequately account for post-glacial isostatic uplift in regional lake level correlations (Glasser et al., 2016). Systematic shoreline datasets and models of post-glacial isostasy are critical to the robust correlation of shorelines across basins and accurate linkages of glaciolacustrine landforms to former water levels (e.g. Breckenridge, 2013, 2015). Moreover, improved understanding of the extent and depth of former proglacial lakes is essential to the correct interpretation of cosmogenic nuclide exposure ages used to constrain the timing of ice lobe retreat (Glasser et al., 2012). To resolve these limitations, this thesis uses high-resolution mapping (section 2.2) and a systematic, GIS-based approach to palaeolake reconstruction that accounts for regional post-glacial isostatic uplift.

2.3.2 Mapping criteria for shoreline identification

Shoreline features (Figure 2.2) were mapped in ArcGIS v10.3 as a critical element of the regional glacial geomorphology (section 2.2.2), and were carefully reviewed prior to conducting DEM-based analysis. Features were identified on high-resolution (<5 m) satellite images (ESRI “World Imagery” images) and a mosaic of ASTER G-DEM tiles. The DEMs have a vertical accuracy of 20 m (95% confidence; ASTER GDEM Validation Team, 2011) and a horizontal accuracy of 30 m (95% confidence; ASTER GDEM Validation Team, 2011). For reliable mapping of shoreline features non-illuminated slope-gradient models were created from the ASTER DEMs (cf. Smith and Clark, 2005) where the brightness of each pixel relates to the slope angle, for example, the brighter colours in Figure 2.3 indicating higher slopes. Mapped shoreline features include wave-cut scarps or terraces, raised deltas, and isthmuses (Figure 2.2). Shoreline features were manually digitised by tracing a line along the break slope where a former waterline was inferred (Figure 2.3).

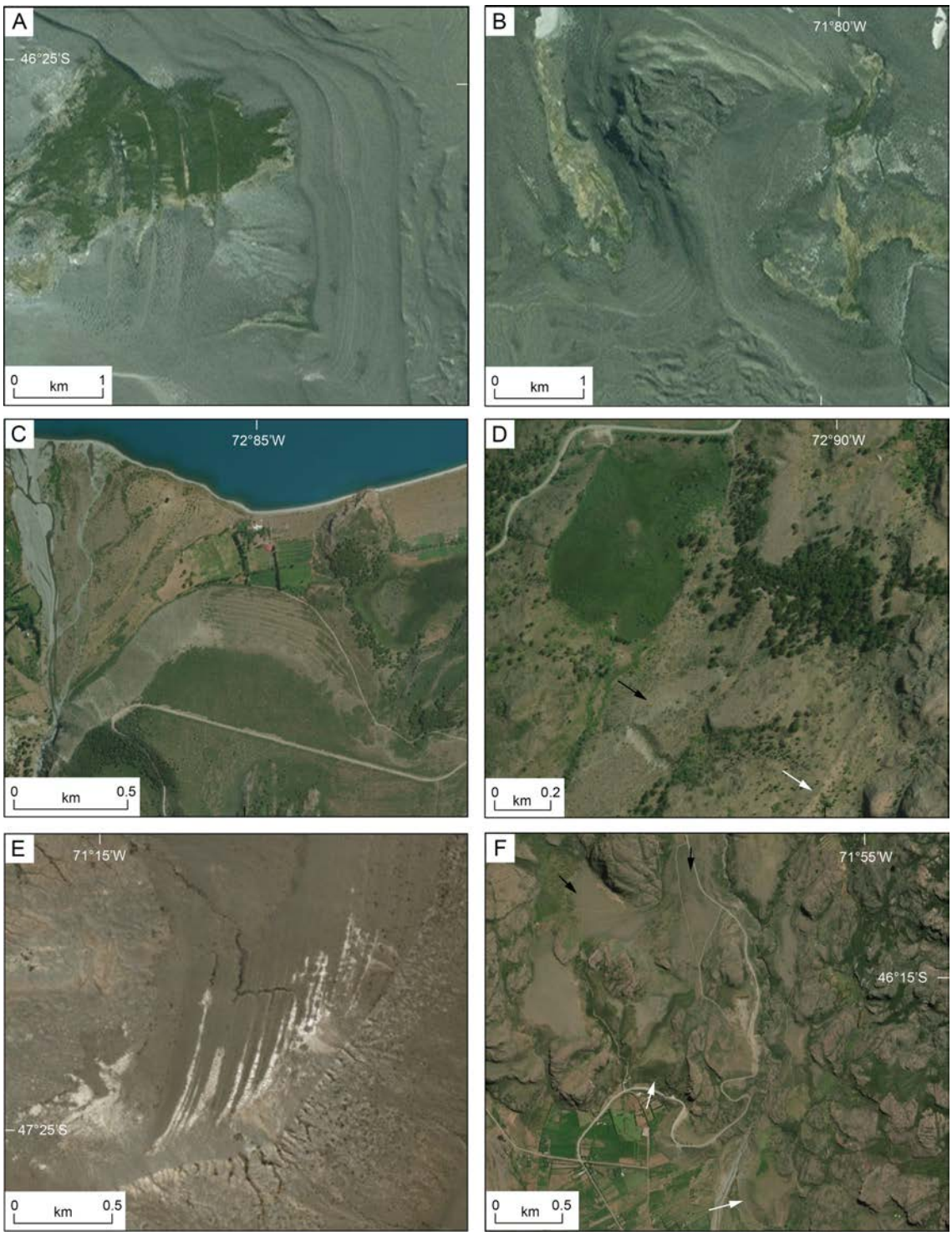

Figure 2.2. Examples of glaciolacustrine landforms mapped to constrain former proglacial lake extents and levels. (A) wave-cut scarps incised into unconsolidated glacigenic sediments with subtle intervening beach ridges. (B) Isthmus separating former lake embayments; (C) raised delta with wave-cut terraces on delta front. (D) Wave-cut scarp incised into bedrock and thin surface debris cover (white arrow) and inset depositional terrace (black arrow). (E) Closely-spaced beach ridges. (F) Raised deltas (white arrows) and infilled bedrock depressions (black arrows).

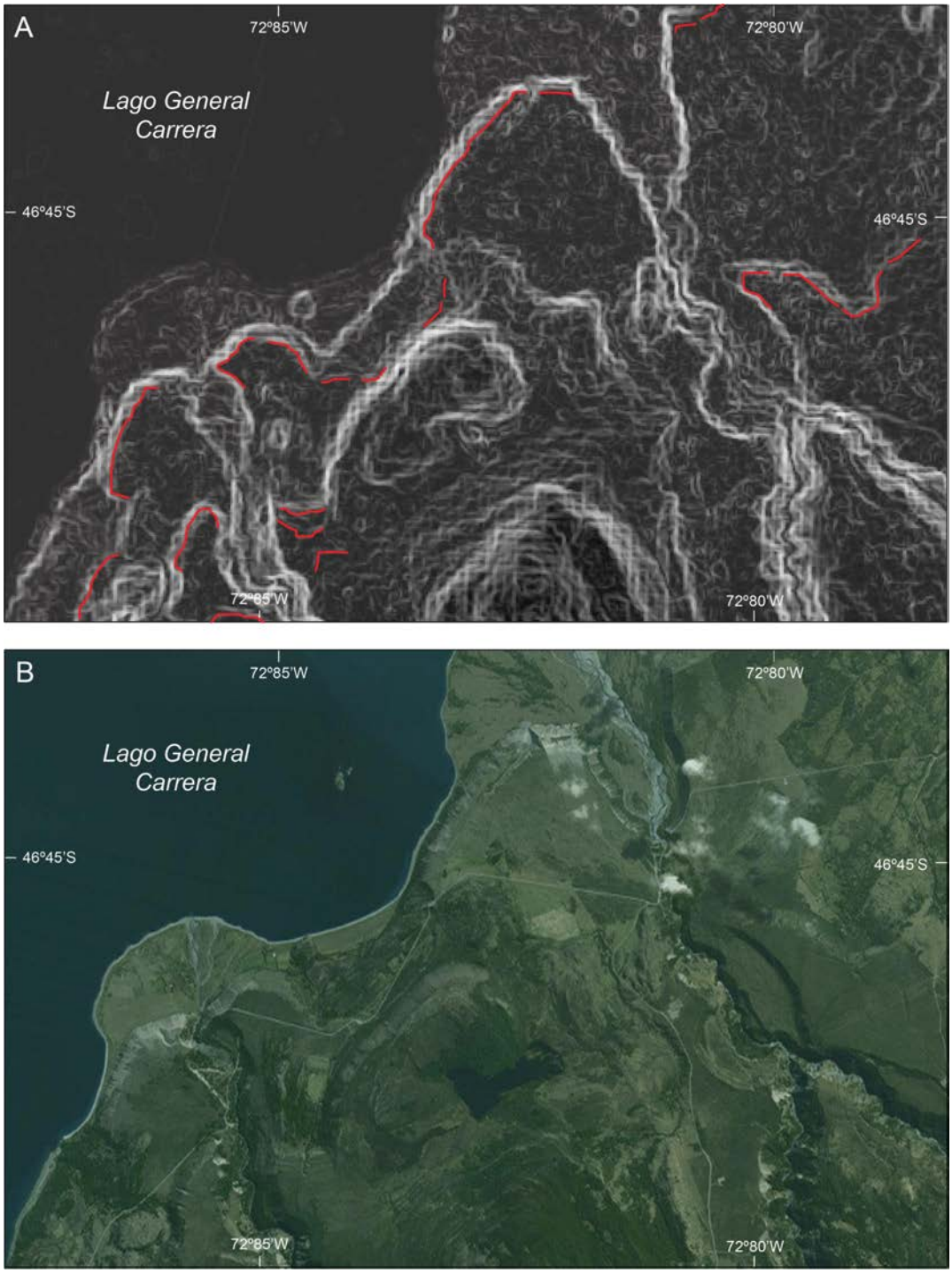

Figure 2.3. Example of image datasets used to map potential lake levels. (A) slope-gradient shaded model created from ASTER G-DEM, with lighter colours indicating steeper slopes. Former lake levels (red lines) were defined as breaks in slope which, in this example, are associated with raised lacustrine deltas. Unmapped breaks in slope relate to geological or non-lacustrine features. (B) DigitalGlobe satellite image of the same area.

2.3.3 Determining rebound isobases and former lake levels

This processing step follows that developed in Breckenridge (2013, 2015) to reconstruct glacial lake systems that existed around the waning Laurentide Ice Sheet in North America, and is described in detail below. Digitised shorelines were converted into points at 30 m spacing, and the elevation for each point extracted from the ASTER G-DEM mosaic (20 m vertical accuracy at 95% confidence; ASTER GDEM Validation Team, 2011) using the XTools Pro extension in ArcGIS v10.3 (step-by-step processing instructions are given in Appendix). To visualise spatial patterns in shoreline elevation, a surface was interpolated from the point elevations using a Natural Neighbor function. Using this raster, rebound isobases were constructed as distance contours at 10 km intervals perpendicular to the direction of maximum uplift, and a new raster interpolated for this rebound surface (Figure 2.4). The position of the 0-km isobase is defined by the easternmost extent of shoreline evidence, and intersects the former Río Deseado outflow (~398 m asl) at Río Fenix Chico (Figure 2.4). For every shoreline point, distance along the direction of maximum uplift was then extracted from the rebound surface and plotted against elevation, and palaeo-waterlines correlated. To assess the rebound surface, a histogram analysis was performed to determine the fit of shoreline elevations to a regression line (cf. Breckenridge, 2013, 2015). Beginning with the best-developed shoreline level, the complete point dataset was split along the lake centre-line, into 'south' and 'north' basin datasets, and a 2nd-order polynomial regression line fitted to the most densely populated (i.e. containing the most shoreline points) dataset. This defines a modelled shoreline, based on the polynomial equation that describes the elevation as a function of uplift (cf. Breckenridge, 2013, 2015). A histogram was then created for each side of the basin using the resultant regression line equation. Using 1 m-wide x-axis bins for variations in the y-intercept (shoreline elevation) of the regression line, the y-axis plots the number of points that fall within 1/2 m of the shoreline equation. The fit of the rebound surface was assessed by comparing the 'north' and 'south' basin histograms. Where slight offsets occurred, isobases were re-contoured through trial and error and the regression analysis reapplied until histograms precisely overlapped, and a final set of isobases was determined. Once the isobase surface was validated for the best-developed shoreline level, the histogram analysis was extended to all other palaeolake levels. Through this approach former water levels were robustly defined within the DEM (20 m) resolution, and shoreline curvature (and thus uplift) calculated.

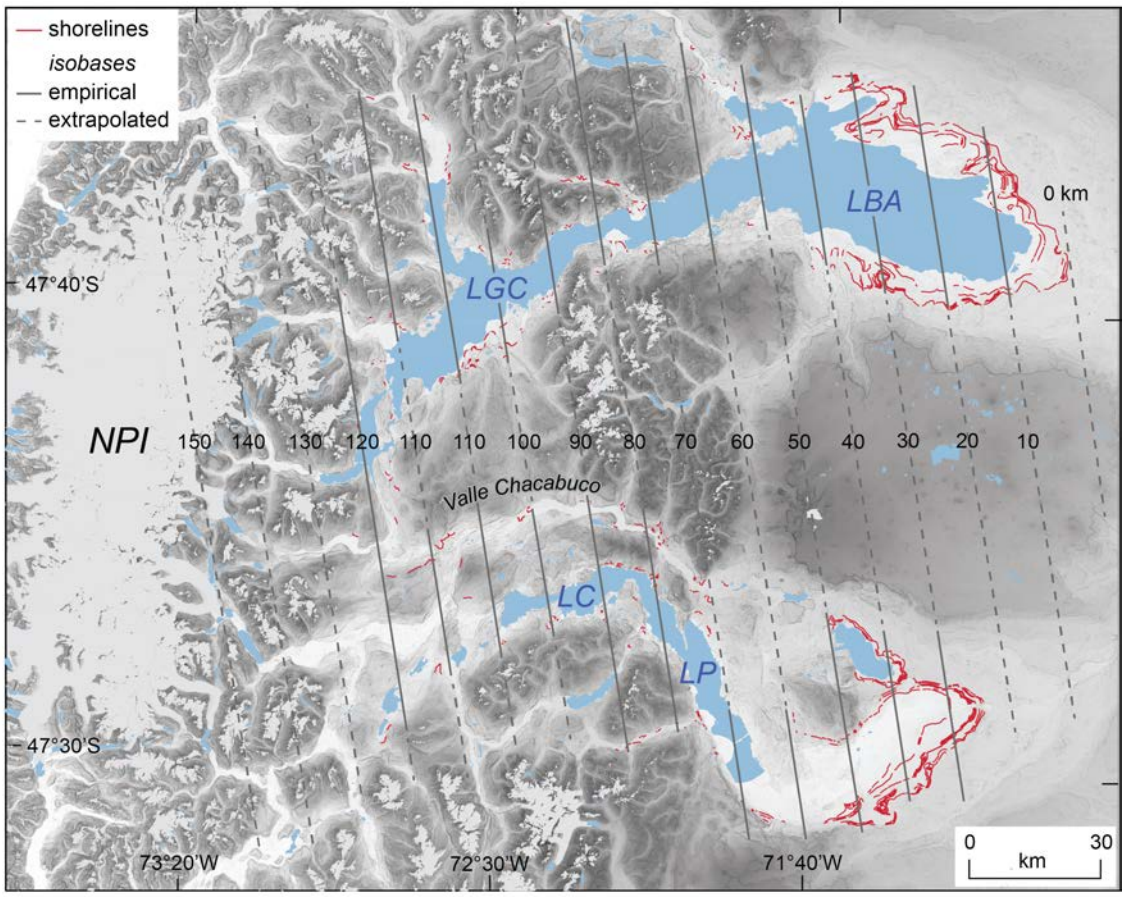

Figure 2.4. Rebound isobases at 10 km intervals based on spatial interpolation of shoreline elevation data. The 0-km isobase is the Deseado outflow at Río Fenix Chico.

2.4 Phase 3a: Investigating the sedimentology of laminated glaciolacustrine deposits

2.4.1 Rationale

In Phases 1 (section 2.2) and 2 (section 2.3) glaciolacustrine sedimentary deposits were mapped and related to former lake levels. The laminated glaciolacustrine sediments located at Río Fenix Chico (see section 1.2.2) were selected for detailed analysis because the sites of deposition are associated with prominent late LGM moraines, enabling investigation of (1) the timing of ice lobe deglaciation; (2) the dynamics and rates of ice lobe retreat, given the availability of ice-marginal pinning points.

The laminated sediments found at Río Fenix Chico were first interpreted as varves by Caldenius (1932). However, detailed sedimentological analysis confirming their annual structure is absent. This analysis, therefore, forms a fundamental part of this thesis, and is necessary to establish the processes responsible for the formation of laminated couplets, to evaluate whether they are annual in nature (e.g. Lamoureux, 2001; Brauer,

2004; Ojala et al., 2012) or result from other processes that may produce laminated sediment structures (e.g. Mulder and Alexander, 2001). In relict glaciolacustrine systems, assessments of lamination origins are complicated by a lack of modern analogue studies (Gustavson, 1975), and because annual structure cannot be confirmed by counting back from actively-forming varves, as is often possible in extant lakes (see Ojala et al., 2012 for review).

For such situations, researchers have established descriptive protocols for the objective classification of lamination sedimentology (e.g. Ashley, 1975; Smith and Ashley, 1985; Ringberg and Erlström, 1999; Palmer, 2005; 2012). The microscopic analysis of thin sections has become increasingly standard in such efforts (Ojala et al., 2012; Brauer et al., 2014) because it offers unparalleled levels of sedimentological detail (e.g. Lamoureux and Gilbert, 2004; Brauer et al., 2008; Neugebauer et al., 2012; Palmer et al., 2012). For example, this approach enables differentiation of seasonal sub-layers, which form part of the annual cycle in varves, from intercalated 'event' layers (e.g. Mangili et al., 2005; Czymzik et al., 2013). However, thin section analysis is not commonly used to investigate glaciolacustrine varves, generally because their greater thicknesses (e.g. >1-2 cm) allow sufficient sedimentological data to be obtained from fresh sediment surfaces or digital images (e.g. Hang, 2003; Hyttinen et al., 2011; Ridge et al., 2012).

Laminated deposits in the Río Fenix Chico valley occur in thick (~20–50 m) vertical sequences and display a wide range of lamination thicknesses (Figure 2.5). These two factors meant that continuous sampling for laboratory analysis was neither practical nor strictly necessary. Accordingly, the sedimentary characteristics of thick couplets, defined as couplets ≥1 cm in thickness (Figure 2.5a), were primarily studied in the field. Nonetheless, samples were taken at frequent intervals for thin section preparation and particle-size measurements (see below). Samples were chosen based on facies changes observed at the macroscale, or where structures were unclear. In contrast, thin couplets, defined as couplets <1 cm (Figure 2.5b), were studied using microscale techniques, as their sedimentary characteristics cannot be accurately established with the naked eye (Brauer, 2004; Palmer et al., 2012). The practical limit of 1 cm for microscale analysis surpasses the Varve Working Group's recommendation of 0.5 cm (Ojala et al., 2012).

2.4.2 Macroscale analysis of laminated sediments

Laminated sediments were investigated from overlapping field sections. Macroscale sedimentological descriptions were made for each laminated couplet, and focused on

particle-size, sorting, structure, and the nature of contacts between laminations. Specific attention was given to the overall structure of laminated couplets, especially the stratigraphic arrangement of very fine structures within the coarse (silt) layers (Figure 2.5a). This process also involved the identification of irregular sediment structures, such as coarser-grained sand layers that interrupt the regular laminated pattern.

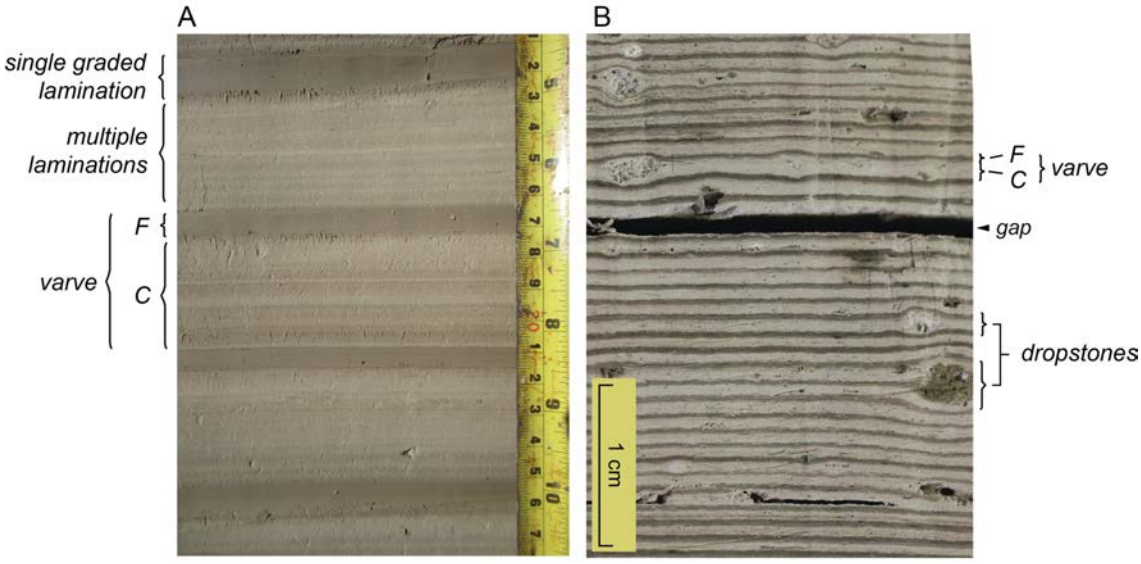

Figure 2.5. Examples of (A) ≥ cm-scale laminated couplets; and (B) < cm-scale laminated couplets. Coarse layers (*C*) are composed of multiple very fine laminations of silt-sized sediment, whereas fine layers (*F*) are single laminations of very fine silt and clay-sized sediment.

2.4.3 Sampling and thin section preparation

To facilitate micromorphological analysis of laminated sediments, samples were extracted from fresh sediment exposures using 200 mm-long plastic or metal D-channels. 60 single spot samples (equating to 120 100-mm-long thin sections) were taken from sections containing ≥cm-scale couplets to verify macroscale descriptions and further examine lamination composition and structure (e.g. Ashley, 1975; Ringberg and Erlström, 1999; Palmer et al., 2010; 2012). Nine continuous samples (eighteen thin sections) were taken through a 48.05 cm section of laminated sediments at one site, which contained very thin (<1 cm-scale) couplets. Overlaps of at least 2 cm were ensured throughout sampling, in which distinctive marker layers were identified for correlation purposes (Lamoureux, 2001). Samples were impregnated with a crystic resin under vacuum and thin sections prepared using standard methods developed in the Centre for Micromorphology, Royal Holloway, University of London (Palmer et al., 2008b).

2.4.4 Microscale analysis of laminated sediments

Thin sections were analysed using a Leica M205C petrological microscope under magnifications of 0.78x to 200x and described using a microfacies approach (e.g. Brauer et al., 2004; Palmer et al., 2010, 2012). Through this procedure, individual laminations were classified in terms of their internal composition and structure. This enabled the identification of various lamination types and intercalated 'event' layers. The classification of lamination properties was based on subtle variations in particle-size, texture, sorting, structure (e.g. massive or graded), the presence of irregular structures (e.g. load deformation) and the nature of contacts between laminations.

2.4.5 Particle-size analysis of laminated sediments

The particle-size of laminated sediments was measured to evaluate field- and thin section-based grain-size estimations, and to support the interpretation of couplet formation. Repeat samples were extracted from regular coarse- and fine-grained laminations and intercalated 'event' layers (e.g. graded sand layers). Measurements were made using a laser diffraction-based Malvern Mastersizer 2000 with a Hydro-MU sampler. Prior to analysis, samples were mixed with 0.5% sodium hexametaphosphate and placed within an ultrasonic bath for 30 seconds to ensure complete disaggregation of particles.

2.5 Phase 3b: Constructing a varve chronology

2.5.1 Rationale

The sedimentological analysis confirmed the presence of glaciolacustrine varves at Río Fenix Chico (Chapter 5) and a varve chronology could be developed. Such chronologies offer the potential to develop continuous records of ice lobe dynamics, based on the evolution of varve thickness trends (e.g. Leonard, 1997; Palmer et al., 2010; Larsen et al., 2011; Ridge et al., 2012). Moreover, counts of the number of annual layers can provide precise constraints on the timing and duration of discrete deglacial events (e.g. retreat phases).

In practice, there is no standard method for the construction of a varve chronology, due to the variable characteristics (e.g. visual distinctiveness, thickness) of varves and the range of techniques used to count and measure them (Ojala et al., 2012). The primary aim therefore was to minimise errors during the counting process to ensure a robust chronology was produced (Lamoureux and Bradley, 1996; Lamoureux, 2001). The

process used to produce the Río Fenix Chico varve chronology (Chapter 5) is described below.

2.5.2 Site selection

To produce the longest and most robust chronology at Río Fenix Chico, preliminary stratigraphic analysis (see section 2.5) was conducted along the entire valley length west of the Río Deseado outflow (Figure 2.6; Chapter 5) to identify the spatial extent of varved deposits, and zones of minimal sediment disturbance (e.g. slumping). A final consideration was the inferred pattern of ice lobe retreat, based on geomorphic evidence (Chapter 3) and the valley lithostratigraphy (Chapter 5). Specifically, varved sequences located between former ice-limits (e.g. moraines) could potentially be used to constrain the timing and rates of discrete retreat phases (e.g. Ridge et al., 2012). In total, five sequences were selected and named FC-B, FC-C/D, FC-E, FC-F and FC-F1 (Figure 2.6 and 2.7). These sites (i) characterised changes in lamination facies across the basin; (ii) avoided major sediment disturbances; and (iii) contained common marker layers with distinctive sedimentological properties (Figure 2.8) to allow correlation between sites. FC-B and FC-C/D are located between the Fenix I and Menucos moraines (Figure 2.6); FC-E directly overlies the Menucos moraine; and FC-F and FC-F1 are located immediately west of ('behind') the Menucos moraine.

2.5.3 Varve counting procedure

Two independent varve counts were produced at each site, with one count made by JMB (author) and another made by APP (supervisor). The thick (~20–50 m) vertical sequences in Río Fenix Chico demonstrate a wide range of varve thicknesses (>80 cm to <1 cm), and required a combination of macro- (field) and micro-scale techniques for robust measurements and counts (see below). The sequences contained numerous sedimentological 'marker layers' (Figure 2.8) that were critical to the counting procedure (e.g. Lamoureux and Bradley, 1996; Brauer et al., 1999; Lamoureux, 2001). These layers provided robust pinning points for comparisons between repeat counts, and for correlations across the former lake basin, over distances of ~0.25–3.25 km. Specific macro- and micro-scale counting processes are described below.

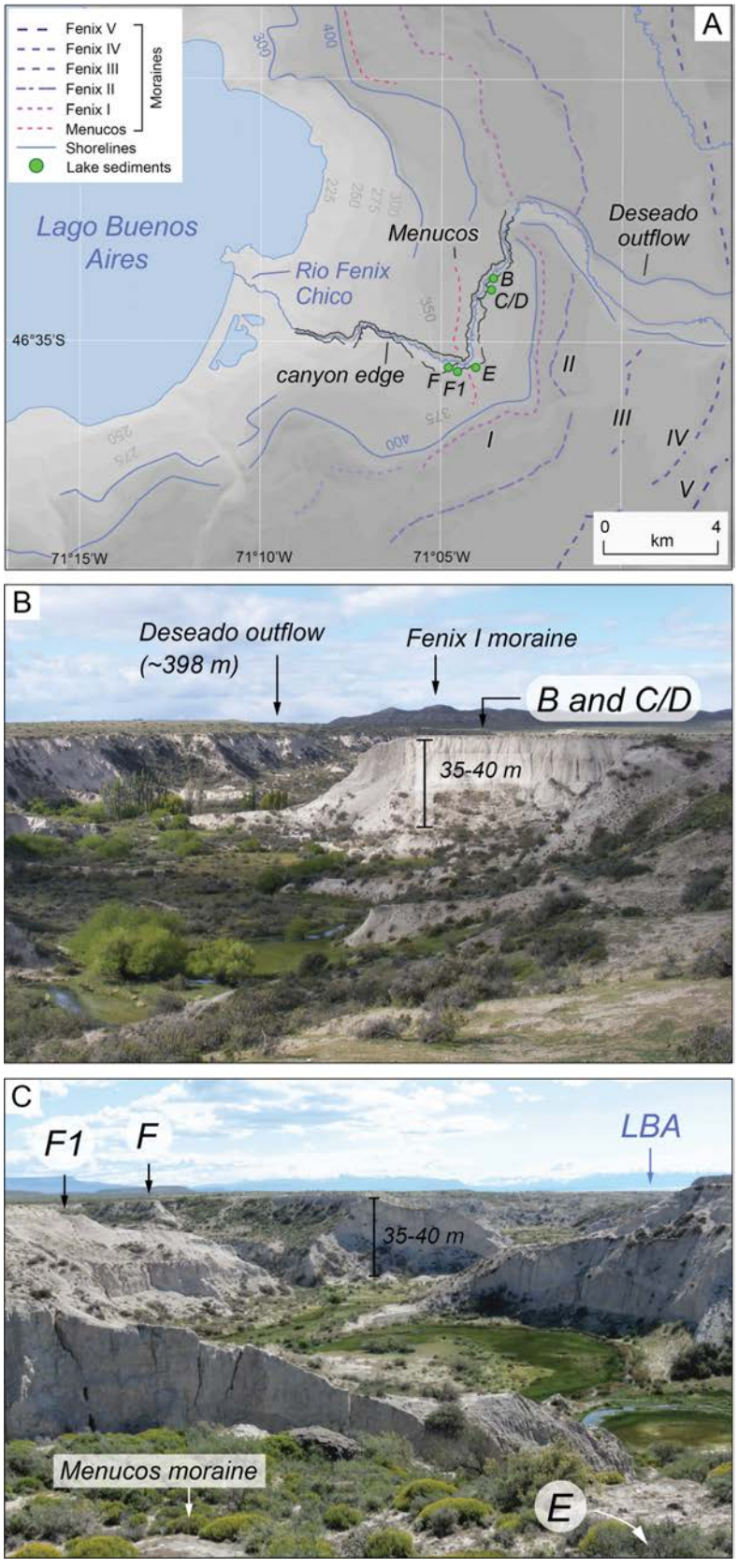

Figure 2.6. (A) Location of sites (green circles) used for detailed investigations of laminated sediments, plotted in relation to major Fenix moraine limits (cf. Singer et al., 2004; Douglass et al., 2006). (B) Photograph taken from Menucos moraine looking northeast to Fenix I moraine and Deseado outflow. The approximate position of sites FC-B and FC-C are shown, ~3 km from the Menucos moraine. (C). Photograph taken from the Menucos moraine looking west towards Lago Buenos Aires. Sites FC-F and FC-F1 are shown, ~0.5 km from the Menucos moraine.

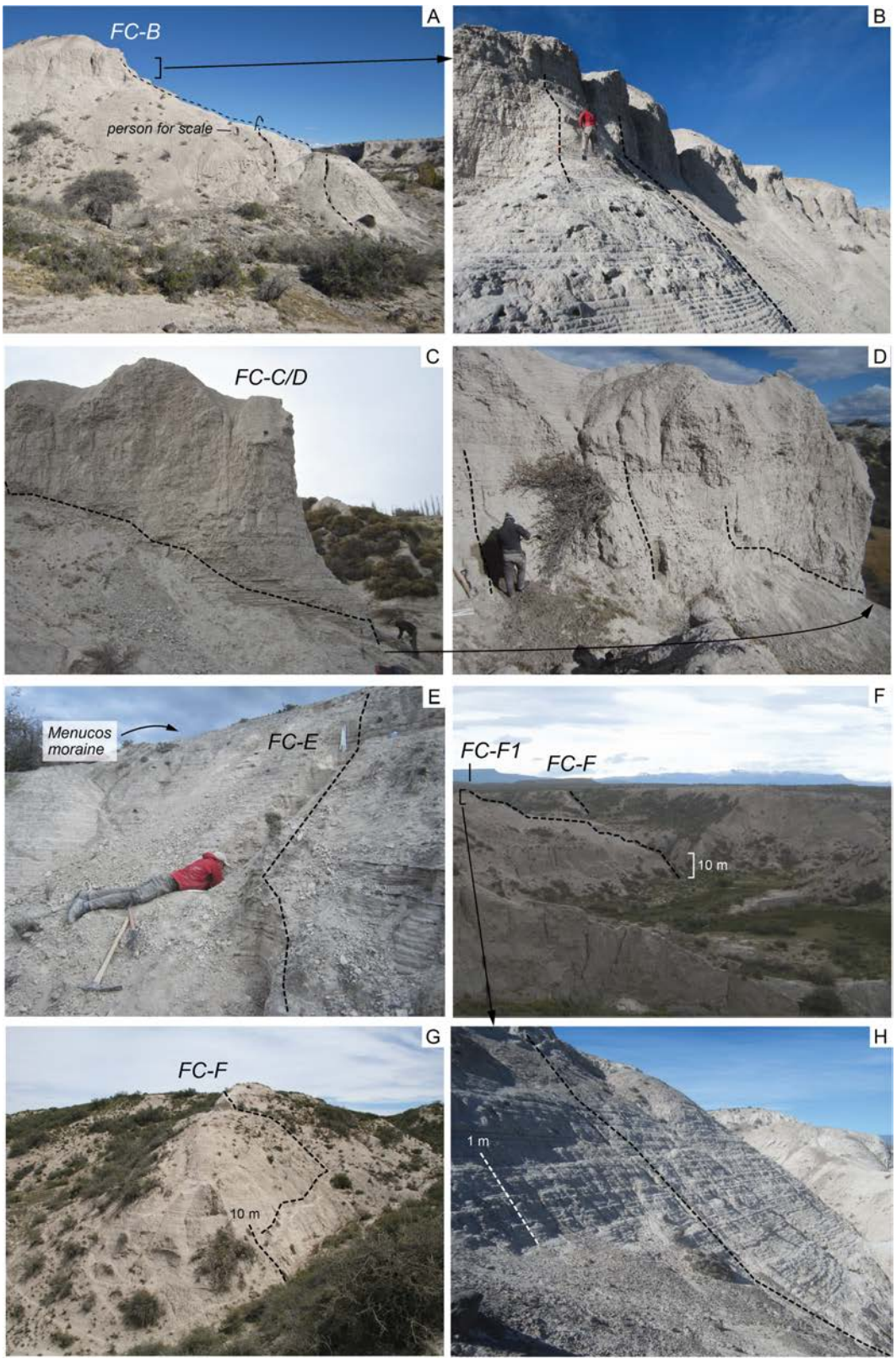

Figure 2.7. Field photos of laminated sediment sites examined in Río Fenix Chico valley. Black dashed lines show approximate location of continuous sampling sections. (A) Laminated sequences at site FC-B. View south-west along the Río Fenix Chico gorge. (B) Upper sections at FC-B. (C) Lower laminated sections at site FC-C/D. View to the south-west. (D) Middle laminated sections at FC-C/D. (E) Laminated sequences at site FC-E, on the ice-distal flank of the Menucos moraine ridge. View to the west. (F) Laminated sequences at site FC-F and FC-F1 <0.5 km west of Menucos moraine. View to west. (G) Laminated sequence at FC-F. View to southeast. (H) Upper laminated sections at FC-F1. View to southeast.

2.5.4 Macroscale varve counting

Macroscale counts were made over three field seasons between 2014 and 2016. Prior to counting, overlapping sections were created, and overlaps between sections marked. Field counting offered the advantage of being able to inspect the lateral integrity of varve structures and thickness over 10's to 100's of metres. This meant that local disturbances (e.g. deformed varves) could be avoided when creating sections (something that is not possible when extracting sediment cores), and the continuity of the site varve chronologies was maintained. Field counts and varve thicknesses were marked directly on to tapes from the cleaned sediment exposures (De Geer, 1912; Caldenius, 1932; Hang, 2003; Ringberg et al., 2003; Hyttinen et al., 2011). The lamination thicknesses were then measured under laboratory conditions at an accuracy of ~1 mm. Marker layers were recorded during the counting process. Distinctive marker layers included very thick or thin varves, graded sand layers or turbidites, zones of varve disturbance or deformation, and a basin-wide visible tephra layer. Detailed sediment descriptions were made throughout to inform subsequent decisions concerned with the generation of composite site chronologies and cross-correlation.

2.5.5 Microscale varve counting

Thin sections were used to perform counts on the <cm-scale varves (Figure 2.5b), which were present within the uppermost 48.05 cm of the FC-E sequence (Figure 2.6). Initially, thin sections were inspected on a light table to verify overlaps (~1-3 cm) between slides and identify distinctive marker layers. This process enabled varve counts and thickness measurements to be made within regularly spaced counting sections delimited by prominent laminations (Lamoureux and Bradley, 1996; Lamoureux, 2001). This also served as a means of comparing the number and thickness of varves established through repeat counts. Thin sections were inspected using a Leica M205 microscope under normal and cross-polarised light conditions. Varve definition was based on detailed micro-stratigraphic descriptions (e.g. Brauer, 2004; Palmer et al., 2012). This approach enabled the precise definition of varve boundaries according to microfacies data. This was especially important for complex varve facies that contained multiple sub-layers, to avoid over-estimation of the number of varves. Varves were counted in two passes along a single vertical transect of the thin section. Where a disturbance occurred on one transect, an adjacent transect was used to allow varve counting continuity. Digital images were captured using a Pixera 600es camera and varves measured within the Image-Pro Express software package.

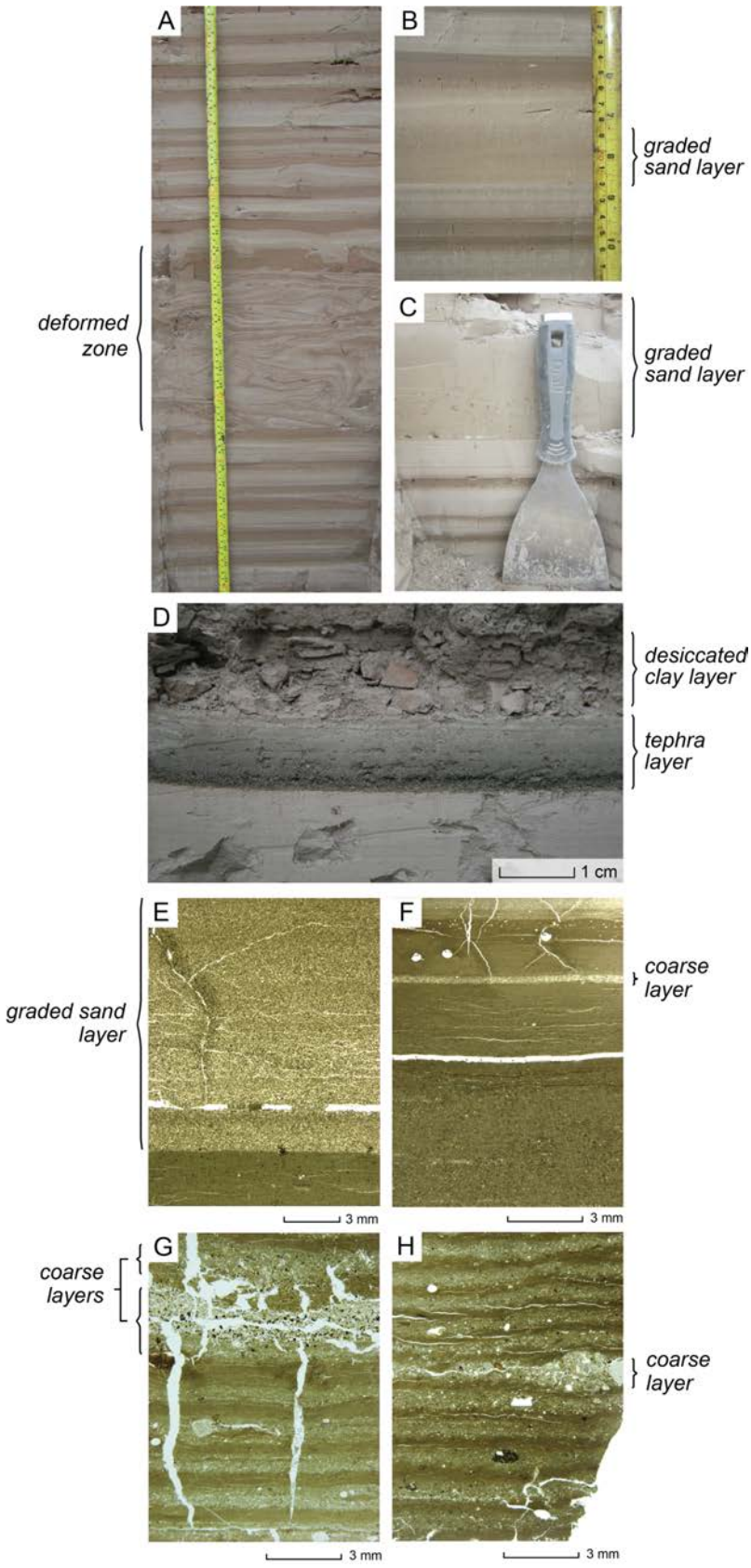

Figure 2.8. Example of sedimentary marker layers observed at the macroscale (A–D) and microscale in thin section (E–H). (A) Zone of deformed laminations bounded by regular varve structures. (B) and (C) Graded sand layers in coarse component laminations. (D) Tephra layer capped by desiccated clay layer. Photomicrographs (plane polarised light) of: (E) graded fine sand; (F) coarse silt layer within fine component lamination; (G) and (H) coarse grained layers within regular varve structures.

2.5.6 Constructing site varve chronologies and evaluating counting uncertainties

An independent varve chronology was established for each site using repeat count series. This process involved the comparison of short intervals between prominent marker layers to identify the number of recorded varves in each section and any counting discrepancies between counters. Counting discrepancies were most commonly associated with zones of sediment disturbance or vague structure, and consist of (i) laminations interpreted as two or more varves in one count, but only one year in the comparison count; and (ii) 'missed' or 'extra' varves in one count around the boundaries of disturbed sediment sections. Counting discrepancies were tabulated as ±1 varve year (vyr) differences, and allow an estimate of cumulative counting uncertainty to be produced for each site. Following this assessment, a composite varve chronology was generated for each site by calculating the mean varve thickness from repeat counts (one count by JB, and one count by AP).

2.5.7 Cross-dating to construct a composite varve chronology

The five independent varve series were correlated across the former lake basin to generate a composite ('master') varve chronology for the Río Fenix Chico valley (Chapter 5). This multi-site correlation approach, commonly referred to as cross-dating (Lamoureux, 2001; Ojala et al., 2012), also permitted the identification of discrepancies in local site varve series. Discrepancies can result from (i) errors introduced during measurement (e.g. misidentified varve structure); (ii) inconsistent production of a varve couplet across the lake basin, with 'missing' varves at some sites; or (iii) disturbance or erosion of varves at a given locality. Marker layers recorded during the counting process (Figure 2.8) allowed the identification of discrepancies between site varve series within short counting intervals, and the isolation of sections where count uncertainties were greatest.

Before correlating, varve series data were standardised to account for systematic varve thickness differences between sites. Such differences primarily arise from variable sediment fluxes due to the relative proximity of a given site to former ice-marginal sediment delivery centres (e.g. Gustavson, 1975; Ashley, 1975; Heideman et al., 2015). Raw (mm) varve thickness values were normalised using a log-transformation and then standardised through the calculation of z-score values (e.g. Desloges and Gilbert, 1994; Heideman et al. 2015). Z-scores of log-transformed varve (and seasonal sub-layer) thickness data were calculated as:

$$Vs_y = \frac{(V_y - \overline{V}_y)}{\sigma_{Vy}}$$

where Vs_y is the standardised varve thickness for a given year (y), V_y the log-transformed varve thickness, $\overline{V}_y$ the mean varve thickness, and σ_{Vy} the standard deviation of varve thickness. The standardised values could then be combined as an unweighted mean thickness, Vs_y, for each year across any given number of correlated varve series. Statistical correlations (Pearson's) were carried out to test the apparent visual agreement between the records observed during the cross-dating phase.

2.5.8 Error estimation

The precise quantification of varve counting errors can be difficult because it necessitates subjective interpretations, and because varve disturbances may vary through a sequence (Brauer et al., 1999). However, because the composite chronology was divided into shorter counting sections, defined by the existence of basin-wide marker layers (Figure 2.8), sections of greater (lesser) counting uncertainty could be isolated. Counting errors were identified through the cross-dating process and were recorded as either missed varves (Type A) or erroneously identified varves (Type B; cf. Lamoureux and Bradley, 1996) in site chronologies. This process also highlighted the existence of breaks in site varve chronologies, which ranged from ~2-13 years in duration. Where possible, i.e. for the uppermost 48.05 cm at site FC-E, thin sections were revisited to determine the cause of counting discrepancies. The final varve counting errors were expressed in years as the maximum counting difference between two or more correlated varve series. Because the basal 217 ± 15 varves of the master varve chronology, and the uppermost 289 varves counted from thin sections, are each represented by a single varve series (FC-B and FC-E respectively) the counting error for these sections rely on recorded discrepancies between repeat counts.

2.6 Phase 3c: Dating the floating varve chronology using tephrochronology

2.6.1 Rationale

Tephrochronology involves the use of primary tephras as isochronous marker layers to synchronise and/or date Quaternary sediment sequences (Lowe, 2011). To be effective, the physical and/or chemical properties of disparate tephra deposits must be characterised using laboratory methods (e.g. Hayward, 2012), and correlated with previously identified ('known') eruptions. When dating evidence is available for known

tephra deposits, geochemical fingerprinting and correlation allows the transfer of age information between sedimentary sequences.

The integration of tephrochronology and varve chronology has provided precise chronological constraints on the timing and duration of palaeoenvironmental events (e.g. Brauer et al., 2008; Neugebauer et al., 2012; Wulf et al., 2012; 2013; Rach et al., 2014), as well as regional leads and lags in past environmental changes (e.g. Lane et al., 2013). However, this approach has yet to be widely applied in relict glaciolacustrine environments (e.g. MacLeod et al., 2015), despite minimal organic remains in such systems and, therefore, the limited potential for radiocarbon dating (although see Ridge et al., 2012).

However, tephrochronology has great potential in Patagonia, as the eruptive histories of several regional volcanoes have received increasing attention (e.g. Wastegård et al., 2013; Weller et al., 2015; Fontijin et al., 2016; Alloway et al., 2017). The closest volcano to the study site, Cerro Hudson (Figure 1.3), was active throughout the late Pleistocene (Weller et al., 2015), and tephras from this volcano are identified in both marine (Carel et al., 2011) and terrestrial (e.g. Haberle and Lumley, 1998; Weller et al., 2014; 2015; Stern et al., 2015; 2016) sediment records.

Therefore, the Río Fenix Chico varve sequences were carefully examined for possible tephra deposits. In this thesis, varve chronology and tephrochronology are combined to absolutely date the timing of ice sheet deglaciation, and changes in ice lobe retreat dynamics (Chapter 5), and to facilitate direct comparisons with other palaeoenvironmental records for the examination of climatic influences on ice lobe deglaciation (Chapters 6 and 7).

2.6.2 Field sampling

A single visible tephra layer was identified in 4 of the 5 investigated varve sequences (Figure 2.9), occupying a common position in the varve thickness stratigraphy. The tephra layers were described, and then sampled from fresh sediment surfaces (at 3 sites) to facilitate analyses of chemical composition. At one site (FC-E) the tephra layer was sampled in ~2–3 mm-thick increments, yielding a total of five sub-samples, to assess for chemical stratification.

2.6.3 Electron microprobe analysis of individual glass shards

The major-element chemical composition of tephra samples was derived from wavelength dispersive electron microprobe analysis (WDS–EPMA) of individual glass

shards (Hayward, 2012). Each sample was sieved at 125 and 15 μm to obtain the vitreous size fraction. This optimum fraction was separated from non-tephra particles (e.g. diatoms) using sodium polytungstate (SPT) at 2.55 g cm^{-3} density (Blockley et al., 2005). A portion of each extraction was examined under a high-powered polarising microscope to define glass content and shard morphology, and was subsequently mounted into a probe stub using Specifix 40 epoxy resin. The shards were hand polished using a 0.10 μm Al_2O_3 paste to create sections through shard surfaces for chemical analysis. Plugs were cleaned in an ultrasonic bath before carbon coating. Major-element analyses were obtained using a Cameca-SX100 WDS-EPMA at the Tephra Analytical Unit, University of Edinburgh. Analyses were undertaken using a beam diameter of 5 µm at 15 keV; a 2 nA beam current was employed for Na, Al, Si, Fe, K, Ca, Mg and a 80 nA beam current for Mn, Cl and Ti (Hayward, 2012). The uncertainty on this analysis is <1%. International standards Lipari 1 (rhyolitic) and BCR2G (basaltic) were analysed at regular intervals to monitor for instrument drift.

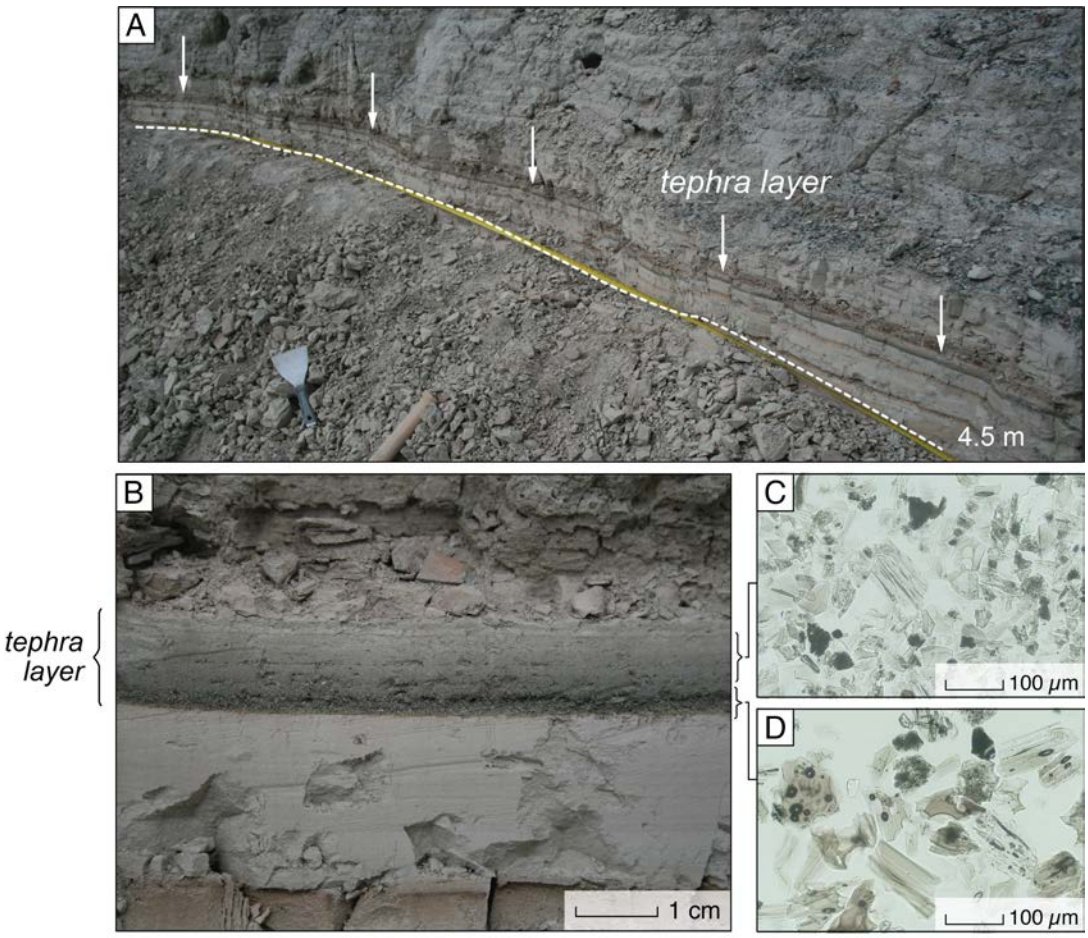

Figure 2.9. Example of visible tephra layer observed at four of the five studied sites. (A) and (B) show tephra layer in section at FC-E. The tephra occurs in upper part of a single coarse component layer. (C) Characteristic glass shards and minerals extracted from the lower portion of the tephra layer. (D) Characteristic glass shards and minerals extracted from the upper portion of the tephra layer.

2.6.4 X-ray fluorescence spectrometer analysis of bulk tephra

Alongside major-element analyses, the trace-element composition of bulk tephra samples was acquired using X-ray fluorescence (XRF) spectrometry. This step was necessary because major-element analyses (section 2.8.3) yielded wide geochemical envelopes (Chapter 5) that, unaccompanied, limited the ability to form robust correlations with known tephra layers. Moreover, trace-element analyses have previously been obtained for several regional tephra layers, and demonstrate the potential to discriminate between individual eruptions from the same, or different, volcanoes (e.g. Weller et al., 2015; Stern et al., 2015; 2016).

Five bulk tephra samples of ~10-12 g (from 3 sites) were prepared for trace-element analysis. Samples were sieved at 15 μm to remove the clay fraction, powdered in a tungsten carbide mill, and pressed into 40 mm pellets. Pellets were analysed using a PANalytical Axios Sequential X-ray Fluorescence Spectrometer at Royal Holloway, University of London. Matrix corrections were applied using the major-element chemical dataset obtained using the WDS-EMPA analysis, and Limits of Detection (LoD) were calculated using long-term data collected using the same equipment.

2.6.5 Assigning an eruption and age

Major- and trace-element geochemical data were compared with existing regional tephrochronological datasets to identify possible correlatives. Where identified deposits were associated with published chronological data, the age was recalibrated (and remodeled where necessary) in Oxcal v4.3 (Bronk Ramsey, 2009).

2.7 Phase 3d: Bayesian age-modelling of ice lobe deglaciation

2.7.1 Rationale

Bayesian age modelling is increasingly employed to rigorously constrain the deglaciation histories of former glaciers (e.g. MacLeod et al., 2011; Chiverrell et al., 2013; Lane et al., 2014). This method allows disparate strands of chronological information to be integrated within a probabilistic framework (Bronk Ramsey, 2008) to refine the chronology of deglacial events (e.g. moraine emplacement). Using Bayesian terminology, age models comprise 'prior' morphostratigraphic information (e.g. ice-margin position) with the likelihood distributions of radiometric dating evidence (e.g. cosmogenic nuclide exposure ages) and/or time intervals derived from layer-counting (e.g. varve chronology; Bronk Ramsey, 2009a). The model output contains 'posterior' cumulative probability functions that represent the likely age of each input sample

(Bronk Ramsey, 2009a). The method uses Markov Chain Monte Carlo iterations to form a probability distribution of input dates, and refine the likelihood distribution of individual ages, utilising both the 'prior' model and original dates (Bronk Ramsey, 2009a). As used in this thesis, the main advantages of this approach are (i) the ability to integrate all available chronological data into a single model of ice lobe retreat dynamics and, therefore, avoid subjective selection of evidence; (ii) the ability to produce age estimates for discrete events (e.g. moraine emplacement).

2.7.2 Modelling of ice lobe retreat dynamics

Bayesian age modelling was used to integrate (i) the new chronological data produced in this thesis, namely the absolutely dated varve chronology; with (ii) existing cosmogenic nuclide exposure ages derived from moraine boulders (Kaplan et al., 2004; Douglass et al., 2006), and luminescence ages derived from glaciofluvial outwash sands (Smedley et al., 2016). A prior model of ice lobe retreat was generated through stratigraphic investigations in the Río Fenix Chico valley. Prior to age modelling, cosmogenic nuclide exposure ages were recalibrated using Southern Hemisphere production rates (Putnam et al., 2010; Kaplan et al., 2011; Chapter 5). Age modelling used Sequence algorithms (Bronk Ramsey, 2008) and outlier analysis, namely the General outlier model (Bronk Ramsey, 2009b). Outliers were retained but were down-weighted (so-called 'model-averaging'; Bronk Ramsey, 2009b).

2.8 Phase 4: Investigating high-frequency variations in varve thickness using spectral analyses

2.8.1 Rationale

Often superimposed on longer term varve thickness trends, which in glaciolacustrine systems are typically related to glacier advance and retreat cycles (Chapter 5), are inter-annual to decadal fluctuations in sedimentation rate (e.g. Leonard, 1997; Ohlendorf et al., 1997; Bird et al., 2009; Thomas and Briner, 2011; Glur et al., 2015). Spectral analyses approaches can test varve thickness trends for regular cycles, or periodicities, and may elucidate climatic controls on sedimentation (e.g. Ólafsdóttir et al., 2013; Ojala et al., 2015). Owing to a lack of high-resolution records, the impact of short-term climate variability on Patagonian Ice Sheet deglaciation are unknown, providing the motivation for spectral analyses (Chapter 6).

2.8.2 Removal of low-frequency trends

To explore the potential climate significance of short-term cyclicities in varve thickness, low-frequency (>centennial-scale) cyclic components were identified and removed. The non-linear nature of most low-frequency trends (Mudelsee, 2013) prevented the simple subtraction of a linear least-squares regression for trend removal. Instead, Singular Spectrum Analysis (SAA; Vautard and Ghil, 1989) was used, which can decompose a time series into non-linear trends, periodic components and noise. SSA was applied using the "Rssa" package in R (Golyandina and Korobeynikov, 2014) to isolate leading non-linear, low-frequency trends. The window length, *L*, represents the main parameter in the identification of low-frequency trends. In general, too small a *L* leads to decomposition errors (Golyandina and Zhigljavsky, 2013). There is consensus that *L* should be near, but not exceed one-half the time-series length, *N*, (Golyandina, 2010; Golyandina and Zhigljavsky, 2013; Mudelsee, 2013; Golyandina and Korobeynikov, 2014). This was taken into consideration when selecting *L* values, and was optimised for each *N*. Once identified, centennial-scale non-linear trends were subtracted from the varve series, and the residuals used for spectral analyses.

2.8.3 Spectral analysis

The REDFIT program of Schulz and Mudelsee (2002; employed in 'Past3' cf. Hammer et al., 2001) was used to test for periodic features in the detrended varve thickness series. This method is widely applied in palaeoclimatology (Mudelsee, 2013). The REDFIT program computes a bias-corrected Lomb-Scargle periodogram (Lomb, 1976; Scargle, 1982) and a theoretical red (autoregressive, AR(1)) noise background, given the null hypothesis that the data are red-noise, and tests if spectral peaks are significant against this red-noise background. REDFIT uses Welch overlapped segment averaging, with the number of segments controlling the degree of smoothing of the time-series. We calculated periodograms using 1 segment, i.e. no smoothing, given the subjective nature of selecting an appropriate number of segments (Ojala et al., 2015). 'False-alarm' significance levels (90–99%) were computed using parametric approximations (chi-squared) and Monte Carlo iterations (n=1000) of the AR(1) process, to ensure confidence in estimated periodicities.

The Multi-Taper Method (MTM; Thomson, 1982; employed in 'kSpectra toolkit' v2.13) for spectral estimation was applied to verify the REDFIT analysis. This method uses a small set of tapers, or windowing functions, to reduce the overall variance of power spectrum estimates (Thomson, 1982), and retains high-frequency resolution. One potential disadvantage of this method is reduced spectral resolution. Increasing the number of tapers can reduce noise, but also decrease spectral resolution. The number

of tapers therefore represents a trade-off between spectral resolution and the stability of the spectral estimate (Thomson, 1982). Spectral estimates were tested using 1–3 tapers. However, one taper was used in the final analyses, which is conservative, but optimal for minimising spectral leakage (Thompson, 1982; Park et al., 1987). Peaks estimated in the MTM power spectrum were tested for significance against a null hypothesis of a red-noise background (Mann and Lees, 1996). Confidence levels relative to the estimated red-noise background were determined through chi-squared computations.

2.8.4 Wavelet analysis

Alongside REDFIT and MTM (spectral) analysis, continuous wavelets (Torrence and Compo, 1998) were derived for detrended varve thickness series to investigate temporal variations in spectral power. This method was chosen because continuous wavelets allow a dataset to be inspected over short, intermediate, and long timescales simultaneously. Moreover, continuous wavelets are suitable for time series that contain non-stationary power at definite frequencies and, therefore, allow the strength of cyclic features to be monitored over time. This analysis used the Morlet mother wavelet, the most commonly used wavelet in geophysics for sequences containing non-stationary power at different frequencies (Torrence and Compo, 1998; employed in 'Past3' cf. Hammer et al., 2001). Varve series were zero-padded to limit edge effects and a "cone of influence" calculated. Prior to computing wavelets, an autoregressive–moving-average (ARMA) analysis (Melard, 1984) was undertaken to determine an appropriate lag-1 coefficient (null hypothesis) for a red-noise computation of 95% (chi-squared) confidence regions.

Chapter 3. The glacial geomorphology of the Lago Buenos Aires and Lago Pueyrredón ice lobes of central Patagonia

Bendle, J.M., Thorndycraft, V.R., Palmer, A.P. (2017) The glacial geomorphology of the Lago Buenos Aires and Lago Pueyrredón ice lobes of central Patagonia. Journal of Maps, 13, 654–673.

Abstract

This paper presents a glacial geomorphological map of landforms produced by the Lago General Carrera-Buenos Aires and Lago Cochrane-Pueyrredón ice lobes of the former Patagonian Ice Sheet. Over 35,000 landforms were digitised into a Geographical Information System from high-resolution (<15 m) satellite imagery, supported by field mapping. The map illustrates a rich suite of ice-marginal glacigenic, subglacial, glaciofluvial and glaciolacustrine landforms, many of which have not been mapped previously (e.g. hummocky terrain, till eskers, eskers). The map reveals two principal landform assemblages in the central Patagonian landscape: (i) an assemblage of nested latero-frontal moraine arcs, outwash plains or corridors, and inset hummocky terrain, till eskers and eskers, which formed when major ice lobes occupied positions on the Argentine steppe; and (ii) a lake-terminating system, dominated by the formation of glaciolacustrine landforms (deltas, shorelines) and localised ice-contact glaciofluvial features (e.g. outwash fans), which prevailed during deglaciation.

3.1 Introduction

The Patagonian Ice Sheet has episodically expanded across the southern Andes of South America (38–56ºS) throughout the Quaternary (Figure 3.1; Caldenius, 1932; Rabassa, 2008). During such times, substantial ice lobes advanced along major valleys constructing nested terminal moraine sequences and extensive outwash plains on the extra-Andean steppe (Caldenius, 1932). Interest in these glacial landform assemblages has increased in recent years as information on the timing of glacier fluctuations may yield insight into past variations in Southern Westerly Wind changes (Moreno et al., 2009, 2015; García et al., 2012; Boex et al., 2013) and interhemispheric glacial and climate synchroneity (Denton et al., 1999; Sugden et al., 2005; Murray et al., 2012). Moreover, geomorphological studies, including glacial landsystem approaches, have enabled detailed reconstructions of former ice-dynamics (Bentley et al., 2005; Lovell et al., 2012; Darvill et al., 2016). Whilst such methods have been applied in southernmost Patagonia, around central Patagonia and the Northern Patagonian Icefield (NPI; ~46-48ºS) previous work has focused on constraining the timing of glacial fluctuations, with less attention given to the detailed nature of landform-sediment assemblages (Glasser et al., 2009). Therefore, we aim to produce a comprehensive map of the glacial geomorphology related to two major ice lobes of central Patagonia. The map will provide the foundation for new reconstructions of ice lobe and palaeolake dynamics through the application of glacial inversion methods (Kleman et al. 2006) and landsystem analysis (Evans, 2003), and will underpin future chronological investigations.

3.2 Study location and previous work

3.2.1 Study location

The mapping conducted in this study focuses on the area between ~46–48ºS and ~74–70ºW (Figure 3.1), a region characterised by both high mountains (>3–4000 m asl) and deep troughs incised to below present sea level. The west of the study area is dominated by the modern NPI and its surrounding deep valleys and fjords (Glasser and Ghiglione, 2009). These valleys feed into two major west-east trending overdeepened troughs occupied by the transnational lakes of Lago General Carrera–Buenos Aires (LGC–BA) and Lago Cochrane–Pueyrredón (LC–P). East of the Patagonian mountain front, the landscape transitions into a broad, semi-arid

steppe interspersed with Plio-Pleistocene sedimentary and basalt plateaus (Gorring et al., 2003).

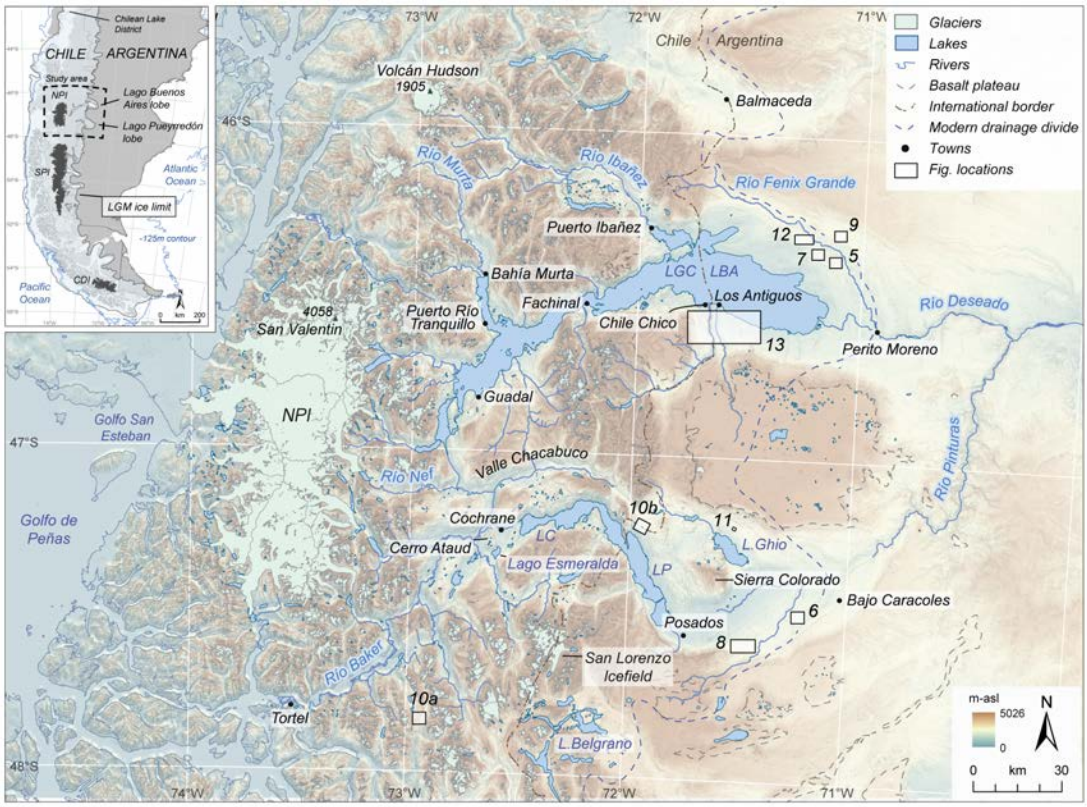

Figure 3.1. Location map of the studied area in central Patagonia. Boxes indicate the location and number of additional figures. Inset shows the extent of the Patagonian Ice Sheet (PIS) at the Last Glacial Maximum (LGM); redrawn after Singer et al. (2004). The -125 m contour provides an indication of the approximate sea level drop at the LGM (e.g. Yokoyama et al., 2000; Peltier and Fairbanks, 2006; Lambeck, et al., 2014). NPI: Northern Patagonian Icefield; SPI: South Patagonian Icefield; CDI: Cordillera Darwin Icefield. Contemporary icefield limits extracted from the 'Randolph Glacier Inventory' dataset (Pfeffer et al., 2014).

Previous studies indicate that fast-flowing outlet glaciers of an expanded Patagonian Ice Sheet periodically occupied the LGC–BA and LC–P depressions (Glasser and Jansson, 2005). These ice lobes advanced to the Argentine steppe (Caldenius, 1932), blocked regional river systems, and caused a ~200 km westward shift in the drainage divide towards the Patagonian cordillera, which diverted meltwater eastward to the Atlantic Ocean (Turner et al., 2005; Bell, 2008; Glasser et al., 2016). During deglaciation, large proglacial lakes developed in the basins between terminal moraines and the ice front (Turner et al., 2005; Bell, 2008). The eventual release of this freshwater to the Pacific Ocean disturbed vertical mixing patterns and regional climate (Glasser et al., 2016).

3.2.2 Previous mapping

Caldenius (1932) was the first to extensively map the glacial deposits of the region, providing the foundation for other early studies (Feruglio, 1950; Fidalgo and Riggi, 1965). Caldenius (1932) identified four terminal moraine systems on the Argentine steppe east of LGC–BA and LC–P, and argued that they formed over multiple glaciations based on their state of preservation. Since Caldenius (1932), several studies have presented geomorphological maps from the region (Figure 3.2), with mapping scale and detail tailored to specific research objectives (Table 3.1).

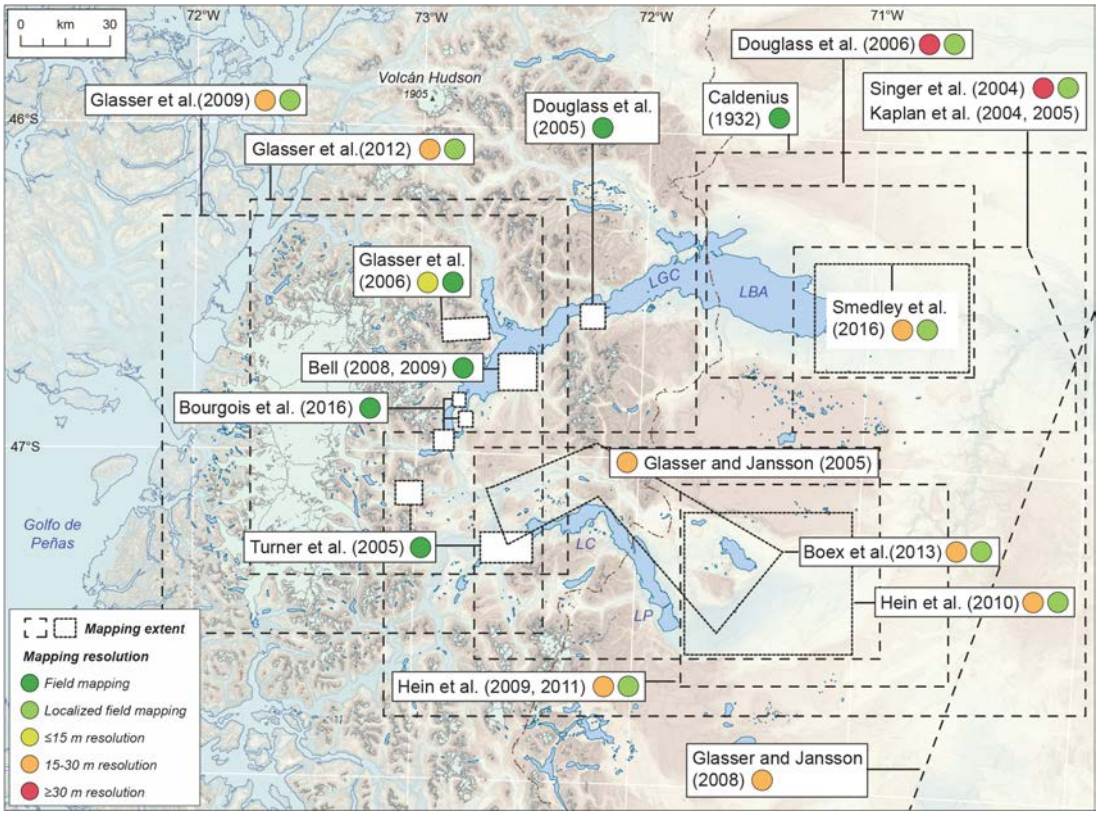

Figure 3.2. Extent and resolution of previous glacial geomorphological mapping studies, with mapped features listed in Table 3.1.

Glasser and Jansson (2008) produced a map of glacial landforms formed at the margins and bed of the former Patagonian Ice Sheet between 38–56°S, to infer ice-sheet scale ice-dynamics (Glasser et al., 2008). This map currently represents the most complete representation of glacial geomorphology at the ice lobe scale, but the low mapping resolution is such that subtle or complex features were necessarily omitted or generalised. For example, on the plains east of LGC–BA a complex system of ice-marginal meltwater channels and outwash corridors are noticeably simplified (Glasser and Jansson, 2008).

Table 3.1. Features mapped in previous studies. Mapping resolution refers to satellite imagery used in geomorphological mapping, as stated in original publications. Additional landform types mapped in this study are listed in Table 3.2 and 3.3.

Previous studies			Mapped landforms										
Reference	Mapping purpose	Mapping resolution	Drift or moraine complex	Moraine ridges	Trimlines	Outwash plains	Ice-contact glaciofluvial deposits	Meltwater channels	Ice-scoured bedrock	Glacial lineations	Raised deltas	Palaeolake Shorelines	Glaciolacustrine deposits
Caldenius (1932)	Morphostraigraphic	Field	✓			✓							✓
Feruglio (1950)	Morphostraigraphic	Field	✓			✓							
Fidalgo and Riggi (1965)	Morphostraigraphic	Field	✓			✓							
Kaplan et al. (2004)	Chronostratigraphic	30m; LF	✓	*									
Singer et al. (2004)	Chronostratigraphic	30m; LF	✓	*									
Glasser and Jansson (2005)	Geomorphic	15-30m		✓			✓	✓		✓	✓		
Kaplan et al. (2005)	Chronostratigraphic	30m; LF	✓	*									
Turner et al. (2005)	Morphostratigraphic Chronostratigraphic	Field		✓			✓				✓	✓	
Douglass et al. (2006)	Chronostratigraphic	30m; LF	✓	*		✓							✓
Glasser et al. (2006)	Morphostratigraphic Chronostratigraphic	15m; Field		✓		✓	✓	✓	✓				
Bell et al. (2008)	Geomorphic Morphostratigraphic	Field									✓		
Bell et al. (2009)	Geomorphic Morphostratigraphic	Field									✓		
Glasser and Jansson (2008)	Morphostratigraphic	30m		✓	✓	✓		✓		✓	✓	✓	

Hein et al. (2009)	Chronostratigraphic	15-30m; LF											
Glasser et al. (2009)	Geomorphic	15-30m; LF		✓	✓	✓	✓		✓	✓	✓		
Hein et al. (2010)	Chronostratigraphic	15-30m; LF		✓		✓					✓	✓	
Hein et al. (2011)	Chronostratigraphic	15-30m; LF											
Glasser et al. (2012)	Chronostratigraphic	15-30m; LF		✓		✓							
Boex et al. (2013)	Chronostratigraphic	15-30m?; LF		✓									
Bourgois et al. (2016)	Morphostratigraphic Chronostratigraphic	Field		✓							✓	✓	
Glasser et al. (2016)	Morphostratigraphic Chronostratigraphic	15-30m; LF									✓	✓	
Smedley et al. (2016)	Morphostratigraphic Chronostratigraphic	15-30m; LF		✓		✓						✓	✓

Morphostratigraphic = study focused on relative depositional order of ice-marginal and/or glaciolacustrine landforms.
Chronostratigraphic = study focused on landform identification for radiometric dating applications.
Geomorphic = study focused on landform and/or sediment form, pattern and/or distribution, to infer former glacier or lake dynamics.
LF = localized areas of field mapping and/or ground-truthing
* = moraine ridges identified in the field, but not reproduced on geomorphological map.

Other studies have concentrated on smaller study areas around former glacier margins. For instance, Glasser and Jansson (2005) mapped subglacial lineations across the LC–P ice lobe bed and inferred former ice flow direction, regional ice-divide locations and ice thickness at local LGM extent. Similarly, and with the specific intention of supporting geochronological studies (Figure 3.3; Table 3.1), Kaplan et al. (2004), Singer et al. (2004) and Douglass et al. (2006) re-mapped the outer moraine complexes at LGC–BA. In addition, Hein et al. (2009, 2010, 2011) re-mapped the outer moraine systems of LC–P and identified a series of well-preserved moraine ridges, outwash terraces, palaeo-shorelines and landslide deposits. Hein et al. (2010) also noted some morphological differences between local-LGM moraine sets, which included hummocky and sharp-crested forms.

Moraine ridges and other ice-contact landforms have also been mapped further west, in the Rio Bayo, Leones, Nef, Plomo and Colonia valleys, and at Lago Esmeralda (Figure 3.1 and 3.2), and dated to ascertain the timing of regional glacier readvances since the local LGM (Glasser et al., 2006; 2012). Turner et al. (2005), Bell (2008) and, more recently, Glasser et al. (2016), mapped palaeo-shorelines and raised lacustrine deltas formed at proglacial lake margins during glacier recession that contribute to a regional model of deglacial palaeolake development and drainage.

Several studies have mapped glacial landforms at the valley scale, close to contemporary icefields, to constrain the pattern of Holocene glacier fluctuations (e.g. Douglass et al. 2005; Glasser et al., 2005; Harrison et al 2006, 2008; Davies and Glasser, 2012; Nimick et al., 2016). Finally, Glasser et al. (2009) compiled geomorphological and sedimentological evidence from eleven contemporary outlet glaciers to investigate the controls on landform formation around the NPI.

Overall, a lack of consistent, detailed mapping at the ice lobe scale has led to many important features (e.g. meltwater channels) being misidentified or overlooked in this region. Further mapping conducted at a high resolution (<15 m) is required for refined reconstructions of regional ice-sheet history and dynamics.

3.2.3 Ice lobe chronology

Across the study area, the timing of major ice lobe fluctuations is relatively well constrained owing to numerous dating studies (Figure 3.3). Early palaeomagnetic studies at LGC–BA (Mörner and Sylwan, 1987, 1989) and LC–P (Sylwan et al.,

1991) established that some of the outer terminal moraines formed at the time of the Matuyama Reversed Chron over ~780 ka ago (Singer and Pingle, 1996). Subsequent $^{40}Ar/^{39}Ar$ dating of basaltic lava flows, interbedded within moraine sequences, provided additional constraints on the timing of ice lobe advances (Ton-That et al., 1999; Singer et al., 2004). These studies dated the outermost moraines at LGC–BA to ~1016 ka, and confirmed the timing of this 'Greatest Patagonian Glaciation', first recognised by Mercer (1976). At LGC–BA a further six terminal moraine sequences were deposited between ~1016 ka and ~760 ka, with another six formed between ~760 ka and ~109 ka (Singer at al., 2004).

The chronology of major ice lobe fluctuations has since been refined through direct dating of glacial deposits, including cosmogenic nuclide exposure dating of moraine boulders (Kaplan et al., 2004, 2005, 2011; Douglass et al., 2006; Hein et al., 2010; Boex et al. 2013) and outwash gravels (Hein et al. 2009, 2011), and luminescence dating of glaciofluvial outwash sediments (Glasser et al., 2006; Harrison et al., 2012; Smedley et al., 2016). These studies have supported the $^{40}Ar/^{39}Ar$ ages of earlier investigations, and provided evidence for additional ice lobe advances during MIS 2, 3, 6 and 8.

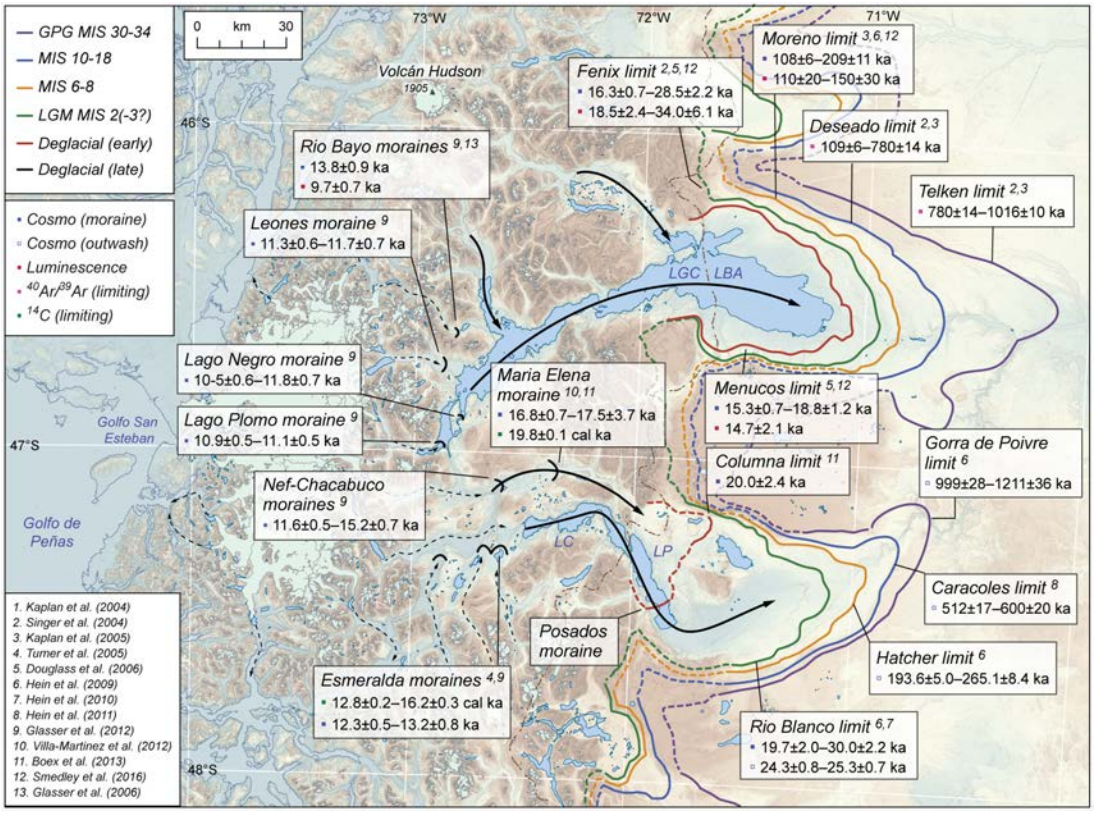

Figure 3.3. Major glacier limits and compilation of associated dating evidence based on previous studies. Cosmogenic nuclide exposure ages are presented as reported in original publications; however, where available, we report recalculated ages obtained from the use of southern hemisphere production rates (e.g. Putnam et al., 2010; Kaplan et al. 2011). Luminescence ages are presented as reported in original publications. Published ^{14}C determinations were recalibrated in Oxcal v4.3 (Bronk Ramsey, 2009) using the southern hemisphere calibration curve of Hogg et al. (2013). Arrows represent major ice lobe flow lines (Glasser and Jansson, 2005).

Recent studies have also attempted to constrain the pattern of glacier retreat following the local LGM (Figure 3.3), and the consequent growth and drainage of ice-dammed proglacial lakes. The exact timing of glacier stillstands, and whether the retreat patterns of the LGC–BA and LC–P lobes were synchronous, however, remains equivocal. For example, Boex et al. (2013) dated a stabilisation of the LC–P lobe at the Maria Elena moraine (~17.1 ka) in Valle Chacabuco. However, basal radiocarbon dates from lake basins that were exposed subaerially after ice retreat at this location, have yielded older ages (~19.8 cal ka; Villa-Martínez et al., 2012). Moreover, these radiocarbon dates are significantly older than either the exposure age of the Menucos moraine (~16.9 ka; recalculated age cf. Kaplan et al., 2011), which represents an early deglaciation limit on the Argentine steppe at LGC–BA (Figure 3.3), or the luminescence age of Menucos-related outwash deposits (~14.2 ka; Smedley et al., 2016). Similarly, Turner et al. (2005) produced basal radiocarbon ages that exceed ~12.8 cal ka from kettle holes at Lago Esmeralda and Cerro Ataud, and interpreted these dates as evidence for early deglaciation in this area. Recently, Nimick et al. (2016) produced boulder ages from moraines in the Colonia valley that coincide in timing with the Antarctic Cold Reversal (ACR). In contrast, Glasser et al. (2012) proposed a regional stabilisation of NPI outlet glaciers, including at this location, around the time of the European Younger Dryas (YD), based on a suite of cosmogenic nuclide exposure ages of ~11.0 to 12.8 ka, and supporting luminescence ages from local ice-contact deposits (Glasser et al., 2006). These alternative chronologies have hampered attempts to develop a coherent regional model of ice lobe and proglacial lake evolution that reconcile all dating evidence (Bourgois et al., 2016; Glasser et al., 2016). New high-resolution mapping will enable refinements in the morphostratigraphic order of deglacial events and will contribute to resolving disparate retreat chronologies.

3.3 Methods

Geomorphological mapping was achieved through satellite image interpretation and field checking (Figure 3.4; Table 3.2). The map is presented at 1:420,000 scale using the WGS-1984 UTM-Zone18S coordinate system. Glacial landforms were digitised in ArcGIS (v10.3) at imaging scales of 1:8,000 to 1:50,000, using a combination of 2.5 m resolution SPOT-5 and ~1-2 m resolution DigitalGlobe (GeoEye-1, IKONOS) images available through the ESRI™ 'World Imagery' service. Areas of poor image quality (e.g. obscured by clouds) were examined in GoogleEarthPro™ software (v7.1), which also offers SPOT-5 and DigitalGlobe images for our study area. These image sources were used in preference to relatively low resolution satellite scenes (e.g. Landsat: 30 m) as they allowed a greater diversity of features to be mapped, and provided clarity in the identification of previously un-recorded, subtle landform types. Both relief-shaded (315º and 45º azimuth) and slope gradient-shaded models were constructed from ASTER G-DEMs (30 m cell-size) following procedures outlined in Smith and Clark (2005), primarily to provide topographic context in areas of complex relief. Additionally, oblique three-dimensional views were created in GoogleEarthPro™ to aid landform identification, especially in areas where field verification was not possible. A copy of the final geomorphological map can be found in the Appendix.

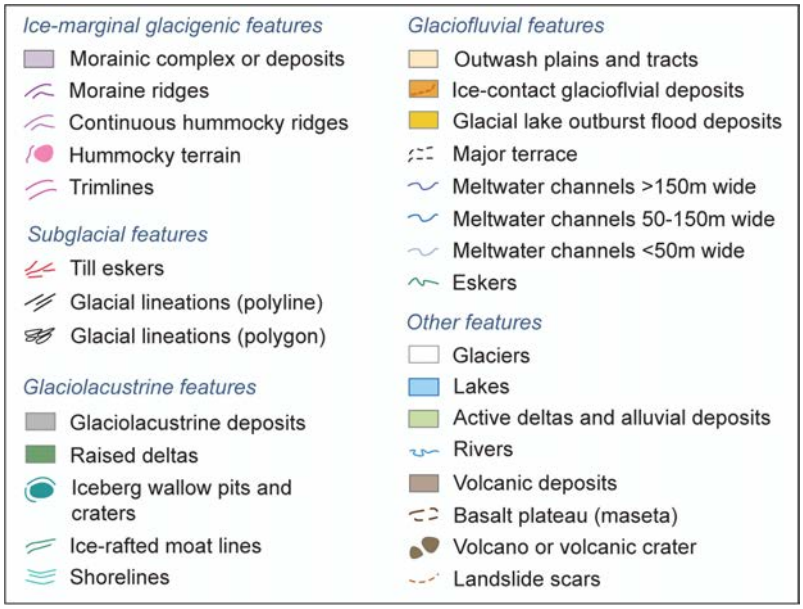

Figure 3.4. Mapping legend to accompany Figures 3.5–3.13. Note that on some figures, certain layers (e.g. 'morainic complexes or deposits') are not shown to enhance the visual clarity of our landform interpretations. Contemporary glacier extents were extracted from the 'Randolph Glacier Inventory' dataset presented in Pfeffer et al. (2014).

Table 3.2. Summary of glacial geomorphology mapped in this study and criteria used in landform identification.

Landform	Morphology	Identification characteristics	Uncertainties	Significance	Previous mapping
Morainic complexes or deposits	Undulating topography within which distinctive moraine ridges occur.	Texture/colour difference from adjacent terrain. Presence of moraine ridges. Elevated above surrounding terrain.	Extent of morainic material difficult to delimit on imagery.	Marks approximate extent of ice-marginal deposition	Caldenius (1932); Feruglio (1950); Fidalgo and Riggi (1965); Kaplan et al. (2004, 2005); Singer et al. (2004); Douglass et al. (2006)
Moraine ridges	Ridges of positive relief that display arcuate, crenulate or saw-tooth planform, and sharp crestlines. Ridges range from ~100 to >5000m long and ~30 to 300m wide.	Dark/light shadowing on opposing moraine flanks indicative of positive relief. Texture/colour difference from adjacent terrain.	Very low-relief ridges may be difficult to detect in imagery.	Marks former terminal position of glacier.	Glasser and Jansson (2008); Hein et al. (2010); Glasser et al. (2012)
Continuous hummocky ridges	Medium relief (<20m) hills and short (<200m) ridges connected to form longer undulating chains. Ridges separated by narrow (<10-20m) meltwater channels. Crestlines less well-defined than moraine ridges.	Best identified on high-resolution images. Shadowing indicates subtle changes in relief, and highlights linear order of ridges.	Boundaries of individual ridges are difficult to delimit. Linear patterns are difficult to map in the field.	Marks former terminal position of glacier.	Unmapped
Hummocky terrain	Densely-spaced hills and hollows of 5-20m high and 20-200m wide. Crestlines are less well-defined than moraine ridges. Exhibit chaotic organization or crude linearity.	Dark/light shadowing indicate positive relief of hummocks. Hollows may be water-filled. Texture/colour difference from adjacent terrain.	Boundaries of small (<5m high) hummocks may be difficult to define.	Marks former ice-marginal zone, or zone of stagnant ice.	Unmapped
Trimlines	Sub-horizontal linear features on valley sides separating vegetated and non-vegetated ground.	Sharp definition at boundary of vegetated and non-vegetated terrain. Occur close to existing glacier margins.	Potential confusion with shorelines or moraines.	Indicative of former glacier thickness and slope.	Glasser and Jansson (2008); Glasser et al. (2009)
Till eskers	Straight to sinuous ridges of ~50-500 m long and 5-15 m high, with undulating crests.	Light/dark shadowing indicates positive relief. Occur in groups that display similar orientations oblique to ice flow. Often merge into the limbs of saw-tooth push moraines.	Potential confusion with eskers.	Indicative of sub-marginal squeezing of saturated till into tunnels/crevasses.	Unmapped

Glacial lineations	Linear, elongate, parallel landforms formed in bedrock or sediment (drumlins, flutings), and ranging from ~100m to >3000m in length.	Occur in groups showing parallel conformity. Dark/light shadowing indicates positive relief. Structural alignment may differ from surrounding (non-lineated) bedrock.	Misclassification of non-glacial bedrock structures as glacial lineations.	Indicative of former ice-flow direction, and fast flow where length:width is high.	Glasser and Jansson (2005, 2008)
Meltwater channels	Deeply incised, and generally steep-sided, conduits of sinuous form. Channels vary from ~10m to >1km in width and from ~100m to >10km in length. Rarely contain, or follow, modern drainage routes.	Channel margins defined by shadowing due to relative relief change. Occur as closely-spaced 'flights' (lateral) or isolated meanders (proglacial) on images. Often occur in association with moraines.	Potential misidentification of modern drainage routes, although unlikely.	Marks approximate position of glacier margin. Indicates significant ice-marginal meltwater production.	Glasser and Jansson (2008)
Outwash plains and tracts	Large, open, approximately flat surfaces graded to former ice-limits (e.g. moraines). Often dissected by meltwater channels and relict stream networks.	Clear colour/texture difference due to soil/vegetation cover change. Often begin and end abruptly with sharp terrace edges (break in slope).	Exact extent of outwash difficult to delimit. Difficult to separate from channels where occurring as narrow corridors.	Indicative of major meltwater drainage pathways.	Caldenius (1932); Glasser and Jansson (2008); Hein et al. (2010); Smedley et al. (2016)
Eskers	Straight to sinuous ridges or conical mounds, ranging from ~100m to >1000m in length. Esker crestlines can be sharp, rounded and/or undulating. Surficial sediments consist of sands and gravels.	Dark/light shadowing indicates positive relief. Occur as isolated ridges with few (dis)tributaries, or in dense interconnected networks. Usually oriented oblique to former ice flow.	Potential confusion with till eskers. Low-relief eskers difficult to detect on imagery.	Indicative of marginal meltwater channel configuration.	Unmapped
Ice-contact glaciofluvial deposits (e.g. outwash fans, kame terraces)	Flat-topped or gently sloping glaciofluvial accumulations raised above valley floors, displaying steep ice-contact faces and pitted surfaces (subaerial), or broad, low-gradient valley-fills prograded from former ice margins (subaqueous).	Homogenous surface texture and colour. Shadowing (break in slope) along former ice-contact slope. Often associated with other ice-marginal deposits (e.g. moraines).	Potential confusion with raised deltas, due to surface colour and texture, but fans/kame terraces are often pitted.	Marks former terminal or marginal position of glacier. Indicative of high meltwater discharges.	Glasser and Jansson (2008); Glasser et al. (2009)
Glacial lake outburst flood (GLOF) deposits	Flat to sloping surfaces of sand and gravel with sharp edges and raised above modern fluvial systems. Can exhibit carapace of large (>5m) boulders and surface may be	Shadowing indicates terrace edges. May exhibit bar-like morphology. Presence of large boulders on terrace surfaces.	Possible confusion with other flat-topped accumulations (deltas, kame terraces), but unlikely due to lag	Indicative of palaeoflood flows an order of magnitude larger than contemporary floods.	Harrison et al. (2006)

	scoured.		boulders and surface scouring.		
Iceberg wallow pits and craters	Semi-circular to elongate depressions of 5-35m depth, enclosed by sharp-crested rim-ridges or lateral berm ridges.	Light/dark shadowing distinguishes pits and craters from adjacent ridges. Occur in dense networks.	Possible misidentification as ice-marginal ridges, but unlikely due to differing orientation.	Indicative of floating snout breakup within shallow ice-marginal lake.	Unmapped
Ice-rafted moat lines and dump mounds	Curvilinear chains (~100-700m long) of low-relief mounds (<4m) and short ridges inset with push moraine ridges. Rare, locally sporadic mounds.	Faint shadowing and vegetation change associated with mounds. Give appearance of closely-spaced parallel shorelines.	Low-relief and discontinuous nature could hamper identification in imagery.	Marks the presence of an ice-contact lake system.	Unmapped
Shorelines	Near-continuous curvilinear terraces with lake-side break in slope, and up to >10km in length. Often align parallel to modern lake shorelines. Occur as shoreline 'flights' in areas.	Shadowing along former lake-side break in slope of feature. Flat or very gently grading upper surface.	Very faint in areas of low surficial cover (e.g. bedrock) and where narrow (due to minimal shadowing).	Marks elevation of former glacial lake water-plane.	Turner et al. (2005); Hein et al (2010); Bourgois et al. (2016); Glasser et al. (2016)
Raised deltas	Gently sloping sediment accumulations occurring in stepped sequences upstream of modern (actively forming) lake deltas. Often flanked by raised beaches. Sharp break in slope and steeply-inclined lake-side faces.	Homogeneous surface texture and colour distinct from adjacent terrain. Shadowing (break in slope) along former delta front.	May be mistaken for kame terraces, owing to similar texture/colour, although unlikely.	Delta front break in slope approximates former (glacial) lake level.	Turner et al. (2005); Bell (2008, 2009); Hein et al. (2010); Glasser et al. (2009, 2016)
Glaciolacustrine deposits	Broad, flat accumulations of fine-grained glaciolacustrine sediment (e.g. rhythmites) around former ice margins, lake embayments or valley sides.	Distinctive white colouration of terrain on satellite images, distinct from adjacent deposits (e.g. moraines).	Underestimation of spatial extent on imagery. Best identified in the field.	Indicative of glacial lake existence and former lake levels.	Caldenius (1932)

Table 3.3. Landforms mapped in this study classified according to depositional environment. Despite meticulous mapping, it is likely that the 'true' occurrence of landforms is underrepresented on the final geomorphological map (see Appendix) owing to image resolution limitations and landform concealment in areas of dense vegetation cover.

Environment	Landform type	Feature on map	Abundance
Ice-marginal glacigenic	Moraine ridges	Polyline	16,753
	Continuous hummocky ridges	Polyline	4082
	Hummocky terrain	Polygon/line	1552
	Trimlines	Polyline	182
Subglacial	Glacial lineations	Polygon/line	61/5305
	Till eskers	Polyline	161
Glaciofluvial	Outwash plain or tracts	Polygon	429
	Outwash terraces	Polyline	417
	Ice-contact glaciofluvial deposits	Polygon	66
	Eskers	Polyline	344
	Meltwater channels >150m wide	Polyline	350
	Meltwater channels 50-150m wide	Polyline	1198
	Meltwater channels <50m wide	Polyline	188
Glaciolacustrine	Glaciolacustrine deposits	Polygon	153
	Shorelines	Polyline	1632
	Raised deltas	Polygon	228
	Iceberg wallow craters/squeeze ridges	Polygon/line	176/226
	Iceberg rafted moat lines	Polyline	23
Volcanic	Volcanic deposits or flows	Polygon	8
	Masetsas	Polygon	19
	Volcanic cones or craters	Polygon	155
Modern hydrology	Active deltas and alluvial deposits	Polygon	69
	Lakes	Polygon	998
	Rivers	Polyline	771
			35,546

3.4 Glacial geomorphology

Fourteen main landform types were recorded on the geomorphological map (Figure 3.4; Table 3.2) and a total of 35,546 features (Table 3.3), which we describe herein. We also mapped trimlines, lakes, rivers, landslide scars, and volcanic landforms including basalt mesetas, cones and lava flows, to provide further geological or topographic context.

3.4.1 Moraine ridges

Prominent linear ridges of positive relief are interpreted as moraines that demarcate the limits of former glacier margins. Moraines can be single, cross-valley ridges, or occur within complex, multi-ridge systems. Moraines exhibit ~5–40 m relief and sharp, level or undulating crests. Most often, moraines are closely-spaced, with arcuate, crenulate or saw-tooth planforms (Figure 3.5). The ice-contact face of

prominent moraines can be adorned with low-relief hummocks, and in places are interspersed amongst larger assemblages of hummocky terrain (section 3.4.3). Elsewhere, moraine fragments exhibit weak barchanoid form, suggestive of overriding by active ice (Evans, 2009). On the Argentine forelands around the main depressions, moraine complexes run continuously for 10's of kilometres (Figure 3.5C) and form tightly nested latero-frontal arcs (Kaplan, et al., 2009). These arcs are locally dissected by meltwater channels, which feed into ice-marginal outwash corridors or graded outwash plains (Figure 3.5). The regional distribution of moraines reflects a pattern of westwards glacier retreat towards the modern NPI (Glasser et al., 2012).

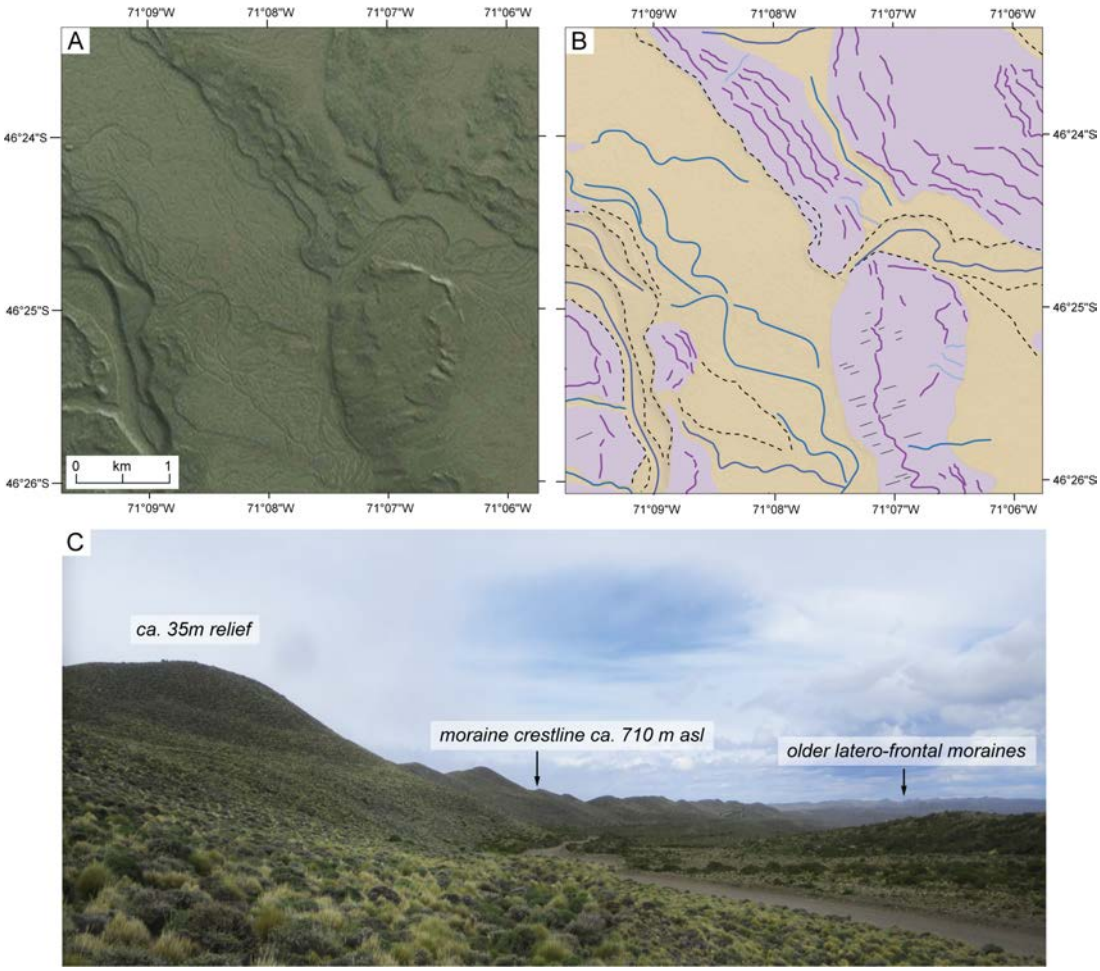

Figure 3.5. (A) Satellite image (DigitalGlobe 2015; ESRI™) and (B) mapped moraine ridges and outwash deposits from the northern margin of the LGC–BA lobe. Outwash occurs within narrow meltwater channels incised through moraines (left of image) or as broader lateral corridors between moraine sequences (centre-left of image). Moraines are locally dissected by former meltwater streams (right of image) which feed into broad sandur plains. (C) View across latero-frontal moraine arc east of Puerto Ibañez with higher elevation (older) moraine sequence in distance (right of image).

3.4.2 Continuous hummocky ridges

These features comprise accumulations of closely-spaced hummocks and short (<300 m) ridges of moderate relief (~5–25 m). Individual mounds can be difficult to delimit, but when viewed in planform represent semi-continuous parallel chains oriented perpendicular to ice flow (Figure 3.6). Occasionally, high-relief, sharp-crested ridges are interspersed amongst continuous hummocky ridges These landforms may represent active push ridges fed by supraglacially dumped debris (e.g. Boulton and Eyles, 1979; Lukas, 2005), perhaps in the absence of a widespread deforming layer.

Alternatively, they could represent degraded moraines, or moraines that have been dissected by meltwater channels. Continuous hummocky ridges are exclusive to the southern LC–P margin, where they have previously been depicted as discrete, unbroken moraine ridges (Glasser and Jansson, 2008, Hein et al. 2010).

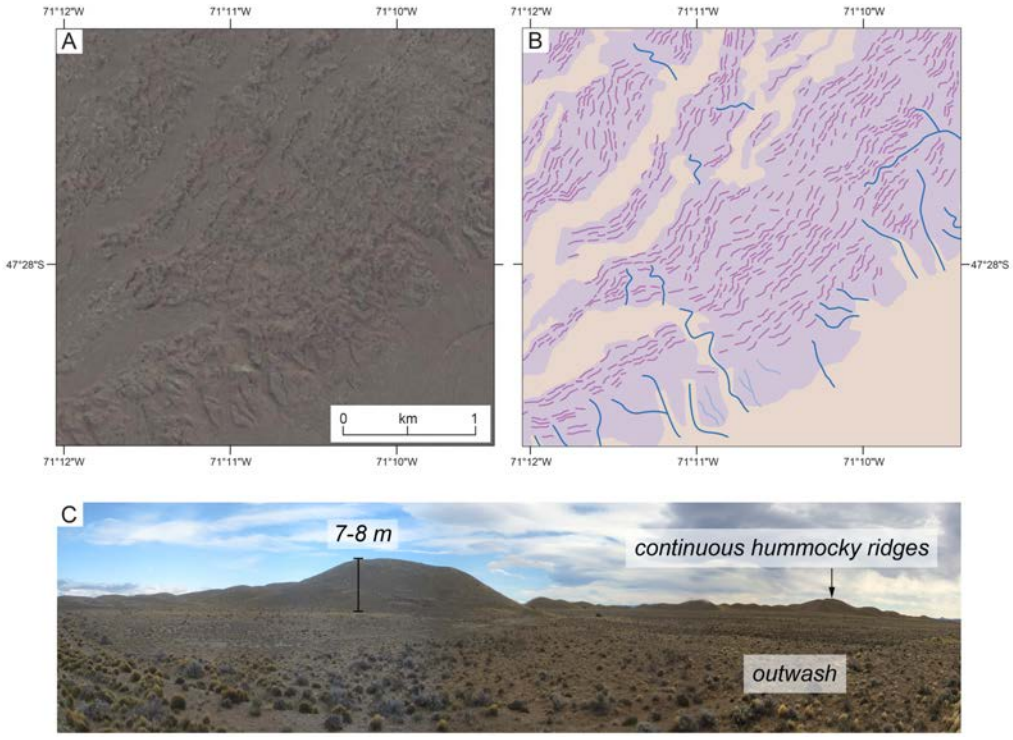

Figure 3.6. (A) Satellite image (DigitalGlobe 2015; ESRI™) and (B) continuous hummocky ridges mapped along the southern LC–P ice lobe margin. The image shows numerous short ridges and hummocks that connect to generate longer ice-margin parallel chains when viewed in planform. Sequences of closely-spaced ridges are separated by narrow lateral outwash corridors, whilst individual ridges may be separated by minor marginal meltwater channels of <50 m wide. The outer ridges (bottom right of image) are heavily dissected by meltwater channels which feed a lateral sandur plain. (C) View across continuous hummocky ridge chain, showing variable hummock height and lengths, and proglacial outwash deposits.

3.4.3 Hummocky terrain

Several forms of hummocky terrain were identified around former ice margins. Small-scale hummocks (Figure 3.7) are more common, and consist of densely-spaced circular to semi-rounded hills of <10 m relief. The hummocks are largely chaotic, but may be organised into crude arcuate bands. Push moraines are often dispersed amongst the more chaotic hummocks. Large scale hummocky terrain (Figure 3.8) is limited to a small zone on the southern LC–P margin, and consists of densely-spaced irregular hummocks (polygons) and ridges (polylines) with intervening depressions. Hummocks range from 5–30 m high and 10–200 m wide and form chaotic assemblages. Their morphology is varied, and includes circular or oval-shaped mounds and linear ridges with straight or corrugated crests. These deposits are morphologically comparable to hummocky terrain produced by stagnant glacier snouts that foundered into saturated basal tills (Eyles et al., 1999; Boone and Eyles, 2001).

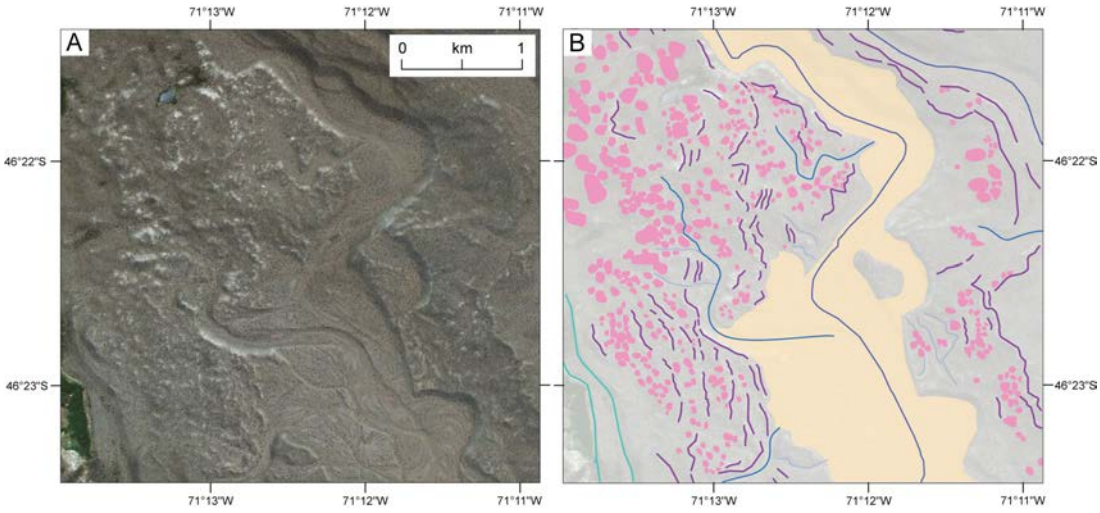

Figure 3.7. (A) Satellite image (DigitalGlobe 2013; ESRI™) and (B) mapped hummocky terrain on the northern LGC–BA ice lobe margin. These small-scale hummocks are largely chaotic but may be organised into crude arcuate bands (top-left of image) that are interspersed with low-relief push moraine ridges.

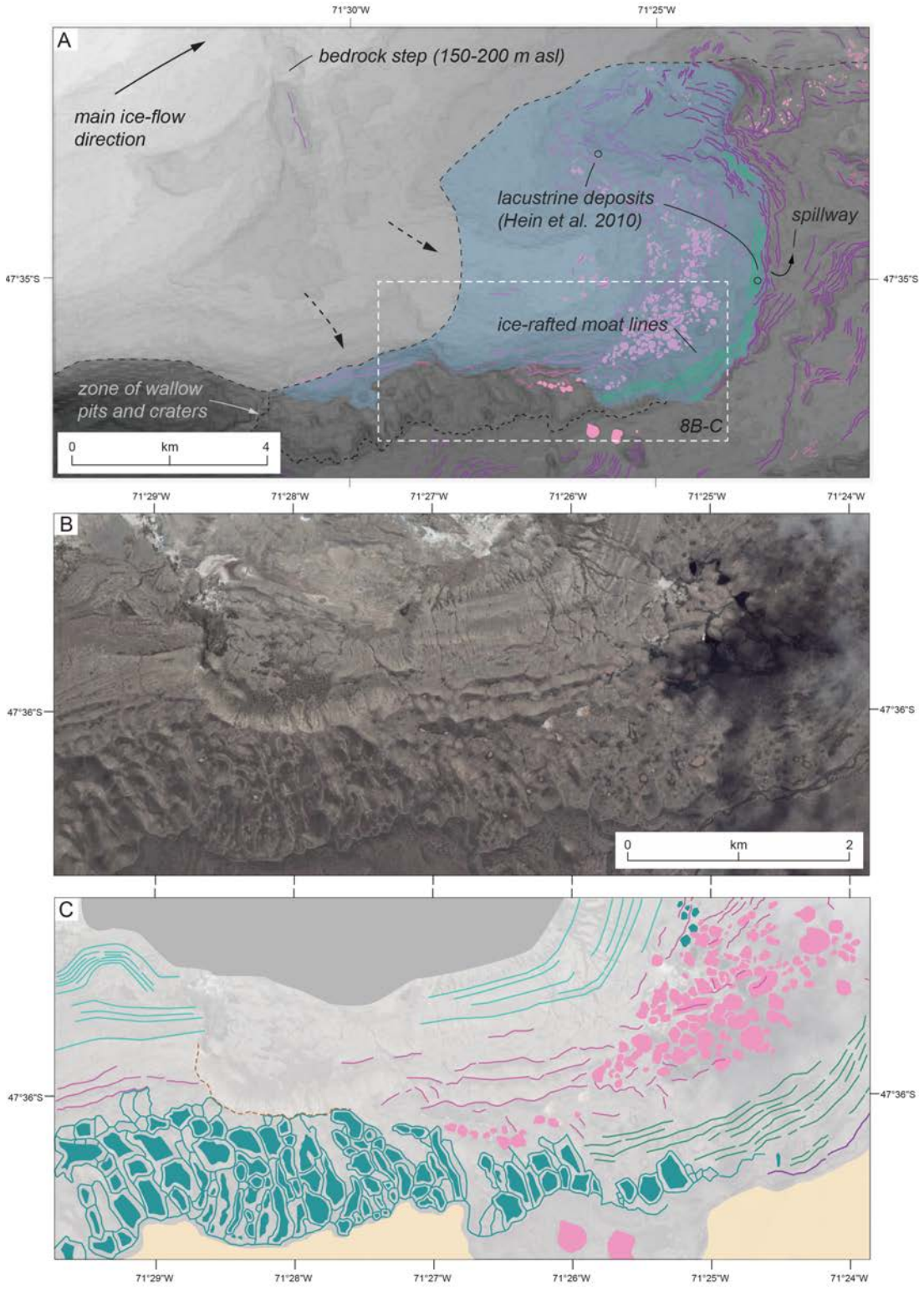
71°30'W
71°25'W
A
bedrock step (150-200 m asl)
main ice-flow direction
lacustrine deposits (Hein et al. 2010)
spillway
47°35'S
ice-rafted moat lines
zone of wallow pits and craters
8B-C
0 km 4
71°29'W
71°28'W
71°27'W
71°26'W
71°25'W
71°24'W
B
47°36'S
0 km 2
C

Figure 3.8. (A) Context for landform interpretation along the southern LC–P ice lobe margin, east of Posados. Late LGM glacier and proglacial lake limits after Hein et al. (2010), based on the identification of lacustrine deposits (black circles). At the time of the reconstruction, Hein et al. (2010) suggest ice was grounded around a prominent north-south trending bedrock step, and experienced insufficient flux to fully occupy the upper basin. The lake level contour (625 m a.s.l) was extracted from an ASTER-GDEM model. The extent of (B) and (C) is indicated by the dashed white box. (B) Satellite image (DigitalGlobe 2013; ESRI™) and (C) mapped landforms, showing a complex arrangement of geomorphic features. The right-hand section of the image shows an assemblage of densely-spaced circular or oval-shaped mounds and linear ridges that display morphological resemblance with examples of ice-stagnation hummocky terrain (Eyles et al.,1999; Boone and Eyles, 2001). The hummock assemblage merges into a large complex of inferred iceberg wallow pits and craters, which exhibit deep semi-circular to elongate depressions and are enclosed by high-relief rim-ridges or lateral berm ridges (e.g. Barrie et al., 1986; Woodward-Lynas, 1991). Low-relief hummock chains are interpreted as moat line ridges deposited at the margins of a small ice-contact lake ice (cf. Hall et al., 2006). Inferred moat line ridges occur outside the limits of hummocky terrain, and along the ice-contact face of prominent sharp-crested ridges. Their distribution and 'shoreline-like' pattern (A) is consistent with the perimeter and estimated water level of the proglacial lake system mapped by Hein et al. (2010).

3.4.4 Till eskers

These features are straight-to-sinuous ridges with undulating crests, of between 50–500 m long and 5–15 m high. The ridges are orientated oblique to outer moraine crests, but not parallel with former ice-flow indicators (Figure 3.9). The ridges often merge into, or closely align with the limbs of saw-tooth moraines. These features are present on adverse topographic slopes inside larger, sharp-crested moraine ridges along the northern LGC–BA margin. Based on their morphology, we interpret these landforms as infilled water conduit systems, or so-called 'till eskers', as identified in modern Icelandic settings (Christoffersen et al. 2005; Larsen et al., 2006; Evans et al., 2016). Their origin is hypothesised to reflect the squeezing of saturated till into elongate basal cavities or *R*-channels after meltwater abandonment (Evans et al., 2010). Data on the sedimentary nature of these landforms could test our current interpretation.

3.4.5 Glacial lineations

Linear, parallel, positive relief landforms displaying high directional conformity were mapped as glacial lineations (Figure 3.10). Their regional distribution mirrors the principal ice-discharge pathways along major west–east trending valley axes (Glasser and Jansson, 2005). Bedrock lineations are well developed in areas of ice-scoured terrain and range from ~200–3000 m long and ~30–100 m wide. Tightly

clustered oval-shaped drumlins and flutes are identified near the Chacabuco-Pueyrredón junction, and around the base of Sierra Colorado. Subdued sediment flutings (1–3 m high) occur on the Argentine forelands between moraine ridges (Figure 3.5), though they are difficult to detect, even within high-resolution imagery.

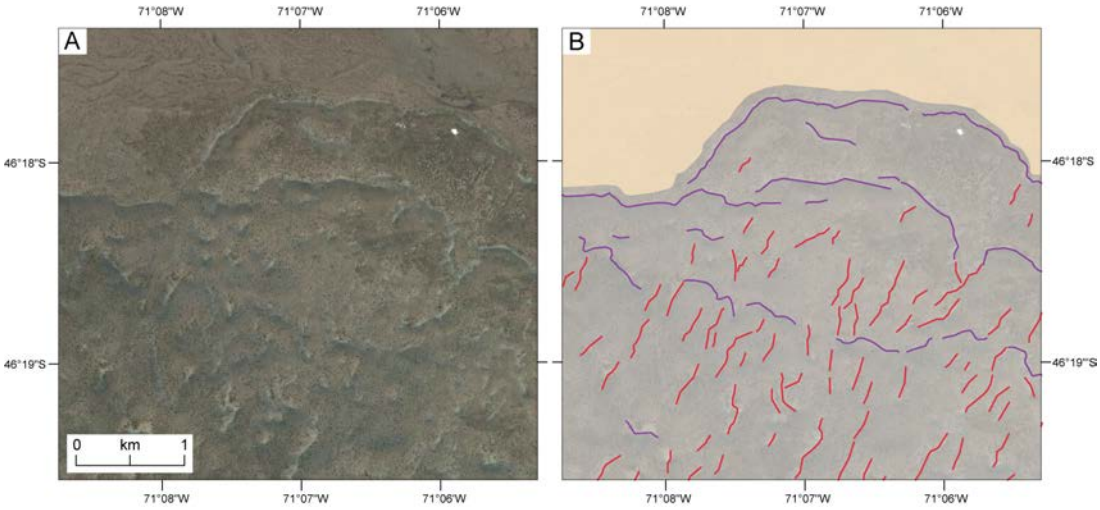

Figure 3.9. (A) Satellite image (DigitalGlobe 2012; ESRI™) and (B) mapped landforms on the northern margin of the LGC–BA lobe. Image shows sawtooth push moraines and straight-to-sinuous inset ridges that align sub-parallel to former ice flow direction, and are interpreted as preserved till eskers as recorded on some modern glacier forelands (Christoffersen et al., 2005; Evans et al., 2016).

3.4.6. Meltwater channels

Straight, sinuous, or meandering channels that are devoid on contemporary drainage and begin and end abruptly are interpreted as meltwater channels. In total, we map 1736 channels, which are ubiquitous around former ice lobe margins. Channel length reaches ~30 km and channel width ranges from ~20–800 m, the widest forming corridors of outwash-infill and converging with broader outwash plains (Figure 3.5). Meltwater channels follow former ice margins (Figures 3.5 and 3.7) or issue from frontal moraine systems. Along the southern LGC–BA margin, meltwater incision has eroded all but certain localised upstanding moraine fragments. Here, ice-marginal meltwater channels provide a clearer indication of former glacier position and surface gradient than moraines (e.g. Bentley et al., 2005; Darvill et al., 2014).

3.4.7 Outwash plains and tracts

Broad, gently sloping surfaces of glaciofluvial sand and gravel represent outwash plains and tracts. Around the NPI, outwash deposits mantle the floor of major

erosional corridors (Glasser et al., 2009). On former glacier forelands, coalescent outwash fans prograde eastwards from latero-frontal moraine complexes to form extensive outwash plains (Figure 3.5; Caldenius, 1932; Hein et al., 2009, 2011; Smedley et al., 2016), or occur within ice-margin parallel corridors due to topographic constraints (e.g. moraines; Figure 3.5). Outwash deposits may be pitted, either in narrow ice-marginal strips, or at fan apices, due to melt-out of buried glacier ice (Evans and Twigg, 2002; Evans and Orton, 2015). The surfaces of outwash plains are often imprinted with complex abandoned channel networks, or exhibit clear terrace levels (Figure 3.5). These features may record the evolution of the proglacial drainage system, reflecting changes in glacier margin position, ice-marginal topography, or meltwater discharge (Evans and Twigg, 2002).

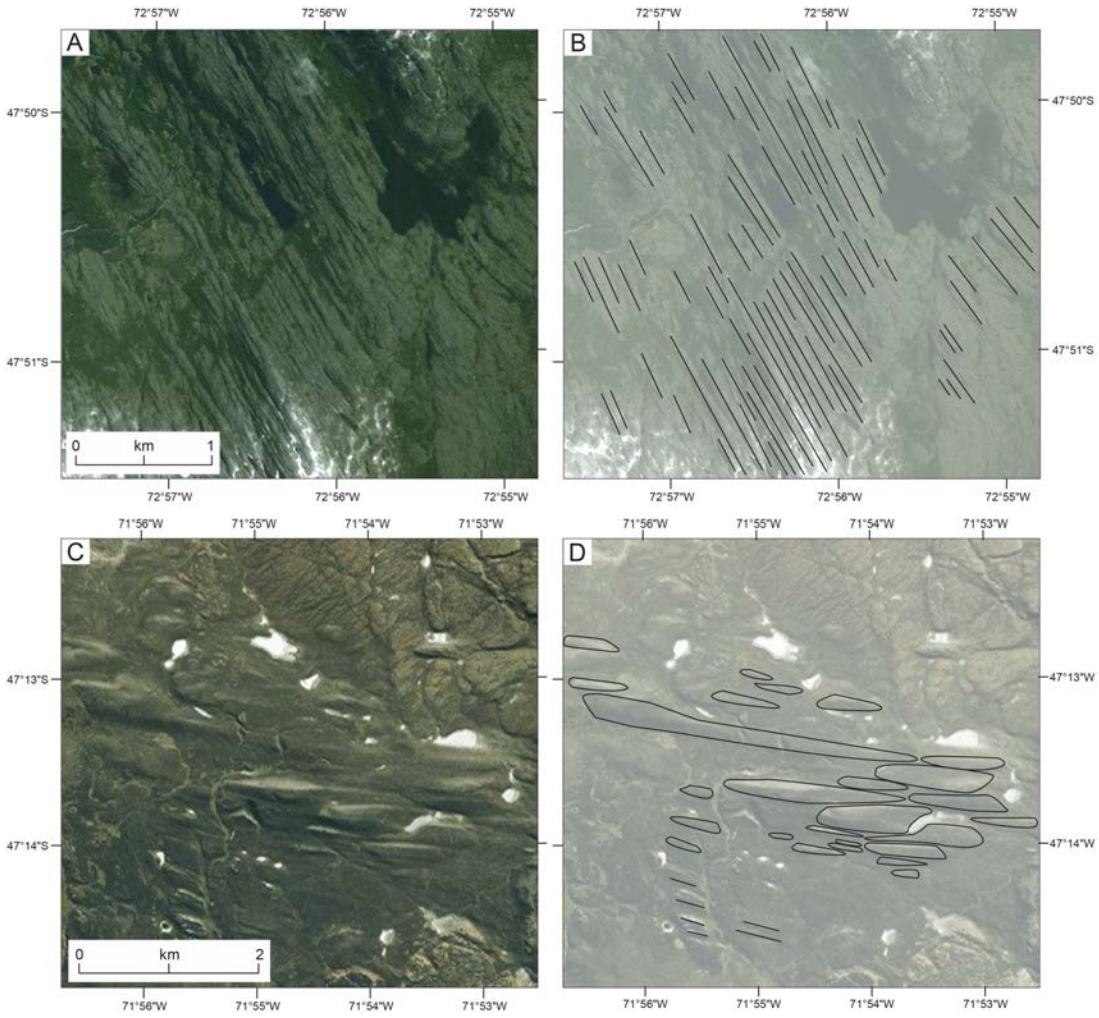

Figure 3.10. Examples of glacial lineations from across the study area. (A) satellite image (DigitalGlobe 2014; ESRI™) and (B) mapped lineations formed in bedrock south of Los Ñadis. (C) Satellite image (DigitalGlobe 2015; ESRI™) and (D) mapped lineations formed in sediment at the junction of Valle Chacabuco and the Pueyrredón basin.

3.4.8 Eskers

These features are described as straight-to-sinuous ridges with oblique orientation relative to former ice-flow direction. Ridges can be isolated landforms (Figure 3.11) or occur within dense networks (Figure 3.12). These features are inset behind outer moraine crests along the northern LGC–BA and LC–P margins. Whilst no open sections were identified in the field, the ridge surfaces contained sands, gravels and cobbles. We interpret these landforms as eskers (e.g. Storrar et al., 2015), but acknowledge that only a single esker has been identified previously in Patagonia (Clapperton, 1989; Lovell et al., 2011; Darvill et al., 2014).

An additional zone of enigmatic landforms was mapped at LGC–BA. These features form a densely-spaced complex of near-straight ridges and conical mounds, ranging from 20–150 m wide and 100–800 m long (Figure 3.12). The ridges are characterised by hummocky long-profiles and variable widths, and their surfaces comprise sand and gravel sediments. These features might represent large-scale crevasse fills (cf. Bennett et al., 2000), however, we speculate that they are eskers. Their existence alongside another inferred esker network, shown in Figure 3.12B, might support this interpretation.

3.4.9 Ice-contact outwash deposits

Gently sloping terraces of glaciofluvial sand and gravel, perched on valley sides or at valley confluences, are interpreted as ice-contact outwash deposits. These accumulations represent ice-contact glaciofluvial depo-centres and include: pitted, valley-side kame terraces; outwash fans with pitted ice-contact slopes (outwash heads; *sensu* Kirkbride, 2000); and low-gradient subaqueous fans draped over low-lying bedrock outcrops. These landforms occur within narrow valleys around the modern NPI, their location perhaps a reflection of favourable topographic setting (e.g. valley narrowings; cf. Barr and Lovell, 2014). Examples occur at Lago Brown, Lago Esmeralda, and at the Colonia-Baker confluence (see main map in Appendix). Such deposits are often considered to have formed during periods of temporary glacier stabilisation (Spedding and Evans, 2002).

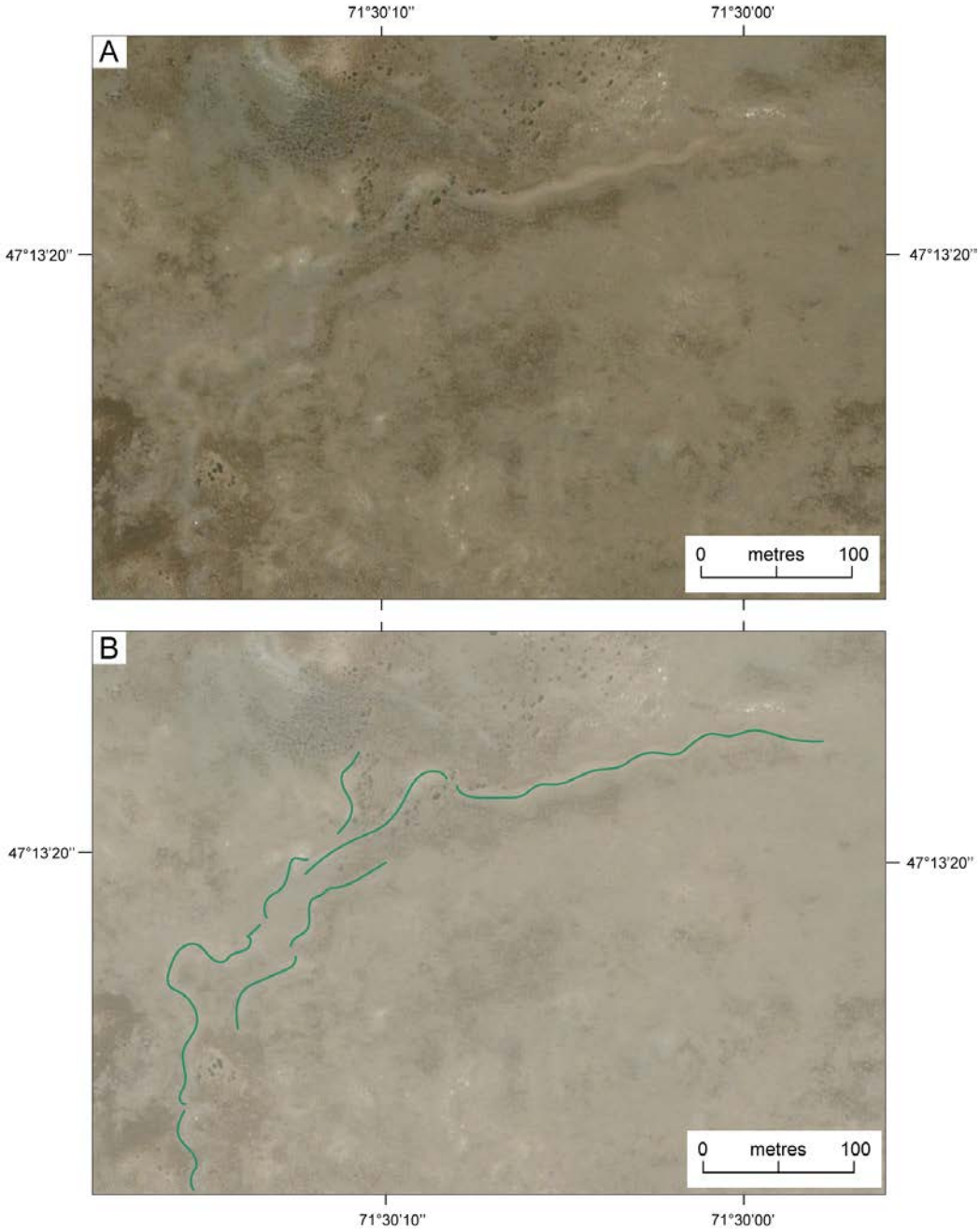

Figure 3.11. (A) Satellite image (DigitalGlobe 2017; ESRI™) from the northern margin of the LC–P lobe and (B) mapped landforms. The image shows a prominent, positive-relief, sinuous ridge interpreted as an esker, alongside multiple smaller esker ridges. Ice flow direction was from left to right.

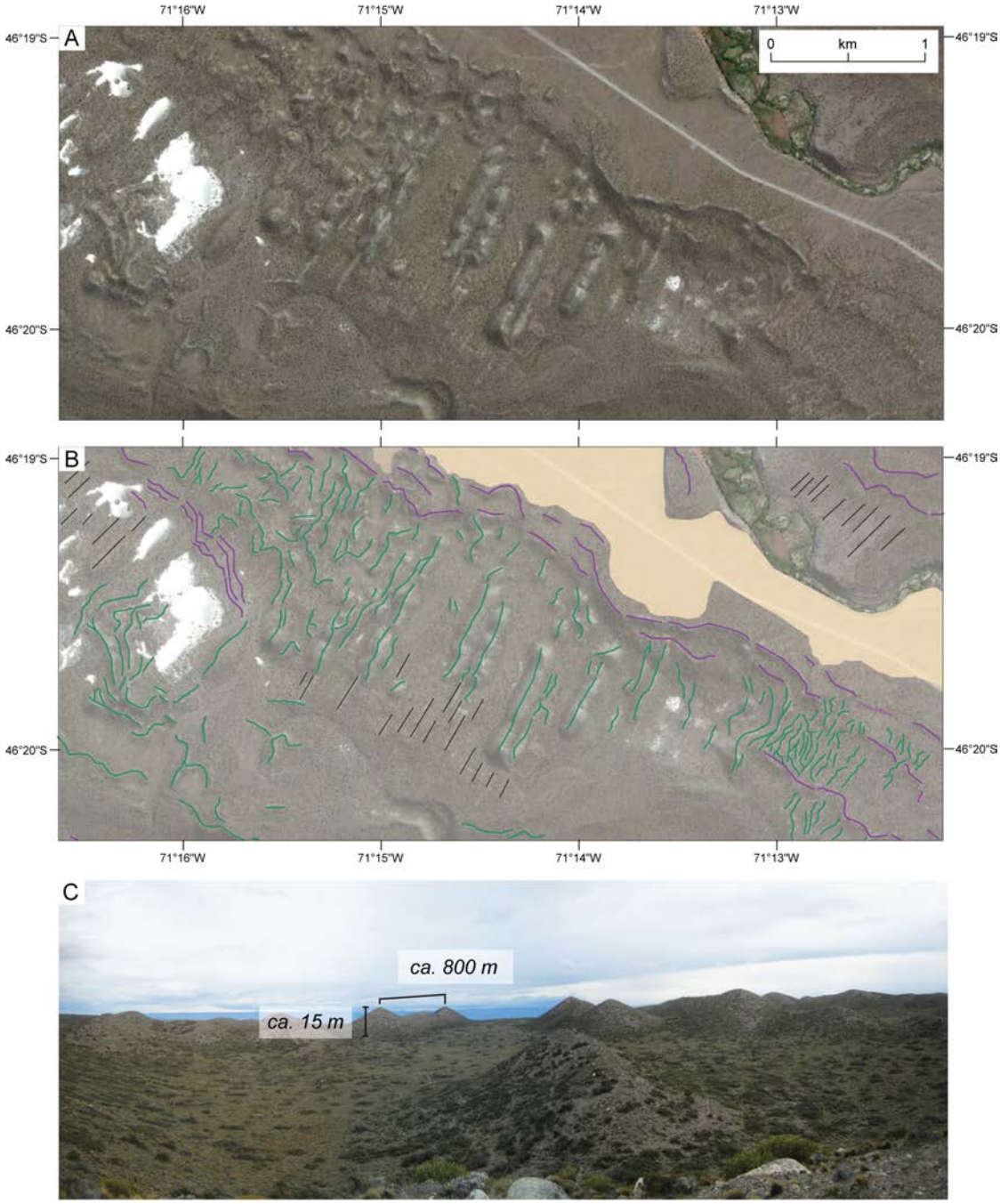

Figure 3.12. (A) Satellite image (DigitalGlobe 2013; ESRI™) from the northern margin of the LGC–BA lobe and (B) interpretation of the glacial geomorphology. The image shows push moraine ridges, inset eskers and sediment flutings. The inferred eskers range from sinuous ridges that are either isolated or occur within complex networks (lower right of image), to more enigmatic, near-straight ridges and conical mounds (centre of image) of comparatively high relief (C).

3.4.10 Glacial lake outburst flood (GLOF) deposits

Large-scale gravel bars or flat-topped accumulations that exhibit channeled surfaces and imbricated boulder lags, with boulders of 1–10 m height, are interpreted as GLOF deposits (e.g. Harrison et al., 2006). Such accumulations are elevated above the modern Río Baker west of Valle Chacabuco, and northwest of Cochrane (see main map in Appendix).

3.4.11 Iceberg wallow pits and craters

These landforms consist of semi-circular pits or elongate craters of between 5–35 m depth, flanked by semi-circular ring-ridges, or steep-sided (>35°) lateral berm ridges (Figure 3.8). The structures occur within a densely-spaced network of regular NNW-SSE orientation, approximately sub-parallel to former ice-flow direction (Hein et al., 2010). These features occur along a narrow sector of the southern LC–P margin, where based on the distribution of lacustrine sediments, Hein et al. (2010) have mapped the extent of a small ice-marginal lake at ~625 m asl (Figure 3.8A). We interpret the landforms as iceberg grounding structures. In glaciomarine settings, these include various pits, craters and scours (Woodward-Lynas et al., 1991). When embedded in the seafloor, icebergs excavate deep depressions due to vertical (impact) loading and wave-induced horizontal loading that facilitates iceberg rotation and wallowing, and sediment displacement to form berm ridges (e.g. Barrie et al., 1986; Clark and Landva, 1988). Our morphologically based interpretation is consistent with the presence of a transient lake system at this site (Hein et al., 2010).

3.4.12 Ice-rafted moat lines

Around the margins of the small ice-contact lake mapped by Hein et al. (2010), we have identified curvilinear chains of closely-spaced, low-relief (<4m) small ridges and mounds, which are discontinuous but can be linked together and run for ~100-700 m (Figure 3.8). In contrast to other linear features (e.g. moraines), these curvilinear chains are more subdued, less continuous, and are not sharp-crested. Given the ice-marginal lacustrine context and their morphological nature, we interpret these landforms as moat lines of ice-rafted debris let down through the unfrozen margins of an ice-contact lake (cf. Hall et al., 2006). Sedimentological analyses are needed to test this interpretation.

3.4.13 Shorelines

Continuous linear terraces that run unbroken for 10's of kilometres and exhibit no positive relief are interpreted as wave-cut scarps and benches (Glasser and Jansson, 2008). The most prominent lake shorelines occur east of LGC–BA and LC–P (Figure 3.13) and rise to ~300 m higher than contemporary lake levels. Previous shoreline mapping has enabled several reconstructions of proglacial lake evolution (Turner et al., 2005; Bourgois et al., 2016; Glasser et al., 2016). In comparison, we mapped a greater number of shoreline features, including very faint, closely-spaced shoreline fragments located between the major wave-cut scarps. These features are only discernible from high-resolution images and hint at a complex lake level history.

3.4.14 Raised deltas

Flat-topped, sediment accumulations in the mouths of tributary valleys, and perched above modern lakes, represent raised lacustrine deltas (Figure 3.13; Turner et al., 2005; Bell, 2008, 2009; Glasser et al., 2016; Hein et al., 2010). At LGC–BA, raised deltas are often flanked by beaches (Figure 3.13d). Narrow, wave cut terraces are present on some delta fronts, and are cited as evidence of either staged lake lowering (Bell, 2008) or lake transgression (Bourgois et al., 2016).

3.4.15 Glaciolacustrine deposits

On satellite imagery, glaciolacustrine deposits are flat, pale-coloured sediment accumulations deposited in former proglacial lakes (Table 3.2). Field sections confirm the presence of glaciolacustrine sediments. Significant glaciolacustrine accumulations occur around former ice margins, palaeolake embayments (Figure 3.8), and on valley sides, where they drape bedrock or glacigenic deposits.

3.5 Summary and conclusions

This paper presents a new glacial geomorphological map (Appendix) of the central Patagonian region. Mapping is conducted at a consistent, high level of detail that exceeds that of previous works, and encompasses the complete area occupied by two major outlet lobes of the former Patagonian Ice Sheet.

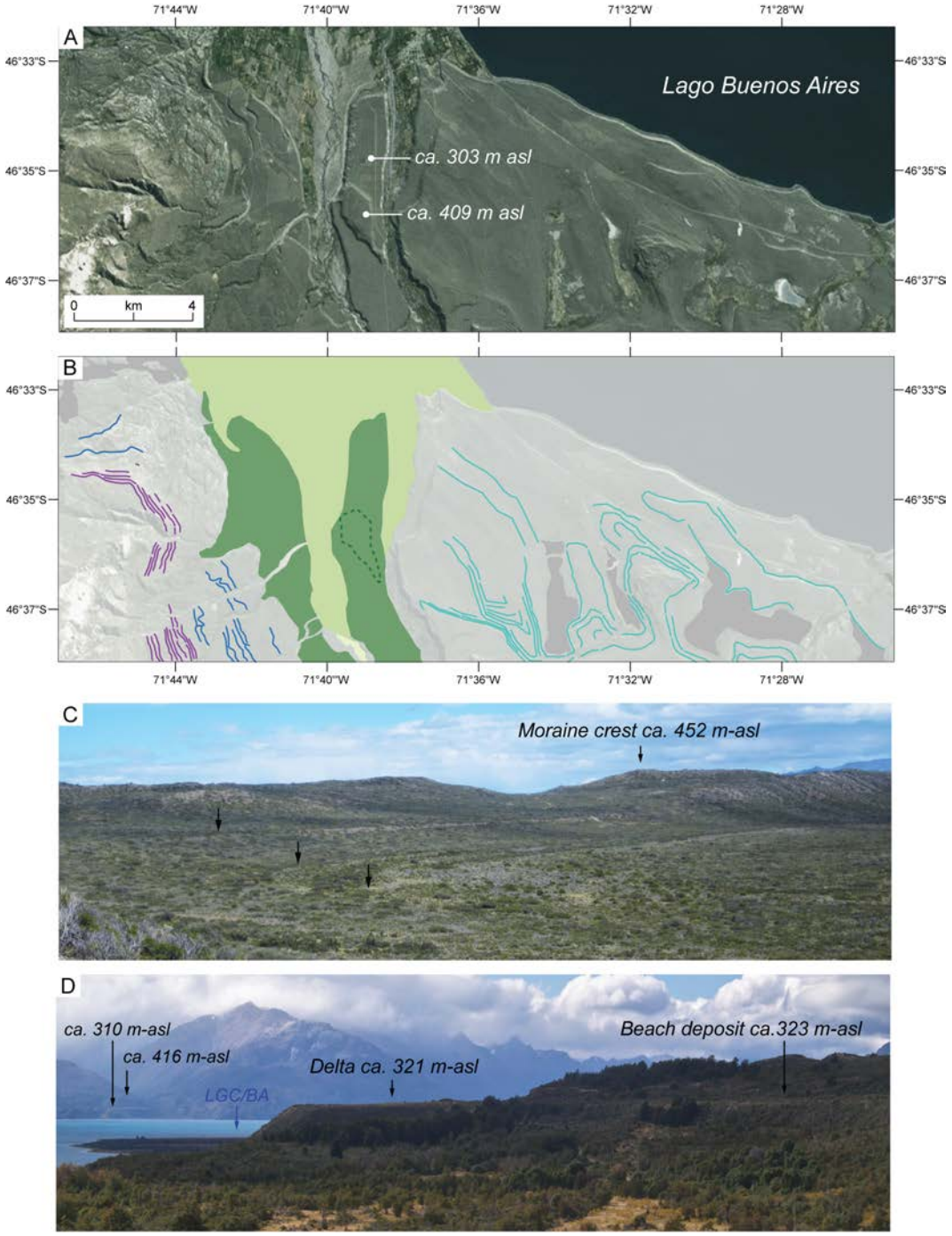

Figure 3.13. (A) Satellite image (DigitalGlobe 2014; ESRI™) and (B) mapped glaciolacustrine landforms along the southern margin of Lago General Carrera-Buenos Aires. Features include raised deltas, wave-cut lake shorelines and areas of lacustrine sediment accumulation within palaeolake embayments. Also note the high-level lateral moraine ridges and marginal meltwater channels of the southern LGC–BA lobe margin. Field photos of (C) former lake shorelines cut into glacigenic deposits and (D) raised lacustrine deltas and adjacent beach deposits formed in the mouths of tributary valleys of Lago General Carrera-Buenos Aires. The ca. 310 m and 321 m deltas are coeval though have experienced different amounts of postglacial uplift. The ca. 416 m delta pre-dates the lower elevation features and records stepped lake level lowering.

The map reveals a complex suite of landform assemblages that includes (i) previously unmapped components of the glacial geomorphological record (e.g. continuous hummocky ridges, hummocky terrain, till eskers, eskers, and iceberg features); and (ii) updated spatial and morphological representations of features mapped previously from lower resolution imagery (e.g. moraines, meltwater channels).This new evidence allows the preliminary sub-division of mapped landform assemblages into two principal assemblages. (1) An outer assemblage developed on the former ice lobe forelands documents the evolution of piedmont glaciers emerging from mountainous catchments. This assemblage contains nested latero-frontal moraine arcs and associated glaciofluvial outwash tracts, with localised eskers and till eskers inset behind larger moraine complexes. (2) An inner assemblage that developed as ice margins retreated into overdeepened valleys in the western sector of the study area, and led to evolution of a glaciolacustrine environment. This assemblage comprises widespread raised deltas, shorelines and fine-grained glaciolacustrine sediment piles. In addition, ice-contact glaciofluvial depo-centres (e.g. subaqueous fans) were constructed in topographically favorable locations (e.g. valley narrowings). Beyond these preliminary findings, the new geomorphological dataset presented here will facilitate the application of glacial inversion methods (Kleman et al. 2006) and, for the first time, landsystem analysis (Evans, 2003) at the ice lobe scale. We anticipate that the dataset will be used to produce detailed reconstructions of (i) ice-margin recession; (ii) evolving ice-dynamics; and (iii) evolving palaeolake systems.

3.6. Software

Landforms were recorded in Esri ArcGIS (v10.3) and final map production undertaken in Adobe Illustrator.

Chapter 4. A new reconstruction of glacial lake evolution and the dynamics of Atlantic-Pacific drainage reversals during deglaciation of the Patagonian Ice Sheet (46–48°S)

Thorndycraft, V.R., Bendle, J.M., Benito, G., Sancho, C., Palmer, A.P., Davies, B.J., Martin, J., Medealdea, A., Rodriquez, X. (in prep). A new reconstruction of glacial lake evolution and the dynamics of Atlantic-Pacific drainage reversals during deglaciation of the Patagonian Ice Sheet (46-48°S) *Geomorphology*

Abstract

The deglaciation of the former Patagonian Ice Sheet (PIS) at 46–48°S resulted in the formation of large proglacial lakes. Coupled atmospheric-ocean modelling experiments indicate that a continental-scale (Atlantic-Pacific) drainage reversal associated with lake drainage may have altered regional climate through freshwater forcing. However, much of the area remains unmapped in detail, and the chronology of glacier and palaeolake evolution is incomplete. Consequently, multiple palaeolake evolution models exist, with the timing of Atlantic-Pacific drainage reversal(s) ranging from 15.5–10.5 ka. To evaluate these models, we use geomorphological mapping of glacial landforms to conduct a regional analysis of shoreline isostasy and palaeolake extent and level. We also conduct an altitudinal-based review of published geochronology to assess the possible timing of glacial lake evolution. Using these datasets, we present a seven-stage event sequence for palaeolake evolution. Our reconstruction supports two drainage reversal events to the Pacific. A first drainage reversal event to the south of the North Patagonia Icefield (NPI) from the Lago Cochrane–Pueyrredón (LC–P) basin likely occurred by 15.3–15.1 cal ka BP, and this was followed by a second event to the north of the NPI between ~15.1 and 13.0 ka. Geomorphological evidence (e.g. boulder bars) also suggests that at least three Early Holocene (pre-7.8 ka) high-magnitude glacial lake outburst floods (GLOFs) routed through the Baker and Cochrane valleys from Lago General Carrera–Buenos Aires (LGC–BA) and LC–P, respectively. Our new reconstruction highlights the need for updated models of freshwater forcing that incorporate multiple drainage events. Our palaeolake reconstruction has implications for the theory of a regional glacier re-advance at the time of the Northern Hemisphere Younger Dryas, as we find that the majority of morainic boulders used for cosmogenic nuclide exposure dating of the event were shielded by lake waters and, instead, likely date lake drainage.

4.1 Introduction

During deglaciation of Quaternary ice sheets, modification of glaciofluvial drainage systems can take place, and in suitable geomorphological settings, proglacial lakes can develop as glaciers recede (Carrivick and Tweed, 2013; García et al., 2014; Palmer and Lowe, 2017). These lakes can store significant volumes of freshwater that may be released over very short timescales, for example, by glacial lake outburst floods (GLOFs) (Baker, 2009), with the potential to trigger freshwater forcing of abrupt climate change through influences on oceanic circulation (Condron and Winsor, 2012). In combination, morphological and sedimentological archives of former ice sheets offer a key source of evidence towards understanding glacial landscape evolution at a range of temporal scales, the nature of ice-sheet dynamics (Clark et al., 2012), and potential climatic influences on the pattern of deglaciation.

The deglaciation of the former Patagonian Ice Sheet (PIS) between 46–48°S (Figure 4.1) was associated with major landscape changes, including the growth, evolution, and drainage of proglacial lakes, and the continental-scale re-direction of glacial meltwaters from the Atlantic to the Pacific Ocean (Turner et al., 2005; Bell, 2008). Using a freshwater 'hosing' experiment, Glasser et al. (2016) suggest that such a drainage reversal event may have initiated a negative salinity anomaly that altered oceanic vertical mixing and regional climate between 45°S and the southernmost tip of South America (56°S). However, the exact configuration, extent and volume, timing, and drainage pathway(s) of former glacial lakes remains equivocal for the study area, as suggested by a number of competing models of palaeolake evolution (Turner et al., 2005; Hein et al., 2010; Bourgois et al., 2016; Glasser et al., 2016; Martinod et al., 2016), none of which have been able to reconcile all available geochronological data. Well-constrained palaeolake reconstructions are needed for robust climatic inferences from freshwater forcing events, as demonstrated by Breckenridge (2015), for example, in relation to the drainage of former glacial lake Agassiz in North America. Systematic geomorphological analyses, which facilitate the quantification of regional glacio-isostatic histories, are especially important in realising this goal (e.g. Breckenridge, 2013, 2015).

The majority of previous mapping in the area (46–48°S) has used LANDSAT and/or ASTER satellite imagery, with ground resolutions of 15–30 m (Glasser and Jansson, 2008; Glasser et al., 2008), while much of the region remains unmapped in the field. Using high-resolution satellite imagery, however, Chapter 3 developed a detailed map (>35,000 landforms) of regional glacial landforms, which included the systematic mapping of relict glacial lake shorelines. The main aim of this paper is to interrogate this

geomorphological dataset to evaluate existing palaeolake models, and to develop a new reconstruction of regional ice-sheet and glacial lake evolution, including the dynamics of Atlantic-Pacific drainage reorganisation.

To provide constraints on palaeolake extent, elevation, and relative chronology, post-glacial isostatic rebound is quantified using a systematic analysis (cf. Breckenridge, 2013, 2015) of a regional shoreline dataset. Currently, no assessment of isostatic adjustment has been produced at the regional scale. Instead, isostatic information is based on isolated spot-height measurements obtained from raised lacustrine deltas (Turner et al., 2005; Martinod et al., 2016), and it is uncertain whether these analyses accurately characterise shoreline distance-elevation relationships. Second, targeted field mapping was undertaken to better characterise palaeolake geomorphology in areas central to understanding lake evolution. The Río Baker valley (Figure 4.1b), for example, is critical to understanding the potential coalescence of former lake systems (Turner et al., 2005), as well as the opening of a westwards drainage pathway to the Pacific, but requires detailed field mapping. Third, an altitudinal-based assessment of published geochronology was undertaken to evaluate potential timings for ice-margin and palaeolake extents and levels, in light of our isostatic shoreline data. Existing geochronological reviews have focused on the planform distribution of available dates (Mendelova et al., 2017), and overlook important geomorphological information on sample altitude and, therefore, landform relationships with palaeolake levels. We use our palaeolake data to evaluate regional glacial history, for example, the proposed regional advance of NPI outlet glaciers at the time of the Northern Hemisphere Younger Dryas (Glasser et al., 2012). Finally, we explore possible topographic controls on palaeolake history in the region, given the recent recognition of dynamic uplift (Guillaume et al., 2013) over the southern sector (Figure 4.1b) of the NPI region.

4.2 Regional context

4.2.1 Geomorphological context

The study area (Figure 4.1c) lies between 46–48°S and 70–74°W, and encompasses the North Patagonian Icefield (NPI) and Río Baker catchment (Figure 4.1b). During glacial periods, the area was occupied by two major ice lobes of the former PIS: the LGC–BA and LC–P ice lobes, which advanced over 150 km east of the modern NPI to terminate on the Argentine steppe (Caldenius, 1932; Glasser and Jansson, 2005). At such times, these ice lobes blocked the westwards drainage of rivers to the Pacific Ocean, and diverted glacial meltwater eastwards to the Atlantic Ocean (Turner et al. 2005). The Last Glacial Maximum (LGM) limits of the LGC–BA and LC–P ice lobes are

dated to between ~26.0–18.7 ka (Kaplan et al., 2004; Douglass et al., 2006) and ~28.8–21.0 ka (Hein et al., 2010) respectively, based on cosmogenic nuclide exposure dating (CND) of moraine boulders (weighted mean ages derived from the recalculated ^{10}Be determinations of. Kaplan et al., 2011). Two major ice-sheet divides are inferred for maximum LGM conditions in the study area (Glasser and Jansson, 2005; Hubbard et al., 2005): a north-south NPI divide aligned along the Andean Cordillera, and a broadly east-west divide that connects Monte San Lorenzo (MSL) to the Andean Cordillera, across the Río Baker valley (Figure 4.1c).

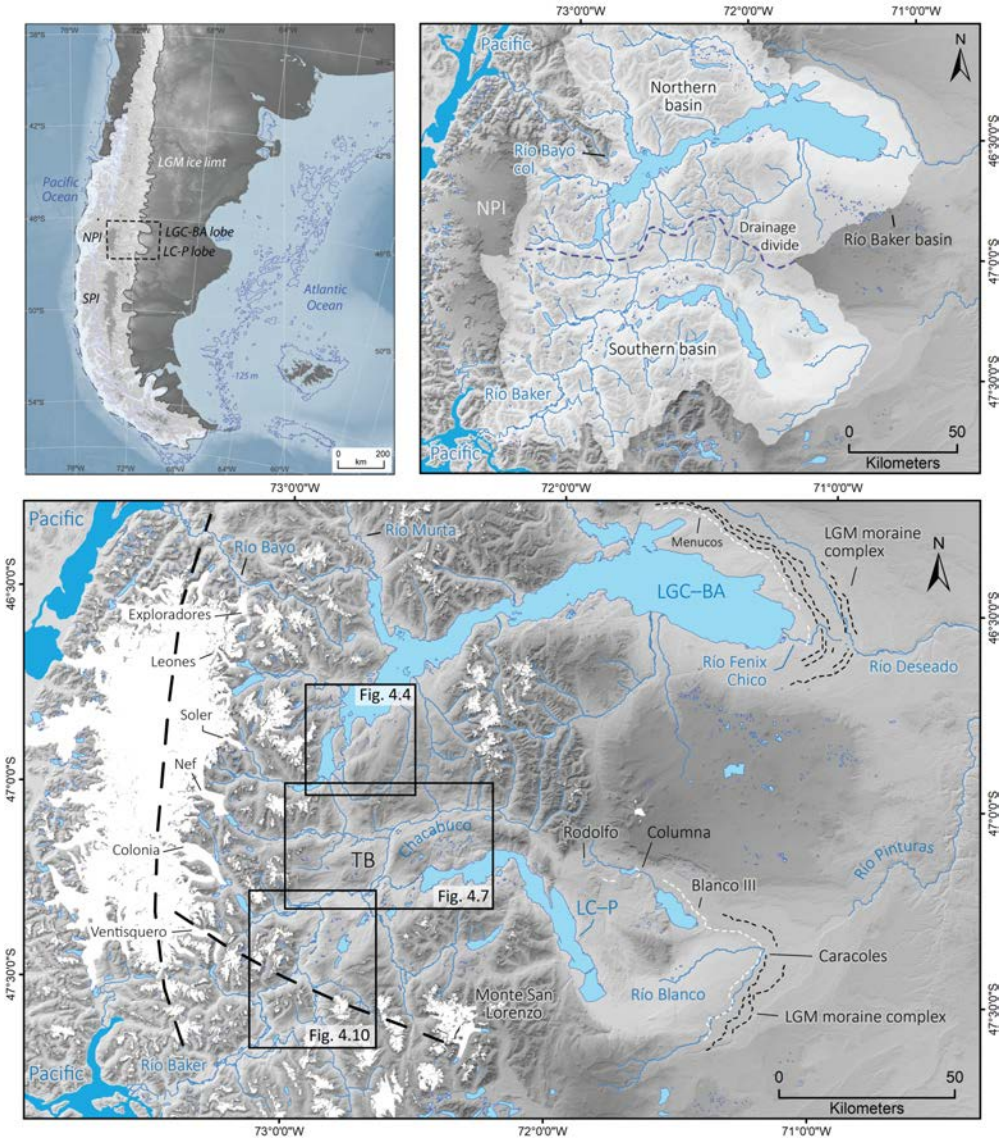

Figure 4.1. (a) The LGM ice limit of the former Patagonian Ice Sheet (PIS) and study area in southern South America. (b) The Río Baker catchment, with the northern and southern basins, as used in the text, shown. (c) Location of the study region and sites of field mapping (black boxes). The Lago General Carrera–Buenos Aires (LGC–BA) and Lago Cochrane–Pueyrredón (LC–P) basins are indicated, as is the Tamango Basin (TB). LGM ice lobe limits (thin dashed lines) shown after Singer et al. (2004), and Coronato and Rabassa (2011), and LGM ice divides (thick dashed lines) after Hubbard et al. (2005). The main ice divide is aligned along the Patagonian mountains, while a subsidiary ice divide links the NPI with Monte San Lorenzo (MSL) across the Río Baker. Contemporary glacier extents are shown in white (cf. Pfeffer et al., 2014).

The onset of deglaciation at LGC–BA has been dated to ~18.1 ± 0.21 cal ka BP, using a calendar-year varve chronology constrained by the well dated Ho tephra (see Weller et al., 2014) of Cerro Hudson (Chapter 5). Following this, the PIS thinned (Boex et al., 2013) and retreated (Hein et al., 2010; Glasser al., 2012), and large proglacial lakes developed at the ice lobe margins (Turner et al., 2005, Bell, 2008). The culmination of this retreat phase is marked by moraine ridges formed around the morpho-tectonic boundary of the Patagonian Cordillera (Turner et al., 2005; Glasser et al., 2012; Boex et al., 2013), to the west of the Tamango Basin (Figure 4.1c). These moraines indicate a phase of regional glacier stabilisation, or re-advance, dated to ~12.8–11.0 ka using CND of moraine boulders, coincident in time with the Northern Hemisphere Younger Dryas interval (Glasser et al., 2012). This empirical data opposes the PIS deglaciation simulation of Hubbard et al. (2005), which predicts regional ice-margin stabilisation at ~13.5 ka, coincident in time with the Southern Hemisphere Antarctic Cold Reversal (ACR: ~14.7–13.0 ka). This model was forced with a Vostok (Antarctic) temperature record (Petit et al., 1998), which exhibits a ACR cooling event, and thus a coeval glacier response is not unexpected. Nonetheless, recent CND dates from moraines in the Colonia valley (~47°S) produce ages that overlap the ACR (Nimick et al., 2016), and thus the regional glacial response to hemispheric climate events remains a source of much debate.

The major morphological feature of present-day regional drainage is the Río Baker catchment (Figure 4.1b), which drains an area of ~27,000 km^2 (Dusaillant et al., 2012). The main Río Baker valley flows north to south and cuts across the west-east trending valleys occupied by NPI outlet glaciers during Quaternary glaciations. The Río Baker is fed by the LGC–BA and LC–P outflows, and the drainage of both lakes is reversed (westwards) relative to the flow pathways of the former ice lobes (Figure 4.1b; Glasser et al., 2005).

4.2.2 Palaeolake evolution

Figure 4.2 summarises the main palaeolake evolution models for the region. The models are underpinned by contrasting geochronological datasets (Table S1). Turner et al. (2005) relied mainly on basal radiocarbon ages from small, infilled kettle holes around former ice margins, whereas Hein et al. (2010) and Bourgois et al. (2016) used CND ages from morainic and ice-rafted boulders. Glasser et al. (2016) obtained optically stimulated luminescence (OSL) ages of former shoreline features (direct) or overlying aeolian deposits (indirect). In all models, during the initial retreat from LGM ice limits, glacial lakes drained eastwards to the Atlantic Ocean through the Deseado and Pinturas rivers (Figure 4.1c), the main difference between the models being a higher LGC–BA

lake level, 480–550 m asl, in the Glasser et al. (2016) model (not shown in Figure 4.2). The geomorphology of raised deltas and palaeoshorelines provide evidence for subsequent lake level falls (Bell, 2008), in response to retreating ice-dam positions (Turner et al., 2005; Glasser et al., 2016).

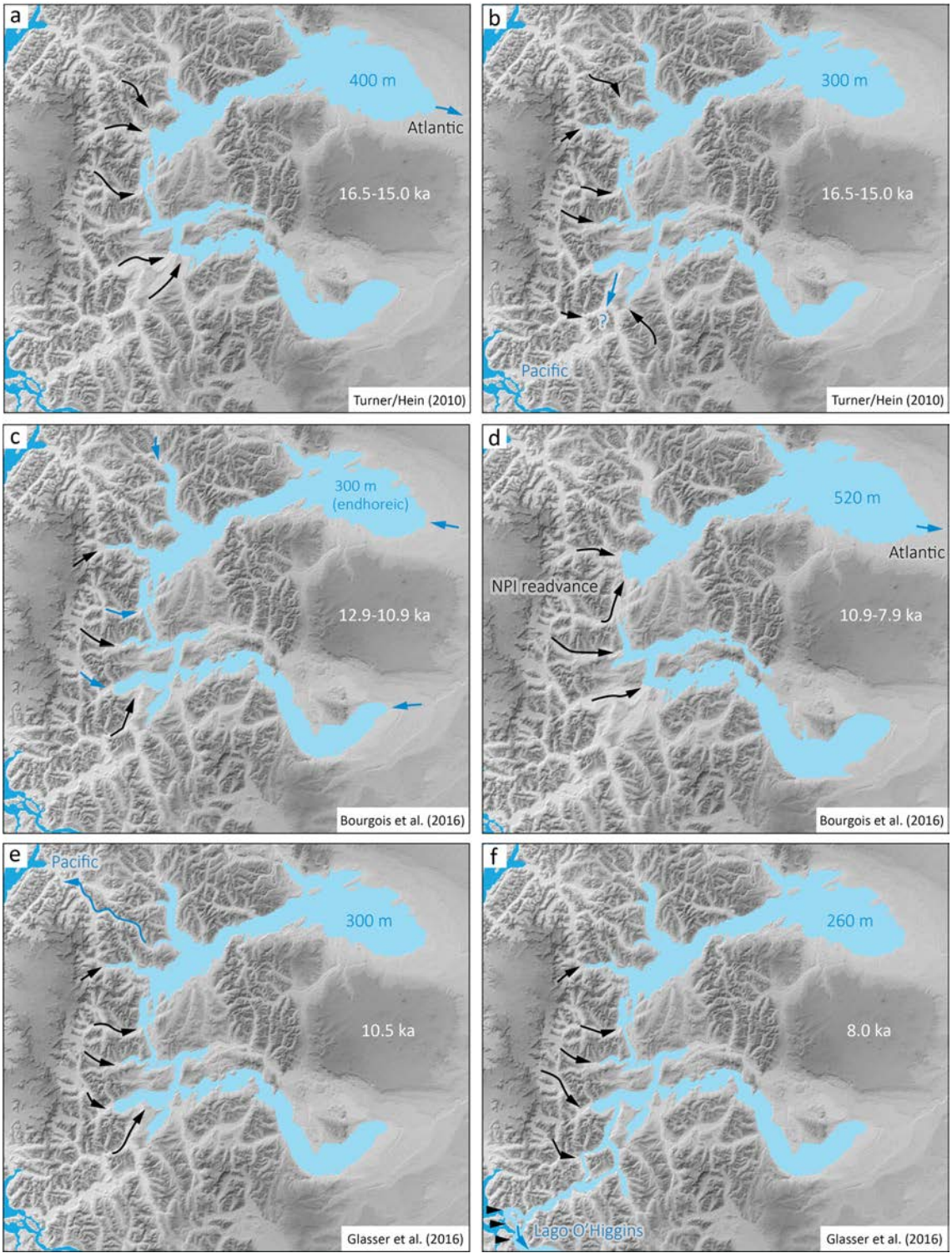

Figure 4.2 Summary of published palaeolake evolution models for the NPI region. (a) The upper unified lake at ~400 m asl level (Turner et al., 2005; Hein et al., 2010), drained to the Atlantic through the Río Deseado. (b) The lower unified lake at ~300 m asl level, with a hypothesised, but currently unidentified, drainage pathway to the Pacific Ocean (Hein et al., 2010). (c) An endhoreic drainage stage proposed by Bourgois et al. (2016). (d) The lower unified lake level at ~300 m asl, with Pacific drainage via the Río Bayo valley (Glasser et al., 2016). (e) Proposed Holocene transgression of LGC–BA to ~520 m asl (Bourgois et al., 2016). (f) A unified lake at ~260 m asl, dammed in the Río Baker valley, with a drainage pathway via Lago O'Higgins (Glasser et al., 2016), a glacial lake of the SPI.

The models also have in common the reconstruction of a large 'unified' palaeolake (Turner et al., 2005; Hein et al., 2010; Glasser et al., 2016), formed when separate lakes in the LGC–BA and LC–P basins joined through the Río Baker valley, as the Soler and Nef outlet glaciers retreated from the western embayment of LGC–BA (Figure 4.1). However, the models differ in terms of the inferred location of former lake drainage outlets, and the timing of lake unification and drainage. In the Turner-Hein model the lakes become unified at an upper ~400–440 m asl level (Figure 4.2a) by ~16.0 ka, with a lower ~300–340 m lake (Figure 4.1b) established when drainage switched from the Atlantic (east) to Pacific (west). In this model, final lake drainage through the Baker Valley occurred by ~12.8 ka (Turner et al., 2005) or earlier (~15.5 ka) depending on a possible, but unidentified, Baker valley drainage pathway (Figure 4.2b, Hein et al., 2010).

Bourgois et al. (2016) suggested a multi-phase lake evolution model that includes an endorheic stage (Figure 4.2c), caused by a reduction in regional precipitation, before lake drainage and a subsequent Holocene (~10.9–7.9 ka) transgression phase up to ~520 m asl (Figure 4.2e), an interpretation questioned by Martinod et al. (2016), who suggest the higher elevation deltas relate to smaller ice-marginal lakes. Alternatively, Glasser et al. (2016) hypothesised a first Atlantic-Pacific drainage reversal through the Bayo Valley by ~10.5 ka (Figure 4.2d), before a spatially extensive lake system formed at ~280 m asl, dammed by coalesced outlet glaciers of Northern (NPI) Southern Patagonian Icefields (SPI) across the mouth of the Río Baker (Figure 4.2f). In this scenario, outflow drainage was proposed via Lago O'Higgins, a proglacial lake of the SPI. Glasser et al. (2016) argue that the NPI and SPI separated by ~8 ka, allowing final lake drainage to contemporary levels.

The range of models can be explained by a lack of systematic regional mapping of palaeolake features using high-resolution imagery and field verification (Chapter 3), and differing interpretations of the available geochronological data. Consequently, there is a ~5000-year gap between the oldest (~15.5 ka) and youngest (~10.5 ka) age for the timing of the first Atlantic-Pacific drainage reversal (Mendelova et al., 2017).

4.3 Materials and methods

4.3.1 Geomorphological mapping

This paper uses data from a previously published geomorphological map of the NPI region of the former PIS (Chapter 3). Glacial and lacustrine landforms were mapped in ArcGIS v10.1 from ESRI™ 'World Imagery' datasets (mainly ~1 m DigitalGlobe and GeoEye IKONOS imagery) and GoogleEarthPro™, and verified in the field where possible (Chapter 3). In addition, new field mapping was undertaken in three sectors: (1) the LGC–BA outflow at Lago Bertrand (northernmost box Figure 1c); (2) the Chacabuco-Cochrane sector of the Baker and Cochrane valleys (central box Figure 1c); and (3) the Colonia-Juncal area encompassing the Baker and Barrancos valleys (southernmost box Figure 4.1c). Sectors 1-2 are important for understanding the blocking/opening of the upper Río Baker and the potential unification of palaeolakes between the main LGC–BA, LC–P and Chacabuco basins, whereas sector 3 is key for understanding the blocking/opening of Pacific drainage through the lower Río Baker valley.

4.3.2 Proglacial lake reconstruction and post-glacial isostasy

Using a dataset of former shoreline features mapped in Chapter 3, we quantify post-glacial isostasy and palaeolake levels using methods similar to those outlined in Breckenridge (2013, 2015; Figure 4.3). Mapped shoreline features included wave-cut scarps, terraces, raised deltas, and isthmuses. Individual shoreline features were digitised by drawing a line along the break slope of an inferred former waterline. These polylines were converted into points at 30 m spacing, and the elevation of each point extracted from an ASTER G-DEM (20 m vertical and 30 m horizontal resolution (95% confidence); cf. ASTER G-DEM Validation Team, 2011). To visualise spatial trends in shoreline elevation(s), a surface was interpolated from the point elevations using a Natural Neighbour function. Using this raster, rebound isobases were constructed as distance contours at 10 km intervals, perpendicular to the direction of maximum uplift. The 0-km isobase was defined by the easternmost extent of shoreline evidence, and intersects the former Río Deseado outflow (~398 m asl) at Río Fenix Chico. For every shoreline point, distance along the direction of maximum uplift was then extracted from the rebound surface and plotted against elevation, and palaeo-waterlines correlated.

Assessments of the isobase surface were made using an iterative histogram analysis (cf. Breckenridge, 2013, 2015), to determine the fit of shoreline elevations to a best-fit regression line. In analysing palaeoshorelines of Lake Agassiz, Breckenridge (2013) used 3 m resolution LiDAR data. The ASTER G-DEM has a comparatively low vertical

resolution (20 m), but represents the highest resolution topographic dataset available to the authors. Beginning with the best-developed shoreline level (a ~300–350 m asl level, named the 'Bayo' level, in LGC–BA), the complete point dataset was split along the lake centre-line into north and south shoreline datasets, and a 2nd-order polynomial regression line fitted to the most densely populated dataset (i.e. containing the most shoreline points). A histogram was then created for each side of the basin using the resultant regression line equation. This defines a modelled shoreline, based on the polynomial equation that describes shoreline elevation as a function of distance (cf. Breckenridge, 2013, 2015). Using the polynomial regression line, histograms were created for each side of the basin. Using 1 m-wide x-axis bins for variations in the y-intercept (shoreline elevation) of the regression line, the y-axis plots the number of points that fall within 1/2 m of the shoreline equation. The fit of the isobase surface was assessed by visually comparing the output histograms. Where slight offsets occurred, isobases were re-contoured through repeated iterations, and the regression analysis reapplied until histograms precisely overlapped and a final set of isobases was achieved. Once the isobase surface was validated for the best-developed (Bayo) shoreline level, the histogram analysis was extended to all other palaeolake levels in the northern (LGC–BA) and southern (LC–P and Chacabuco) basins using the optimal reconstructed isobases.

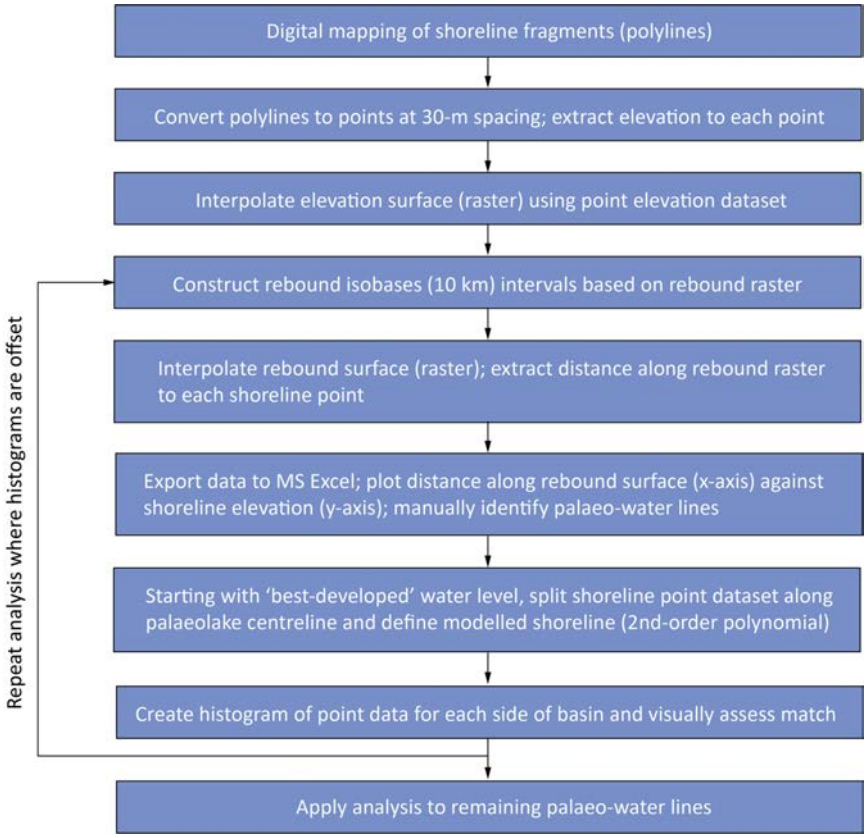

Figure 4.3 Summary flowchart of analysis steps taken to reconstruct former glacial lake waterlines and regional glacio-isostatic adjustment trends.

4.3.3 Altitudinal-based review of published geochronology

Published dating evidence from samples relevant to understanding the chronology of PIS deglaciation and proglacial lake evolution, were reviewed (section S1 of Appendix for database, and date selection rationale). The review makes use of sample altitude information to provide a topocentric dataset to examine alongside the analysis of shoreline isostasy and palaeolake levels (section 4.3.2), and facilitates a more complete assessment of palaeolake evolution and timings. To date, published ages have mainly been presented on 2D maps (Glasser et al., 2012, 2016). Boex et al. (2013) use the altitude of CND samples to infer the timing of former PIS surface elevation, but their analysis is limited to the Chacabuco/Cochrane area. Similarly, Glasser et al. (2016) plot the OSL age of shoreline features on an altitudinal scale, but no elevation-based comparison is made to other chronological datasets (e.g. Turner et al., 2005; Glasser et al., 2012; Boex et al., 2013; Bourgois et al., 2016).

The geochronological database includes: (a) CND ages from moraine boulders (Glasser et al. 2012; Boex et al., 2013; Bourgois et al., 2016); (b) CND ages from glacially-transported erratic boulders and/or inferred ice-rafted dropstones, with ages relevant to palaeolake levels (Hein et al., 2012; Boex et al., 2013; Bourgois et al., 2016); (c) OSL ages from palaeolake landforms (Glasser et al. 2016); and (d) radiocarbon dates from basal organic remains in small kettle holes and lake basins (Turner et al., 2005; Villa-Martinez et al, 2012). Prior to analysis, CND ages were recalculated using the time-dependent scaling scheme (Lm) of Lal (1991) and Stone (2000) and 0 cm-yr^{-1} weathering rates. The Putnam et al. (2010b) New Zealand (44°S) production rate was used to calibrate ^{10}Be determinations (Table S1 in Appendix). This production rate has been widely used in central Patagonia (Glasser et al. 2012; Boex et al., 2013) and overlaps at 1σ with the Patagonian production rate from Lago Argentino (50°S; Kaplan et al., 2011). Exposure ages were calculated using the CRONUS-Earth online calculator (http://hess.ess.washington.edu/) developed by Balco et al. (2008). Radiocarbon ages were recalibrated in Oxcal v.4.3 (Bronk Ramsey, 2009a) using the SHCal13 calibration curve (Hogg et al., 2013).

4.3.4 Optically stimulated luminescence dating

Alongside the review of published geochronology, we provide one additional OSL age from loess deposits in the Nef-Chacabuco reach of the Río Baker valley. The aim of this date was to provide a limiting age for final lake drainage (section 4.2.2). The single aliquot method was used, with 24 quartz multi-grain aliquots (30 grains each) measured using

blue OSL. The equivalent dose was estimated using the Central Age Model (Galbraith et. al., 1999) on the distribution, excluding three outliers.

4.4 Results and discussion

4.4.1 Glacial geomorphology

4.4.1.1 Lago Bertrand sector

In this sector, mapping identified a moraine complex that extends across multiple valleys situated to the north of the contemporary Lago Bertrand outflow into the Río Baker (Figure 4.4a). Remotely sensed mapping (Chapter 3) reveals two main sets of moraine crests. The first occur in the southeast of the Bertrand sector, in the Chinito valley and at Lago Negro (Figure 4.4a), with a second set to the north of the modern LGC–BA outflow (Figure 4.4b and Figure 4.5b,c and d). In this second area, lateral moraines extend from an elevation ~700 m asl (~0.5 km above Lago Bertrand) on the northern valley side to ~490 m asl at their eastern limit above LGC–BA (Figure 4.4b). The morphology of the moraine complex indicates that the ice-margin divided into three smaller lobes at this site, with the most northerly lobe sat on a col (~530 m asl) between the Bertrand and Río Canal valleys (Figure 4.4b and 4.5c).

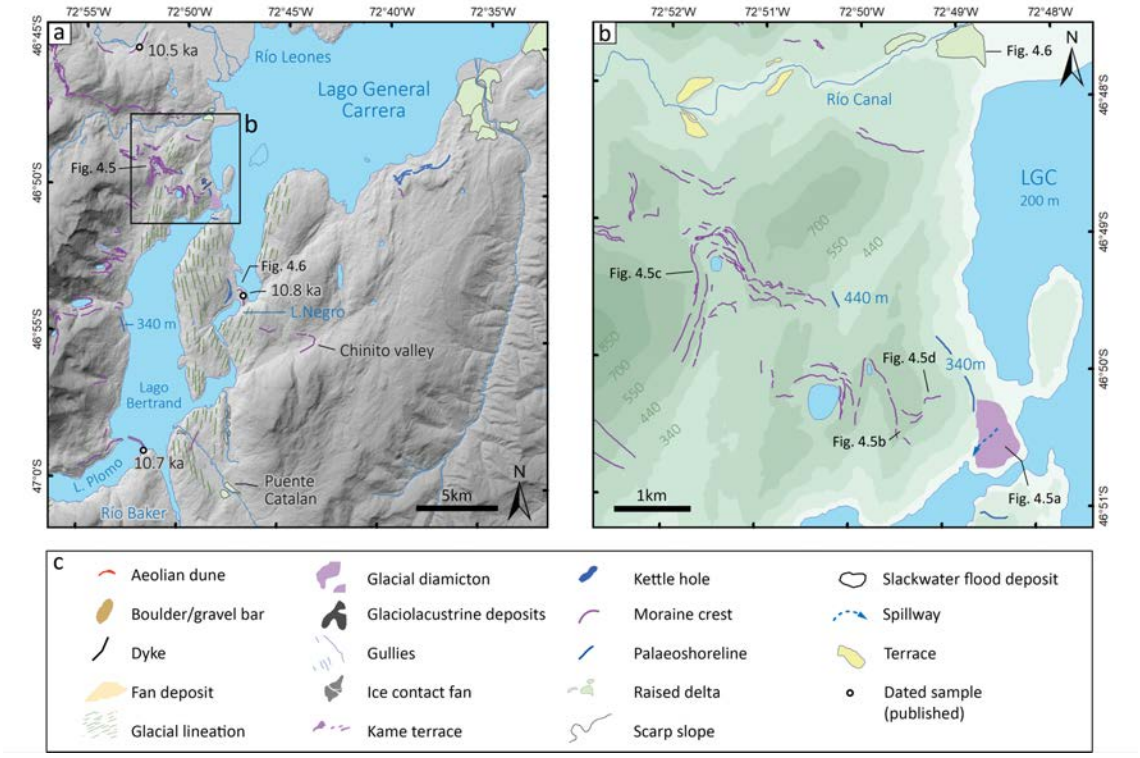

Figure 4.4. (a) Geomorphological map of the Lago Bertrand sector showing moraine crests extending from a col between the Lago Bertrand and Canal valleys (Chapter 3). (b) Map of the moraine complex adjacent to the LGC–BA outflow into Lago Bertrand. (c) Geomorphological mapping legend for Figures. 4.4, 4.7, and 4.10.

From here, the ice-margin can be traced to the present-day LGC–BA outflow, where a thick glacigenic diamict sequence is evident (Figure 4.5a). This feature has been described as a moraine, and sampled by Bourgois et al. (2016) for CND dating (17.4 ± 3.7 ka). We interpret the feature as an ice-contact deposit, possibly a grounding-line fan, formed at the terminus of the Soler Glacier. Exposures through the Lago Negro moraine (Figure 4.6a) are consistent with this interpretation, as north-westerly dipping sand and gravel clinoforms provide evidence for ice-proximal glaciofluvial sediment delivery (e.g. Evans et al., 2012, 2013) to a lake system dammed by northwards flowing ice. This lake likely existed at ~440 m asl, as suggested by shorelines mapped between the Canal and Bertrand valleys (Figure 4.4b), consistent with the elevation of numerous raised deltas (Figure 4.4a) mapped further east (Bell, 2008, 2009; Glasser et al., 2016; Chapter 3).

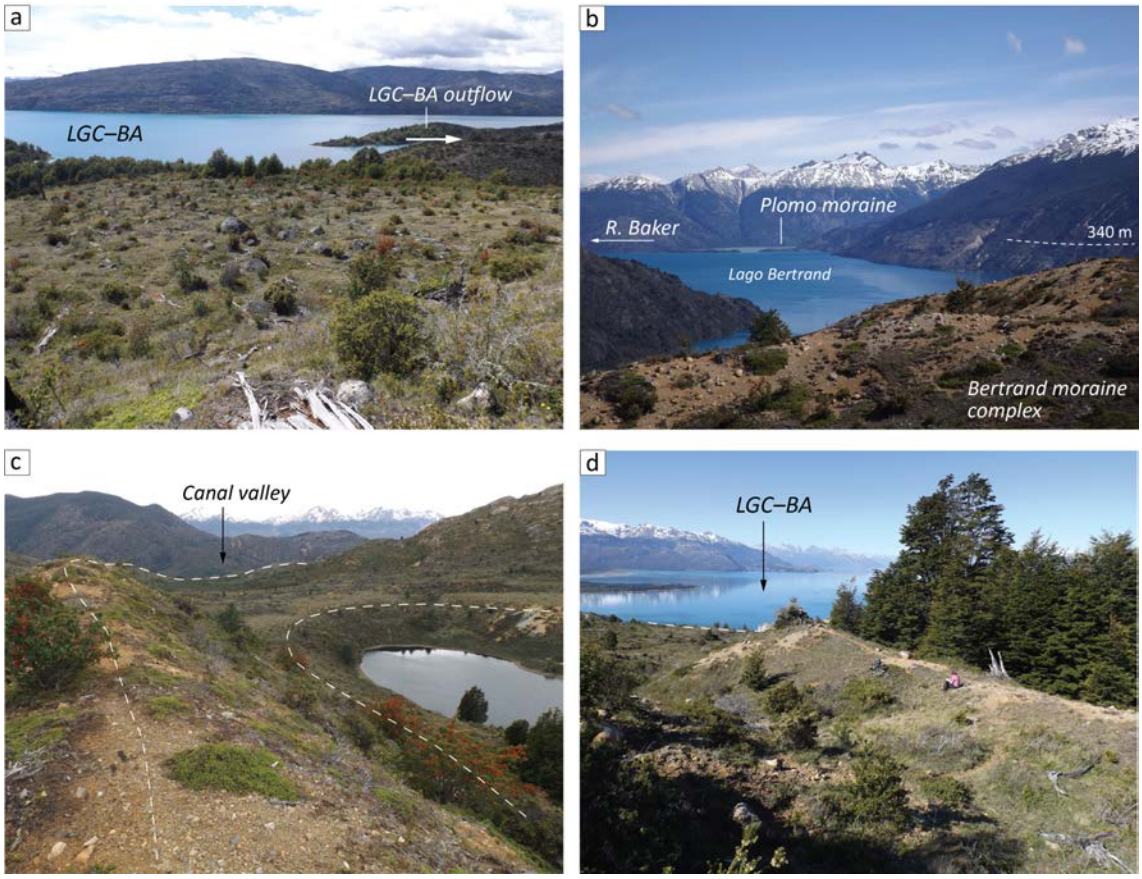

Figure 4.5. Field photographs showing the setting and geomorphology of the Bertrand sector moraine complex. (a) Boulder strewn diamict accumulation at the contemporary LGC–BA outflow, interpreted as an ice-contact deposit, possibly a groundling-line fan. (b) View southwards from the Bertrand moraine complex, showing ~340 m asl shoreline fragments, the Lago Plomo cross-valley moraine, at the LGC–BA outflow at the head of the Río Baker. (c) Multiple moraine crests (dashed white lines) of the Bertrand moraine complex. (d) Moraine crest of the Bertrand moraine complex. View northeast across LGC–BA.

A lower shoreline cut into unconsolidated sediments occurs at ~340 m asl, and runs along the western margin of Lago Bertrand (Figure 4.4b). At the mouth of the Río Canal valley to the north, a raised delta occurs at ~340 m asl, and overlies a glacigenic diamict sequence (Figure 4.6b), but no higher elevation delta was mapped. Near Puente Catalan (Figure 4.4a), to the south of Lago Negro, relict deltas occur at ~340 m and ~460 m. The ~460 m delta exceeds the previous reported elevation for the uppermost lake level in western LGC–BA, and the palaeoshoreline mapped in Figure 4.4b, a finding supported by our regional palaeoshoreline analysis (section 4.4.2). We therefore interpret the delta as evidence for a separate ice-marginal lake, dammed by the southeast lateral margin of ice occupying the Bertrand valley. In summary, landform-sediment assemblages mapped in western embayments of LGC–BA provide evidence for an extensive ice-margin likely sourced from an advanced Soler glacier, and which prevents linkage between the northern (LGC–BA) and southern (LC–P) basins. The former ice-margin has a minimum ice-thickness of ~0.5 km at the LGC–BA outflow, and extended for ~15 km, from the LGC–BA outflow to the Chinito valley (Figure 4.4a), equivalent to ~160 km^2 of ice between LGC–BA and the Lago Plomo moraine (Figure 4.5b) that demarcates the Soler Glacier terminus following opening of the upper Baker Valley.

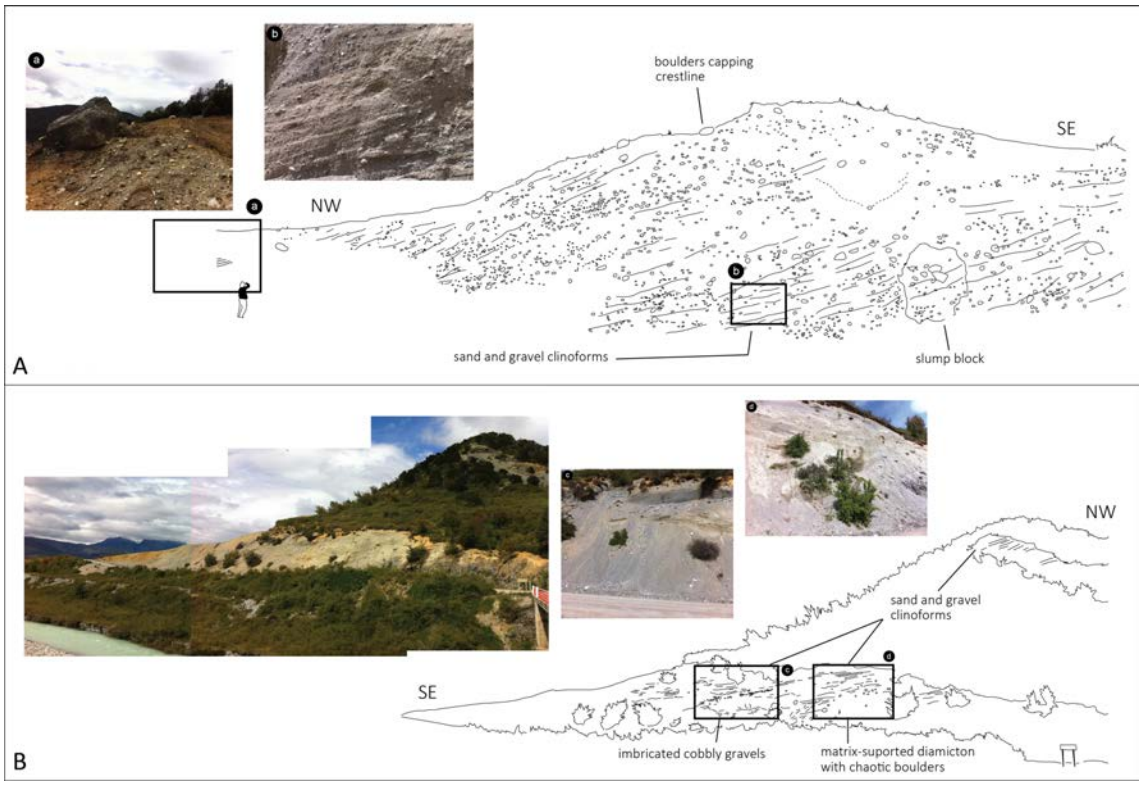

Figure 4.6. Section sketches from (a) the Lago Negro moraine, showing northwesterly dipping sand and gravel clinoforms; and (b) the mouth of the Canal valley, showing matrix-supported diamict overlain by northwards dipping sand and gravel clinoforms (see text for interpretation of sedimentological data).

4.4.1.2 Chacabuco-Cochrane sector

In this sector (Figure 4.7), the landform evidence for palaeolakes includes deltas, wave-cut shorelines and glaciolacustrine sediments (Figure 4.8), the latter outcrop on both the Chacabuco and Cochrane valley floors (Figure 4.7 and 4.8). The upper deltas range from ~460–470 m asl, whilst a lower set occurs at ~340–350 m asl (Figure 4.7b, 4.8a, and 4.8b). The delta elevations coincide with two prominent shorelines. The 460–470 m shorelines can be traced along the eastern margin of the Baker valley, ~2 km upstream of the Nef tributary (Figure 4.7b), and also occur in the Maiten valley (Figure 4.7a), indicating that the Nef Glacier had retreated back to (at least) its valley mouth while a ~460–470 m lake level existed. It is likely, therefore, that this lake level extended to the southern margin of an advanced Soler Glacier that occupied the Lago Bertrand valley (section 4.1.1.1), as demonstrated by the ~460 m asl delta at Puente Catalan (Figure 4.4a). Downstream of the Baker–Chacabuco confluence, the ~460 m shoreline cuts along the upper limit of morainic deposits on the eastern valley side (Figure 4.7a and 4.7b). Additional shorelines are mapped at ~340–350 and ~460 m asl on the northern margin of the Cochrane valley (Figure 4.7c), and at higher altitude the contemporary LC–P outflow (Figure 4.7c), demonstrating a palaeolake connection between the LC–P and Chacabuco valleys at this elevation.

In addition to the evidence for palaeolake levels, sedimentary terraces and boulder-capped bars were mapped along the valley floors in this sector (Figure 4.9). A large boulder bar, with metre-sized boulders, occurs in a zone of valley expansion of the Río Baker (Figure 4.9a and 4.9b), upstream from the Río Cochrane confluence. Boulder bars are also evident around the western margin of LC–P (Figure 4.9c), ~5-10 m above the contemporary lake outflow, and ~30 m below the surface of glaciolacustrine sediment sequences north of Lago Esmeralda. We interpret both sets of boulder bars as evidence for high magnitude glacial lake outburst floods (GLOFs) that passed through the Río Baker and Cochrane valleys. The Baker flood likely triggered terrace incision in the Nef-Chacabuco reach, and backflooding in the wider valley floors, as suggested by the presence of slackwater flood sediments at ~180 m asl immediately upstream of the Baker gorge (Figure 4.9d and 4.9e), ~50 m above the contemporary valley floor. The sediments are composed of a ~10 m thick unit of cross-bedded fine gravels and sands (Figure 4.9e) that display climbing ripple structures and rip-up clasts, as reported for GLOF deposits elsewhere (e.g. Carling, 2013). The deposit is capped by a loess unit that was sampled for OSL, yielding a minimum post-flood age of 7.8 ± 0.5 (Figure 4.7b).

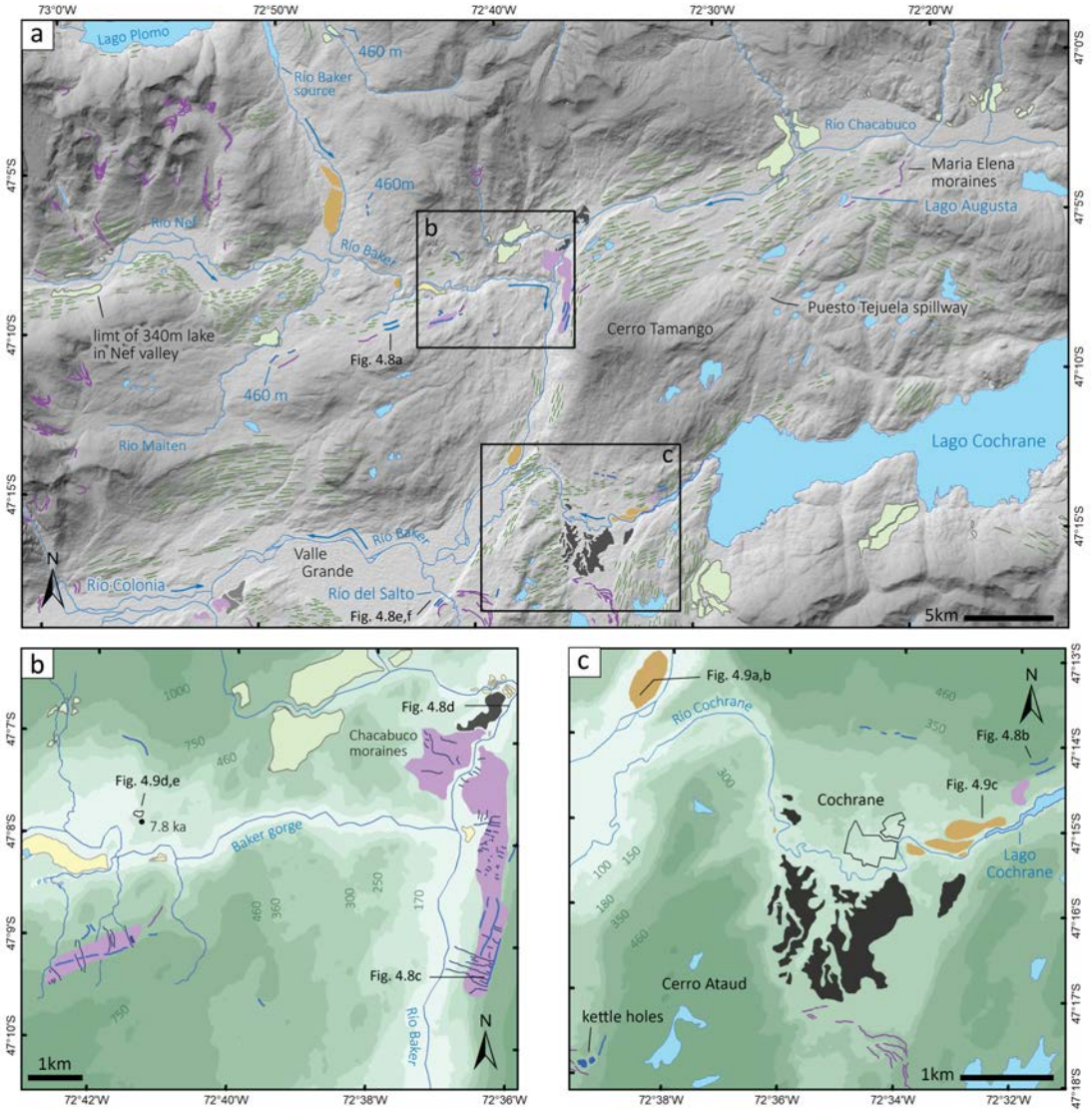

Figure 4.7. (a) Geomorphological map of the Chacabuco-Cochrane sector of the Río Baker valley, showing extent of the ~460 m asl palaeoshoreline in the Maiten and upper Río Baker valleys. (b) Geomorphology of the Baker-Chacabuco confluence sector showing the Chacabuco moraine complex and ~460 m asl palaeoshorelines. Also shown are slackwater deposits, located upstream of the Baker gorge, where GLOF flow hydraulics were controlled by valley narrowing. (c) Geomorphological map of the Cochrane sector showing glaciolacustrine sediments, palaeoshorelines and GLOF bars in the Río Cochrane and Río Baker valleys.

The major implication of the evidence for flood events is that when the GLOF events occurred there were subaerial conditions in the Rio Baker and Cochrane valleys. Therefore, the floods post-date lake-level fall from the local ~340–350 m lake level in the Nef-Chacabuco and Cochrane sectors (Figure 4.7a and 4.7b). As a large volume of water would have been required to produce the mapped flood geomorphology (Figure 4.7 and 4.9), we hypothesise that both LGC–BA and LC–P were dammed by moraines following lake level lowering. In the northern basin, the most likely dam site is the ice-contact glacigenic sediment accumulation deposited at the LGC–BA outflow (Figure 4.4b). The fan surface exhibits a carapace of imbricated boulders (Figure 4.9f), providing

evidence for southwards flow of water towards the Río Baker. Fluvial incision of the fan surface is indicated by localised terraces (Figure 4.9f) and a ~40–50 m high scarp slope (Figure 4.4b) that flanks the contemporary lake outflow. In the southern basin, morainic deposits on the northern flank of the present-day LC–P outflow (Figure 4.7c) represent the best evidence for a former moraine dam, making a breach at this site the most likely source of the LC–P flood.

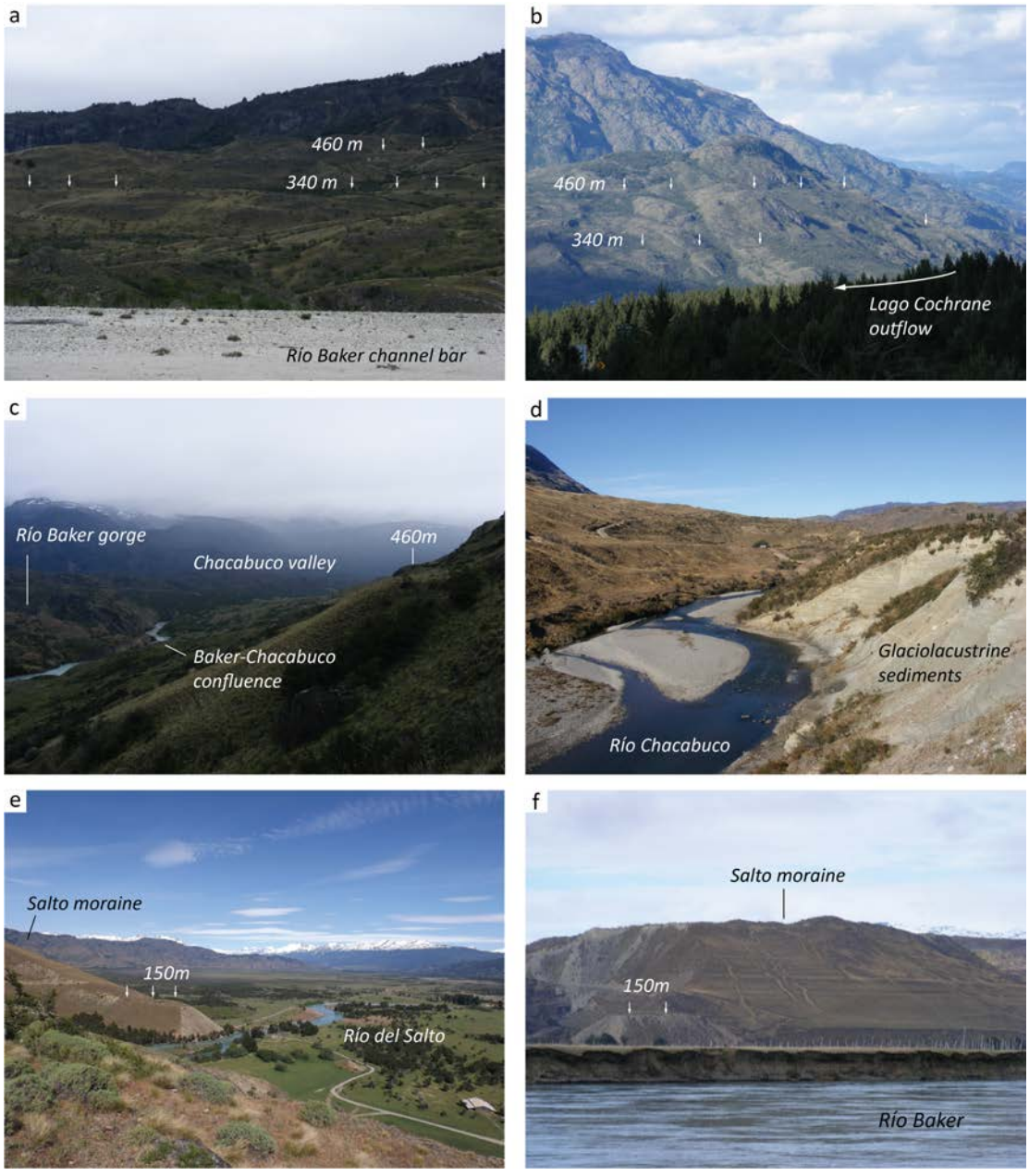

Figure 4.8. Field photographs of palaeolake landforms identified in the Chacabuco-Cochrane sector, and at the Río del Salto moraine complex (see Figure 4.10a). (a) ~460 m and ~340 m shorelines in the Nef valley. (b) ~460 m and ~340 m shorelines above the LC–P outflow (Figure 4.7c). (c) View upstream (northeast) towards the Baker-Chacabuco confluence, showing the ~460 m asl shoreline cut into morainic deposits that blanket the valley side (Figure 4.7b) (d) Glaciolacustrine sediments located immediately east of the Baker-Chacabuco confluence. (e) ~150 m lacustrine delta below the Río del Salto moraine complex. (f) ~150 m lacustrine delta, and wave-cut terraces incised into the front (ice-distal end) of the Río del Salto moraine complex.

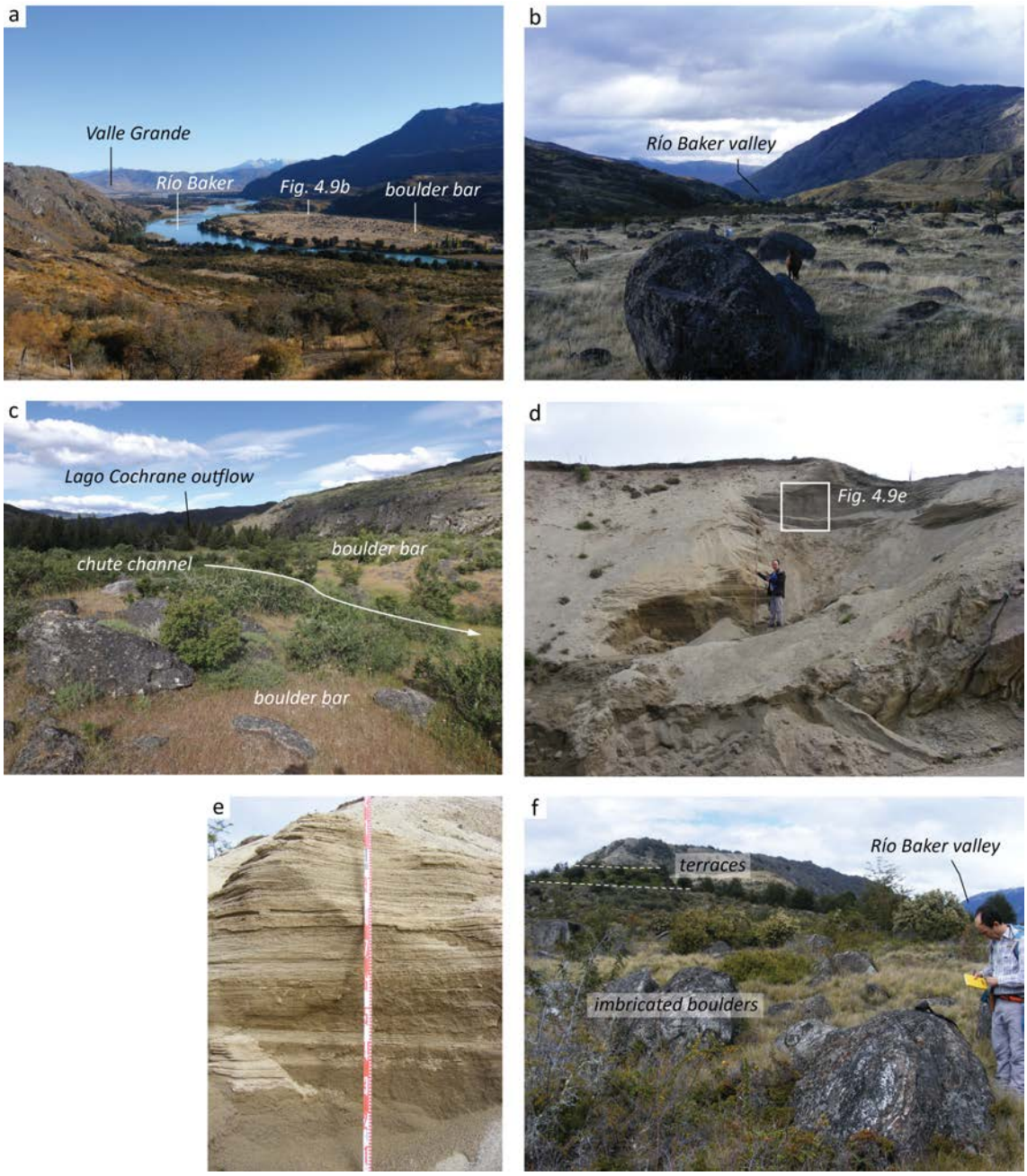

Figure 4.9. Field photographs of palaeoflood (GLOF) sediments and landforms identified along the upper Río Baker valley. (a) Boulder bar deposited in a zone of valley expansion, at the entrance to Valle Grande. (b) Boulder strewn surface of bar feature in (a). (c) Boulder bars and chute channel downstream (west) of the LC–P outflow. (d) Slackwater flood deposits deposited at ~180 m asl in the Nef-Chacabuco reach. (e) Cross-bedded sands with localised climbing ripple and rip-up structures. (f) Surface of the ice-contact sediment accumulation deposited at the LCC–BA outflow (see Figure 4.4), illustrating a carapace of imbrication flood boulders, and terraces surfaces indicative of incision through the deposit surface.

4.4.1.3 Colonia-Barrancos sector

The topographic context for the two study sites in this sector is shown in Figure 4.10a. The Barrancos sector (Figure 4.10b) lies at a watershed at ~420 m asl between the Juncal Valley and the Río Barrancos, a tributary of Río de los Ñadis that feeds into the

lower Río Baker (Figure 4.10a). Here there is evidence for a former lake spillway at ~445–470 m asl, with an inner gorge incised into bedrock (Figure 9c). For this spillway to function, ice would have needed to block the lower ~420 m asl col. Moraine fragments on either side of Lake A (Figure 4.10b), and a submerged moraine segment beneath the current lake (evident in satellite imagery), provide evidence for an ice margin at this location. The lake morphology itself is interpreted as evidence for high-energy scouring by meltwater, as it is analogous to a levee and wiel in fluvial landscapes (Hudson et al., 2010), with deep scour pools formed by levee collapse. This suggests the possible rapid collapse of an ice dam at this locality, which caused downcutting of the inner bedrock gorge at the spillway. This interpretation is further supported by the morphology of Lake B (Figure 4.10b), which fans out from an apex at the exit of a bedrock channel, and a small terrace preserved on the north margin of the channel exit where flow separation and eddying would have occurred in response to water flowing over the col. Following the collapse of this ice margin, and abandonment of the valley side spillway, lake drainage may have continued at ~420 m asl over a broad col (Figure 4.10b). This interpretation is supported by a fan-shaped sand and gravel deposit that dips to the southwest into the Barrancos valley (Figure 4.10b). A relict shoreline at ~360–370 m asl (Figure 4.10b), and north of the ~420 m asl col, provides evidence for the first stable lake level post-dating abandonment of the Barrancos spillway.

In the Colonia sector (Figure 4.10d), a suite of ice-marginal landforms demarcate a previously unmapped glacial limit. These include a fan shaped deposit at the Colonia–Baker confluence that dips northwards towards the Río Baker valley floor. Exposures through the landform reveal northwesterly-dipping gravel beds, which we interpret to reflect ice-proximal subaqueous outwash facies (e.g. Evans et al., 2012; 2013). The fan apex connects to a series of lateral kame terraces and moraine crests (Figure 4.10d) that initially run southwards for ~3.5 km, before turning eastwards towards the Juncal valley, where they mark the limit of a second lobe of ice (Figure 4.10a). Due to forest cover in the Río Baker valley, it is uncertain whether this ice was sourced from (i) the Cordon Trunco massif (Figure 4.10a), which flanks the west of the valley, or (ii) the Ventisquero and/or Río Los Ñadis valleys to the south (Figure 4.10a). As the valley side moraines and kame terraces at this site occur at ~400 m asl, this ice margin is likely related to the ~340-370 m asl lake shorelines mapped further upstream (Figure 4.7).

On the western side of the Río Baker, a morainic deposit, capped with large boulders, is cut by a channel at ~150 m asl, an elevation that coincides with the Río del Salto delta in Valle Grande (Figure 4.8e and 4.8f). Scarp slopes and terrace surfaces are cut in to

the boulder deposit demonstrating incision of the moraine, whilst a few kilometres downstream, imbricated boulders occur on the valley sides to a maximum elevation of ~115 m asl. The channel and delta indicate a moraine dammed lake, that we name Lago Colonia, at ~150 m asl in Valle Grande, and likely into the lower Colonia valley. The downstream boulder deposits and terrace scarps indicate GLOF drainage of this lake. The multiple terrace scarps eroded in to the moraine deposit likely may have been formed by subsequent flood events from LGC–BA and LC–P (section 4.1.1.1), but we note that one of those events may have triggered the Lago Colonia GLOF by overtopping. Following the final GLOF event routed through this reach, there was a phase of aeolian activity evidenced by sand dunes (Figure 4.6d).

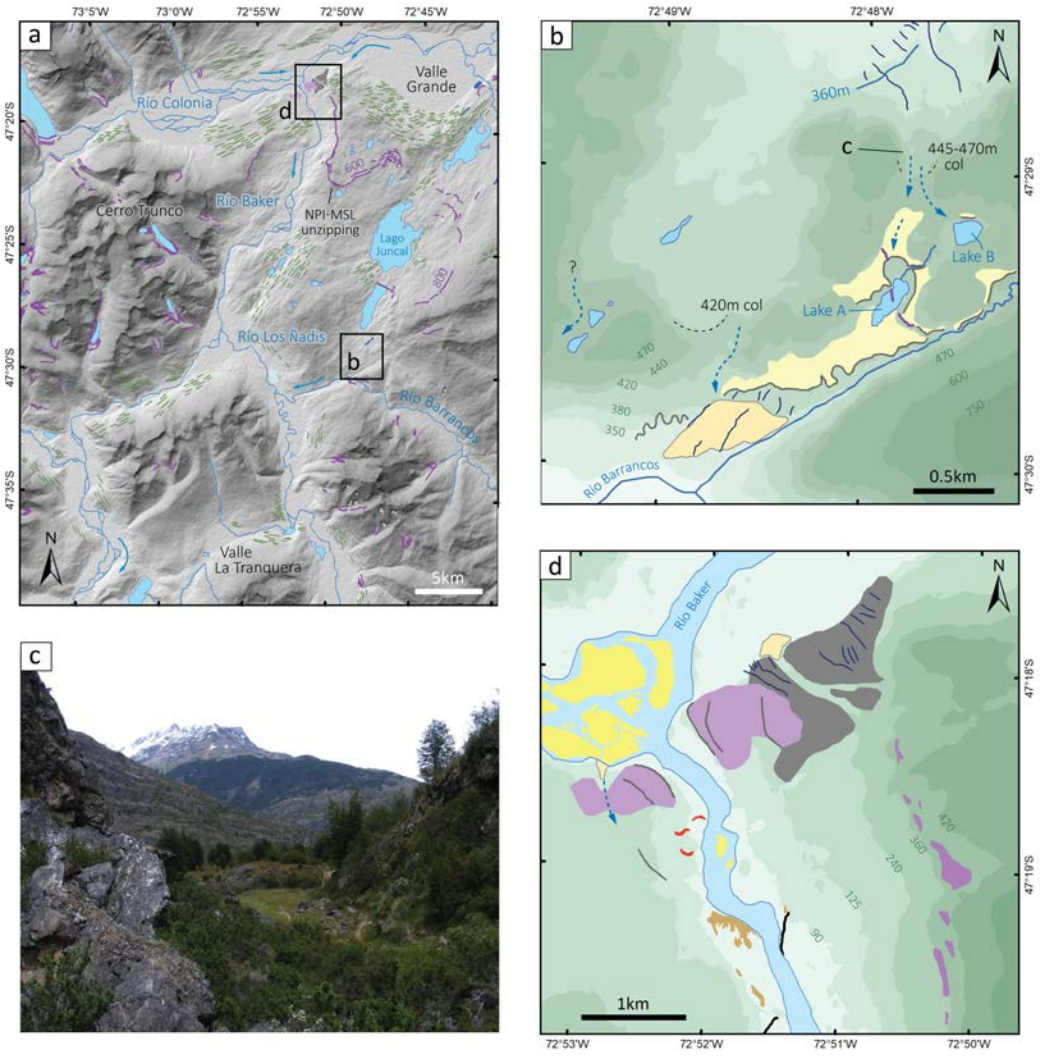

Figure 4.10. (a) Geomorphological map of the Colonia-Barrancos sector. (b) Geomorphological map of the watershed zone between the Juncal and Barrancos valleys, showing the evidence for lake drainage over two col levels into the Barrancos valley. We identify this locality as the previously unknown Pacific drainage pathway of Hein et al. (2010; see Figure 4.2b). Glacial lake water may have drained via the Río Baker or Tranquera valley. (c) Field photograph from the inner bedrock cut channel (~445-460 m asl) with view southwards, along pathway of lake drainage, towards the Barrancos valley. (d) Geomorphological map of the Colonia sector, showing ice-marginal landforms and evidence for high-magnitude GLOFs.

4.4.2 Palaeoshoreline analysis

Figure 4.11a shows the results of the histogram analysis of palaeoshoreline data alongside the elevation of major cols, spillways and ice dams identified in previous studies (Turner et al., 2005; Glasser et al., 2016) and our own mapping (section 4.4.1). The peaks in the histogram data (Figure 4.11a) identify major lake levels, whereas the height of the peaks indicate the frequency of shoreline data points associated with each lake level. The width of each peak documents the distribution of shoreline data points with respect to the polynomial regression, where a narrower peak indicates a closer fit between the shoreline data and the polynomial regression. The degree of correlation of former lake levels across the study area is a function of the modelled isobase surface.

Major lake level frequency peaks occur at ~498, ~392, and ~298 m asl for LC–P; and ~405 and ~299 m asl for LGC–BA (Figure 4.11a). The upper lake in the Chacabuco valley has a frequency peak at ~588 m asl. However, given the wide range of elevations associated with each former lake level (Figure 4.11b), we have named the levels in relation to their controlling outflow. We term the upper Chacabuco lake the Rodolfo level. We term the upper lake in LC–P the Caracoles level, and the upper (~400–450 m asl) lake in LGC–BA the Deseado level. The ~300–350 m asl lake level, observed widely across both northern (LGC–BA) and southern (LC–P) basins, is termed the Bayo level following the earlier recognition of a likely spillway in the Bayo valley (Glasser et al., 2016; Martinod et al., 2016). In addition to the main (previously identified) shoreline levels (Turner et al., 2005; Hein et al., 2010; Glasser et al., 2016; Martinod et al., 2016), our data reveals several additional lake levels not previously associated with outflows. We broadly classify these as: the sub-Caracoles levels of LC–P (478 m asl), the sub-Deseado levels of LGC–BA (383 m asl), and the sub-Bayo levels (249 m asl) of LGC–BA. Each of the sub-levels comprise multiple, closely-spaced shoreline flights (Chapter 3) that likely encapsulate several (possibly short-lived) lake level stages. These levels cannot currently be differentiated due to the vertical resolution (~20 m) of the ASTER G-DEM.

Figure 4.11b plots the shoreline elevation data along a best-fit unidirectional axis of maximum uplift, as defined through the iterative histogram analysis of shoreline data points, and broadly coincides with former ice lobe flow trajectories along the major valleys (Chapter 3; Glasser and Jansson, 2005; Hubbard et al., 2005). The curves display three main features. First, the lower lake levels reveal a greater westwards extent of shoreline evidence, consistent with progressive ice lobe retreat and glacial lake expansion.

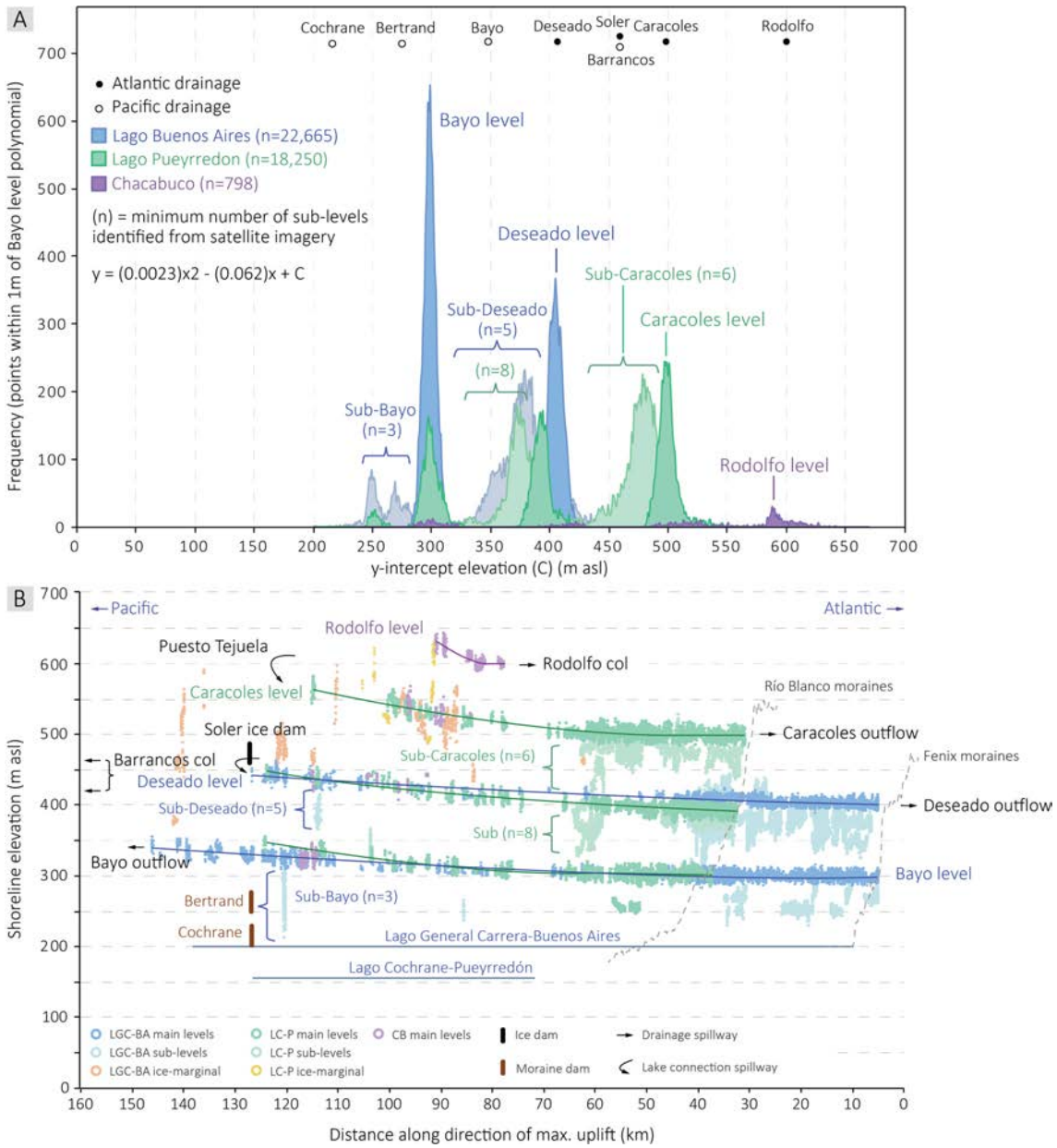

Figure 4.11. (a) Shoreline histogram analysis showing multiple lake levels in the study area. A second order polynomial regression was fitted to Bayo level shoreline point data. The histogram peaks show the number of points that fit within 1 m of the polynomial regression line (equation shown on plot). Peaks indicate the number of points that fit the polynomial, with higher peaks indicating better constrained lake levels. Also shown are the elevations of key cols and inferred ice-dam spillways. (b) Shoreline point elevations plotted against distance perpendicular to the maximum inferred uplift. Cols, inferred ice-dam spillways, and drainage pathways are shown.

The upper Rodolfo lake level extends only ~13 km in to Valle Chacabuco, whilst in LGC–BA, the upper Deseado level extends for ~122 km and the lower Bayo level extends for ~141 km. Second, as the relative age of palaeolake levels decreases, shoreline slope gradients also decrease. In the southern basin, the Caracoles level has the greatest degree of isostatic warping, with an average gradient of 0.78 m km^{-1} towards the

Patagonian Cordillera, compared to the Deseado (0.65 m km^{-1}) and Bayo (0.51 m km^{-1}) levels. In contrast, the average slope of the two main lake levels in LGC–BA are more similar, with 0.31 m km^{-1} for the Deseado level compared to 0.30 m km^{-1} for the Bayo level. Third, average shoreline gradients are higher in LC–P than for the same lake levels in LGC–BA. For example, the Bayo level shoreline gradient is 0.51 m km^{-1} in LC–P, compared to 0.30 m km^{-1} in LGC–BA. This may reflect ice-sheet thinning along the NPI-MSL ice divide (Figure 4.1c), as modelled by Hubbard et al. (2005), forming an additional axis (north-south) of isostatic uplift (section S2 in Appendix). The Hubbard et al. (2005) ice-sheet simulation suggests that by ~13.5 ka, the NPI and MSL outlet glaciers had separated, and that the Río Baker valley was ice-free. In contrast, the model predicts that ice persisted in the western embayments of LGC–BA at this time (Hubbard et al., 2005). This scenario would imply a faster reduction of ice thickness in the southern basins of Cochrane and Chacabuco (Figure 4.1), with >1500 vertical metres of ice loss here compared to 1000 m in the western embayment of LGC–BA.

4.4.3 Altitudinal-based review of geochronology

Recalibrated ages (Table S1 in Appendix) relevant to the chronology of palaeolake evolution are plotted against sample altitude in Figure 4.12. The precision of ages differs according to technique, with CND boulder ages and OSL shoreline ages exhibiting greater uncertainties than radiocarbon dates from basal organic remains.

4.4.3.1 The northern basin (LGC–BA)

In LGC–BA, the onset of glacial retreat at the end of the local-LGM is precisely constrained by a new varve chronology from the Fenix Chico valley (Chapter 5), which is anchored to the calendar-year timescale by the Ho tephra of Cerro Hudson (Weller et al., 2014). This chronology informs a Bayesian age modelling experiment of earlier CND ages derived from the late-LGM Fenix I and Menucos moraines at LGC–BA (Kaplan et al., 2004; Douglass et al., 2005), which yield ages of 18.1 ± 0.21 and 17.7 ± 0.12 cal ka BP, respectively (Chapter 5). The varve record suggests that the LGC–BA ice lobe margin maintained a position in eastern LGC–BA until at least 16.9 ± 0.12 cal ka BP (Chapter 5).

The next dated ice limits occur in the Bayo valley (Glasser et al., 2006, 2012) and the western embayment of the LGC–BA basin (Glasser et al., 2012; Bourgois et al., 2016; Figure 4.12). Three CND samples from the Lago Negro moraine (all ~250 m asl) yield ages of between 9.9–12.5 ka, and overlap ages of 10.1–11.6 ka for the Lago Plomo moraine (Glasser et al., 2012), with an estimated removal of ~160 km^2 of ice between these two ice margins (section 4.1.1.1). In addition, Bourgois et al. (2016) dated a single

boulder from the LGC–BA outflow and yielded an age of 17.7 ± 3.8 ka (Figure 4.4). Glasser et al. (2016) used OSL dating to estimate the age of LGC–BA shorelines, and thus palaeolake stages. Ages associated with the Deseado (~400–450 m) lake level (Table S2 in Appendix) exhibit a large maximum scatter (~17–7 ka), in comparison to the tighter clustering of the Bayo (~300–350 m) level shoreline ages (~12–9 ka), excluding two younger outliers (Glasser et al., 2016; Figure 4.12).

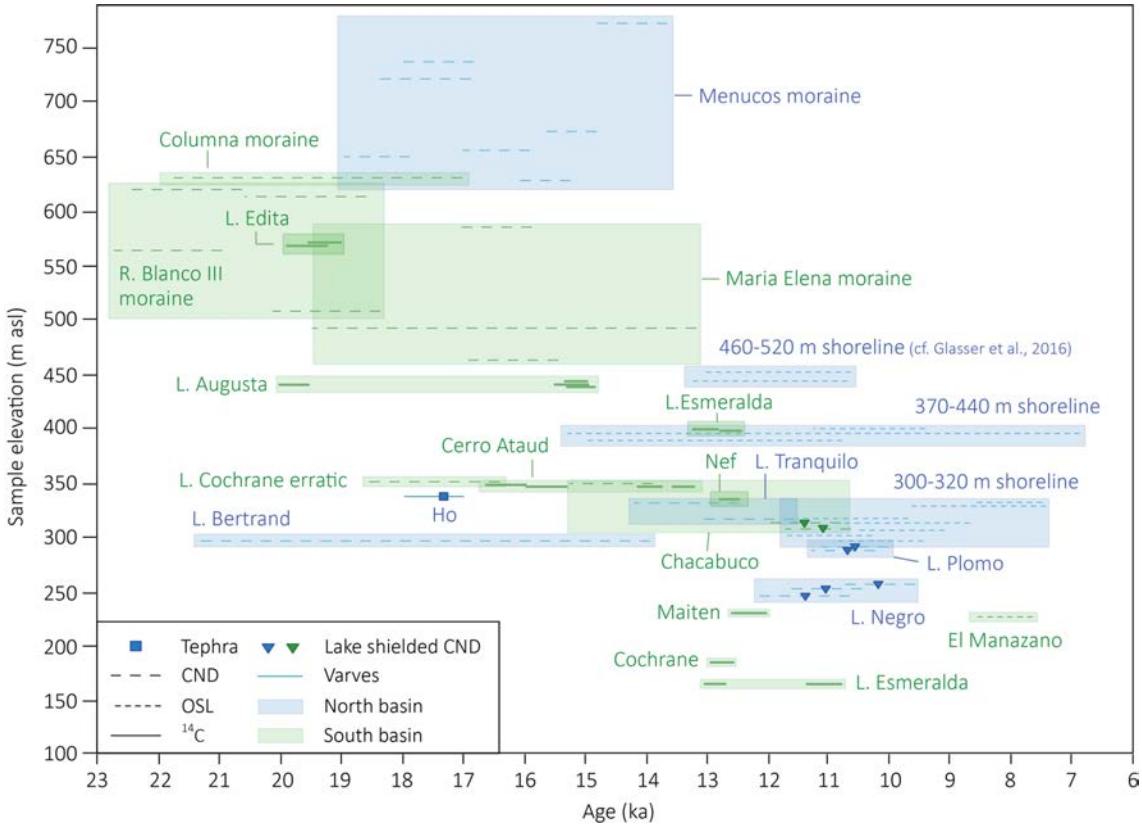

Figure 4.12. Age versus sample altitude for the compiled geochronological database (section S1 in Appendix). Samples are organised according to dating method, and whether they are derived from the northern (LGC–BA; blue shading), or southern (Chacabuco/LC–P; green shading) basins. Note the position of the dated Ho tephra, which anchors a varve chronology from LGC–BA (see Chapter 5), and provides a more precise age constraint on the onset of deglaciation, compared to the CND boulder ages derived from the Fenix, Menucos (LGC–BA), Blanco, and Columna (LC–P) moraines. Note the CND ages inferred to have been sampled from moraine boulders shielded beneath the Bayo lake level, and which therefore date the timing of Bayo lake level fall.

4.4.3.2. The southern basin (LC–P and Chacabuco valleys)

The onset of glacial retreat in LC–P and the Chacabuco valley is broadly constrained by CND dates from the innermost Río Blanco moraines (21.9 ± 0.8 ka to 19.2 ± 0.9 ka; Hein et al., 2010; Figure 4.12), and the morphostratigraphically younger Columna moraine (19.4 ± 2.4 ka; Boex et al., 2013). There is no additional data on the timing of ice-margin retreat in LC–P. While a single erratic boulder located at 352 m asl, below Sierra

Colorado, was CND dated to 17.4 ± 1.0 ka, this boulder was interpreted as having been shielded by lake water, and thus constrains the timing of lake level fall instead of ice retreat (Hein et al., 2010). In the Chacabuco valley, three CND dates (463–586 m) sampled from the Maria Elena moraine, located ~60 km west of the Columna moraine, yield recalculated ages of 16.2 ± 0.7, 16.3 ± 3.1 ka, and 16.4 ± 0.6 ka (Boex et al. 2013).

Three radiocarbon dates of organic remains derived from a sediment core at ~440 m asl in Lago Augusta (Figure 4.12), which is located on the ice-proximal side of the Maria Elena moraine, provide a minimum age of between 15.3 ± 0.2 and 15.1 ± 0.2 cal ka BP for the end of glaciolacustrine sedimentation at this elevation (Villa-Martinez et al. 2012). The morphostratigraphic position of Lago Augusta dictates that the Maria Elena ice limit must have pre-dated the glaciolacustrine sedimentation phase, and highlights a possible issue with the CND ages obtained from this site. The oldest radiocarbon age for lake sedimentation (19.8 ± 0.15 cal ka BP) was excluded from the Lago Augusta age model by Villa-Martinez et al. (2012), and therefore our review also, though we note the similar recalibrated ages (19.6 ± 0.28 and 19.3 ± 0.21 cal ka BP) from the higher elevation (~570 m asl) Lago Edita, located ~3 km south of Lago Augusta (Henríquez et al., 2017). A further ~15km of glacier retreat in the Chacabuco valley is demonstrated by moraine mounds near the Baker–Chacabuco confluence. CND ages for three boulders at this location (Glasser et al., 2012) yield ages of: 11.6 ± 0.5 ka (309 m asl); 11.9 ± 0.6 ka (314 m asl); and 15.2 ± 0.7 ka (350 m asl).

The 350 m asl CND sample from the Baker–Chacabuco confluence lies at a comparable elevation to kettle holes on the Salto moraines, which were cored and sampled for radiocarbon dating (of peat (bulk) and macrofossil remains) by Turner et al., (2005), and yield recalibrated ages of between 16.3 ± 0.31 to 13.4 ± 0.14 cal ka BP. In addition, in the Nef Valley, a landform interpreted by Turner et al. (2005) as a kame delta (~340 m asl), but mapped here as a raised delta (Figure 4.7a; Chapter 3), was radiocarbon dated to 12.7 ± 0.07 cal ka BP. Similarly, basal radiocarbon dates obtained from kettle holes in the Cochrane and Maiten valleys (<200 m asl) are dated to 12.7–13.0 and 12.2–12.8 cal ka BP, respectively. The youngest age in our geochronological database is 7.8 ± 0.5 ka, from the loess deposit that caps slackwater flood deposits (this study) at ~210 m asl in the Nef–Chacabuco reach of the Río Baker valley.

4.4.4 Synthesis

The combination of new geomorphological (field) mapping, a systematic analysis of shoreline isostasy (Figure 4.11), and a detailed review of the available chronological data

(Figure 4.12), enable us to raise several key implications for the evaluation of previous lake evolution models (Figure 4.2).

First, our shoreline isostasy data and inferred lake-level correlations (Figure 4.11) suggest that many of the moraine boulders used for CND dating of glacial limits, were likely shielded beneath lake water (Figure 4.13). This finding is essential to robust interpretations of regional palaeolake history because the published ages for ice-margin positions may be erroneous, and some of these moraines, such as at Chacabuco (Figure 4.7b) and Lago Negro (Figure 4.4a), are in key localities for blocking lake drainage (and thus lake unification) through the upper reaches of Río Baker valley. This problem is illustrated using data from the Chacabuco valley, where at least five lake levels are evident (Figure 4.11 and 4.13): the Rodolfo (620 m asl), Puesto Tejuela (570 m asl), Caracoles (520–540 m asl), Sub-Caracoles (including Soler, 460 m asl) and Bayo (340 m asl). Two of the Maria Elena moraine boulders (Boex et al., 2013) were likely shielded beneath the Caracoles level, whilst all three of the Chacabuco moraine mound boulders (Glasser et al., 2012) were submerged beneath the local sub-Caracoles levels, and two of those were sampled from beneath the local Bayo level (Figure 4.13; see Figure S1; Table S1 in Appendix). There is overlap between the ages of the 586 m asl boulder at Maria Elena (16.4 ± 0.6 ka) and the lake shielded sample at 463 m asl (16.1 ± 0.7 ka), suggesting that ice retreat towards the Nef–Baker Valley confluence occurred within the errors on these ages. There is however a marked difference between the Chacabuco moraine mound dates (Glasser et al., 2012), with an age of 15.2 ± 0.7 ka from the boulder above the Bayo level, compared to ages of 11.6 ± 0.5 and 11.9 ± 0.6 ka from the lower altitude samples. Lake water shielding therefore provides an alternative interpretation for the older age, previously considered an outlier (Glasser et al., 2012). Nevertheless, our data suggests that the higher altitude boulder (15.2 ± 0.7 ka) post-dates lake level fall from the sub-Caracoles levels, whilst the lower boulders (11.6 ± 0.5 and 11.9 ± 0.6 ka) were exposed by the Bayo level lake level fall, as opposed to ice retreat. In total, Glasser et al. (2006, 2012) dated eleven moraine boulders that yield a mean age of ~11.3 ka, and which our mapping and palaeoshoreline analysis suggest were located beneath the Bayo lake level (Figure 4.13). The implications of this interpretation for the timing of regional glacier advance(s) are discussed in section 4.4.6.

Second, we consider basal radiocarbon dates from kettle holes and lake basins that can be used to constrain lake level falls. Our data show that the elevations of the sampled basins are effective at constraining some key lake level changes, whilst necessitating caution for others. The dated transition from glaciolacustrine to gyttja sedimentation at Lago Augusta (440 m asl) provides critical age control for lake level fall below ~450 m

asl in the Chacabuco valley (Villa-Martinez et al., 2012) The Lago Augusta site lies beneath the Caracoles shoreline curve (Figure 4.11 and 4.13), and therefore the basal radiocarbon dates must post-date the abandonment of the Caracoles outflow in eastern LC–P, and drainage to the Atlantic via the Rio Pinturas. We infer Pacific drainage of the Soler level (~460 m asl) via the Barrancos col.

Turner et al. (2005) targeted kettle hole basins at elevations between and below their upper (this study: Soler) and lower (this study: Bayo) unified lakes (Figure 4.2), to constrain the age of lake levels through radiocarbon dating of basal organic remains. However, these sites were chosen without reference to systematic isostatic shoreline data (Figure 4.11), with one anomalous finding the early ages of between ~16.3 ± 0.31 and 13.4 ± 0.14 cal ka BP from kettle holes at Cerro Attaud (Figure 4.7c), which were exposed following drainage of the lower unified (this study: Bayo) level (Figure 4.13). To explain these early ages, Turner et al. (2005) hypothesised that isostatic adjustment may have raised the kettle holes above the local lake level, and inferred that the radiocarbon ages of these samples were contemporaneous to, rather than post-dating, the Bayo lake level. Our data, including the recognition of a previously unreported SW-NE axis of isostatic uplift (section S2 in Appendix), lends support to this hypothesis.

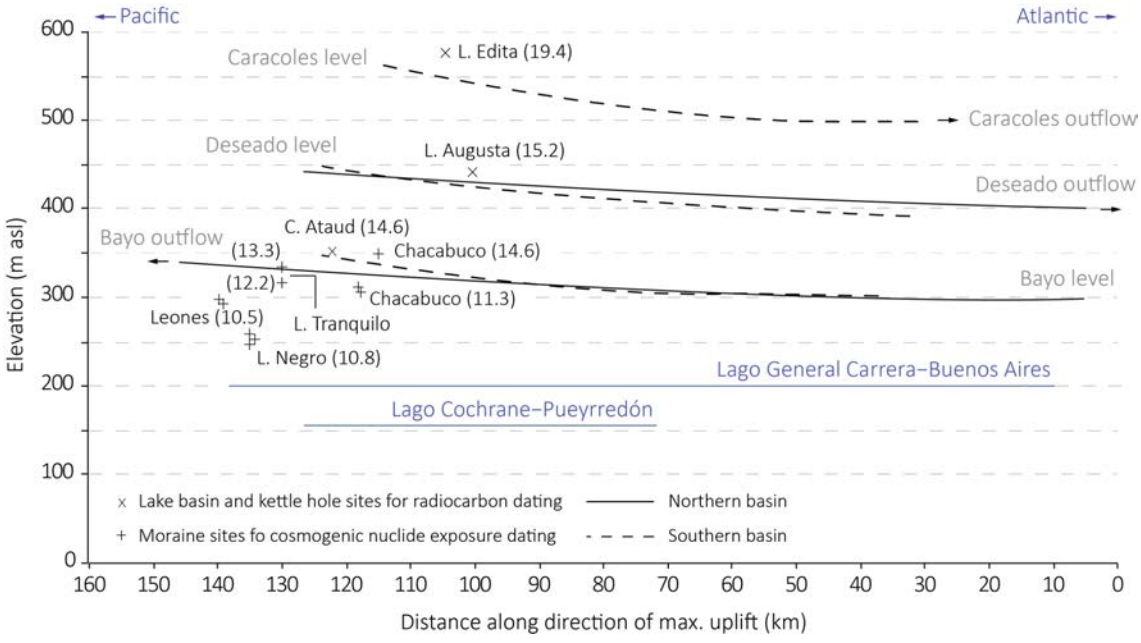

Figure 4.13. Comparison of isostatically adjusted shoreline curves (Figure 4.11; this study) and the elevation of CND and radiocarbon dating evidence. Many of the moraine boulders used for CND dating of glacial limits, were likely shielded beneath the Bayo lake level, and therefore date the timing of lake level drop.

Synthesising our data highlights key contrasts with previously published lake models. We find limited evidence for the proposed high (>500 m asl) elevation lake levels in LGC–BA, as suggested by Glasser et al. (2016; not shown in Figure 4.2), or the Holocene transgression (also >500 m asl) of Bourgois et al. (2016). Instead, our data support the view of Martinod et al. (2016) that the high level raised deltas and shorelines relate to ice-marginal lakes dammed by the lateral margins of glacial ice occupying the main LGC–BA valley. Moreover, the stratigraphy at Río Fenix Chico, at the eastern end of LGC–BA, demonstrates that the palaeolake formed (18.1 ± 0.21 cal ka BP) at the Deseado level (~400 m asl), and there is no evidence for a subsequent lake transgression above this elevation (Chapter 5). The identification of an ice dam at the southern margin of the Soler Glacier (Figure 4.4), and a new spillway at the Juncal-Barrancos watershed (Figure 4.10b), suggests that unification of the LGC–BA and LC–P lakes at the upper ~400–450 m asl (Deseado) level (Figure 4.2a) need not be inferred to explain lake drainage pathways. If correct, drainage via the Barrancos spillway (locally ~445–470) occurred by at least 15.3 ± 0.2 cal ka BP, based on the recalibrated radiocarbon ages for the end of glaciolacustrine sedimentation at ~450 m asl in Lago Augusta. This supports the Hein et al. (2010) timing for abandonment of the Caracoles spillway of LC–P. Hein et al. (2010) left open the possibility of a Baker valley drainage pathway to the Pacific Ocean at ~15.5 ka (Figure 4.2b) and the Barrancos spillway may provide the first geomorphological evidence for this route. This would imply a first Atlantic-Pacific drainage reversal by 15.3 ± 0.2 cal ka BP, rather than at ~12.8 ka (Turner et al., 2005) or ~10.5 ka (Glasser et al., 2016). The geomorphology (Figure 4.4) and geochronology (Figure 4.12) are equivocal in relation to the timing of the onset of the Bayo level, as there is no precise dating on when the Soler Glacier ice-dam ceased to function. Drainage through the Bayo valley (cf. Glasser et al., 2016) may have operated independently of lake unification, however, ice-meltwater dynamics in the valley are poorly constrained at present. Finally, our geomorphological evidence does not support a unified ~260 m asl lake level dammed by a coalescent NPI-SPI (Glasser et al., 2016) following the fall of the Bayo lake level. This is because our flood geomorphological evidence (Figure 4.7 and 4.9) suggests that large magnitude GLOFs passed subaerially along the Río Baker valley from separate LGC–BA and LC–P lake sources, with both lakes likely dammed by moraines after lowering of the Bayo level.

4.4.5 Event sequence of palaeolake evolution and drainage reversals

We present a new 7-stage event sequence for outlet glacier and palaeolake evolution (Figure 4.14 and Table S2 in Appendix) that uses our regional (Chapter 3) and local-scale mapping, shoreline analysis (Figure 4.11), and geochronological review (Figure

4.12 and 4.13). Where data is inconclusive we highlight alternative hypotheses that can be tested with further geomorphological mapping and/or geochronological data.

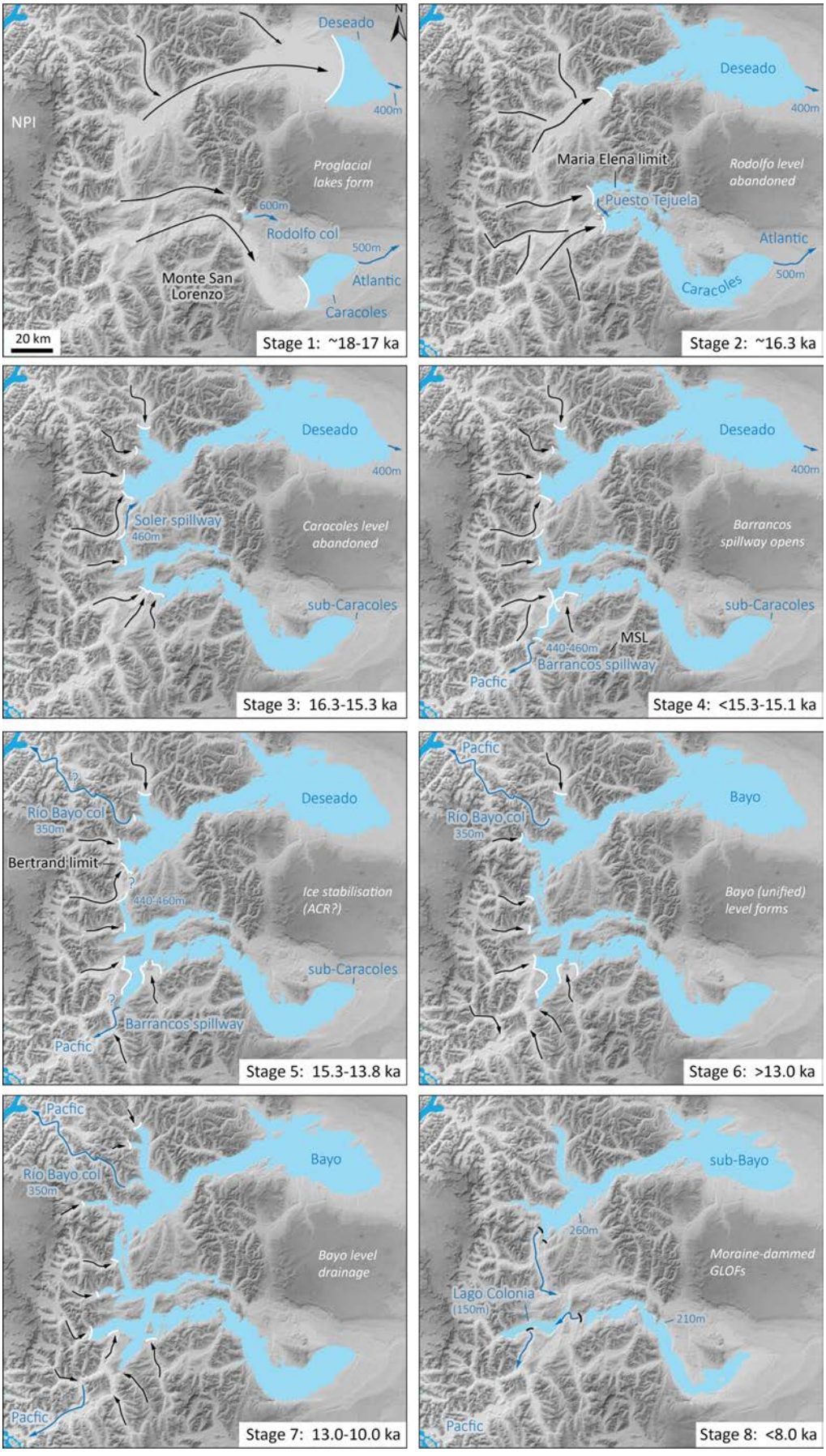

Figure 4.14. Palaeolake evolution model inferred from new datasets presented in this Chapter. Palaeolake elevations refer to altitude of the associated drainage spillway. *Stage 1* (18.0-17.0 ka): proglacial lakes develop following the onset of deglaciation, and drain eastwards to the Atlantic Ocean. *Stage 2* (~16.3 ka): retreat of the Chacabuco ice lobe from the Maria Elena moraine (Boex et al., 2013) allows drainage of the ~600 m Rodolfo level into LC–P (Caracoles level; 500 m) via the Puesto Tejuela spillway (Glasser et al., 2016). *Stage 3* (16.3-15.3 ka): the Caracoles level (~500 m) is abandoned as lake waters drain via the Soler Glacier (460 m) into LGC–BA. *Stage 4* (prior to (<) 15.3-15.1 ka): 'unzipping' of NPI and Monte San Lorenzo ice allows the sub-Caraoles level (460 m) to reach the Barrancos col, and drain to the Pacific Ocean via the lower Río Baker. *Stage 5* (15.3-13.8 ka): glaciers stabilise in the western embayment of LBC–BA (possibly during the Antarctic Cold Reversal). A second drainage reversal may occur during this stage, as the Deseado level drains to the Pacific via the Río Bayo spillway. *Stage 6* (after (>) 13.0 ka): the Bayo level forms following retreat of the Soler Glacier and lake unification through the upper Río Baker valley. The Bayo level drains to the Pacific via the Bayo spillway. *Stage 7* (13.0-10.0 ka): an ice dam fails at a currently unknown location, and the Bayo lake level is abandoned with drainage to the Pacific via the Río Baker. *Stage 8* (prior to (<) 8.0 ka): independent lakes form behind moraine dams, following Bayo lake level fall. GLOF events are triggered, lowering LC–P and LGC–BA to their contemporary levels.

Stage 1: The onset of deglaciation results in ice retreat from the eastern moraine systems forming glacial lakes in the LGC–BA, Chacabuco and LC–P valleys, at the Deseado, Rodolfo and Caracoles levels, respectively. The onset of lake formation in LGC–BA is dated to 18.1 ± 0.21 cal ka BP (Chapter 5).

Stage 2: In the LGC–BA (northern) basin, the last major ice limits were deposited between 17.7 ± 0.12 (Menucos) and 17.3 ± 0.12 cal ka BP (Santa Maria), however, ice likely persisted in eastern LGC–BA until at least 16.9 ± 0.12 cal ka BP (Chapter 5). The presence of the large contemporary LGC-BA and LC-P lakes limit the evidence for further ice margins in the central sectors of these major valleys. However, the Maria Elena moraine (Figure 4.7a), dated to between 16.4 ± 0.6 to 16.1 ± 0.7 ka (Boex et al., 2013), provides timing for an intermediary ice margin position in the Chacabuco valley. This age constrains the abandonment of the Rodolfo col, as this ice position allows drainage from the Chacabuco valley to LC–P over the Puesto Tejuela spillway (Glasser et al., 2016). This is associated with the Caracoles level of LC–P, with outflow drainage to the Atlantic through Río Pinturas.

Stage 3: The Chacabuco ice lobe separates into the Nef and Colonia outlet glaciers, which retreat from the Baker-Chacabuco confluence. The opening of the Nef-Baker reach enables lake water to reach the Soler Glacier where it is impounded by an ice dam. This level likely drained to LGC–BA (Deseado) around the margins of the Soler Glacier, rather than around (or through) Colonia ice that blocked the Río Baker valley, given drainage here would be restricted by the ice-surface gradient. The shoreline evidence indicates a lake at ~460 m asl extended from the Soler Glacier margin into the

Chacabuco and Cochrane valleys. This lake level post-dates the formation of the Maria Elena moraine at 16.4 ± 0.6 to 16.1 ± 0.7 ka (Boex et al., 2013), and pre-dates the onset of organic sedimentation (between 15.3 ± 0.2 and 15.1 ± 0.2 cal ka BP) at Lago Augusta in the Chacabuco valley (Villa-Martinez, et al., 2012).

Stage 4: Failure of the Barrancos spillway (~445–470 m asl) ice-dam enabled Atlantic-Pacific drainage reversal from the southern basin. This event occurred after the 15.3 ± 0.2 to 15.1 ± 0.2 cal ka BP shift from glaciolacustrine to organic sedimentation at Lago Augusta (Figure 4.12), which Villa-Martinez et al. (2012) interpret as a lake level fall below ~450 m asl. The exact drainage pathway to the Pacific, however, remains uncertain, as there is insufficient constraint on glacier configurations in this sector due to inaccessibility, and forested valley sides that conceal landforms. Whether the drainage was subaerial, subglacial or a combination of the two, and whether it followed the Río Baker or Tranquera valleys (Figure 4.10a) cannot be established. Once the ~420 m asl Barrancos col was abandoned (Figure 4.10b), likely by the opening of the upper Baker valley, this Pacific pathway was abandoned as the Bayo level in the southern basin became ice-dammed at the Colonia-Baker confluence (Figure 4.10d).

Our inferred reconstruction for Stages 3-4 is comparable to the simulated ice sheet deglaciation model of Hubbard et al. (2005) for the ACR (14.7–13) time-slice, which predicts a spatial extent of the Soler Glacier that broadly matches our empirical evidence (Figure 4.4a). The model simulates a stable Soler Glacier in the western embayment of LGC–BA (~13.5 ka), which would have prevented lake drainage to the Río Baker valley, while at the same time NPI and MSL ice separated further south, possibly opening a Pacific drainage pathway. We find empirical evidence to support NPI-MSL unzipping across the Juncal Valley, as the planform of moraine ridges indicates NPI retreated westwards across the valley margin (Figure 4.10a).

Stage 5: The opening of the Bayo valley to the north of the NPI (Glasser et al., 2016) triggered abandonment of the Deseado drainage pathway in LGC–BA, and a second drainage reversal event to the Pacific Ocean (Stage 5a, Table S2). This was dated to ~10.5 ka by Glasser et al. (2016) based on a single OSL date to the west of the Bayo spillway. However, CND dates of 13.8 ± 1.0 ka (336 m asl) and 12.2 ± 0.8 ka (317 m asl) (Table S1) from glacial erratics on ice-scoured bedrock east of the col at Lago Tranquilo (Glasser et al., 2006), are reinterpreted in our model as having been shielded by the Bayo lake level. We therefore interpret these dates as an earlier minimum age for the opening of the Bayo drainage pathway and drop of the Deseado level. The oldest OSL ages for Bayo level shorelines date to 11.0 ± 0.7 ka (Glasser et al., 2016). The drainage

reversal via the Bayo valley could have occurred independently of the reversal event in the southern basin (Stage 4), as the opening of the Bayo pathway solely depends on ice-meltwater dynamics in the Bayo and Exploradores valleys, although at present these are poorly understood. The lack of geomorphological (Figure 4.4) or sedimentological (Figure 4.6b) evidence for a Deseado lake level in the Canal and Bertrand valleys of western LGC–BA support this hypothesis, and suggest that the western embayments of LGC–BA were occupied by glacial ice as the lake dropped to the Bayo level. This ice limit (Figure 4.4) has not yet been directly dated, however, this limit must have been attained before the subsequent unification (*Stage 6*) and fall of the Bayo level (*Stage 7*) between ~13–10 ka ago. It is possible that this stillstand occurred during the ACR, consistent with timing of ice lobe readvances elsewhere in Patagonia (Moreno et al., 2009; Strelin et al., 2011), but requires confirmation.

Stage 6: Sometime after the drop to the Bayo lake level, unification occurs as the northern and southern basins are joined through the Río Baker valley (Turner et al., 2005; Hein et al., 2010), following the retreat of the Soler Glacier.

Stage 7: The lower reaches of the Río Baker valley opened, due to ice-dam failure at an unknown locality, and the Bayo level was abandoned. This occurred between ~13–10 ka ago, based on the inferred water-shielded CND ages of Glasser et al. (2012; Figure 4.13), and the basal radiocarbon ages dates from kettle holes in the Cochrane and Maiten valleys (Turner et al., 2005). The falling Bayo level stabilised behind previously submerged moraines at ~150 m asl in the Colonia valley, at ~210 m asl in LC–P, based on terrace surfaces located upstream of a unconsolidated glacigenic at the LC–P outflow, and at ~260 m asl in LGC–BA, based on the elevation of the lowest lake shorelines (Figure 4.7c and 4.9c).

Stage 8: The moraine dams at the Colonia, LC–P, and LGC–BA outflows failed, and caused GLOFs to pass down the Cochrane and Baker valleys. The final flood event, likely from LGC–BA based on its more developed shorelines, occurred prior to the minimum age of 7.8 ± 0.5 ka for the loess deposit that caps slackwater flood deposits in the Nef-Chacabuco reach of the Río Baker valley (Figure 4.9).

4.4.6 Implications for regional glacial geomorphology

4.4.6.1 Evaluating the timing for NPI re-advance

Our interpretation of lake water shielding of many morainic boulders used for CND dating of former ice-margin limits (Figure 4.13; section 4.4.4), suggests that the model of NPI re-advance at the time of the Northern Hemisphere Younger Dryas (cf. Glasser et al.,

2012) can be re-evaluated. Glasser et al. (2012) cited the existence of palaeolakes as a rationale for dating boulders from a high elevation lateral moraine in the Nef Valley. These samples from >1100 m asl have a mean age of 11.03 ka (all ± 0.5 ka), although, to date there is limited geomorphological mapping from this site to demonstrate possible relationships to down-valley ice-marginal limits. This is relevant because Glasser et al. (2016) link the lateral moraines to the moraine mounds positioned at the Chacabuco-Baker confluence, whereas our geomorphological (shoreline) evidence favours the retreat of the Nef Glacier towards the Nef Valley mouth while the sub-Caracoles lake level was still in existence, prior to the 15.3 ± 0.2 to 15.1 ± 0.2 cal ka BP lake level drop recorded at Lago Augusta (Villa-Martinez et al., 2012).

In addition, the Nef lateral moraine dates are younger high elevation CND samples (>900 m asl) from lateral moraines of the Colonia Glacier. Nimick et al. (2016) dated the Colonia Glacier re-advance to 13.92 ± 0.95 ka, which coincides with the Southern Hemisphere ACR event (14.7–13.0 ka) that has been shown to exhibit strong cooling south of 40^{0}S (Pedro et al., 2016). Therefore, we argue that the mapped re-advance of several NPI outlet glaciers (Glasser et al., 2012) occurred earlier than the Northern Hemisphere Younger Dryas, and most likely corresponds to the ACR, as demonstrated elsewhere in Patagonia (Moreno et al., 2009; Strelin et al., 2011) and New Zealand (Putnam et al., 2010a).

This hypothesis is further supported by the Lago Augusta record from the Chacabuco valley (Villa-Martinez et al., 2012), where the core stratigraphy supports either lake freezing or deeper inundation between ~15.2–14.2 cal ka BP, following a glacial re-advance; and where pollen evidence has been interpreted to reflect cold and wet conditions between ~13.4–11.8 cal ka BP, followed by a warm pulse with reduced precipitation from ~11.8–9.8 cal ka BP. Nonetheless, support for an early Holocene glacier re-advance may be provided by Nimick et al. (2016) who dated a lateral moraine at the mouth of the Claro valley, a tributary of the Colonia valley (Figure 4.1c), to 11.0 ± 0.47 ka. We note, however, that these samples are from beneath the Bayo lake level, but at present there is no detailed mapping of palaeolake extent in the Colonia valley. The Younger Dryas/ACR glacial re-advance debate therefore needs further testing, but could be achieved by targeting CND samples from above the known lake levels based on our palaeoshoreline analysis (Figure 4.11 and 4.13).

4.4.6.2 The role of topography on ice-meltwater dynamics during deglaciation

As part of our interpretation of palaeolake evolution, we investigated the role of regional relief and topography (section S4 in Appendix). We hypothesise contrasting ice-lake

dynamics in the northern (LGC–BA) and southern (LC–P) basins due to differences in bed topography. Our data provide evidence for reverse bed gradients in the southern basin, with the steepest gradient observed in the Chacabuco valley, which slopes westwards from an elevation of ~620 m asl at the Rodolfo col, to ~70 m asl at Valle Grande in the Tamango basin (Figures S8d and S8e, in Appendix). Once the Nef and Colonia glaciers retreated into the Río Baker valley from the Chacabuco-Baker confluence moraines (Figure 4.4b), lake depth at the ~460 m level (Figure 4.4) would have increased to >300 m in the Nef valley, and to ~400 m in Valle Grande. The implications for ice dynamics in the Tamango basin may have included: (a) increased rates of hydrofracturing in the snout zone (Pollard et al., 2015); (b) enhanced subglacial melting due to reverse bed gradients (Mouginot et al., 2015); and (c) enhanced ice-margin flotation and calving (Boyce et al., 2007). Together these processes may have acted to enhance ice-margin retreat rates in the southern basin. In contrast, our geomorphological mapping in the western embayment of LGC–BA (Chapter 3; Figure 4.4) provides evidence for ice-margin stabilisation at topographic pinning-points, i.e. the narrow and shallow valleys that surround the modern LGC–BA outflow.

Further south, we identify the Juncal Valley as a likely zone of weakness during the unzipping of NPI and MSL ice (Figure 4.10a), when topographic controls likely began to exert greater influence on ice-meltwater dynamics. In the southern sectors of the study area, the Juncal Valley would have likely been the first zone to become starved of ice, from both NPI and MSL sources, because of its relief and orientation in relation to the major outflow valleys (Figure 4.10a). Once the Colonia Glacier had retreated into Valle Grande, and started to separate from MSL ice (Figure 4.7a), lake water at the ~460 m level (Soler) would have encroached southwards into the Juncal Valley and, eventually, to the Barrancos spillway (Figure 4.10b), where collapse of the ice-margin allowed water to drain into the lower Río Baker catchment.

4.4.7 Future research framework

The data presented in this study provide a framework for further geomorphological and geochronological research into the dynamics and timing of ice-sheet and palaeolake evolution in the NPI region. The identification of new lake levels (Figure 4.11), and the possibility of separate lakes in the northern (LGC–BA) and southern (LC–P) basins prior to the ~300–350 m asl Bayo level, highlights the need for additional chronological data. The Lago Augusta record in the Chacabuco valley (Villa-Martinez et al., 2012) demonstrates the potential of lake basin sediment cores for dating the timing lake level falls. Using the new isostatic shoreline data presented in this study, lake basins and kettle

holes (cf. Turner et al., 2005) can be systematically targeted for radiocarbon dating. Moreover, advances in regional tephrochronology (Weller et al., 2015; Alloway et al., 2017) may help to refine palaeolake chronologies. A significant advantage of this lake basin approach is that basin stratigraphy could be used to systematically test for possible lake transgressions (Villa-Martinez et al., 2012) that may have occurred during the ACR, for example, but at present remain unresolved. One specific target is to better constrain the timing of the unified Bayo lake level fall, as this involved release of the largest volume of freshwater through the lower Río Baker to the Pacific, likely influencing regional ocean circulation (Glasser et al., 2016). Similarly, further testing of the magnitude and timing of regional freshwater forcing events is needed, because multiple drainage events likely occurred in the period ~15.5–7.8 ka.

5. Conclusions

The NPI sector (46–48°S) of the former PIS is an important region for understanding mid-latitude glacial response to Southern Hemisphere climate change through the late Quaternary, driven, for example, by migration of the southern westerly winds (Boex et al., 2013) or freshwater forcing (Glasser et al., 2016). Here, we demonstrate that despite the wide application of advanced geochronological techniques in the region, the underpinning geomorphological framework is more complex than previously considered. In this paper, we have evaluated published geochronological datasets alongside new geomorphological data, which includes the first systematic assessment of regional isostatic adjustments. This has led us to propose a new palaeolake evolution model with two Atlantic-Pacific drainage reversal events. We summarise our main findings below.

1) Our palaeoshoreline analysis (Figure 4.11) provides the first systematic regional data on west-east aligned isostatic adjustment. The data indicates that the two main lake levels in LGC–BA (Deseado and Bayo) have similar warping, whilst the three main lake levels in LC–P (Caracoles, Soler and Bayo) show a progressive decline in slope gradient.
2) The digital shoreline analysis has identified previously unmapped palaeolake levels, for example, the Sub-Caracoles level(s) in LC–P and Chacabuco (Figure 4.11). Field mapping of a ~460 m asl shoreline over much of the southern basin provides further empirical evidence for at least one Sub-Caracoles level that we term the Soler level. We identified two new drainage pathways associated with this lake level: first into LGC–BA around the margins of the Soler Glacier; and second via the Río Baker, after the unzipping of NPI and MSL ice led to the collapse of a glacier margin at the Barrancos col. This second event likely

represents the first Atlantic-Pacific drainage reversal, and occurred shortly after ~15.3–15.1 cal ka BP, also demonstrating that LGC–BA and LC–P lakes need not be unified at the upper (~400–450 m asl) Deseado level.

3) Our shoreline data confirms the Bayo valley drainage pathway to the Pacific Ocean, along the northern boundary of the NPI (Glasser et al., 2016; Martinod et al., 2016). The relative chronology of our lake model, and our reinterpretation of available CND ages, suggest that this route functioned between ~15.3–15.1 cal ka BP (the timing of the first Atlantic-Pacific reversal event) and ~13.0–10.0 ka, when the Bayo lake level was abandoned.
4) Our datasets do not lend support to the model of regional NPI glacier re-advance during the Northern Hemisphere Younger Dryas and early Holocene periods (Glasser et al., 2012). Instead, isostatic shoreline data suggest that most CND ages from boulders related to this re-advance were shielded by lake water, and more likely date the fall of the Bayo lake level. As such, there is limited empirical evidence for a glacier re-advance at that time in the NPI region, and it is more likely that this occurred during the ACR, as dated by Nimick et al. (2016) and modelled by Hubbard et al. (2005).
5) We find geomorphological evidence for at least two large magnitude GLOFs, one sourced from LC–P, and the second from LGC–BA. These events had occurred before 7.8 ± 0.5 ka, and suggest that both valley experienced a final moraine-dammed lake stage, following the drainage of the ice-dammed Bayo lake level.

Chapter 5. High-resolution chronology for deglaciation of the Patagonian Ice Sheet at Lago Buenos Aires (46.5°S) derived from varve chronology and Bayesian age modelling

Bendle, J.M., Palmer, A.P., Thorndycraft, V.R., Matthews, I.P. 2017. High-resolution chronology for deglaciation of the Patagonian Ice Sheet at Lago Buenos Aires (46.5°S) revealed through varve chronology and Bayesian age modelling. Quaternary Science Reviews, 177, 314—339.

Abstract

Glaciolacustrine varves offer the potential to construct continuous, annually-resolved chronologies for ice-sheet deglaciation, and improved understanding of glacial retreat dynamics. This paper investigates laminated glaciolacustrine sediments deposited around the waning margins of the Patagonian Ice Sheet, following the local Last Glacial Maximum (LGM). Detailed macro- and microfacies analyses, confirm an annual (varve) structure within these sediments. The correlation of annual layers (varves) across five sites in eastern Lago General Carrera–Buenos Aires (LGC–BA) yields a 994 ± 36 varve-year (vyr) chronology and thickness record. The floating chronology has been anchored to the calendar-year timescale through identification of the Ho tephra (17,378 ± 118 cal a BP) in the varve sequences. Using a Bayesian age model to integrate the new varve chronology with published moraine ages, the onset of deglaciation at 46.5°S is dated to 18,086 ± 214 cal a BP. New age estimates for deglacial events are combined with high-resolution analysis of varve thickness trends, and new lithostratigraphic data on ice-margin position(s), to reconstruct ice-margin retreat rates for the earliest ca. 1000 years of ice-sheet demise. Glacier retreat rates were moderate (5.3–10.3 m yr^{-1}) until 17,322 ± 115 cal a BP, but subsequently accelerated (15.42–17.99 m yr^{-1}). Sustained influxes of ice-rafted debris (IRD) after 17,145 ± 122 cal a BP suggest retreat rates were enhanced by calving after ice contracted into deeper lake waters. Ice persisted in eastern LGC–BA until at least 16,934 ± 116 cal a BP, after which the ice lobe started to retreat towards the Patagonian mountains.

5.1 Introduction

Understanding the dynamics and rates of ice sheet deglaciation, and potential sensitivities to climatic changes, necessitates the development of accurate and precise chronologies. In southern South America, efforts to characterise past fluctuations of the Patagonian Ice Sheet have focused on cosmogenic nuclide exposure dating of moraine boulders (e.g. Glasser et al., 2012; Moreno et al., 2012; Boex et al., 2013) and luminescence dating of outwash sands (e.g. Smedley et al., 2016). This approach has allowed the advance-retreat history of many former ice lobes to be established across multiple glacial cycles (e.g. Kaplan et al., 2004, 2005; Darvill et al., 2015; Hein et al., 2009, 2011 2017). However, the moraine record can be incomplete, and is biased towards episodes of relative glacier stability (i.e. moraine construction) that may lead to a fragmentary picture of former ice lobe behaviour. In Patagonia, this problem is exacerbated by the existence of large lakes in the valleys of many former ice lobes, under which some ice-marginal features (e.g. moraines) are likely to be concealed. Moreover, the ages derived from such techniques are typically associated with around ±10% uncertainties that preclude the investigation of short-term (≤millennial-scale) glaciological changes (Balco, 2011).

Varved sediment sequences offer the possibility of developing annually-resolved chronologies that enable precise estimations of the rate and duration of glaciological and climatic events (e.g. Palmer et al., 2008a, 2010; MacLeod et al., 2011). Varved sediment records covering the last deglacial cycle already exist in Scandinavia (e.g. De Geer, 1912, 1940; Stromberg, 1989; Wohlfarth et al., 1997) and North America (e.g. Antevs, 1922, 1928; Breckenridge, 2007; Breckenridge et al., 2012; Ridge et al., 2012) and provide information about ice-marginal processes and glacial dynamics at annual resolution with only minor breaks. More recently, the complementary use of tephrochronology as a means of anchoring floating varve chronologies to the absolute calendar-year timescale has provided greater dating precision for palaeoenvironmental events (e.g. Brauer et al., 2008; Neugebauer et al., 2012), and facilitates direct comparisons with other high-resolution climate records (e.g. ice-cores) at the hemispheric scale (e.g. Lane et al., 2013). Such records are rare in glacial settings (e.g. MacLeod et al., 2014, 2015) but offer great potential to refine the chronologies of ice lobe fluctuation during deglaciation and provide a link between ice sheet dynamics and climate.

Laminated glaciolacustrine sediments accumulated in proglacial lakes that formed as major ice lobes of the Patagonian Ice Sheet retreated from their local Last Glacial

Maximum (LGM) positions (Caldenius, 1932). At some locations, these deposits are interpreted as varves, but no direct investigations have been undertaken since Caldenius (1932), despite: (1) the potential of varved sediments to refine existing models of ice sheet dynamics, through chronological constraint on the rates of ice lobe advance/retreat (e.g. Ridge et al., 2012); (2) improved understanding of limnological and depositional processes within proglacial lakes (e.g. Gustavson, 1975; Smith and Ashley, 1985; Carrivick and Tweed, 2013); (3) new technologies (e.g. thin sections) that enable detailed micro-sedimentological inspections and robust counting of very thin annual layers (Ojaja et al., 2012); and (4) the growing integration of independent dating techniques, such as radiocarbon dating and tephrochronology, to produce continuous, time-anchored chronologies that allow the timing and duration of glacier and/or lake existence to be tested (e.g. MacLeod et al., 2011). Consequently, it is now possible to generate robust palaeoglaciological reconstructions through detailed analyses of glaciolacustrine varves.

This paper produces a new glacial varve chronology through investigations of laminated glaciolacustrine sediments from the Río Fenix Chico valley (46.58°S, 71.07°W) at the eastern end of Lago General Carrera–Buenos Aires (LGC–BA), first suggested to represent varves by Caldenius (1932). The varve chronology is constructed through analyses of the laminated sediment structures and measurements of varve thickness, which are used to constrain changes in ice-margin position. Subsequently, the floating varve chronology is anchored to the calendar-year timescale using tephrochronology, and through the development of a Bayesian age model, which integrates (i) the new, absolutely-dated varve chronology; with (ii) published ages for moraine deposition; (iii) and new morphostratigraphic data on the relative sequence of ice-margin contraction, the paper explores the chronology and dynamics of ice lobe retreat through the earliest stages of deglaciation.

5.2 Regional context and background

5.2.1 Site location and geological context

The Río Fenix Chico valley lies at the eastern limit of the LGC–BA basin, east of the Patagonian mountain front (Figure 5.1). The major contemporary feature of the region is the North Patagonian Icefield (NPI) that sits astride the north-south trending ridge of the Patagonian Andes. The area surrounding the NPI displays numerous deep, geologically controlled fjords and valleys (Glasser and Ghiglione, 2009). The most prominent valley is a broadly west-east trending depression occupied by the transnational lake: Lago

General Carrera (Chile)–Buenos Aires (Argentina), which has a maximum depth of ~600 m (Murdie et al., 1999).

The LGC–BA basin lies ~200 km east of the Chile Triple Junction, the convergence point of the Antarctic, Nazca and South American plates, and marks the division point between the Southern Volcanic Zone (SVZ), north of ~45.5°S, and the Austral Volcanic Zone (AVZ) that extends southwards into Tierra del Fuego. At this location, subduction of the active Chile ridge produces strike-slip deformation along the Liquiñi-Ofqui fault zone, along which several Quaternary volcanoes are closely aligned (Figure 5.1; Cembrano et al., 1996; Cembrano and Lara, 2009). The nearest active volcanoes of the SVZ are Hudson, Cay, Macá, Mentolat and Melimoyu (Figure 5.1b; Naranjo and Stern, 1998; 2004; Fontijn et al., 2014; 2016). The closest of these, Cerro Hudson, has produced explosive eruptions throughout the late Pleistocene and Holocene, depositing volcanic material in terrestrial (e.g. Haberle and Lumley, 1998; Stern, 2008; Stern et al., 2015, 2016) and marine (Carel et al., 2011) sedimentary sequences. The largest of these was the Ho eruption, dated to 17,340 ± 90 cal a BP (Weller et al., 2014). Thick deposits from this event have been identified ~100 to 225 km north of Lago Buenos Aires (LBA; Figure 5.1b) in small lakes near Coyhaique (Weller et al., 2015; Van Daele et al., 2016) and the Río Cisnes valley (Stern et al., 2015).

5.2.2 Late Quaternary ice lobe and palaeolake context

A major ice lobe of the Patagonian Ice Sheet advanced across the LGC–BA basin periodically throughout the Quaternary. The ice lobe flowed from a regional ice-divide over the Patagonian mountains (Glasser and Jansson, 2005) to the Argentine plateau ~150–200 km further east (Caldenius, 1932; Figure 5.1c). Moraine sequences preserved on the plateau extend from ~1 million years ago to the local Last Glacial Maximum (LGM; Singer et al., 2004; Kaplan et al., 2004, 2005; Douglass et al., 2006). Smaller, cross-valley moraine ridges are identified further west, and provide evidence for glacier stillstands during ice sheet contraction after the LGM (Glasser et al., 2006; 2012; Boex et al., 2013; Chapter 3).

The Río Fenix Chico valley extends broadly east to west from Perito Moreno into LGC–BA (Figure 5.1c). West of the LGM-age Fenix moraine complex, the valley comprises a narrow, steep-sided gorge incised through thick sequences of laminated glaciolacustrine sediment, preserved between ~310–360 m asl. These sediments are banked against the innermost moraine of the Fenix complex, the Fenix I moraine, which has a weighted mean age and standard deviation of 18.7 ± 1.7 ka (calculated using recalibrated ^{10}Be dataset of Kaplan et al., 2011) based on cosmogenic nuclide exposure dating of moraine

boulders (Kaplan et al., 2004; Douglass et al., 2006). The lacustrine deposits started to accumulate as ice retreated from the Fenix I moraine (Caldenius, 1932). ~2 km west of the Fenix I limit, another glacier stillstand deposited the Menucos moraine, only the crest of which outcrops above the lacustrine sediments (Figure 5.1c). This younger limit has weighted mean age of 17.5 ± 1.3 ka (cf. Kaplan et al., 2011).

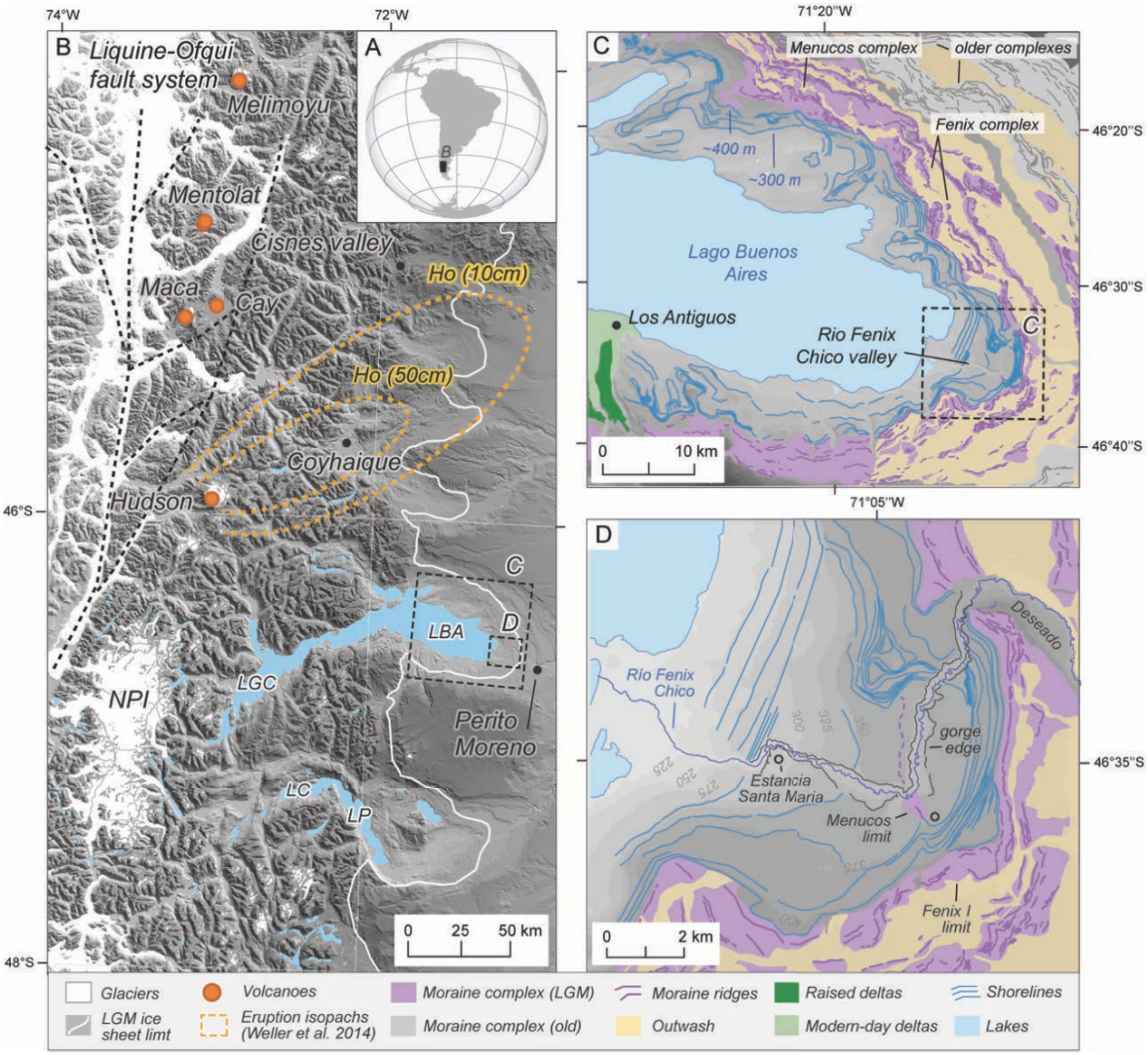

Figure 5.1. Location of the Río Fenix Chico valley and the LGC–BA glacial system. (A) Location of LBA in southern South America. (B) Regional map overlain on SRTM data (Farr et al., 2007) illustrating the extent of the modern North Patagonian Icefield (cf. Pfeffer et al., 2014; 'Randolph Glacier Inventory'), and the extent of the Patagonian Ice Sheet at the local LGM (cf. Singer et al., 2004). Major volcanoes are indicated, along with 50 cm and 10 cm tephra isopachs for the Ho eruption (cf. Weller et al., 2014). (C) Map of the LBA basin with major moraine complexes and shorelines indicated (cf. Chapter 3). (D) Local map of the Río Fenix Chico valley, showing major geomorphological features and the gorge edge. Major moraine systems are labelled. The dashed purple line shows the projected crestline of the Menucos moraine, which is mostly buried beneath lacustrine sediments. The Location of Estancia Santa Maria and Estancia Menucos (unlabelled) are indicated with open black circles.

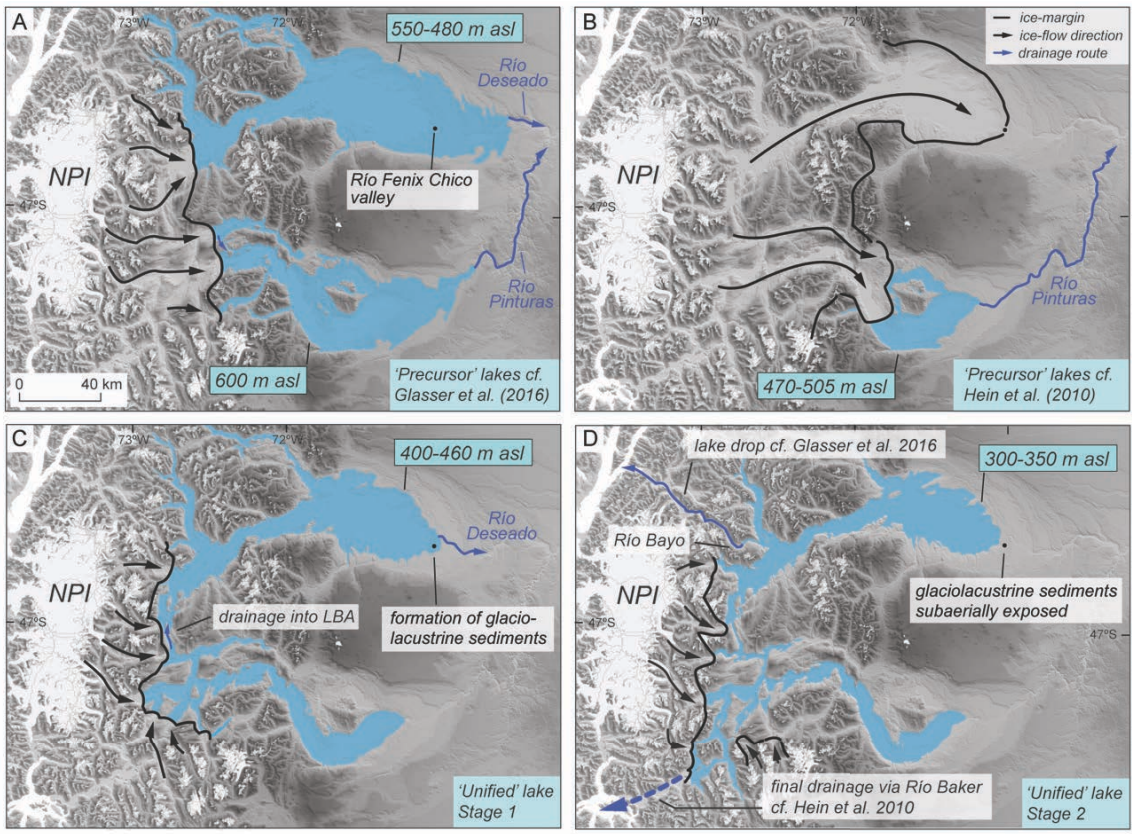

Figure 5.2. Synthesis of the main stages of palaeolake evolution to follow the local LGM based on published models (Turner et al., 2005; Hein et al., 2010; Glasser et al., 2016). The location of the Río Fenix Chico valley is indicated by the filled black circle. Stages (A) and (B) represent competing models for the configuration of precursor lake levels, which existed prior to the unification of lakes between the LBA and Lago Pueyrredón (LP) basins. (A) Glasser et al. (2016) reconstruct a 550–480 m asl lake system in LBA, which overtops the LGM-age Fenix moraine complex, based on the existence of high-level raised deltas in tributary valleys west of the mountain front. (B) Hein et al. (2010) reconstruct a 505–470 m precursor lake system in LP, but no corresponding lake system in LBA, based on the elevation of the highest shorelines east of the mountain front, which are cut into the late LGM-age Fenix I moraine at ~400 m asl. (C) Glacier retreat exposes a linking valley at Lago Bertrand and allows a unified glacial lake system to develop at ~400–460 m asl (Turner et al., 2005; Bell, 2008; Hein et al., 2010). This lake system drained to the Atlantic via the Río Deseado at LBA. The laminated glaciolacustrine sediments were deposited during this lake stage (Caldenius, 1932). (D) Glacier retreat in the Río Bayo valley opens a drainage route to the Pacific Ocean, and causes a lake level drop to 300–350 m asl (Glasser et al., 2016). This drainage reversal represents the likely mechanism for the formation of the Río Fenix Chico gorge, and subaerial exposure of glaciolacustrine sediments. Hein et al. (2010) argue that final lake drainage (dashed blue arrow) to the Pacific occurred at ~12.8 ka (cf. Turner et al., 2005) as the Río Baker valley became ice free.

As ice retreated from the eastern end of the basin, the proglacial LGC–BA expanded, as evidenced by the presence of relict shorelines and raised deltas over ~150 km further west (Turner et al., 2005; Bell, 2008; Glasser et al., 2016). Shoreline mapping has revealed a complex lake history with multiple stages (Figure 5.2; Chapter 3 and 4), the level of the lake(s) being controlled by the position of ice-dams with respect to overflow spillways (Glasser et al., 2016). The glaciolacustrine sediments formed in the Río Fenix

Chico valley are linked to the highest lake levels at the onset of deglaciation. Currently, there are two published models that suggest alternative hypotheses for lake level elevation at that time. Glasser et al. (2016) propose an upper lake level of 480–550 m asl (Figure 5.2a), based on the identification of high-level raised deltas in the western parts of the basin. In contrast, Hein et al. (2010) do not record this lake system at LGC–BA (Figure 5.2b-2c) because their mapping corresponds to the highest shorelines east of the mountain front, which are cut into the Fenix I moraine at ~400 m asl. The reconstruction of Hein et al. (2010) supports the earlier mapping of Turner et al. (2005), who defined a 'united' glacial lake system at this stage, which drained to the Atlantic Ocean via the Río Deseado (Figure 5.2c). This lake eventually dropped to 300–350 m asl as the Río Bayo valley became ice-free and enabled a westwards diversion of meltwater to the Pacific Ocean (Figure 5.2d; Glasser et al., 2016). The consequent change in base level provides the obvious trigger for the incision of glaciolacustrine sediments and their exposure in cliff sections in the Río Fenix Chico valley. These sediments therefore record the earliest phases of ice lobe recession, following protracted stabilisation throughout the local LGM (Kaplan et al., 2004; Douglass et al., 2006), and thus offer insight into the dynamics of Patagonian Ice Sheet ice lobes and palaeolakes during this interval.

5.2.3 Previous reports of laminated lacustrine sediments

Laminated glaciolacustrine sediment sequences (Figure 5.3) were first discovered by Caldenius (1932) in the Río Fenix Chico valley. These laminations were interpreted as varves due to their regular, alternating silt and clay layers. Caldenius (1932) also recorded 'catastrophic' varves, described as anomalously thick laminations of coarser (sand) grade sediment and interpreted as the product of extreme fluvial discharges. Caldenius (1932) counted and measured a total of 500 varves from two sites, and estimated the existence of a further 257 varves of millimetre-scale thickness, which he was unable to measure. Further work on these structures has been limited. Sylwan (1989) counted a sequence of 887 varves as part of a study into the magnetic polarity and relative age of glacial deposits east of LGC–BA. Furthermore, Sylwan (1989), and later Kaplan et al. (2004), sampled carbonate-cemented concretions found within the laminated deposits for radiocarbon dating, and reported ages of 15.0 ± 0.2 cal ka BP to 16.5 ± 0.5 cal ka BP. However, the depositional origin of the carbonate concretions is unknown, and no corrections were applied for potential reservoir effects associated with 'old' carbon in catchment. The accuracy of the ^{14}C ages should therefore be taken with caution, and an exact age for the lacustrine sequences has yet to be established.

5.3. Methods

5.3.1 Stratigraphic logging and selection of laminated sequences

Stratigraphic logging was undertaken to characterise the types and distribution of glacigenic sedimentary facies, and provide context for the formation of laminated glaciolacustrine sediments. Stratigraphic logs were constructed from cliff exposures along a transect that follows the modern Río Fenix Chico. Information on grain-size, sorting, sedimentary structures, deformation structures, bed thickness and geometry, and bed contacts, was recorded to characterise lithofacies units (Evans and Benn, 2004). Outcrops situated between the stratigraphic logging sites were also examined to understand lateral patterns of sedimentation and to establish robust connections between logs. In total, five laminated sequences, of ~15–35 m thick, were chosen for detailed examination and named FC-B, FC-C/D, FC-E, FC-F and FC-F1 (Figure 5.3). These sites were chosen as they (i) characterised changes in lamination facies across the basin; (ii) avoided localised zones of rotational slumping; and (iii) contained common marker layers with distinctive sedimentological properties to allow correlation between sites.

5.3.2 Sedimentological analysis of laminated sediments

Laminated sediments were described at the macro- and micro-scale to evaluate a potential varve origin at the five sites. Macroscale descriptions focused on particle-size, sorting, structure, and the nature of contacts between laminations. Specific attention was given to the overall structure of laminated couplets, especially the stratigraphic arrangement of very fine structures within the coarse (silt) layers. When the sedimentary structures were too fine to discriminate accurately, microscopic analyses of thin sections were undertaken (Brauer, 2004). Single samples were selected based on facies changes observed at the macroscale, whilst continuous overlapping samples were taken from the uppermost 48.05 cm at FC-E to undertake analyses of very thin (<1 cm-scale) couplets at this location.

Thin sections were prepared using standard protocols (Palmer et al., 2008b) and examined using a Leica™ M205-C petrological microscope at magnifications of 0.78x to 16x. The couplets were described using a microfacies approach, where individual laminations are classified according to their internal sediment characteristics (e.g. Brauer 2004; Palmer et al., 2010, 2012). The discrimination of various lamination types was based on differences in particle-size, texture, sorting, structure (e.g. massive or sub-laminated), the presence of irregular structures (e.g. load deformation) and the nature of contacts between laminations, which could only be discerned at the microscale.

The particle-size characteristics of component layers and/or sub-layers was determined using a Malvern Mastersizer 2000 laser diffraction system with a Hydro MU sampler. Prior to analysis, samples were mixed with 0.5% sodium hexametaphosphate and placed within an ultrasonic bath for 30 seconds to ensure complete disaggregation of particles.

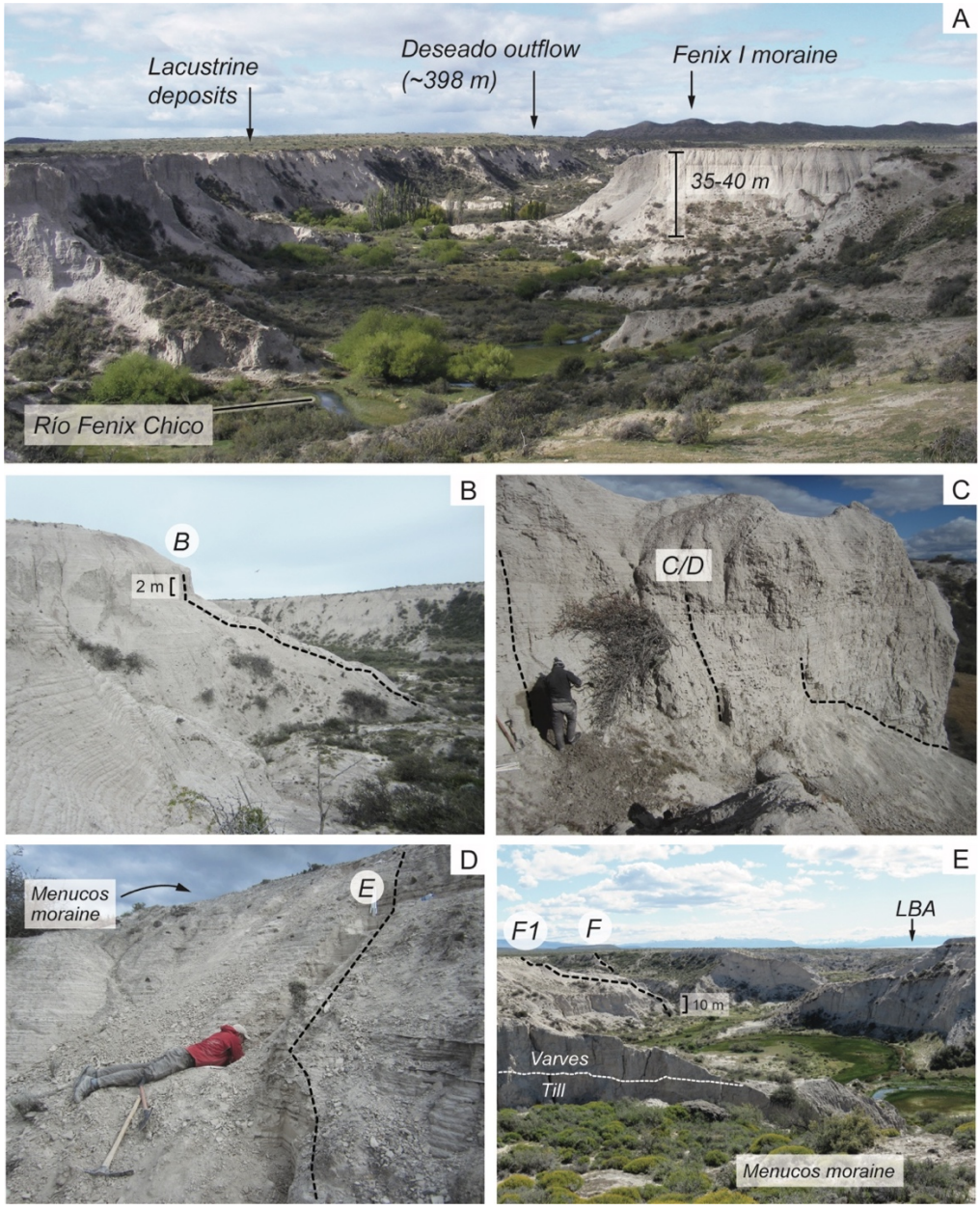

Figure 5.3. Field photos of studied sites in the Río Fenix Chico valley. (A) View north-east along the Río Fenix Chico gorge, taken from the Menucos moraine, with examples of cliff sections through laminated glaciolacustrine deposits. The Fenix I moraine and Deseado outflow site are indicated, ~2 km further east. (B) Laminated sequences at site FC-B. View south-west along the Río Fenix Chico gorge. (C) Laminated sequences at site FC-C/D. View to the south-west. (D) Laminated sequences at site FC-E, on the ice-distal flank of the Menucos moraine ridge. View to the west. (E) Laminated sequences at site FC-F and FC-F1 <0.5 km west of the Menucos moraine. Foreground shows contact between Menucos moraine and overlying laminated sediments. View to the west along Río Fenix Chico gorge with present-day LGC–BA in distance (~9 km).

5.3.3 Counting and measurement of laminated sediments

Measurements of lamination thickness were carried out in the field or from thin sections according to layer thickness and visual distinctiveness, after (micro)sedimentological analyses favoured the interpretation of glaciolacustrine couplets as annually-layered (section 5.4.2). To evaluate possible counting uncertainties two counts were generated at each site, which were undertaken by different analysts.

85.35% of laminated couplets were ≥1 cm thick and the limits of coarse/fine laminations were marked directly on tapes from cleaned sediment surfaces. The lamination thicknesses were measured under laboratory conditions at an accuracy of ~1 mm (e.g. De Geer, 1912; Hang, 2003; Ringberg et al., 2003; Hyttinen et al., 2011). Sampling for continuous overlapping thin sections was not necessary because: (i) macroscopic measurements were only performed for couplets ≥1 cm thickness, whilst a varve thickness of 0.5 cm is recommended as a threshold for microscale analysis (Ojala et al., 2012); (ii) the couplets have been naturally semi-dried, which has enhanced the visual distinction of coarse (silt) and fine (clay) laminations; and (iii) the sequences contained frequent marker layers that enabled robust comparisons during the counting procedure, and the avoidance of local disturbances (e.g. slumps) or irregularities (e.g. pinching out).

For the analysis of thin sections, initial inspections were made on a light table to verify the overlaps between slides and to identify prominent marker layers. Measurements were carried out between marker layers, and enabled robust comparisons of repeat counts (Lamoureux and Bradley, 1996; Lamoureux, 2001). Thin sections were analysed under plane- and cross-polarised light, with the definition of couplet boundaries based on detailed microfacies descriptions (e.g. Palmer et al., 2012). Counts were made along a single vertical transect of each thin section. Digital images were captured using a Pixera 600es camera and laminations measured within the Image-Pro Express software package.

5.3.4 Tephra analysis

The detection of a visible tephra layer in the laminated sequences offers the potential for inter-site correlations and absolute dating. Tephra was sub-sampled in the field for analyses of its chemical composition to determine potential volcanic sources. For major element analyses, each sample was sieved at 125–15 μm and an optimum fraction extracted using sodium polytungstate (SPT) at 2.55 g cm^{-3} density (Blockley et al., 2005). A portion of each extraction was examined using a high-powered polarising microscope to evaluate glass content and characterise shard morphology, and subsequently mounted into a probe stub using Specifix 40 epoxy resin. The shards were hand polished

using a 0.10 μm Al_2O_3 paste to create sections through shard surfaces for chemical analysis. Plugs were cleaned in an ultrasonic bath before carbon coating. Major element analyses were obtained for 195 individual glass shards using a Cameca-SX100 WDS-EPMA at the Tephra Analytical Unit, University of Edinburgh. Analyses were undertaken using a beam diameter of 5 µm and at 15 keV; a 2 nA beam current was employed for Na, Al, Si, Fe, K, Ca, Mg and a 80 nA beam current for Mn, Cl and Ti (Hayward, 2012). The uncertainty on this analysis is <1%. International standards Lipari 1 (rhyolitic) and BCR2G (basaltic) were analysed at regular intervals to monitor for instrument drift.

In addition, five bulk-tephra samples of ~10–12 g were prepared for trace element analyses. Samples were sieved at 15 μm to remove the clay fraction, powdered in a tungsten carbide mill, and pressed into 40 mm pellets. Pellets were analysed using a PANalytical Axios Sequential X-ray Fluorescence Spectrometer at Royal Holloway, University of London. Matrix corrections were applied using the major element chemical dataset obtained using the WDS-EMPA analysis, and Limits of Detection (LoD) were calculated using long-term data collected using the same equipment.

5.4 Sedimentology and stratigraphy

This section focuses on: (i) the stratigraphic architecture of the Río Fenix Chico valley, as a foundation for understanding spatial patterns of sediment deposition, and (ii) the detailed sedimentological properties of laminated glaciolacustrine sediments, to evaluate a varve origin.

5.4.1 Stratigraphy of the Río Fenix Chico valley

5.4.1.1 Lithofacies units

Six principal lithofacies (LF) were recorded in the Río Fenix Chico valley (Table 5.1; Figure 5.4): (1) massive to crudely stratified diamicts, (2) massive to graded tabular sands and channel fills, (3) (sub)horizontally bedded gravels, (4) laminated silts and clays, (5) rippled fine sands and silts, and (6) sorted sands and cobbles.

LF 1 comprises matrix-supported, massive to crudely stratified, clast-poor (~20% to <10%) diamictons. LF 1 is sub-divided into LF 1a, a highly consolidated, clayey-silt diamict with predominantly sub-angular to sub-rounded clasts, and LF 1b, a normally consolidated diamict interbedded with other facies types (e.g. LF 2, LF 3; Figure 5.4a-c). LF 1 sometimes contains contorted sands, silts and clays. Both sub-units of LF 1 are interpreted as glacial diamictons (tills). Additional analysis is needed to ascertain the exact origin of LF 1a, however, its fine-grained, over-consolidated nature; sub-angular to sub-rounded clast forms; and the absence of other interdigitated facies, might support a

subglacial origin (e.g. Evans et al., 2006). In contrast, LF 1b diamicts are interpreted as cohesive to cohesionless debris flow deposits, based on their lateral and vertical inter-layering with stratified sands (LF 2) and gravel (LF 3) facies (Benn, 1996). Localised contorted units provide evidence for glaciotectonic deformation and minor glacier readvance(s) (e.g. Evans et al., 2012, 2013).

LF 2 contains: (i) massive to graded sands in tabular or trough-shaped beds, with decimeter-scale ball and pillow, and water-escape structures (Fig 4d); and (ii) rhythmic tabular beds of graded fine sand with localised fine silt rip-up clasts, draped by horizontally bedded silts containing cm-scale normal and reverse faults (Figure 5.4e). LF 2 occur in units of ~0.2–4.0 m thickness, and are interdigitated amongst LF 1b (Figure 5.4c). LF 2 formed in an ice-proximal subaqueous setting.

Table 5.1. Summary of lithofacies units and interpretation of depositional processes. Lithofacies codes after Evans and Benn (2004).

Lithofacies	Description	Codes	Interpretation	References
LF 1a	Massive to crudely-stratified, matrix-supported, clast-poor diamictons; contains sub-angular to rounded granule to boulder size clasts; clayey-silt matrix; consolidated	Dmm; Dms	Subglacial traction till?	Evans et al. (2006)
LF 1b	Massive to crudely stratified, matrix supported, clast-poor diamicton; contains sub-angular to rounded granule to boulder size clasts; clayey-silt to silty-clay matrix; interdigitated with tabular to trough-shaped lenses of LF 2, LF 3.	Dmm; Dms	Ice-proximal, subaqueous cohesive to cohesionless debris flows (diamicts, gravels) and underflow activity (sands).	Benn (1996); Bennett et al., (2002); Evans et al. 2012, 2013
LF 2	Horizontally-bedded, massive to graded sands; tabular to trough-shaped beds; rhythmic units of massive to graded fine sands (containing silt rip-up intraclasts) and overlying bedded fine to medium silts (with normal and reverse faults); contain ball and pillow, and water escape structures.	Sm, Sm(w), St, Sp, Se, Suf, Suf(w), Sh, Sl	Ice-proximal, subaqueous (hyper)concentrated sediment density currents and turbidity currents (T_{ab} turbidites); meltwater flow confinement produces sand-filled troughs and lenses; rapid sediment aggradation leading to gravitational loading and water escape.	Butrym et al. 1968; Cheel and Rust, 1986; Talling et al. 2012
LF 3	Horizontally- to planar-bedded clast-supported granule gravels or gravels; occur in tabular sheets or trough-shaped lenses.	Gm, Gmi, Gh, Gfu, Gcu, GRch, GRh, GRm	Ice-proximal, subaqueous deposition from hyperconcentrated to concentrated sediment-density flows	Rust and Romaneli, 1975; Mulder and Alexander, 2001;
LF 4	Horizontally bedded rhythmic silts and clays; sporadic dropstones of granule to cobble-size; occasional upwards fining sand beds disturb laminations; localized deformation (folding, faulting, or homogenization) of laminations.	Flv, Flv(d), Suf	Distal lacustrine continuum of ice-proximal sediment-density flows; suspension settling; iceberg rafting and debris release.	Ashley, 1975; Smith and Ashley, 1985
LF 5	Well-sorted fine sands and silts with climbing ripple (Type B) cross-lamination structure.	Sr(B), Frg	Nearshore (littoral) sedimentation from low current velocities and high aggradation rates	Jopling and Walker, 1968; Ashley et al. 1982
LF 6	Sorted fine to medium sands, with pebble-cobble lags; sub-rounded to well-rounded clast forms.	Sm, Suf,	Lake-margin (shoreline) beach sedimentation	Fraser et al. 1991; Thompson and Baedke, 1992

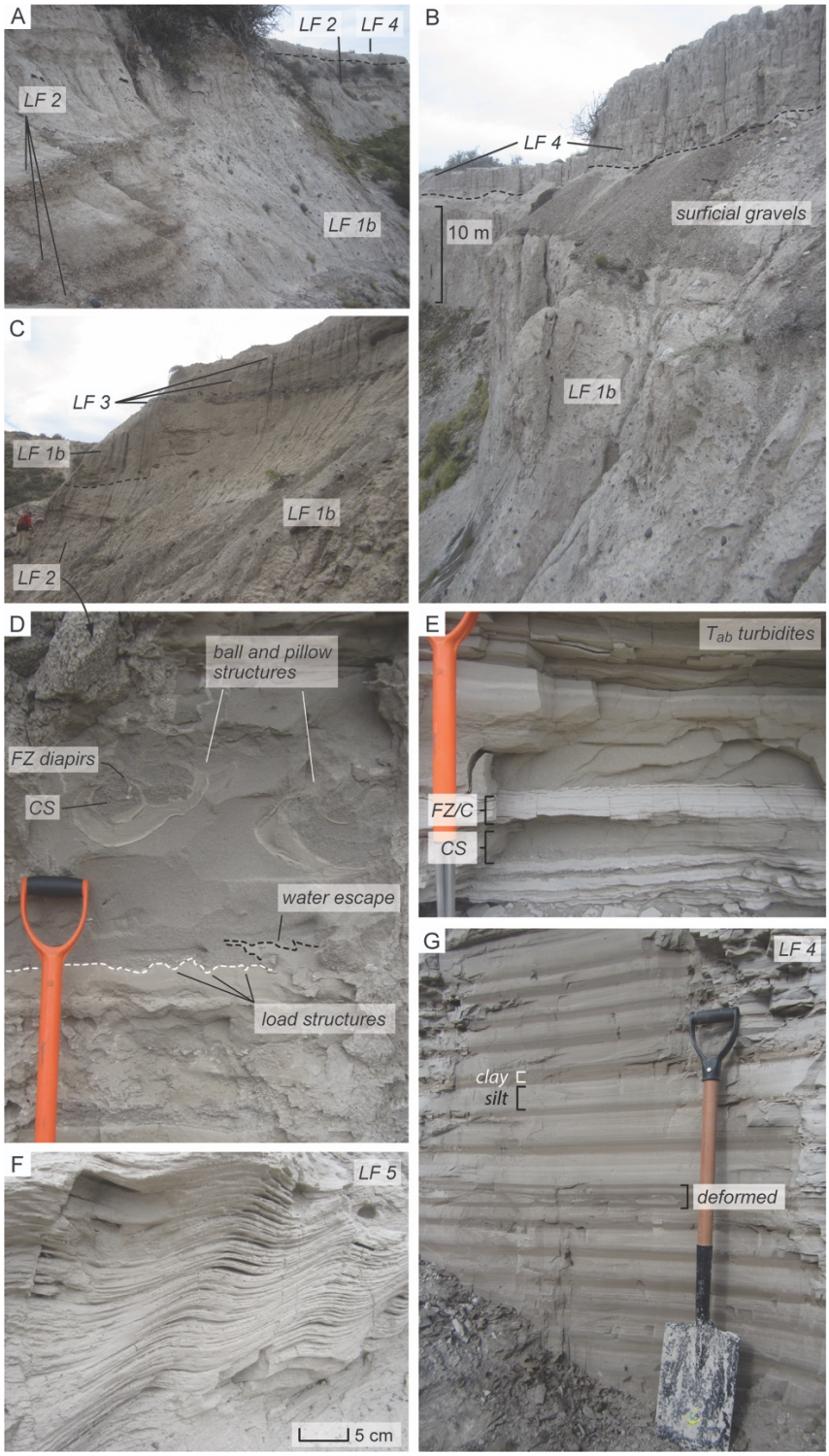

Figure 5.4. Photograph mosaic of main sedimentary lithofacies, structures and facies inter-relationships observed in the Río Fenix Chico valley. (A) Massive, clast-poor diamict (LF 1b) with small-scale granule-filled troughs (LF 2) overlain by laminated silts and clays (LF 4). (B) Massive diamict with local interbedded tabular sands (not shown) overlain by laminated silts and clays. (C) Massive, clast-poor, diamict unit (LF 1b) with interbedded tabular sands (LF 2) and gravel-filled troughs and scours (LF 3). (D) Ball and pillow, load structures, and water escape structures within sand units (LF 2). (E) T_{ab} turbidites (cf. Talling et al., 2012) of coarse-medium sands (*CS*) capped by planar laminated silts (*FZ*) and clays (*C*) that display both extensional and compressive faults. Silt intraclasts occur within coarser sand units. (F) Ripple cross-laminated (Type B) silts and fine sands that cap laminated silts and clays. (G) Laminated silts and clays of decimetre scale, with a localised deformed section.

Tabular fine/medium sand units are interpreted as the product of (hyper)concentrated sediment-density currents (Mulder and Alexander, 2001). Sand-filled troughs result from the confinement of meltwater influxes into discrete channels (Bennett et al., 2002). Ball and pillow structures provide evidence for gravitational loading and dewatering, and suggest rapid aggradation rates (Cheel and Rust, 1986). Rhythmic sand/silt units are interpreted as T_{ab} turbidites, where sands are deposited in high-density turbidity currents, and draped silts the product of waning flow (Talling et al., 2012).

LF 3 comprises clast-supported, massive to (sub)horizontally bedded granule gravel to coarse gravels, often within a medium sand matrix. Clast forms range from sub-rounded to well-rounded. LF 3 occurs in tabular sheets (Figure 5.4c) or trough-shaped lenses (Figure 5.4a) that are interdigitated with LFs 1b-2. LF 3 units range from ~0.5–1.75 m thick, and can be traced laterally over 10's of meters. LF 3 represents the product of ice-proximal meltwater influx in a subaqueous environment. The organisation of LF 3 into (sub)horizontally bedded tabular sheets, or shallow clinoforms, can result from sediment-density flows and/or (hyper)concentrated density flows (Rust and Romanelli, 1975; Mulder and Alexander, 2001; Bennett et al., 2002). Trough-shaped gravel lenses represent infilled channels and scours, and are indicative of fluctuating subaqueous flow directions (Bennett et al., 2002).

LF 4 contains horizontally bedded laminated silts and clays, with localised tabular sand beds and isolated pebble- to cobble-sized clasts (Figure 5.4g). In places, lamination structures are contorted or homogenised. LF 4 result from sediment-density flows (silts) and suspension settling processes (clay) in an ice-distal setting (Ashley, 1975; Smith and Ashley, 1985). Isolated coarse clasts are interpreted as ice-rafted debris (IRD; dropstones; Thomas and Connell, 1984). Further sedimentological classifications of the laminated sediments, which constitutes the major focus of this paper, are given in later sections.

LF 5 comprise tabular units of ripple-bedded to cross-laminated fine sands and silts. Climbing ripple cross-lamination structures are most common (Type B, cf. Ashley et al., 1982; Figure 5.4f). LF 5 is interpreted as the product of nearshore (littoral) subaqueous sedimentation (Fraser et al., 1991). The presence of ripple cross-lamination suggests low current velocities and high aggradation rates in LF 5 (Ashley et al., 1982).

LF 6 contains mixed units of well sorted, massive to graded, medium to coarse sands, and pebble to cobble lags, with sands the dominant facies. Clast forms range from sub-rounded to well-rounded. LF 6 are interpreted as lake-margin (shoreline) beach deposits (Fraser et al., 1991; Thompson and Baedke, 1997).

5.4.1.2 Spatial distribution of lithofacies units

All logged sites are located along a ~15 km east–west transect that drops from ~420 m asl at the crest of the Fenix I moraine (*A'*) to the present-day level of LBA at 200 m asl (*A"*; Figure 5.5). The upper sector of the valley, above ~325 m asl, contains 20-35 m thick sequences of LF 4 (sites FC-B–FC-F1) and a persistent 1-3 m thick cover of LF 5 that crops out between ~355–330 m asl. In this sector, LF 4 occurs in two zones: (i) banked against the Fenix I moraine and extending ~4 km west to the Menucos moraine (site FC-E; Figure 5.5); and (ii) behind the Menucos moraine (sites FC-F/F1) and extending ~1 km west to site L1, where the sequences are thinner (5–10 m; Figure 5.5). LF 1a occurs as a laterally continuous, >30 m thick unit in the middle sector of the valley, between ~8–10 km on *A'–A"*, and crops out at the surface (Figure 5.5). The lower sector of the valley, between ~10–11 km on *A'–A"*, contains 10–30 m thick, cross-valley sequences of interdigitated LF 1b, LF 2 and LF 3 facies, which are overlain by LF 4 units of 2–4 m thickness (Figure 5.4a and 5.4b). Further west, LF 1b is overlain by ~2–3 m thick units of LF 6, which are observed at ~290–260 m asl and coincide with the location of prominent wave-cut shorelines (Figure 5.5).

5.4.1.3 Lithofacies associations and valley lithostratigraphy

Lithofacies associations (LFAs) are assigned according to similarities in depositional environments (Table 5.2). LF 1a reflects direct deposition from glacier ice, probably subglacially, and is classified as LFA 1. Its location suggests deposition either as the ice lobe margin was positioned at the Menucos moraine, or during retreat from this limit. Patterns of lateral and vertical interdigitation suggest that LFs 1b-3 were deposited in the same sedimentary environment, and are grouped into LFA 2. LFA 2 records a phase of ice-proximal subaqueous fan construction involving debris flows (LF 1b; Benn, 1996) and underflow activity (LFs 2–3; Winsemann et al., 2004, 2007; Evans et al., 2013). The location of LFA 2 suggests that a temporary ice-margin stabilisation, or readvance, occurred ~4 km west of the Menucos moraine, at Estancia Santa Maria (Figure 5.5). Glaciolacustrine rhythmites (LF 4) are classified as LFA 3. Rhythmite sequences at sites FC-B, FC-C/D and FC-E (Figure 5.5) most likely started to accumulate as ice retreated from the Fenix I moraine and/or was positioned at the Menucos moraine (Figure 5.5). LFA 3 could have only started to accumulate at FC-F/F1, and subsequently L4-L8 (Figure 5.5), after retreat from the Menucos moraine, and Santa Maria subaqueous fan complex (LFA 2) respectively. LFs 5–6 formed in either a littoral or shoreline environment, and are grouped into LFA 4. The altitudinal distribution of LFA 4 (355–330 and 290–260 m asl) suggests that two major lake-level drops occurred after the deposition of LFA 3.

Table 5.2. Classification of lithofacies units into lithofacies associations (LFAs) and inferred depositional environments.

Lithofacies unit	Lithofacies association	Depositional environment
LF 1a	LFA 1	Subglacial?
LF 1b, LF 2, LF 3	LFA 2	Proximal glaciolacustrine (subaqueous fan)
LF 4	LFA 2	Distal glaciolacustrine
LF 5, LF 6	LFA 4	Nearshore (littoral) and/or lake margin (shoreline)

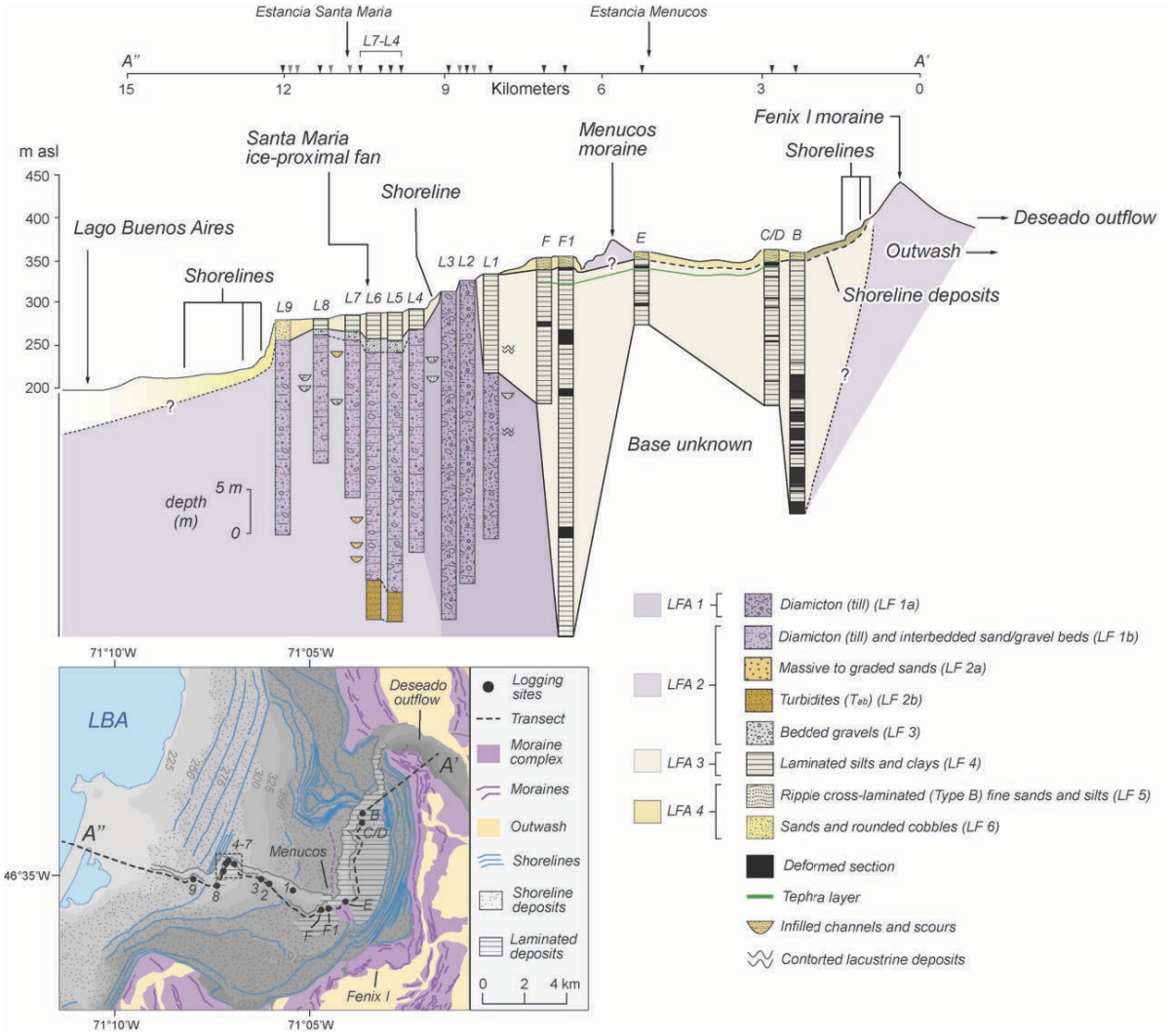

Figure 5.5. Stratigraphic logs of sedimentary deposits and interpretation of basin-wide stratigraphic architecture made through correlation of principal lithofacies types. Inset map shows the location of logged sites along transect A'–A'', the geomorphological context of the valley (cf. Chapter 3), and the distribution of laminated glaciolacustrine deposits. Black arrows on the transect axis show the exact location of logged sites, whilst grey arrows are sites omitted from the final diagram for visual clarity. However, these sites demonstrate equivalent facies profiles to adjacent sequences.

5.4.2 Sedimentology of laminated couplets (LFA 3)

Sedimentological descriptions of the laminated glaciolacustrine couplets (LFA 3) integrates macroscale, microscale and particle size evidence, and is presented for both the ≥cm-scale couplets, and <cm-scale couplets, the latter encompassing the topmost 48.05 cm of the laminated succession at FC-E (Figure 5.6). Regardless of scale, laminated couplets comprise a set of two components: (i) a tan to light-grey coloured coarse component (silt and fine sand); and (ii) an upper, brown to dark-brown coloured fine component (very fine silt to clay), which is typically graded and always sharply truncated by the succeeding coarse component. Further details on the different lamination types and irregular intra-lamination sediment structures are given below.

5.4.2.1 ≥cm scale laminated couplets

Couplets of ≥cm-scale display internally complex coarse component layers that contain multiple graded laminations with sharp basal contacts (Figure 5.6b). These lamination types are pervasive throughout ≥cm scale couplets, and are composed of well-sorted medium or fine silt (Figure 5.6h). Although rare, some silt laminations are capped by a thin (20–70 μm) clay-rich lamina displaying high birefringence. Coarser-grained (fine sand to granule) laminations occur within the regular multi-laminated silt types, and exist at the base, middle or top of the coarse component (Figure 5.6d). These laminations can be well, moderately, or poorly sorted, with sharp contacts. At the macroscale, a darker, clay-rich sediment package is often observed at the base of the coarse component (Figure 5.6a). Microscopic observations show that this package is composed of between 1–6 microlaminations that fine upwards from medium/coarse silt to clayey-silt, and which are well sorted with sharp basal contacts (Figure 5.6c). These laminations display high birefringence under cross-polarised light and low mean particle sizes (Figure 5.6h) that confirm their elevated clay content. Within the clayey-silt package, it is common for the volume of coarse (medium/coarse silt) sediment to increase upwards across 2 or more microlaminations, relative to the volume of fine (clayey-silt) sediment (Figure 5.6c). Where observed, the clayey-silt package is always sharply truncated by overlying coarse (fine/medium silt) units. Intercalated sand layers are identified at the macroscale (≥1 cm and up to 74.5 cm in thickness) and microscale (<1 cm thickness) and are exclusive to coarse component layers (Figure 5.6e). Most sand layers are normally graded from very fine sand to medium silt (Figure 5.6j), although some layers are massive. These layers exhibit sharp (sometimes erosional) contacts to underlying laminations (Figure 5.6e).

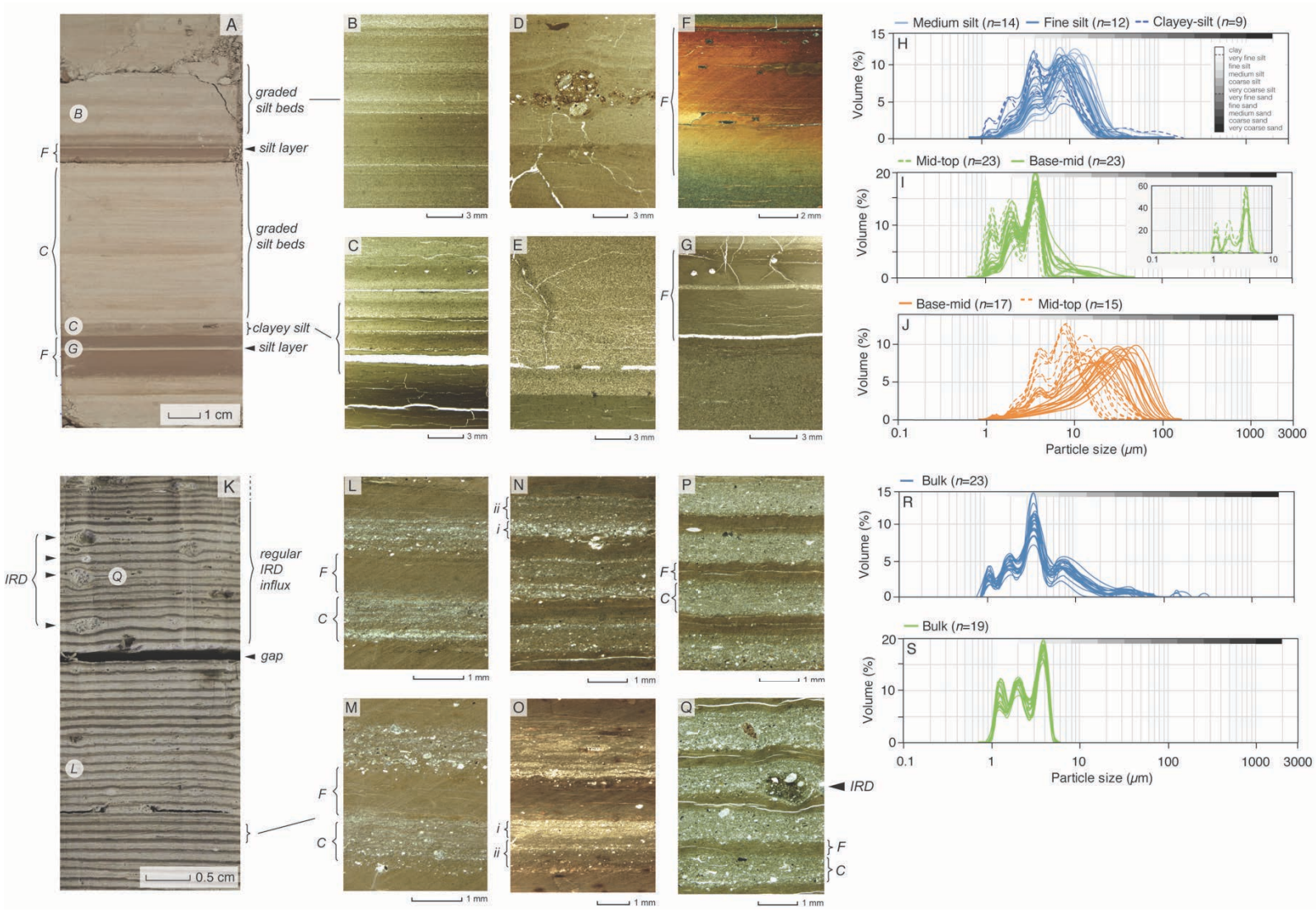
A
B
C
D
E
F
G
H
I
J
K
L
M
N
O
P
Q
R
S
graded silt beds
silt layer
graded silt beds
clayey silt
silt layer
1 cm
3 mm
2 mm
regular IRD influx
gap
IRD
0.5 cm
1 mm
ii
i
Medium silt (n=14)
Fine silt (n=12)
Clayey-silt (n=9)
Mid-top (n=23)
Base-mid (n=23)
Base-mid (n=17)
Mid-top (n=15)
Bulk (n=23)
Bulk (n=19)
Volume (%)
Particle size (μm)
clay
very fine silt
fine silt
medium silt
coarse silt
very coarse silt
very fine sand
fine sand
medium sand
coarse sand
very coarse sand

Figure 5.6. Example of typical varve macro- and microfacies within ≥cm-scale varves (A-G) and <cm-scale varves (K-Q), and supporting particle-size information (H-J and R-S). Letters in (A) and (K) correspond to other photographs. (A) Typical macroscale structures observed within ≥cm-scale varves. Sample from FC-F1 illustrating coarse (melt-season) layers with multiple graded units and normally graded fine (non-melt season) layers. The fine components are overlain by thin (<50 mm) clayey silt sediment packages. Thin (<1 mm) intercalated silt laminations occur within the fine (non-melt season) layers. (B) Graded medium and fine silt units within the coarse (melt-season) component. (C) Package of multiple graded medium silt to fine clayey silt laminations at base of coarse (melt season) layer, overlain by more regular graded silts. Note the upwards decrease in the volume of clayey silt relative to medium/coarse silt across the package. (D) Coarse sand to granule lamination within more regular micrograded silts. (E) Intercalated sand bed within coarse (melt season) component layer grading from fine sand to medium silt (not shown). (F) Typical normally graded fine (non-melt season) component layer with a gradational lower contact to the preceding coarse (melt season) component and a sharp upper contact with the succeeding coarse component. High birefringence relates to the development of masepic fabric, shown under cross-polarised light. (G) Intercalated medium silt lamination within fine (non-melt season) component layer. The silt lamination is massive and displays sharp lower and upper contacts. (K) Typical, finely-laminated structures observed in ≥cm-scale varves. (L-M) Multi-laminated varve types with persistent internal structure. Coarse component layers display alternating medium to coarse silt and fine silt microlaminations with sharp contacts, and can be moderately (L) to poorly sorted (M), the later contains additional fine sand particles. (N-O) Multi-laminated varve types with non-persistent (variable) internal structure. Image (N) shows a basal package of poorly sorted medium silt to fine sand and fine silt microlaminations (i) overlain by a package of alternating medium and fine silt microlaminations (ii). Image (O) shows the reverse of image (N), with a coarser, more poorly sorted microlamination package (i) in the upper coarse (melt season) component. (P-Q) Single lamination varve types. Image (P) shows coarse component layers that are massive, well sorted and composed of medium silt. Image (Q) shows poorly sorted coarse component layers comprising medium silt to medium sand with regular isolated coarse sand to granule-sized grains interpreted as ice-rafted debris.

In ≥cm-scale couplets, the fine component displays a gradational lower contact (Figure 5.6f) and fines upwards from very fine silt at the lamination base, to clay at the lamination top (Figure 5.6i). Under cross-polarised light, these layers display masepic fabrics (Figure 5.6f). On occasion, the fine component will contain thin intercalated silt laminations that are well sorted, massive or graded, with sharp basal contacts (Figure 5.6g).

Other structures observed in ≥cm scale couplets include occasional larger clasts or diamict pellets (cf. Ovenshine, 1970) that penetrate or deform the underlying laminations, and range from gravel to cobble-size when observed at the macroscale. Microscopic observations recorded occasional fine gravel clasts or coarse sand grains within both coarse and fine components. Finally, sediment intraclasts are sometimes observed within the coarse component layer, often immediately above the basal contact.

5.4.2.2 <cm-scale laminated couplets

The coarse component of <cm-scale couplets displays complexity in the arrangement of the very fine structures observed under microscope (Figure 5.6l-q). These can be grouped into three main categories of: (i) multiple (>2) laminations of the same structure, (ii) multiple (>2) laminations with different structures; or (iii) single laminations.

In category (i) the most common types consist of alternating laminations of medium or coarse silt, and fine silt. The laminations typically display moderate (Figure 5.6l) or poor (Figure 5.6m) sorting and sharp contacts. Variations to this regular structure include alternating laminations of well sorted coarse or medium silt, and fine silt. Isolated sand and granule material occurs in some laminations and locally deforms the underlying sediment. In category (ii) the lamination types are comparable to those described in category (i), but differ in terms of their position within the coarse component. The first type displays a basal package of poorly sorted medium silt to fine sand laminations that alternate with fine silt laminations, and is overlain by a package of alternating, well sorted medium and fine silt laminations with sharp to diffuse contacts (Figure 5.6n). This type therefore displays upwards fining across the two microlaminated packages. The second type is essentially a reverse of type one, where the fine lamination package occurs at the base of the coarse component, with the coarse lamination package at the top, and thus coarsens upwards (Figure 5.6o). In category (iii) two lamination types were observed. The first type comprises massive, well sorted medium silt with rare coarse silt grains (Figure 5.6p). The second type comprises poorly sorted medium silt to medium sand with regular isolated coarse sand and granule grains that deform the underlying sediment (Figure 5.6q). Both types exhibit sharp basal contacts to the underlying fine component. Occasional sediment (clay) intraclasts were identified in category (iii) laminations.

Within <cm-scale couplets, the fine component grades upwards from very fine silt at the lamination base to clay at the lamination top (Figure 5.6s), and displays masepic fabric under cross-polarised light. The basal contact to the underlying coarse layer is gradational, whereas the upper contact to the succeeding coarse layer is sharp. Intercalated silt laminations can occur within the fine component, but are very rare and constitute thin (<50 μm wide) layers. Other structures include coarse silt grains that penetrate the upper portions of the fine component and deform the underlying sediment. Moreover, several examples of intercalated 'event' layers were identified in <cm-scale couplets, and include graded sand layers, and coarse, very poorly sorted layers, with numerous sporadic grains >250 μm (medium sand) in size.

5.4.3 Interpretation of varve formation

The structures described above, especially the regular alternation of coarse and fine sediment components, are typical of glaciolacustrine varves observed at the macro- (Ashley, 1975; Smith and Ashley, 1985; Ridge et al., 2012) and microscale (Ringberg and Erlström, 1999; Palmer et al., 2008a, 2010). The coarse (silt/sand) component is deposited during the melt season (spring/summer) as meltwater influxes transport sediment to the lake. The fine (clay) component remains in suspension during the melt season due to the currents within the lake and wind-driven surface currents (Ashley, 1975; Smith and Ashley, 1985). The cessation of glacier melting and the formation of ice-cover at the lake surface allows the finest particles to settle during the non-melt season (autumn/winter). Processes specific to the deposition of certain ≥cm-scale and <cm-scale varve facies are presented below.

5.4.3.1 ≥cm-scale varves

Structures observed within the melt season (coarse) layer, such as multiple graded laminations with sharp (sometimes erosional) contacts (Figure 5.6b), are characteristic of deposition from sediment-laden underflows (Ashley, 1975; Mulder and Alexander, 2001) during peak (summer) melting (Gustavson, 1975; Ridge et al., 2012). The presence of multiple graded laminations reflects the variable nature of underflows entering the basin, or fluctuating sediment concentrations within a quasi-continuous underflow due to, e.g. diurnal melt cycles or changes in meltwater production across the melt season (e.g. Ashley, 1975; Gustavson, 1975). Changes in the velocity of underflows are sufficient to explain occasional influxes of coarse material (sand to granule), whereas the thin clayey-silt laminations that cap some graded silt layers reflect a brief pause in sediment influx (Smith and Ashley, 1985).

The occurrence of clayey-silt laminations at the base of the coarse component (Figure 5.6c) has been recognised previously, in ice-proximal varves, and attributed to low-energy meltwater pulses during the early melt season (Ridge et al., 2012). Under this assumption, the gradual upwards increase (decrease) in the volume of coarser (finer) sediment across the clayey-silt package (Figure 5.6c) might represent gradual increasing discharges over this interval, before an abrupt switch to persistent higher discharges and coarser-grained influxes (Figure 5.6c). Another potential explanation could be that the layers were deposited through local resuspension of clay-sized material as underflows passed across the non-melt season layer, and which subsequently settled after the underflow had waned. Our observations suggest a general (though not complete)

absence of equivalent late melt season clayey-silt laminations, which have been interpreted to reflect waning meltwater discharges towards the end of the melt season (Ridge et al., 2012). Instead, it is common to observe coarse inputs directly below non-melt season (clay) layers. These layers could suggest a rapid transition to quiescent lake conditions at the end of the melt season. Alternatively, these layers could represent single surge events that are more pronounced because the underflow or turbidity current entered a water body of decreased density during the late melt season, after significant settling had already occurred.

Thin silt laminations observed within the non-melt season (clay) layers (Figure 5.6g), described as 'false winters' by Shaw and Archer (1978), likely originate from subaqueous slumps that generated minor turbidity currents or surge deposits. Deformation beneath isolated pebble to cobble-sized clasts reflect an origin as IRD (Thomas and Connell, 1985). The evidence of grading within sand beds (Figure 5.6j) and their sharp (erosional) basal contacts (Figure 5.6e) suggests deposition from sediment-laden turbidity currents (Sturm and Matter, 1978; Mulder and Alexander, 2001). In many cases, sand beds can be traced between sites, where they exhibit proximal-distal thickness relationships. Their occurrence within melt-season layers suggests a source from periodic extreme high discharges that transferred large volumes of sediment from the ice lobe margins across the lake floor.

The structures observed above and the mechanisms of their deposition are typical of glaciolacustrine varves deposited in proximal locations of ice-contact lakes (Ashley, 1975, Smith and Ashley, 1985; Ringberg and Erlström, 1999; Ridge et al., 2012)

5.4.3.2 <cm-scale varves

<cm-scale varves result from multiple sediment influx events during the melt season (Palmer et al., 2008a, 2010, 2012; Livingstone, 2010). The presence of fine, clayey silt between coarser (silt and fine sand) laminations indicates a pause in sediment flux (Smith and Ashley, 1985) and suggests that each coarse lamination relates to a discrete influx of sediment-laden meltwater at a given location (Palmer et al., 2008a, 2010, 2012). The sharp contacts between microlaminations and occasional evidence for erosion (e.g. rip-up clasts) suggests that most of the sediment pulses were transported through the lake as underflows (Mulder and Alexander, 2001). Differences between category (i) and category (ii) lamination types reflect changes in the velocity and persistence of underflows entering the basin that directly influence lamination structure.

In all cases, the sharp contact between the coarse layers and underlying fine layers indicates a rapid switch between melt season and non-melt season sedimentation. Non-

melt season layers were deposited from suspension under quiescent lake conditions (e.g. Ringberg and Erlström, 1999; Palmer et al., 2010). Isolated silt grains within the upper parts of the non-melt season layer are interpreted as aeolian deposits that accumulated on the frozen lake surface during winter, and were released into the water column during early spring melting (Lewis et al., 2002). Isolated coarse sand and granule grains that deform the underlying sediment (Figure 5.6q) represent ice-rafted dropgrains (Thomas and Connell, 1985). The volume of IRD within <cm-scale varves is low, except for the upper 10-20 cm of the varve sequence, in which IRD is abundant (Figure 5.6k). Very poorly sorted, coarse grained layers are deposited when there is sufficient IRD to override the regular melt season microstratigraphy (Devine and Palmer, 2017).

The structures observed above and the mechanisms of their deposition are typical of glaciolacustrine varves deposited in distal locations of ice-contact lakes (Ashley, 1975; Ringberg and Erlström, 1999; Palmer et al., 2008a, 2010).

5.4.4. Tephra analysis

5.4.4.1 Physical description of tephra layer

During the analysis of the varved sequences, a visible green to tan-coloured tephra layer (Fig 5.7a-c) was identified at four of the five investigated sites (no tephra layer was found at FC-B). Where present, the layer ranges from 10.5–13.5 mm thick and consists of multiple fining upwards beds that perhaps reflect pulsed release from meltwater inflows. The thickest bed occurs at the base of the tephra layer, and may represent primary airfall that settled through the water column (Figure 5.7a). Microscopic inspection reveals a diverse range of shard morphologies, including both blocky and elongate shards with abundant stretched and circular vesicles and occasional microlites, as well as isolated mineral grains (Figure 5.7b and 5.7c).

5.4.4.2 Geochemistry of tephra layer

Major element geochemical analyses (data in Appendix) reveal a spectrum of shard chemistries ranging from ~53 to 70 wt % SiO_2, classified as basaltic andesite to rhyolite, with most shards present within the trachy-andesite and trachy-dacite categories (Figure 5.7d). Chemical stratification is not evident in the waterlain tephra. Compared to published datasets, the tephra chemistry falls within the envelope of Cerro Hudson eruptions (Figure 5.7d), rather than the low- to mid-abundance eruptive products of Melimoyu, Mentolat, Maca and Cay, although a definitive correlation cannot be achieved using major elements.

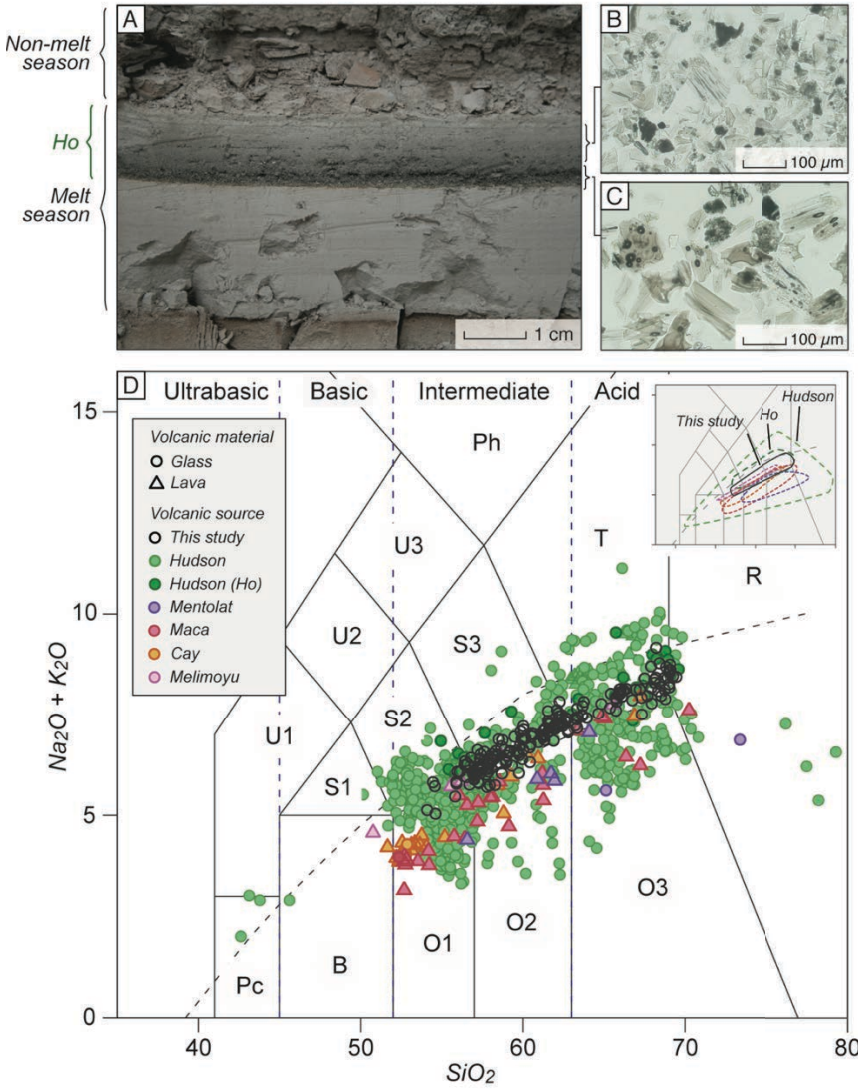

Figure 5.7. (A) Field image of tephra layer (Ho) observed in the upper portion of a melt-season layer at site FC-E. (B) Shard photomicrographs for the lower, coarser-grained portion of the tephra. (C) Shard photomicrographs for the upper, finer-grained portion of the tephra. (D) Total Alkali-Silica (TAS) classification (Le Bas et al., 1986) of major element geochemical compositions obtained for the Río Fenix Chico tephra layer (this study; raw data provided in Appendix) compared with published glass (circles) and lava (triangles) data from the major volcanic sources in central to northern Patagonia (Cay: D'Orazio et al., 2003; Hudson: Haberle and Lumley, 1998; Gutiérrez et al., 2005; Carel et al., 2011; Kratzmann et al., 2009; Van Daele et al. 2016; Macá: D'Orazio et al., 2003; Melimoyu: Naranjo and Stern, 1998; Lopez-Escobar et al., 1993; Mentolat: Lopez-Escobar et al., 1993; Naranjo and Stern, 1998, 2004; Stern et al., 2016).

To establish a potential source eruption, XRF data (this study; Appendix) were compared to available trace element datasets reported in Weller et al. (2014, 2015) and Stern et al. (2015). Before undertaking direct comparisons, a Principal Components Analysis (PCA) was performed to identify elements that explain the maximum amount of variance within the multivariate geochemical dataset. This analysis demonstrates Ba, Sr, Zr, and V to be most influential (Figure 5.8a). Direct comparisons using these key elements suggests a correlation to the Ho tephra (Figure 5.8), originating from the early deglaciation-age Ho

eruption of Cerro Hudson (Weller et al., 2014). Weller et al. (2014) dated the eruption to 17,340 ± 90 cal a BP using radiocarbon measurements of organic remains sampled above ('younger than') and below ('older than') the Ho tephra (cf. Miranda et al., 2013).

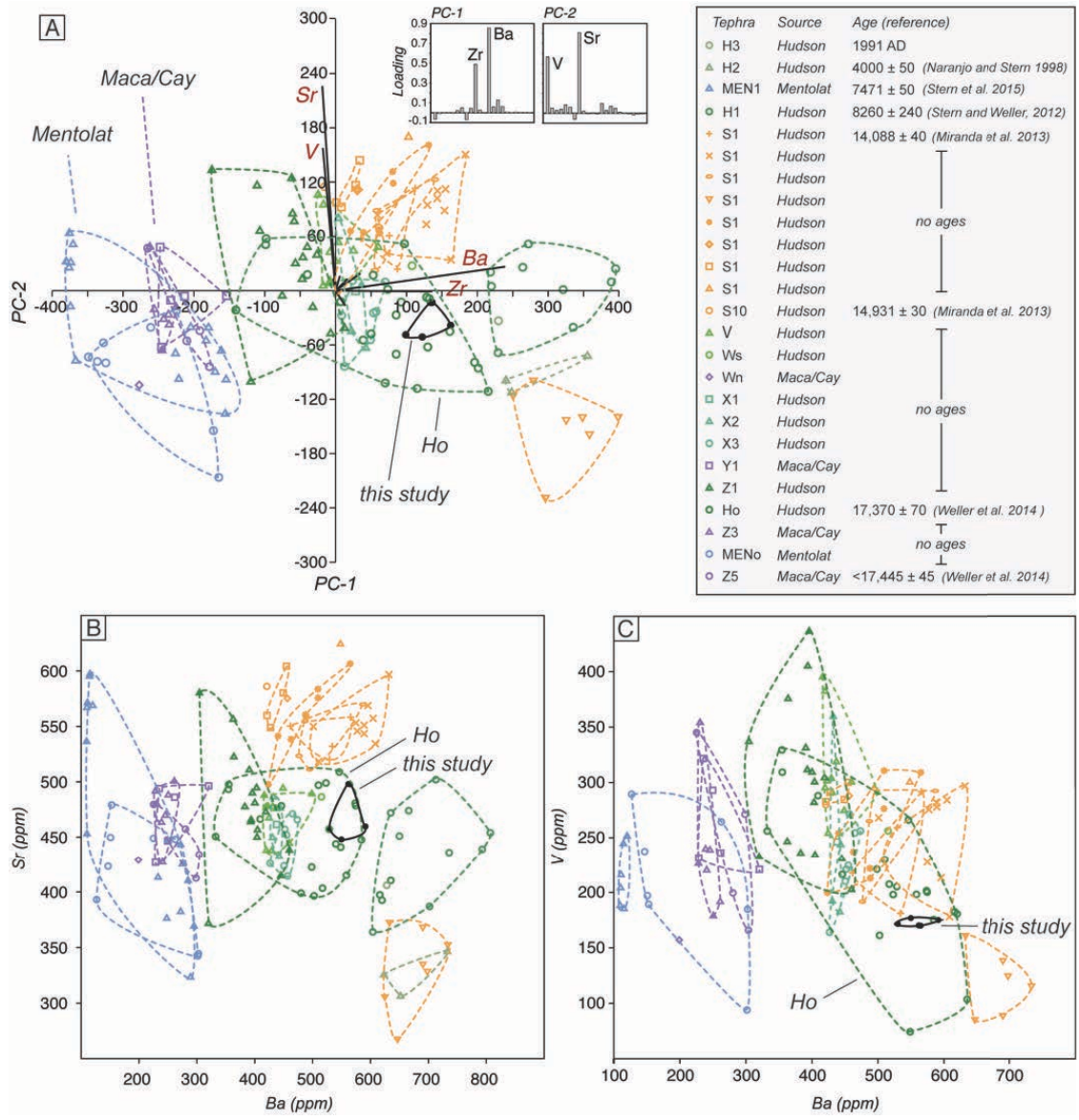

Figure 5.8. (A) Output of Principal Components Analysis (PCA) of trace element compositions of the Río Fenix Chico tephra layer (this study (filled black circles); raw data provided in Appendix) and published data in Weller et al. (2015) and Stern et al. (2015). Inset shows loadings plot. (B) Ba vs. Sr. (C) Ba vs. V. Published trace element data are grouped according to the descriptive tephra zones presented in Weller et al. (2015). Trace element plots reveal consistent correspondence with the Ho tephra layer identified by Weller et al. (2014, 2015).

5.5 Varve chronology

This section develops a continuous varve thickness record and chronology for the Río Fenix Chico valley, based on (micro)sedimentological criteria for the definition of varve boundaries (section 4.2), before analysing the thickness patterns to identify temporal changes in ice lobe extent and retreat dynamics.

5.5.1 Construction of site varve chronologies

Independent site varve chronologies were produced for each investigated varve sequence (Figure 5.9). The site chronologies are termed: the FC-B Site Chronology (FC-BSC17); the FC-C/D Site Chronology (FC-C/DSC17); the FC-E Site Chronology (FC-ESC17); the FC-F Site Chronology (FC-FSC17); and the FC-F1 Site Chronology (FC-F1SC17) in accordance with their position in the valley (Figure 5.5).

Counting discrepancies between the two investigators occur in each sequence around zones of sediment disturbance or vague structure, and consisted of (i) sub-laminations interpreted as two or more varves in one count, but only one varve in the repeat count, and (ii) missing or additional varves in one count associated with disturbed sections. Counting discrepancies were recorded as ±1 year uncertainties to facilitate quantification of counting precision. Following this assessment, site chronologies were produced by averaging varve thickness for each year across the repeat measurement series, and are summarised in Table 5.3.

The Ho tephra layer found in 4/5 of the varve sequences (Figure 5.9) provides an initial basin-wide marker for comparing the site records. The varve thickness records can be divided into (1) a lower section below the Ho tephra (ML6 in Figure 5.9), (2) a middle section between the Ho tephra and a deformed section (ML7 in Figure 5.9) that separates >cm-scale (below) and <cm-scale (above) varves, and (3) an upper section above the deformed layer, which contains <cm-scale varves only. A variable number of varves are recorded in the lower section, owing to the start and end positions of sedimentation at each site. Between 140 (FC-ESC17) and 364 varves (FC-F1SC17) were deposited across five sites (Table 5.4). These are the thickest varves recorded, with average varve thickness ranging from 39.47 mm to 96.99 mm between sites. In all cases, melt-season (silt) layers are thicker than the non-melt season (clay) layers. In the middle section, varves accumulated at sites FC-E, FC-F and FC-F1 (Table 5.4) but not at FC-B and FC-C/D, where the topmost intact varves are overlain by disturbed laminated sections and rippled silts/sands (LFA 4; Figure 5.5).

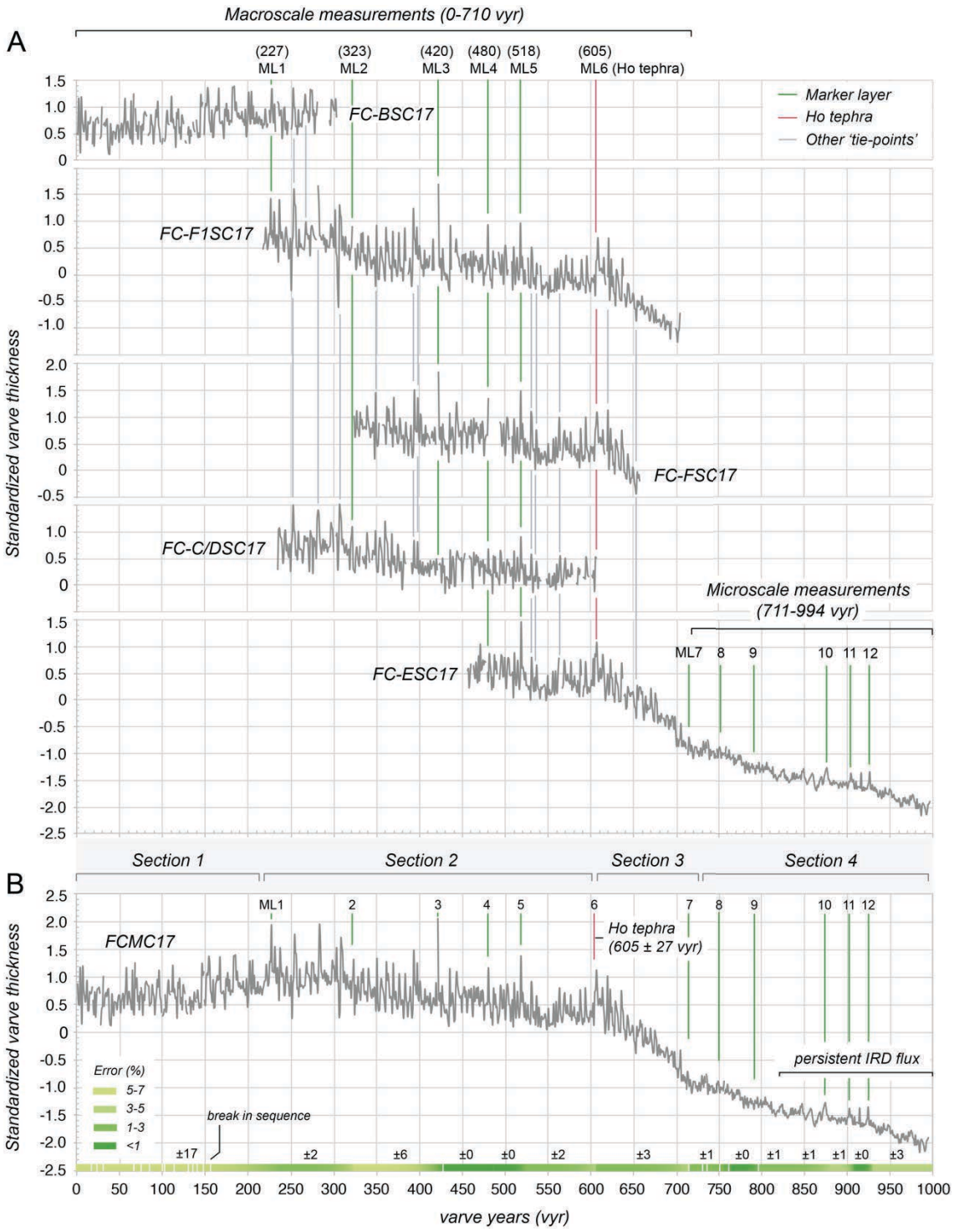

Figure 5.9. (A) Correlated varve thickness records from the Río Fenix Chico valley. Gaps in site varve series indicate sections with missing or disturbed varves, which were identified through cross-dating (cf. Lamoureux, 2001). Twelve prominent marker layers (e.g. sand beds, disturbed zones) were utilised as definitive pinning-points between sequences. Statistical correlations are provided in Table 5.5. (B) The Fenix Chico Master varve chronology (FCMC17) based on the correlation of five site varve series. The 994 ± 36 vyr record is divided into thirteen counting intervals (Table 5.7) separated by marker layers 1-12. Counting errors are attributed to each counting interval to visualise the distribution of error within the composite thickness record. The location of small breaks in the otherwise continuous thickness sequence are indicated. Four major sections of varve thickness variability that are discussed in the main text are highlighted along the upper horizontal axis.

Table 5.3. Summarised varve thickness characteristics and number of varves recorded at each site.

Site	FC-F1	FC-F	FC-E	FC-C/D	FC-B
Varves (n)	458	312	532	343	287
Uncertainty	2.84% (13)	2.24 (7)	2.44% (13)	2.62% (9)	6.62% (19)
Mean (mm)	82.14	54.79	15.21	47.10	71.64
St dev	98.27	41.93	21.50	34.11	36.71
Min (mm)	4.25	8.0	0.34	9.5	21.0
Median (mm)	54.75	46.0	3.13	36.8	61.45
Max (mm)	890.0	468.0	228.63	261.0	208.85
Coarse %	84.08	84.36	65.80*	79.04	82.01
Fine %	15.92	15.64	35.20*	20.96	17.99

*FC-E breakdown: >cm-scale varves = 78.13 mm (coarse %) and 21.88 (fine %); <cm-scale varves = 55.14 (coarse %) and 44.86 (fine %).

Table 5.4. Summarised varve thickness characteristics and number of varves recorded in three major lithostratigraphic sections. *Lower section* = base of sequence to Ho tephra; *Middle section* = Ho tephra to deformed section below <cm-scale varves; *Upper section* = deformed section to top of sequence (see main text for further explanation).

Site	FC-F1	FC-F	FC-E	FC-C/D	FC-B
Lower section					
Varves (n)	364	258	140	338	287
Mean (mm)	96.99	59.71	39.47	47.60	71.91
Middle section					
Varves (n)	92	50	104	-	-
Mean (mm)	23.74	34.12	20.05	-	-
Upper section	-	-		-	-
Varves (n)	-	-	284	-	-
Mean (mm)	-	-	1.48	-	-

Between 92 (FC-F1SC17) and 104 (FC-ESC17) varves accumulated in the middle section. These varves are thinner than those in the lower section, with average thicknesses ranging from 20.05 mm (FC-ESC17) to 23.74 mm (FC-F1SC17). Melt season layers are generally thicker than non-melt season layers, but the ratio of coarse to fine sediment decreases throughout this section, with the upper ~20–30 varves displaying approximately equal component thicknesses. The upper section contains 284 <cm-scale varves deposited at site FC-E, which have an average thickness of 1.48 mm, and melt season layers that are approximately equal to, or thinner than non-melt season layers (Table 5.4).

5.5.2 Cross-dating and construction of composite varve chronology

Cross-dating was performed to construct a composite varve chronology (Lamoureux, 2001) for the Río Fenix Chico valley (Figure 5.9). Using prominent marker layers as 'pinning-points' for site comparisons, errors in site chronologies were identified and removed. Correlations were conducted using standardised thickness series (e.g. Desloges and Gilbert, 1994; Heideman et al., 2015) to account for systematic thickness differences between sites and facilitate robust matches.

Cross-dating demonstrates that individual varves are consistently observed across the former lake basin, are visually well-matched (Figure 5.9), and statistically similar (Table 5.5). The FC-BSC17 contains the oldest recorded varves. The uppermost 66 varves of FC-BSC17 are significantly correlated with FC-C/DSC17 (r=0.69, n=51, p=<0.0001) and FC-F1SC17 (r=0.71, n=66, p<0.0001). The lower 217 varves in FC-BSC17 have no equivalents in other sites. The absence of equivalent varves at sites FC-F1, FC-F, and FC-E implies that these locations were ice-covered during this period. Over the next 493 years, cross-dating demonstrates overlaps of between 122–339 varves, and high inter-site correlations, with significant (p<0.0001) Pearson's correlation coefficients of between r=0.84–0.96 (Table 5.5). The uppermost 284 varves derive from thin section counts of <cm-scale varves at FC-E, and have no equivalents. The highest correlation (r=0.96) was obtained for comparison of the FC-F1SC17 and FC-FSC17 thickness records. These locations record the thickest, most proximal varves, and are <250 m apart. High, but somewhat weaker, correlations are observed when the FC-F1SC17 and FC-FSC17 records are compared with FC-ESC17 and FC-C/DSC17. The reduction in correlation strength can be explained by variations in varve thickness across the basin (Table 5.6), especially for FC-C/DSC17 where n=317 correlated varves are on average 38.61% thinner than in the FC-F1SC17 (Table 5.6).

Table 5.5. Pearson's correlation matrix of standardised varve thickness for total number of correlated varves from five sites. Degrees of freedom (n-2) reported in parentheses. Significance (p-value) <0.0001 (two-tailed) for all correlations.

	FC-F1	FC-F	FC-E	FC-C/D	FC-B
FC/F1	1				
FC-F	0.96 (292)	1			
FC-E	0.95 (223)	0.90 (174)	1		
FC-C/D	0.89 (315)	0.86 (229)	0.84 (120)	1	
FC-B	0.71 (64)	-	-	0.69 (49)	1

- no overlap between site records

Table 5.6. Proximal to distal varve (component) thickness relationships, showing the average thickness (mm yr^{-1}) and % thinner than observed for FC-F1, which shows on average the thickest varves in the Río Fenix Chico valley. The increased average thickness ('>values') of non-melt season layers at some locations might reflect greater erosion of clay layers during melt-season deposition at the proximal FC-F1 site.

		Melt season		Non-melt season		Varve	
Site	*n*	<mm/yr	<%	<mm/yr	<%	<mm/yr	<%
FC-F	295	6.48	5.83	-0.25	>7.48	5.06	3.98
FC-E	225	6.71	10.88	0.13	>0.37	6.82	17.71
FC-C/D	317	44.67	43.88	-0.14	>9.96	44.50	38.61
FC-B	66	82.00	46.90	6.57	26.95	88.19	45.67

n number of varves (laminations) correlated to FC-F1 varve series
<mm/yr = average mm/yr thinner than equivalent varves (laminations) in FC-F1
<% = average % thinner than equivalent varves (laminations) in FC-F1

5.5.3 Fenix Chico Master Chronology (FCMC17)

The high visual (Figure 5.9) and statistical (Table 5.5) correlation of varve series allows the construction of a composite varve chronology for the Río Fenix Chico valley (Figure 5.9). The Fenix Chico Master Chronology (FCMC17) is constructed from a lower sequence of 217 ± 17 varves identified at FC-B, a middle part of 493 ± 14 varves identified across three to four sites, and an upper part of 284 ± 5 varves derived from microscopic counts at FC-E (Figure 5.9). In total, therefore, the FCMC17 contains 994 ± 36 varves.

The total counting error for the FCMC17 is 3.62%. Of this value, 1.41% can be explained by unclear varve structures specifically associated with deformed sections, whilst the remaining 2.21% represent missing (Type A) or erroneously identified (Type B) varves (Lamoureux and Bradley, 1996) that correspond with poorly-defined varve structures. The division of the FCMC17 into thirteen counting intervals (separated by common marker layers) demonstrates that the total counting error is not evenly distributed throughout the composite record (Table 5.7), with the greatest errors associated with sections that contain frequent disturbances (Figure 5.9; Table 5.7).

The FCMC17 provides an estimate for the minimum duration of ice lobe and proglacial lake evolution in the Río Fenix Chico valley, owing to breaks in the composite sequence. 70.0% (*n*=14) of recorded breaks occur within the FC-BSC17 sequence, which covers the oldest 217 ± 17 years of the composite chronology. These breaks likely result from movement of unstable deposits (e.g. slumps) during the early stages of ice lobe retreat and lake expansion, or ice-margin oscillations that distorted sections of varves.

Through the cross-dating process counting discrepancies within local site chronologies could often be bridged by another, better-preserved sequence (Figure 5.9). This process demonstrates that the breaks observed within local site chronologies tend to cover short time-intervals of between 1–13 years (mean: 2.9 years) and thus represent local disturbances, such as slumps or minor erosion events (e.g. Lamoureux and Bradley, 1996). One significant break occurs at varve year 420 ± 25 and could not be bridged. This break represents a basin-wide deformation event, with field evidence for a minimum of 10 distorted varves, and may have occurred in response to glacial unloading (e.g. Mörner, 1985, 1996; Tröften and Mörner, 1997) or a regional geological event (e.g. earthquake; Monecke et al., 2004; Moernaut et al. 2014). Four small breaks between varve year 710 ± 30 and 994 ± 36 could also not be bridged due to a lack of overlapping sequences. Microscopic observations suggest that these breaks are also likely to be of minor duration. In subsequent sections concerned with varve thickness trends and the overall pattern of ice lobe evolution, breaks in the FCMC17 are considered insignificant.

Table 5.7. Number of varves identified and the distribution of counting errors within counting intervals for composite FCMC17. Multiple sites are correlated between vry 217–710, whereas vyr 0–216 (FC/B) and 711–994 (FC/E) come from single sites.

Interval	# sites	vyr	Varves (n)	Error	%
1 (base)	1	0—227	227	17	7.49
2	3	228—323	96	2	2.08
3	3	324—420	97	6	6.19
4	4	421—480	60	0	0.0
5	4	481—518	38	0	0.00
6	4	519—605	87	2	2.30
7	3	606—710	105	3	2.86
8	1	711—756	46	1	2.17
9	1	757—789	33	0	0.0
10	1	790—873	84	1	1.19
11	1	874—902	29	1	3.45
12	1	902—923	21	0	0.0
13 (top)	1	924—994	71	3	4.23
Total		**0—994**	**994**	**36**	**3.62%**

sites = number of sites contributing to composite record

5.5.4 Varve thickness trends

The FCMC17 allows characterisation of ice lobe and meltwater dynamics during the onset of deglaciation, through the analysis of varve thickness trends. As individual site records show comparable thickness patterns (Figure 5.9), major variations in sedimentation rate are described using the continuous FCMC17 series.

5.5.4.1 Description of varve thickness trends

Four principal thickness *Sections* are observed in the standardised FCMC17 series: 0–216, 217–603, 604–704, and 705–994 varve years (vyr). Each section records a shift in the pattern of average varve thickness at the centennial timescale (Figure 5.9). Within these major sections, shorter-term (e.g. decadal) variations and absolute maxima (minima) in varve thickness are recorded.

Within *Section 1* (0–216 vyr), a stable multi-decadal thickness trend is observed between 0–143 vyr. This switches to a trend of increasing varve thickness over the succeeding 72 vyr (144–216 vyr). *Section 1* is recorded at the FC-B site only (FC-BSC17; Figure 5.9), which is positioned between the Fenix I and Menucos moraines (Figure 5.5). Varves accumulated in *Sections 2-4* (below) were deposited across the entire basin.

Section 2 (217–603 vyr) starts with a rapid 9-year increase in varve thickness that coincides with the onset of sedimentation on (site FC-E) and west of (sites FC-F, FC-F1) the Menucos moraine (Figure 5.5, 5.9). After this, varve thickness decreases gradually between 228–603 vyr. However, the initial ~60–70 years of this section record the highest sedimentation rates over the 994 ± 36-year varve series (Figure 5.9). Numerous sub-decadal scale, or absolute increases in varve thickness are observed throughout *Section 2*, and often coincide with coarse sediment influxes (e.g. sand layers; Fig 6e) that are intercalated amongst regular melt-season sediment structures (e.g. Figure 5.6b). The final 55 years of *Section 2*, demonstrate a thickness increase between 548–563 vyr that disrupts the long-term trend of decreasing varve thickness. After this, thickness trends stabilise and then decrease between 564-603 vyr, albeit with several high-magnitude peaks (Figure 5.9).

The centennial-scale varve thickness trend shifts dramatically in *Section 3* (604–704 vyr). This section starts with an abrupt thickness increase lasting <10 years, which incorporates a major thickness maxima immediately after the deposition of the Ho tephra in vyr 605 ± 27 (Figure 5.9). After this, varve thickness decreases rapidly until vyr 704. This 100-year section demonstrates the greatest reduction in average sedimentation rate over the 994 ± 36-year varve series.

The varve thickness trend continues to decrease throughout *Section 4* (705–994 vyr), although the rate of decrease reduces significantly (Figure 5.9). Several rapid thickness increases punctuate the overall decreasing trend, each lasting <20 years. Sedimentological analysis reveals an abrupt increase in the flux of IRD to the basin (Figure 5.6k), which is evident after ~830 vyr and persists until vyr 994 ± 36 (Figure 5.9).

5.5.4.2. Interpretation of varve thickness trends

Sedimentation rates in the Río Fenix Chico basin respond to changes in the erosion and transport of sediment to the former lake. In ice-contact lakes, this flux of sediment is strongly related to the activity of the glacial meltwater system, and modulated over time by various factors (e.g. Gustavson, 1975; Loso et al., 2006; Ridge et al., 2012). Over centennial timescales, glacial extent represents the primary control on local sedimentation rates, where a more proximal (distal) glacier position leads to increased (decreased) varve thickness (Leonard, 1997; Leeman and Niessen, 1994; Ohlendorf et al., 1997; Larsen et al., 2011; Ridge et al., 2012). Over (multi)decadal timescales, the controls on sedimentation rate are more complex. Increased sedimentation rates (varve thickness) have been linked to transitional periods of (i) rapid glacier advance, or (ii) the initial phases (one-to-two decades) of glacier retreat, rather than glacial maxima (Leonard, 1997). Shorter-term (<decadal) thickness variations and absolute thickness maxima, are shown to respond to meteorological factors, such as temperature and precipitation changes (e.g. Leeman and Niessen, 1994; Ohlendorf et al., 1997; Loso et al., 2006; Ólafsdóttir et al., 2013). Based on these previous studies, we interpret the strong first-order trend of varve thickness decrease (Figure 5.9) as the progressive recession of the LGC–BA ice lobe from the catchment over the 994 ± 36 vyr.

The stable decadal-scale thickness trends in *Section 1* are consistent with a glacier stillstand (Leonard, 1997). In this scenario, the increasing sedimentation rates observed between 144–216 vyr most likely reflect increasing ablation rates and meltwater fluxes (Hodder et al., 2007), and a precursor to more widespread ice lobe retreat. While increasing sedimentation rates could represent a readvance to the Menucos moraine, there is no stratigraphic evidence (e.g. glaciotectonised varves) to support this interpretation; instead, varved sediments display an onlapping relationship with both ice-contact and ice-distal faces of the moraine.

Increasing meltwater and sediment fluxes between 144–216 vyr are consistent with the rapid thickness increase observed at the onset of *Section 2*, which is typical of high meltwater and sediment discharges during a transition to glacier recession (Leonard, 1997). The persistent 320-year thickness decline that follows is consistent with a gradual reduction in ice lobe extent (e.g. Larsen et al., 2011). However, high average sediment yields and regular coarse sediment influxes (Figure 5.6e) suggest that the LGC–BA ice lobe remained proximal (Gustavson, 1975; Ashley, 1975). Shorter, decadal-scale oscillations (e.g. seen between 548–563 vyr) could reflect an ice-margin stillstand, minor

readvance or enhanced meltwater production and sediment transport efficiency (e.g. Leonard, 1997; Larsen et al., 2011; Loso et al., 2006).

The abrupt increase in sediment yields at the onset of *Section 3* supports an enhancement in meltwater production, and marks a transition to greater ice lobe recession (Leonard, 1997). The thickness maxima that occurs immediately after the deposition of the Ho tephra might represent an ablation response to the accumulation of low-albedo ash cover on the glacier surface for several seasons (e.g. Kirkbride and Dugmore, 2003), or increased catchment instability and sediment in-washing (Larsen et al., 2011). The abrupt thickness decline that follows this initial increase, and persists until vyr 704, reflects a rapid decrease in ice lobe extent (Leonard, 1997), and recession from the Río Fenix Chico valley.

The sustained reduction in sedimentation rates over *Section 4* suggest that the ice-margin continued to recede. The relative shallowing of thickness trend relative to *Section 3* (Figure 5.9) might reflect a combination of greater distance and glaciological adjustments to a new quasi-equilibrium state, as the margin withdrew into deeper lake waters. The increased influx of IRD after ~830 vyr supports this interpretation, and suggests that an active calving front was established (e.g. Larsen et al., 2011, 2015). Studies of modern lake-calving termini indicate that greater basin depths promote floatation and calving (e.g. Boyce et al., 2007), and support our interpretation of ice lobe recession into LGC–BA. The persistent decrease in sediment yields throughout *Section 4* implies that no major readvance occurred after this.

5.6 Age modelling

This section builds upon the construction of the new, annually-resolved chronology of ice lobe activity and palaeolake duration (Figure 5.9). The FCMC17 is anchored to the calendar-year timescale using the Ho tephra (Figure 5.7, 5.8 and 5.10). Subsequently, Bayesian age models are produced to refine the chronology of ice lobe retreat patterns at the onset of deglaciation (Figure 5.11).

The geochemically fingerprinted Ho tephra (Figure 5.7–5.8) occupies an identical position in the varve stratigraphy of the respective site chronologies, and occurs at vyr 605 ± 27 in the composite FCMC17 (Figure 5.9). Using the eight radiocarbon determinations of Miranda et al. (2013; Table 5.8) the eruption age was remodeled to 17,378 ± 118 cal a BP using the *Phase* command in Oxcal v.4.3 (Bronk Ramsey, 2009a) and the SHCal13 calibration curve (Hogg et al., 2013; model code provided in Appendix). We acknowledge the reported older ages for Ho of ~18.2 ka BP (Stern et al., 2015) and 18.4–17.5 ka BP (Van Daele et al., 2016), however, these ages are based on

interpolated sedimentation rates and considered less robust. When our age estimate for Ho is inserted into the FCMC17 at 605 ± 27 vyr, this indicates that the varve sequence was deposited between 17,997 ± 144 and 16,982 ± 127 cal a BP (Figure 5.10–5.11).

Table 5.8. Radiocarbon determinations for organic material above (<Ho; 'younger than') and below (>Ho; 'older than') the Ho tephra layer across four sites, cf. Miranda et al. (2013), and individual remodeled cal a BP ages.

Stratigraphy	Laboratory code	^{14}C a BP	cal a BP*
<Ho	UCIAMS-122978	13,430 ± 50	16,170 ± 101
<Ho	CAMS-159614	13,720 ± 45	16,499 ± 121
<Ho	CAMS-159606	13,810 ± 110	16, 649 ± 190
<Ho	CAMS-159607	14,220 ± 45	17,222 ± 96
>Ho	CAMS-159613	14,345 ± 45	17,490 ± 90
>Ho	UCIAMS-122999	14,670 ± 45	17,801 ± 87
>Ho	CAMS-154860	14,735 ± 30	17,865 ± 78
>Ho	UCIAMS-123030	14,800 ± 90	17,895 ± 115

*cal a BP age determined in Oxcal v4.3 using SHCal13 cf. Hogg et al. (2013).

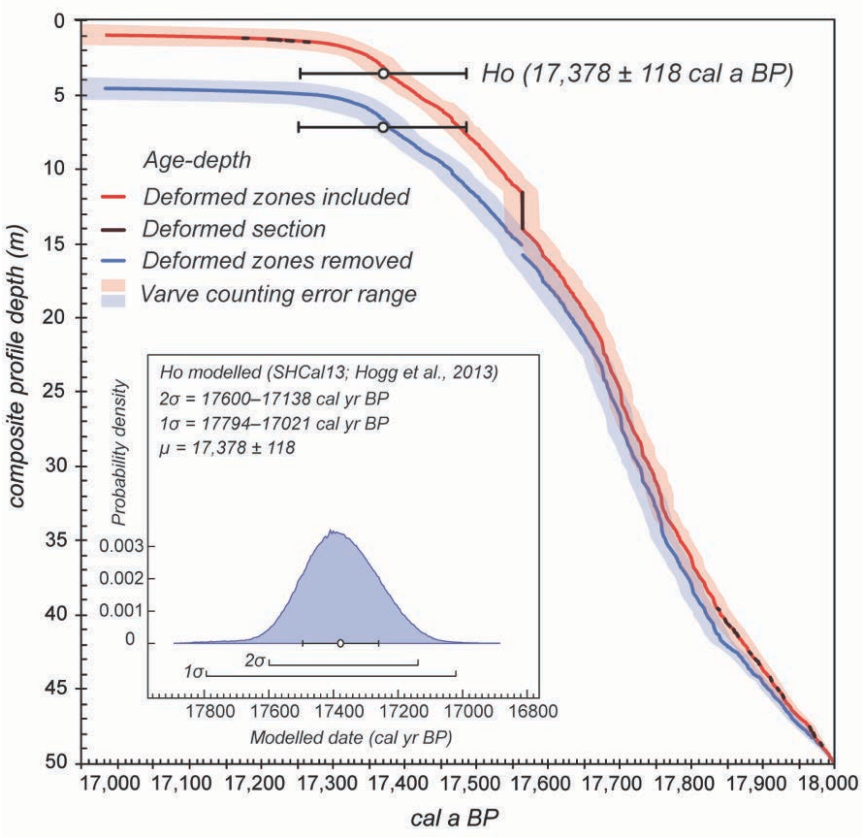

Figure 5.10. Age-depth model for the composite varve profile based on the correlation of varve series across five sites. The model is anchored in time using the Ho tephra layer identified in varve-year 605 ± 27 of the FCMC17. The age of the Ho tephra is remodelled to 17,378 ± 118 cal a BP (inset graph) using eight radiocarbon determinations published in Miranda et al. (2013; Table 5.8) and Weller et al. (2014). The Ho age was modelled using the Phase command in Oxcal v4.3 (model code provided in Appendix).

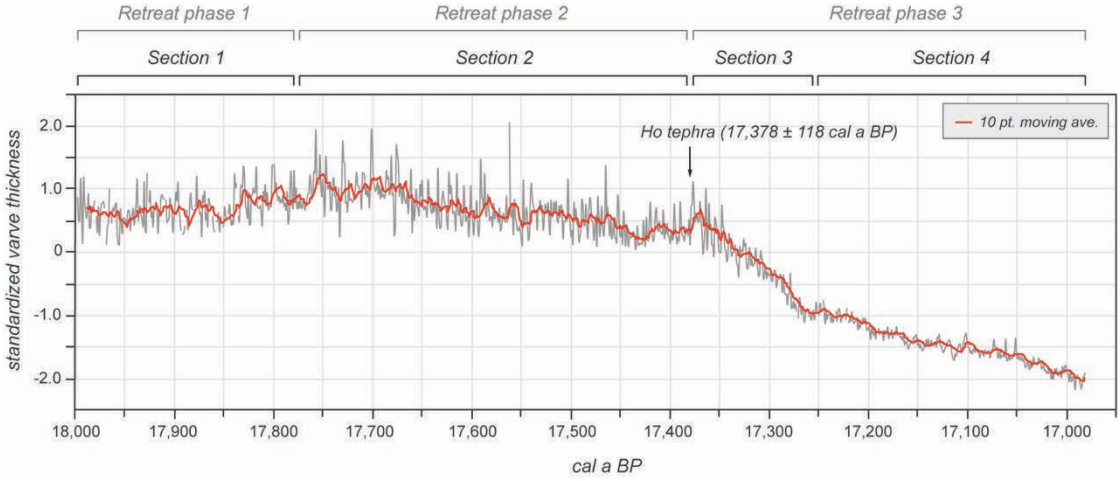

Figure 5.11. Time-anchored FCMC17. The red line represents a 10-year moving average through the annual thickness data. The four major sections of varve thickness variability indicated on Figure 5.9, and discussed in the main text, are highlighted along the upper horizontal axis. The absolute timing of varve thickness variations is established through integration of the remodelled Ho tephra age (17,378 ± 118 cal a BP) at 605 ± 27 vyr. Retreat phases refer to a reconstruction of ice-margin deglaciation in eastern LGC–BA, as presented in Figure 5.13.

This calendar-year chronology can be further integrated with other chronological data to establish the most likely ages for deglacial 'events' (e.g. moraine emplacement). The model input comprises: (i) time intervals defined by varve counting; (i) the remodelled age estimate for the Ho eruption; (iii) cosmogenic nuclide exposure ages for moraine boulders deposited on the Fenix I (n=9) and Menucos (n=6) moraines (Kaplan et al., 2004; Douglass et al., 2006); and (iv) a single luminescence age derived from Menucos-related outwash sediments (Smedley et al., 2016). A final critical input to the model was *prior* information on ice-margin position(s), and their spatial association with varved deposits (Figure 5.5). Before constructing the age model, published exposure ages were recalculated using the time-dependent scaling scheme (Lm) of Lal (1991) and Stone (2000) at 0 cm-yr^{-1} erosion rate, and the Putnam et al. (2010) New Zealand (44°S) production rate to calibrate ^{10}Be determinations (see Appendix). This production rate is in common use in Patagonia (e.g. Glasser et al. 2012; Boex et al., 2013) and overlaps at 1σ with the Patagonian production rate from Lago Argentino (50°S; Kaplan et al., 2011).

Age modelling was performed using *Sequence* algorithms (cf. Bronk Ramsey, 2008; model code provided in Appendix). Outlier analysis with the *General* outlier model (Bronk Ramsey, 2009b) retained outliers but they were down-weighted (i.e. 'model-averaging', Bronk Ramsey, 2009b). The age model consists of two component *Sequence* models. Model 1 utilises the varve-count data and Ho age estimate (Figure 5.10–11) to establish

new timings and durations for ice lobe retreat phases, whilst Model 2 utilises the published luminescence and boulder ages for moraine emplacement.

In Model 1, the varve chronology was divided into three vyr *Intervals*, with varve counting uncertainties treated as uniform error distributions. The first interval (equivalent to *Section 1* in Figure 5.11) has a duration of 200–234 vyr and represents the number of vyr accumulated solely between the Fenix I and Menucos moraines. The second interval (equivalent to *Section 2* in Figure 5.11) has a duration of 376–400 vyr and represents the number of vyr deposited between the onset of sedimentation behind the Menucos moraine and the deposition of the Ho tephra at 17,378 ± 118 cal a BP. The end of this interval coincides with the decrease in varve thickness indicative of a shift to rapid ice-margin retreat. The final interval (equivalent to *Sections 3-4* in Figure 5.11) has a duration of 380–398 vyr and represents the number of vyr formed between the Ho tephra and the uppermost varve in Río Fenix Chico. In Model 2, ages for the Fenix I (*Phase 1*) and Menucos (*Phase 2*) moraines are treated as independent *Phases*. These *Phases* are separated with *boundaries* to determine 'start' and 'end' dates for moraine emplacement.

Model 1 and Model 2 were integrated within the Bayesian framework to further refine the likelihood distributions for deglacial events, and produce a final age model shown in Figure 5.12. The modelled age range of key depositional events are given in Table 5.9. The model significantly improves upon previous estimates for the timing of moraine emplacement (Table 5.9). This results from the time-anchored vyr constraint on Menucos moraine formation (17,710 ± 116 cal a BP) in Model 1, which further constrains the age estimate of Fenix I deposition in Model 2. The final model output (Figure 5.12) provides the foundation for a new reconstruction of ice lobe evolution in eastern LGC–BA (below).

5.7 Discussion

The data presented in this paper offer new insights on the earliest stages of deglaciation at LGC–BA, at a temporal resolution that has hitherto been impossible. Lithostratigraphic analyses have discriminated an ice-proximal subaqueous fan (LFA 2; Figure 5.5), and thus a new ice-margin position at Estancia Santa Maria, ~4 km west of the Menucos moraine, consistent with a pattern of progressive retreat from the well-established Fenix I and Menucos moraines (Figure 5.5; Kaplan, 2004; Douglass et al., 2006). Lithostratigraphic analysis has also enabled linkages between intervals of varve formation and phases of ice lobe retreat, the timings of which have been revised through varve counting (Figure 5.11), tephrochronology (Figure 5.7–5.8) and Bayesian age-modelling (Figure 5.12). Within these broad retreat phases, annual to centennial varve thickness trends (Figure 5.9) and detailed macro- and micro-facies data informs on high-

resolution changes in ice and meltwater dynamics. The next section uses these combined datasets to generate a model of ice lobe and palaeolake dynamics for the earliest 1–2 thousand years of deglaciation at 46.5°S (Figure 5.13). Glacier retreat rates are calculated using the modelled ages for depositional events (Figure 5.12; Table. 9), which are identical (within errors) to direct varve-counted ages.

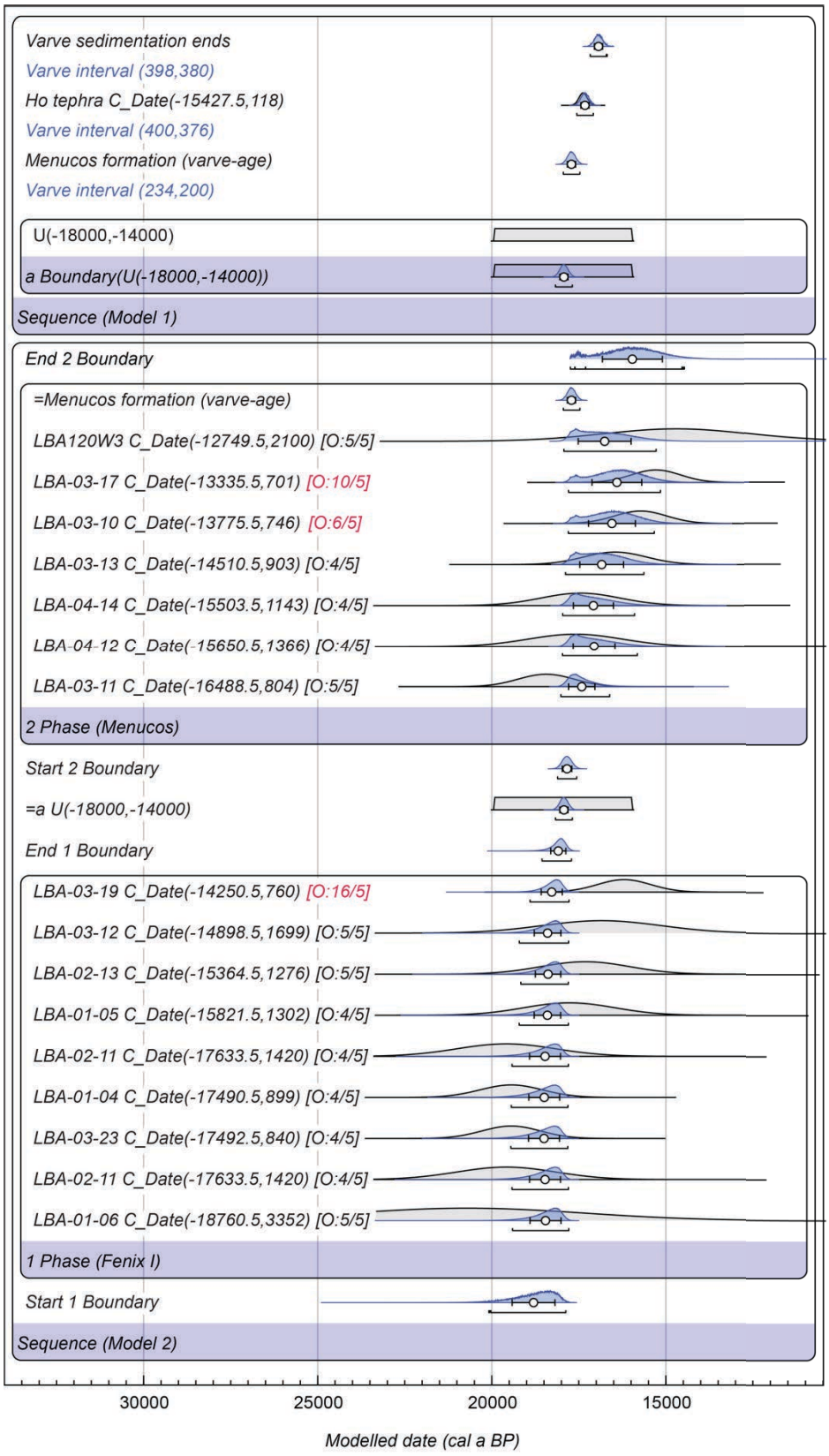

Figure 5.12. Bayesian age model (model code in Appendix) for the timing of ice lobe activity in the Río Fenix Chico valley. Model inputs included the new varve and tephrochronological data presented here (Model 1), and published cosmogenic nuclide exposure ages from the Fenix I (Kaplan et al., 2004; Douglass et al., 2006) and Menucos (Douglass et al., 2006) moraines, and a single luminescence age from outwash sediments linked to the Menucos limit (Smedley et al., 2016; Model 2). Age modelling utilised the *Sequence* approach of Bronk Ramsey (2008) and employed a *General* outlier model (Bronk Ramsey, 2009b) within Oxcal v4.3 (Bronk Ramsey, 2009a). Prior to age-modelling, published boulder ages were recalculated using the time-dependent scaling scheme (Lm) of Lal (1991) and Stone (2000), and the Putnam et al. (2010) New Zealand production rate used to calibrate ^{10}Be determinations (see Appendix). Exposure ages were calculated on the assumption of 0 cm-yr^{-1} erosion rates. Samples considered to be outliers in original publications were removed prior to age-modelling. Exposure ages were calculated using the CRONUS-Earth online calculator developed by Balco et al. (2008).

Table 5.9. Modelled ages (cal a BP) for key depositional and glaciological events during the initial retreat of the LGC–BA ice lobe.

	Modelled ages	
Event	Range (BP)	μ/± (BP)
Fenix I deposition (start)	20,141-17,852	18,778 ± 615
Fenix I deposition (end)	18,558-17,716	18,086 ± 214
Menucos deposition (start)	18,106-17,567	17,837 ± 136
Menucos deposition (end)	17,728-14,499	16,034 ± 906
Menucos formation*	17,944-17,481	17,710 ± 116
Ho tephra deposition	17,551-17,091	17,322 ± 115
End of varve formation	17,173-16,701	16,934 ± 116

* modelled age based on *Sequence* Model 1 in Figure 5.12

5.7.1 Deglacial evolution of the LGC–BA ice lobe and palaeolake system

During the late stages of the local LGM, the LGC–BA ice lobe was positioned at the Fenix I moraine (Figure 5.13; Kaplan et al., 2004). Bayesian modelling yields a date for the start of moraine formation at 18,778 ± 615 cal a BP, and an end date of 18,086 ± 214 cal a BP.

These ages suggest that the ice-margin was stable at the Fenix I moraine for ~700 years. The end date for Fenix I emplacement provides an improved timing for the onset of deglaciation and palaeolake formation at LGC–BA. Shorelines cut into the Fenix I moraine (Figure 5.1; Figure 5.5; Hein et al, 2010; Glasser et al., 2016; Chapter 3) indicate that this lake existed at ~400 m asl and drained through the Río Deseado outflow. This lake level was maintained for the full duration encompassed by Figure 5.13.

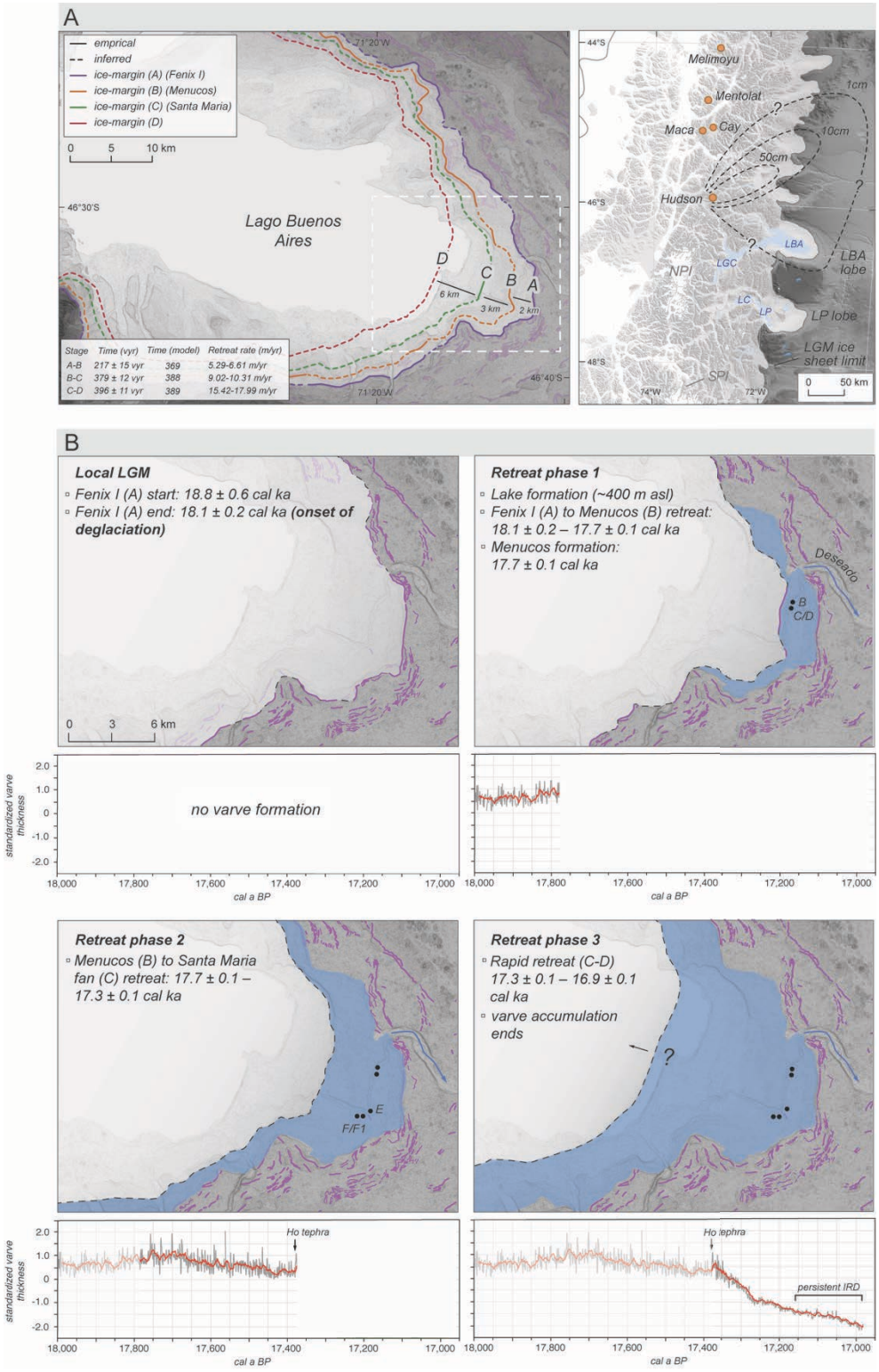

Figure 5.13. Reconstruction of ice lobe and palaeolake evolution for the onset of deglaciation at 46.5°S, based on stratigraphic investigations (Figure 5.4–5.5), varve analysis (Figure 5.9-5.11) and Bayesian age modelling (Figure 5.12). (A) Reconstructed ice-margin positions, stages of ice lobe retreat, and mean retreat rates. Ice lobe margins are based on published geomorphological datasets (Chapter 3) and new morphostratigraphic investigations in the Río Fenix Chico valley (Figure 5.5). The right-hand panel shows the location of the LBA outlet glacier at the local LGM, and other regional ice lobes cf. Singer et al. (2004). Major volcanoes are indicated, along with 50 cm, 10 cm (cf. Weller et al., 2014), and possible 1 cm (this study) isopachs for the Ho tephra. (B) Reconstructed ice-margin positions, lake extents, and retreat phases following the local LGM at LGC–BA.

In *Retreat phase 1*, the LGC–BA ice-margin retreated from the Fenix I to Menucos moraine (Figure 5.13). This period is encapsulated by the deposition of 217 ± 17 varves, after which varves began to accumulate behind the Menucos moraine. The modelled age for formation of the Menucos moraine is 17,710 ± 116 cal a BP, 376 modelled years after the onset of deglaciation (Figure 5.12; Table 5.9). Using these ages, a 2.0–2.5 km retreat from the Fenix I to Menucos moraine yields a mean ice-margin retreat rate of 5.31–6.65 m yr^{-1}. Stable to increasing varve thickness trends over this phase (Figure 5.9-11) are consistent with the retreat and stabilisation of ice at the Menucos moraine, followed by a gradual increase in glacier ablation, prior to ice-margin destabilisation in *Retreat phase 2*.

An abrupt 9-year long varve thickness increase records an enhancement of glacier ablation and marks the onset of retreat from the Menucos moraine in *Retreat phase 2*. Lithostratigraphic evidence (LF 1b-3 in Fig 4a-c; LFA 2 in Figure 5.5) suggests that the next ice-margin position was established at the Santa Maria ice-proximal fan complex, ~3.5–4.0 km west of the Menucos moraine (Figure 5.5). Within this period, the pattern of varve thickness declines persistently to the Ho tephra at 17,322 ± 115 cal a BP, which is taken as an approximate end date for *Retreat phase 2*.

The decreasing thickness trend is consistent with a gradual reduction in ice lobe extent. Coarse-grained sediment influxes are frequent within this interval (Figure 5.11), and support a margin position at this location, given that such influxes are typical of ice-proximal inflows (Gustavson, 1975; Ashley, 1975). The 3.5–4.0 km retreat from the Menucos moraine to the Santa Maria ice-proximal fan complex occurred over 388 modelled years. This yields a mean ice-margin retreat rate of 9.02–10.31 m yr^{-1}, ~38% faster than for *Retreat phase 1*.

The abrupt increase in varve thickness that coincides with deposition of the Ho tephra marks the onset of intense ablation at the beginning of *Retreat phase 3*, and more extensive ice lobe recession from the Río Fenix Chico valley (Figure 5.13). The abrupt reduction in varve thickness that follows between 17,379 ± 118 and 17,279 ± 121 cal a BP (*Section 3* in Figure 5.11) provides evidence for more rapid retreat than in *Retreat phase 2*. Varve thickness trends continue to decline after 17,279 ± 121 cal a BP, but stabilise to some degree (*Section 4* in Figure 5.11). The increased influx of IRD after 17,145 ± 122 cal a BP, suggests that the ice-margin had retreated into deeper lake waters by this time, and had established a calving ice-front (e.g. Larsen et al., 2015). We cannot currently constrain the exact ice-margin position(s) during *Retreat phase 3*. However, road cuttings ~6.0–7.0 km west of the Santa Maria limit preserve sedimentary

sequences characteristic of ice-proximal subaqueous fan deposition, and provide a minimum distance of ice lobe retreat. The varve thickness stratigraphy supports this approximate ice-margin location, as further retreat would have ceased varve formation in the Río Fenix Chico valley. Specifically, the ~30–40 m glaciolacustrine sediment stack that had accumulated by this time would have presented an obstacle to the passage of underflows to the site (Mulder and Alexander, 2001). Until further constraints on ice-margin position(s) are established, taking the modelled age for the end of varve sedimentation (16,934 ± 116 cal a BP) as the upper constraint on *Retreat phase 3* yields a minimum retreat rate of 15.42–17.99 m yr^{-1}. This represents a ~42% acceleration compared with *Retreat phase 2* and supports the inferred development of an active calving margin (e.g. Benn et al., 2007; Boyce et al., 2007) based on increased IRD influx (Figure 5.6k) and rapidly thinning varves (Figure 5.11).

Currently, we have no varve constraint beyond *Retreat phase 3*. Further west, geomorphological mapping and luminescence dating of raised deltas suggest that the 400–460 m asl lake in LGC–BA existed until ~11.5 ka ago (Glasser et al., 2016), ~5.5 ka after varves stopped accumulating at Río Fenix Chico. As such, the culmination of varve formation at 16,934 ± 116 cal a BP is likely a function of diminished sediment input due to reduced ice lobe extent, and provides a constraint on the timing of further (>20 km) westwards retreat towards the Patagonian mountains. Sediment-laden underflows from the ice-margin would have preferentially accumulated in lake floor depressions closer to the retreating ice-front, or in sheltered, low-elevation embayments. Therefore, additional varve sequences may exist to the west of the Río Fenix Chico valley, most likely beneath the contemporary LGC–BA.

The varve and lithostratigraphic data presented above enable an evaluation of the competing models of palaeolake configuration at the onset of deglaciation (Figure 5.2) The high-level (550–480 m asl) precursor lake presented in Glasser et al. (2016; Figure 5.2a) is inconsistent with evidence for ice lobe persistence in eastern LGC–BA until at least 16,934 ± 116 cal a BP. In the Glasser et al. (2016) model, the ice sheet margin has retreated to the Leones valley mouth at this stage, within ~40 km of the modern NPI glacier limits. However, the Río Fenix Chico varves are morphostratigraphically linked to recession from the Fenix I moraine and palaeolake shorelines developed at ~400–460 m asl (Figure 5.2; Figure 5.5), which represent the highest-elevation lake-level expression east of the Patagonian mountain front (Turner et al., 2005; Hein et al., 2010; Glasser et al., 2016; Chapter 3). Furthermore, only outwash deposits have been discovered outside the Fenix I moraine (e.g. Caldenius, 1932; Smedley et al., 2016). For ice-proximal varves to form in the Río Fenix Chico valley, a retreat of <20 km has been

reconstructed (Figure 5.13), some ~125 km east of the Leones margin reported in Glasser et al. (2016; Figure 5.2a). This suggests that the raised lacustrine deltas taken as evidence for >500 m asl lake stands and overtopping of the Fenix I moraine, most likely formed in lateral ice-dammed lakes impounded by the LGC–BA ice lobe that occupied the main trunk valley. This is consistent with the restriction of such features to tributary valleys west of the mountain front (Martinod et al., 2016). Currently, the lithostratigraphic and varve-based evidence presented here is more closely aligned with the model presented in Hein et al. (2010) that reports a maximum lake stand of ~400 m asl in LGC–BA following the local LGM (Figure 5.2c). Below the ~400 m level, shorelines at littoral deposits (LFA 4; Figure 5.5) provide evidence for multiple lake levels in eastern LGC–BA, and support the model of punctuated palaeolake drainage of Bell (2008).

5.7.2 Implications for existing glaciological models

Bayesian age-modelling that integrates high-precision varve and tephrochronological datasets with existing ages for moraine formation has improved the constraint on the timing deglacial events in eastern LGC–BA (Table 5.9; Figure 5.12). In particular, the model predicts, with centennial-scale precision, that ice sheet deglaciation started at 18,086 ± 214 cal a BP, as the ice-margin withdrew from the Fenix I moraine. An equally precise age estimate is achieved for formation of the Menucos moraine (17,710 ± 116 cal a BP). Nonetheless, comparisons with unmodelled ^{10}Be ages (Kaplan et al., 2004, 2011; Douglass et al., 2006) reveal overlaps within errors, and support the application of southern hemisphere production rate models for ^{10}Be calibration (e.g. Putnam et al., 2010; Kaplan et al., 2011) at this latitude. The luminescence age of 14.7 ± 2.1 ka (12.6-16.8 ka) from Menucos-related outwash sediments (Smedley et al., 2016) is somewhat younger than our modelled ages of Menucos moraine formation. The greater chronological precision afforded by the combined varve and tephrochronological dataset suggests that, in this instance, the luminescence technique has underestimated the age of outwash deposits, or the genesis of the deposit is uncertain.

The model of ice lobe evolution for eastern LGC–BA (Figure 5.13) indicates a relatively stable ice-margin and minimal ice losses following deglaciation onset at 18,090 ± 217 cal a BP. Whilst there are periods of ice stillstand, e.g. at the Menucos moraine (17,710 ± 116 cal a BP) and Santa Maria fan complex, we find no evidence for ice lobe readvance over the varved sequences, contrary to earlier proposals (Singer et al., 2004; Kaplan et al., 2004; Douglass et al., 2006; Smedley et al., 2016). However, direct comparisons with existing glaciological reconstructions are difficult due to the non-continuous nature of geomorphic models, and chronological disparities between varve-based analysis (this

study) and radiometric analyses through cosmogenic nuclide exposure dating of moraine boulders (e.g. Kaplan et al., 2004; Douglass et al., 2006; Glasser et al., 2012) or luminescence dating of sands (e.g. Glasser et al., 2016; Smedley et al., 2016). Namely, whilst the latter approaches are currently best-placed to provide an indication of longer-term (e.g. multi-millennial) glacial changes, the significant enhancement in chronological precision afforded with varve-based analysis enables shorter, continuous time intervals to be examined at unprecedented resolution. Where coupled to the morphostratigraphic record, as has been possible here, this approach enables changes in the continuous behaviour of ice lobes to be established (e.g. changing retreat rates) and constrained at centennial-scale temporal resolution.

Currently, the only other temporally continuous model of ice lobe evolution in LGC–BA is the numerical simulation of Hubbard et al. (2005). In terms of glaciological behaviour, the varve-based model for the initial 1–2 thousand years of deglaciation (Figure 5.13) compares closely with the numerical simulation. The Hubbard et al. (2005) simulation is forced by the Vostok palaeo-temperature record of Petit et al. (1999) and depicts a slow but steady ice-margin retreat beginning at ~18 ka ago, with minimal glacier contraction and negligible ice-volume losses prior to 16.5–16.0 ka ago. This is consistent with the varve evidence for <20 km retreat by 16,934 ± 116 cal a BP. The possible implication of this comparison being that, over the first 1–2 millennia of the deglacial cycle, the Patagonian Ice Sheet at ~46.5°S was affected by hemispheric-scale climate forcing that were also recorded in deuterium excess records over Antarctica.

5.7.3 Wider implications

The new model for deglaciation in eastern LGC–BA (Figure 5.13) demonstrates the ability to tightly constrain the chronology of ice sheet fluctuation (Figure 5.12), through integration of varve analysis, tephrochronology and Bayesian age-modelling. In North America and Sweden, varve chronologies for ice sheet deglaciation span longer time-intervals than achieved here, and have enabled high-resolution reconstructions of ice sheet dynamics and advance-retreat rates over entire deglaciation cycles (e.g. Wohlfarth et al., 1997; Breckenridge et al., 2012; Ridge et al., 2012). These longer records have also enabled comparisons with other high-resolution climatic archives (e.g. Greenland ice-core records) to facilitate assessments of hemispheric-scale climatic controls on ice sheet behaviour (Ridge et al., 2012), and provide a realistic target for numerical modelling simulations of ice sheet dynamics.

At LGC–BA, future sedimentological investigations of varve sequences offer the potential to lengthen the existing FCMC17, whilst tephrochronology offers a robust means of

correlating and independently dating disparate records. A longer chronology would enable ice-margin retreat dynamics to be tracked over greater distances (e.g. Ridge et al., 2012). Reports of laminated lacustrine sediments (e.g. Caldenius, 1932; Denton et al., 1999; Stern et al., 2011) and reconstructions of proglacial palaeolake systems (e.g. McCulloch et al., 2005; Sagredo et al., 2011; García et al., 2014; Van Daele et al., 2016) are available for several sectors of the Patagonian Ice Sheet, and suggest that this approach has wider potential. In the future, the potential exists to establish direct comparisons between valleys at sub-centennial temporal resolution, and provide greater opportunities to discriminate differences (or similarities) in the timing and pattern of deglaciation across the former Patagonian Ice Sheet. Such an approach would begin to overcome the current chronological limitations of other radiometric dating techniques, and the fragmentary (non-continuous) nature of dateable geomorphic evidence (e.g. moraines).

5.8 Conclusions

- Detailed analyses of laminated glaciolacustrine couplets deposited in the Río Fenix Chico valley, provide sedimentological evidence for varve formation during deglaciation at LGC–BA (46.5°S).
- Varve records from 5 sites have been integrated to construct a master chronology spanning a minimum duration of 994 ± 36 vyr.
- The Ho tephra anchors the floating varve chronology to the calendar-year timescale, between 17,997 ± 144 to 16,982 ± 127 cal a BP. The identification of Ho in LGC–BA extends the known distribution of this important chronological marker layer to the south east, and highlights the potential of this volcanic event in dating and correlating disparate palaeoenvironmental records in this region.
- Integrating the new varve chronology with existing chronological datasets, using a Bayesian framework, yields refined age ranges for the Fenix I and Menucos moraine limits. This analysis indicates that deglaciation of the Patagonian Ice Sheet at 46.5°S started at 18,086 ± 214 cal a BP.
- The thickness of glaciolacustrine varves indicate that glacier ice existed in eastern LGC–BA until at least 16,934 ± 116 cal a BP. In the period of deglaciation proceeding this, estimated ice-margin retreat rates range from ~5.31–6.65 m yr^{-1} between 18,086 ± 214 to 17,710 ± 116 cal a BP, to ~15.42–17.99 m yr^{-1} between 17,322 ± 115 to 16,934 ± 116 cal a BP, and record a steady, but accelerating ice-margin retreat caused by recession into deeper waters and the onset of calving.
- Glaciolacustrine sediments that accumulated in proglacial lakes around the waning Patagonian Ice Sheet have the potential to generate continuous, high-

resolution chronologies for understanding terrestrial glacial behaviour and response to climate changes. These archives are, however, underutilised at present. A future focus on glaciolacustrine varve sequences will generate continuous, annually-resolved records spanning longer intervals of the deglacial cycle, as has already been possible for former ice sheets in North America and Europe.

Chapter 6. Sensitivity of the Patagonian Ice Sheet to sub-decadal tropical climate variability between ~18–17 ka revealed by a glaciolacustrine varve thickness record at Lago Buenos Aires, Argentina

Bendle, J.M., Palmer, A.P., Thorndycraft, V.R., Matthews, I.P. (in prep) Sensitivity of the Patagonian Ice Sheet to sub-decadal tropical climate variability between ~18–17 ka revealed by a glaciolacustrine varve thickness record at Lago Buenos Aires, Argentina. Earth and Planetary Science Letters.

Abstract

Understanding the sensitivity of ice sheets to short-term climate shifts across the last deglaciation requires annual/decadal chronologies. Glaciolacustrine varves have the potential to resolve such change, though are currently underutilised. This paper presents an annually-resolved record of deglacial meltwater and sediment fluxes for the Lago General Carrera–Buenos Aires (LGC–BA) ice lobe of the former Patagonian Ice Sheet between ~18–17 cal ka BP. High-frequency cyclicity in varve thickness series are investigated using spectral analyses methods, and yield significant periodicities at 2–8, 20–30, and 40–50 years. Most prominent are the 2–8-year cycles, which are interpreted as evidence for El Niño-Southern Oscillation (ENSO)-like controls on inter-annual ice sheet ablation patterns, and suggest that glaciolacustrine varve thickness offers a proxy for austral summer climate conditions. Decadal cycles represent possible modes of Pacific Decadal Variability (PDV) and/or natural variability within the ENSO system. ENSO-like cyclicities are strongly expressed over the full 2–8-year bandwidth between 17,835–17,273 cal a BP. Between 17,186–16,982 cal a BP, 2–5-year cycles dominate, hinting at a potential shift in ENSO periodicity. However, an internal control is also probable, where ice-front retreat and lower sediment fluxes dampened the sensitivity of the record. Despite this, the record provides the first empirical evidence for sub-decadal climate influences on the mid-latitude cryosphere during the last deglaciation, and the potential role of low-latitude (tropical) climate variability on ice sheet demise.

6.1 Introduction

Inter-annual to multi-decadal variability plays a major role in regulating global climate and weather patterns (Allan, 2000; Henley, 2017). Climate anomalies associated with short-term variability can have profound effects on terrestrial systems, which includes contemporary glaciers, ice sheets and ice shelves (Francou et al., 2004; Stammerjohn et al., 2008; Steig et al., 2012; Dutrieux et al., 2014; Walker and Gardener, 2017). However, modern observational records and climate indices are limited in temporal coverage, while climate models cannot yet reproduce all observed features of short-term climate variability (Power et al., 2017). Palaeoclimate records with annual/decadal resolution are therefore fundamental to improving knowledge on the causes, effects, and predictability of short-term climate variations, under a range of background climate states.

Terrestrial glacial records show that former ice sheets of the southern mid-latitudes responded to centennial- and millennial-scale climate changes through the last deglaciation (e.g. Moreno et al., 2015; Putnam et al., 2010; 2013a, 2013b; Strelin et al., 2011; Hall et al., 2013). These records have been used to elucidate potential climatic controls on the initiation and rates of ice sheet decay (Denton et al., 1999a; Putnam et al., 2013a; Moreno et al., 2015). However, a limitation of previous work has been the ability to resolve annual/decadal climate changes, and whether former ice masses were sensitive to such changes. Such information is essential for more complete understanding of ice sheet deglaciation, especially as such changes have far-reaching impacts on the contemporary cryosphere (e.g. Walker and Gardener, 2017).

In southern South America, and the southern mid-latitudes more generally, uncertainties associated with sub-centennial glacial changes, leave major questions open, such as the influence of tropical Pacific climate on ice sheet retreat. The El Niño-Southern Oscillation (ENSO), for instance, represents the primary mode of global inter-annual climate variability (Allen, 2000). However, the importance of ENSO across the last deglaciation is unknown, as records capable of detecting such short-term changes (e.g. Pike et al., 2013; Swann et al., 2013) are rare. While ENSO influences have been identified in high-resolution Holocene lake sediment (Ariztegui et al., 2007; Boës and Fagel, 2008; Fagel et al., 2008) and tree-ring (Villalba, 2009) records in Patagonia, to the authors' knowledge, no annually-resolved records capturing the onset of deglaciation currently exist in the southern mid-latitudes. The potential contribution of high-frequency climate variability to mid-latitude ice sheet demise thus remains largely unknown.

This paper presents a unique, annually-resolved record of meltwater and sediment flux from the former Patagonian Ice Sheet, derived from glaciolacustrine varves at Lago General Carrera (Chile)–Buenos Aires (Argentina; LGC–BA; 46.5°S; Figure 6.1). Recent examination of the LGC–BA sediment record has generated a calendar-year chronology for the timing of deglaciation in this valley, as well as multi-decadal to centennial-scale changes in the dynamics and rates of ice sheet retreat (Chapter 5). Here, we focus on annual/decadal varve thickness variability. Specifically, we aim to identify the role of high-frequency climate oscillations on sediment flux through the ~18–17 ka time-window, a period of major climatic reorganisation (Denton et al., 2010) and widespread deglaciation of the southern mid-latitudes (Putnam et al., 2013a; Moreno et al., 2015).

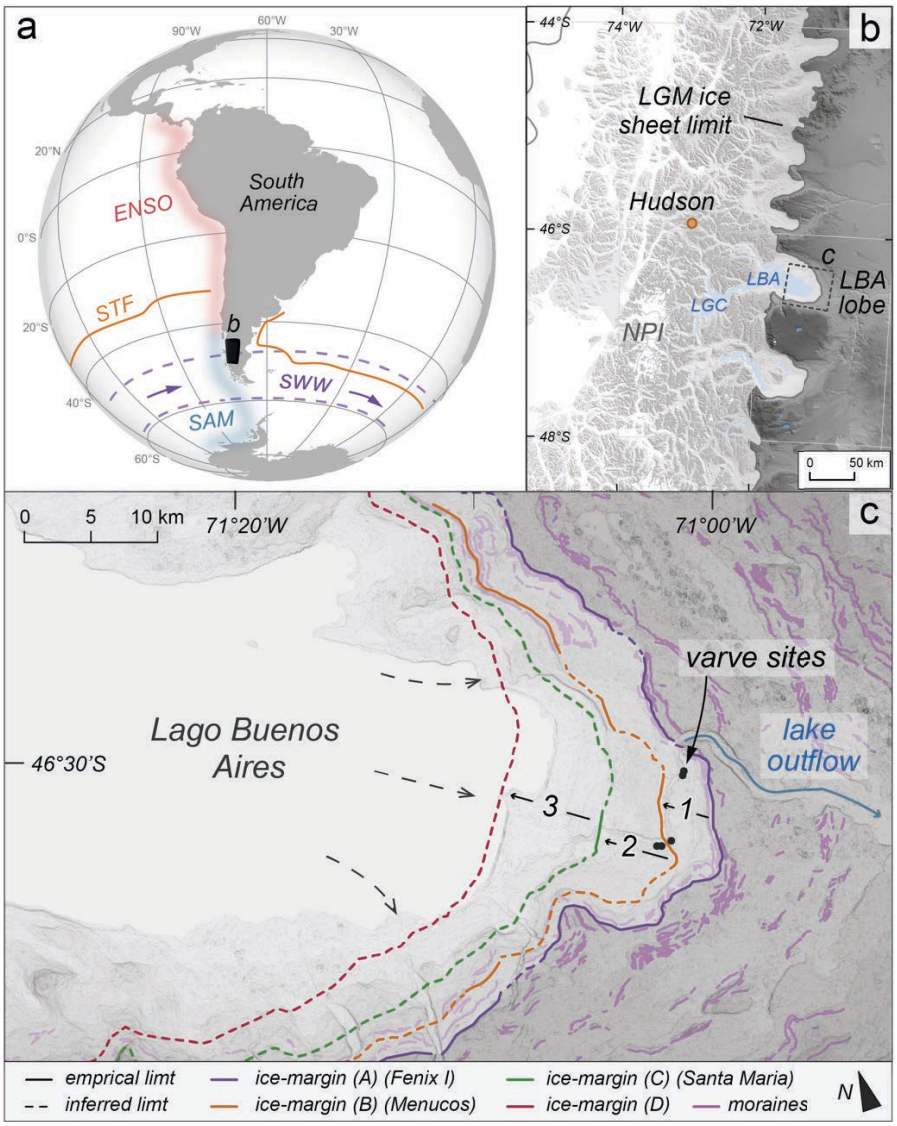

Figure 6.1. (a) Location of Lago General Carrera–Buenos Aires (LGC–BA) in southern South America, with present position of the Sub-Tropical Front (STF; cf. Orsi et al., 1995) and southern westerly wind system indicated. Approximate geographic extent of El Niño–Southern Oscillation (ENSO) and Southern Annular Mode (SAM) influences on South American climate cf. Villalba (2009). (b) Extent of the Patagonian Ice Sheet at the global Last Glacial Maximum (LGM) after Singer et al. (2004). (c) Retreat limits of the LGC–BA ice lobe from Chapter 5.

6.2 Site context

6.2.1 Regional climate setting

As one of the few landmasses in the southern mid-latitudes, Patagonia represents an important region for reconstructions of regional to hemispheric climate change (Killan and Lamy, 2012). Located at 46.5°S (Figure 6.1), LGC–BA sits within a climatically dynamic zone subject to both tropical and extra-tropical (high-latitude) ocean-atmosphere processes (e.g. Silvestri and Vera, 2003; Villalba et al., 2003; Garreaud et al., 2009; Moy et al., 2009), especially between 40–48°S where a strong blend of signals is suggested (Villalba, 2009). Recent studies demonstrate complex interactions between such processes, which can alter in importance on decadal timescales and dictate climate across the southeast Pacific region (e.g. Yeo and Kim, 2015; Fogt and Bromwich, 2006).

The El Niño–Southern Oscillation (ENSO) represents the primary tropical climatic influence over inter-annual timescales (e.g. Daniels and Veblen, 2004; Villalba, 2009; Garreaud et al., 2009), alongside several inter-decadal climate modes of ocean-atmosphere variability (Henley, 2017). ENSO is initiated in the equatorial Pacific and comprises warm (El Niño) and cool (La Niña) phases of anomalous sea-surface temperatures (SST) across the tropics and extratropics (Allen, 2000; Cane, 2005). The strongest SST anomalies in the Southeast Pacific sector are associated with 'conventional' eastern Pacific El Niño conditions, with warming centred on the western coast of South America (Yeo and Kim, 2015). Across Patagonia, ENSO-related climate anomalies, such as changes in sea-level pressure gradients (Schenider and Gies, 2004), are associated with fluctuations in the strength and latitudinal position of the southern westerly wind (SWWs) belt, influencing regional precipitation and surface air temperatures (Garreaud et al., 2009; Moy et al., 2009).

The Southern Annular Mode (SAM) represents the major high-latitude climate influence over Patagonia, and operates over weekly to decadal timescales (Sen-Gupta and England, 2006; Garreaud et al., 2009). The SAM defines a pressure gradient between Antarctica and the southern mid-latitudes (~40–50°S; Thompson and Wallace, 2000; Marshall, 2003). The positive phase of SAM is characterised by lower (higher) relative pressures over Antarctica (mid-latitudes) and a poleward contraction and intensification of the SWWs. The opposite pattern occurs during negative phases. Switches between SAM states influence surface temperatures, zonal wind speeds, and precipitation over southern South America (Sen-Gupta and England, 2006).

The climate state during the last deglaciation was characterised by major reorganisation and warming after the global Last Glacial Maximum (gLGM). Marine sediment cores from

the Chilean margin record an abrupt SST increase (Kaiser et al., 2005; Lamy et al., 2007, Caniupán et al., 2011) beginning at ~18 ka (cf. Lamy et al., 2015), broadly consistent with findings from southwest Pacific (Calvo et al., 2007; De Deckker et al., 2012) and south Atlantic (Barker et al., 2009) marine records. This warming has been interpreted to reflect a southwards migration of the SWWs and associated Sub-Tropical (STF) and Sub-Antarctic (SAF) oceanic fronts (Lamy et al., 2004, 2007) that removed the mid-latitudes from the cooling influence of the Antarctic Circumpolar Current (ACC) and westerly airflow. Sikes et al. (2013) postulate a potential consequence of this shift being a switch from high- to low-latitude control of climate in the southern mid-latitudes, including a shift to persistent ENSO-like conditions. Whether such changes influenced the terrestrial systems of Patagonia remains poorly understood, however, because of a scarcity of high-resolution records that can detect high-frequency (annual/decadal) climatic variability.

6.2.2 Glaciolacustrine setting and varve record

LGC–BA fills a deep, glacially-scoured ~140 km-long depression that extends from close to the North Patagonian Icefield (NPI), to the Argentine steppe east of the Patagonian Andes (Figure 6.1). During gLGM, the LGC–BA ice lobe occupied a position ~10–15 km east of LGC–BA, and constructed a series of moraines between ~26–19 ka ago (Kaplan et al., 2004, 2011; Douglass et al., 2006). During deglaciation, which commenced at ~18 ka (Chapter 5), a glacial lake system formed around the retreating ice-margin and ultimately coalesced with lake systems in Lago Cochrane–Pueyrredón further south (Turner et al., 2005; Glasser et al., 2016).

Glaciolacustrine laminated sediments deposited in these former lakes were first reported at LGC–BA by Caldenius (1932), and later examined by Sylwan (1989). Chapter 5 described the sedimentology of the laminated deposits, demonstrating a varve (annual) structure. Specifically, the deposits exhibit regular alternations of texturally distinct sub-layers comprising: (i) coarse component (silt) layers that are internally complex, and contain multiple laminations (Figure 6.2); and (ii) fine component (clay) layers that grade upwards from very-fine silt to clay (Figure 6.2). The coarse component forms in the melt season (spring/summer) as meltwater plumes transport sediment to the lake; and the fine component settles from suspension during the quiescent non-melt season (autumn/winter) under lake ice-cover (cf. Ashley, 1975; Ringberg and Erlström, 1999; Palmer et al., 2008, 2010, 2012; Ridge et al., 2012). Other notable features include the frequent presence of coarser sand laminations in the melt season layers (Figure 6.2a-c). To develop a robust composite chronology from five sites, varve thickness

measurements were standardised (e.g. Heideman et al., 2015) and correlated on a varve-by-varve basis, using frequent sedimentary marker layers that interrupt regular varve sedimentation (Chapter 5). The calendar age of the record was derived through geochemical identification of the Ho tephra layer (cf. Weller et al., 2014), deposited within varve-year (vyr) 605 ± 27 in the composite chronology. Using eight published radiocarbon ages (Miranda et al., 2013) the tephra age was recalibrated to 17,378 ± 118 cal a BP, and calendar-year ages extrapolated across the remaining varves. This constrains the varve record between 17,997 ± 144 and 16,982 ± 127 cal a BP (Chapter 5).

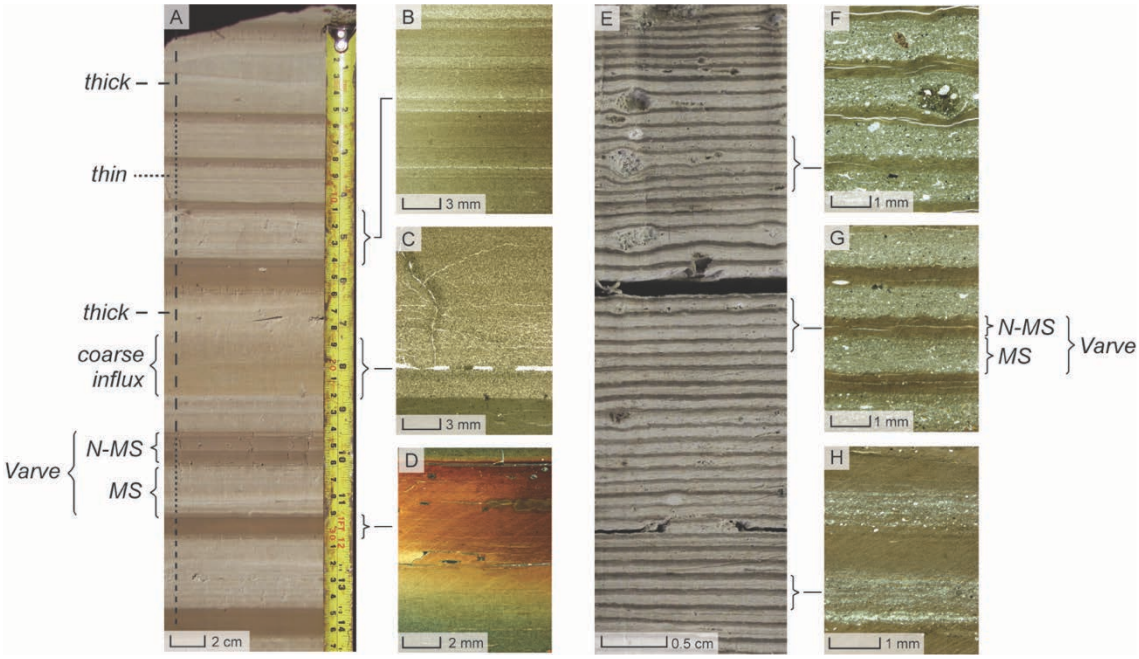

Figure 6.2. Examples of varved sediment structures. MS = melt season layer; N-MS = non-melt season layer. (A) Typical 'thick' varves showing cyclical thickness pattern with coarse-grained sediment influx in thickest melt season layer. (B) Thin section photomicrograph of internal melt season structure, showing multiple fine laminations. (C) Graded fine sand to medium silt layer within melt season. (D) Internal non-melt season structure, grading from very fine silt to clay. (E) Typical 'thin' varves, with ice-rafted debris (IRD); and (F–H) common internal composition and structure observed at microscale.

6.3 Materials and methods

6.3.1 Analysed varve intervals

The 994 ± 36 vyr composite record described above was investigated for spectral analyses of varve thickness changes, which are hypothesised to reflect influences of regional climate variability. We examined 3 continuous varve intervals of *n*=272 (17,835–17,564 cal a BP); *n*=290 (17,562–17,273 cal a BP); and *n*=205 (17,186–16,982 cal a BP) vyr duration. These intervals encompass 767 varves of the total 994 ± 36 vyr chronology.

The remaining 227 years were omitted because of minor breaks (<10-years) within these segments of the composite chronology (see Chapter 5). Varve counting errors are minimal, falling between 1.72–4.80% for the examined sections (Table 6.1). In previous studies, linear interpolation has been used to fill minor breaks in varve sequences and generate longer time-series for spectral analyses (e.g. Ólafsdóttir et al., 2013). However, this procedure biases the spectral estimate by increasing the autocorrelation in the time-series (Mudelsee, 2010). This justifies our focus on selected unbroken varve intervals, given the known inaccuracies of linear varve interpolation methods (Schlout et al., 2012), and the non-linear sedimentation rates typical of ice-contact proglacial lake systems (Gustavson, 1975; Smith and Ashley, 1985).

Table 6.1. Summary statistics and calendar-year age range for varve Intervals 1–3 used for spectral analysis. MS = melt season; N-MS = non-melt season.

Interval	Age		Error		Relative thickness	
	vyrs	cal a BP	vyrs	%	MS %	N-MS %
1	149–420	17,835–17,564	13	4.80	85.72	14.28
2	421–710	17,562–17,273	5	1.72	79.91	20.09
3	790–994	17,186–16,982	5	2.44	55.21	44.79

6.3.2 Spectral analysis

Our objective was to explore the potential climate significance of short-term varve thickness cycles, so low-frequency (≥centennial-scale) components were filtered out. The non-linear nature of most low-frequency trends (Mudelsee, 2013) prohibited the simple subtraction of a linear least-squares regression for trend removal. Instead, we use Singular Spectrum Analysis (SAA; Vautard and Ghil, 1989), which can decompose a time series into non-linear trends, periodic components and noise. We applied SSA using the “Rssa” package in R (Golyandina and Korobeynikov, 2014) to isolate leading non-linear, low-frequency trends. Window length (*L*) was optimised for each varve interval, and followed the recommendation that *L* should approximate, but not exceed, one-half the series length (Golyandina and Zhigljavsky, 2013; Golyandina and Korobeynikov, 2014). Centennial-scale (~120–290-year; Figure S1 in Appendix) non-linear trends (Figure 6.3) were subtracted from the varve series, and the residuals used for spectral analyses.

The detrended varve thickness series were examined for periodic features using the REDFIT program of Schulz and Mudelsee (2002; using ‘Past3’ software cf. Hammer et al., 2001), which is widely applied in palaeoclimatology (Mudelsee, 2013). This program calculates a bias-corrected Lomb-Scargle periodogram (Lomb, 1976; Scargle, 1982) and

a theoretical red (autoregressive, AR(1)) noise background using the null hypothesis that the data are red-noise. The computation then tests if spectral peaks are significant against the theoretical red-noise background. REDFIT uses Welch overlapped segment averaging, where the number of segments control the smoothing of the time-series. We calculated periodograms using 1 segment, i.e. no smoothing, given the subjective nature of selecting an appropriate number of segments (Ojala et al., 2015). 'False-alarm' significance levels (90–99%) were computed using parametric approximations (chi-squared) and Monte Carlo iterations (n=1000) of the AR(1) process, to ensure confidence in estimated periodicities. For comparison, we repeated the analysis using the widely applied Multi-Taper Method (MTM; Thomson, 1982) and 1 or 2 tapers (with 1 taper being most conservative, but minimising spectral leakage). If the REDFIT and MTM methods yield similar periodicities we can assign greater confidence to our results.

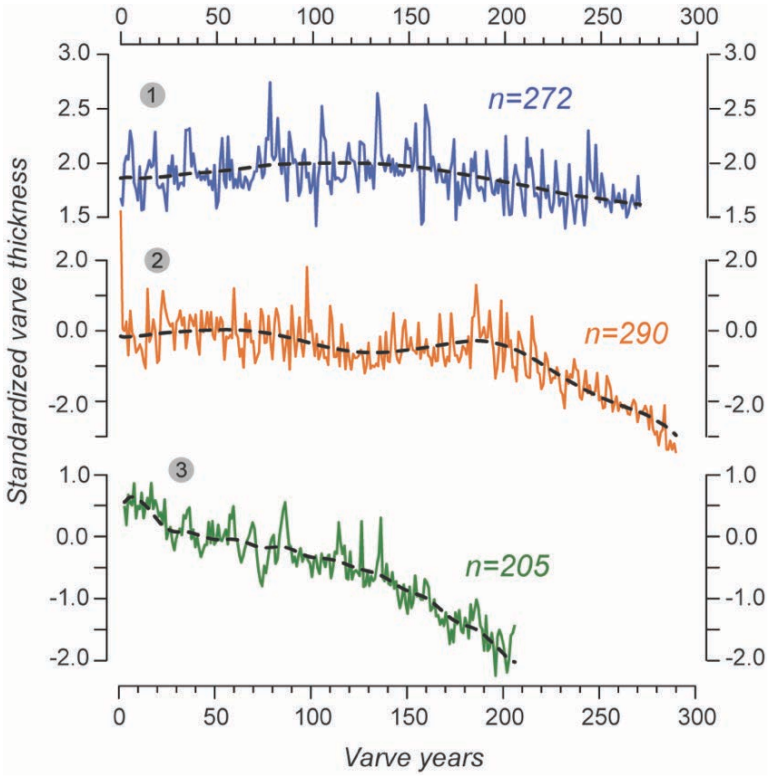

Figure 6.3. Original standardised varve thickness for Intervals (a) 1; (b) 2; and (c) 3, along with respective non-linear long-term trends estimated through SSA and removed prior to spectral analysis.

In addition, continuous wavelets (Torrence and Compo, 1998) were derived for each varve thickness series, to investigate temporal variations in spectral power. This analysis (applied in 'Past3' software) used the Morlet mother wavelet, the most commonly used wavelet in geophysics for sequences containing non-stationary power at different frequencies (Torrence and Compo, 1998). Varve series were zero-padded to limit edge effects and a "cone of influence" calculated. Prior to computing wavelets, autoregressive–moving-average (ARMA) analysis (Melard, 1984) was undertaken to determine an appropriate lag-1 coefficient (null hypothesis) for a red-noise computation of 95% (chi-squared) confidence regions.

6.4 Results

6.4.1 High-frequency variations in varve thickness

Regular short-term variations in varve thickness are visually evident as intervals of similar duration separating thickness maxima (peaks) or minima (troughs) (Figure 6.4b). The shortest oscillations contain peaks (troughs) every ~2–8 years, and exhibit a common structure: (i) an abrupt, 1-year increase from thickness minima to maxima; followed by (ii) a return to thickness minima over the succeeding ~2–5 years. Sometimes, the decreasing limb exhibits a secondary, lower amplitude thickness peak, normally 2 or 3 years after the initial thickness maxima. Whilst not always perfectly resolved, this structure can be readily observed in field sections for thicker varves (Figure 6.2a). The inter-annual patterns appear to occur alongside decadal periods of increasing (decreasing) thickness observed over ~20–60-year timescales. These observations are statistically tested using the REDFIT (Figure 6.4) and MTM (Figure S2 in Appendix) estimations. We describe significant (>95%) frequencies below.

The REDFIT power spectrum of varve Interval 1 (17,835–17,564 cal a BP) and Interval 2 (17,562–17,273 cal a BP) shows significant periodicities at 2.00–2.20, 3.20–3.50, 4.10–4.90, 5.90, 6.00–6.80, 7.10–7.70-year wavelengths (Figure 6.4c). Additional periodicities are recorded at 5.90-year wavelength in Interval 1; and the 8.40 and 52.60-year wavelengths in Interval 2. The REDFIT estimate for varve Interval 3 (17,186–16,982 cal a BP) shows significant periodicities at 2.50, 3.10–3.15, 5.60–5.70, 9.00–10.00, and 24.60-year wavelengths (Figure 6.4c). Compared with Intervals 1–2, the most obvious difference is the lack of spectral power at the ~6.00–7.00-year wavelengths; however, similarities are evident for the ~2.00, 3.00, and 5.00-year bands. 23.80-year and 19.20-year cycles are present in Intervals 2–3, however, these peaks only surpass the 90% significance limit (Figure 6.4c). The MTM analysis yields comparable periodicities at the

90–99% confidence range for all three varve intervals (Figure S1 in Appendix) suggesting that the REDFIT predictions are robust.

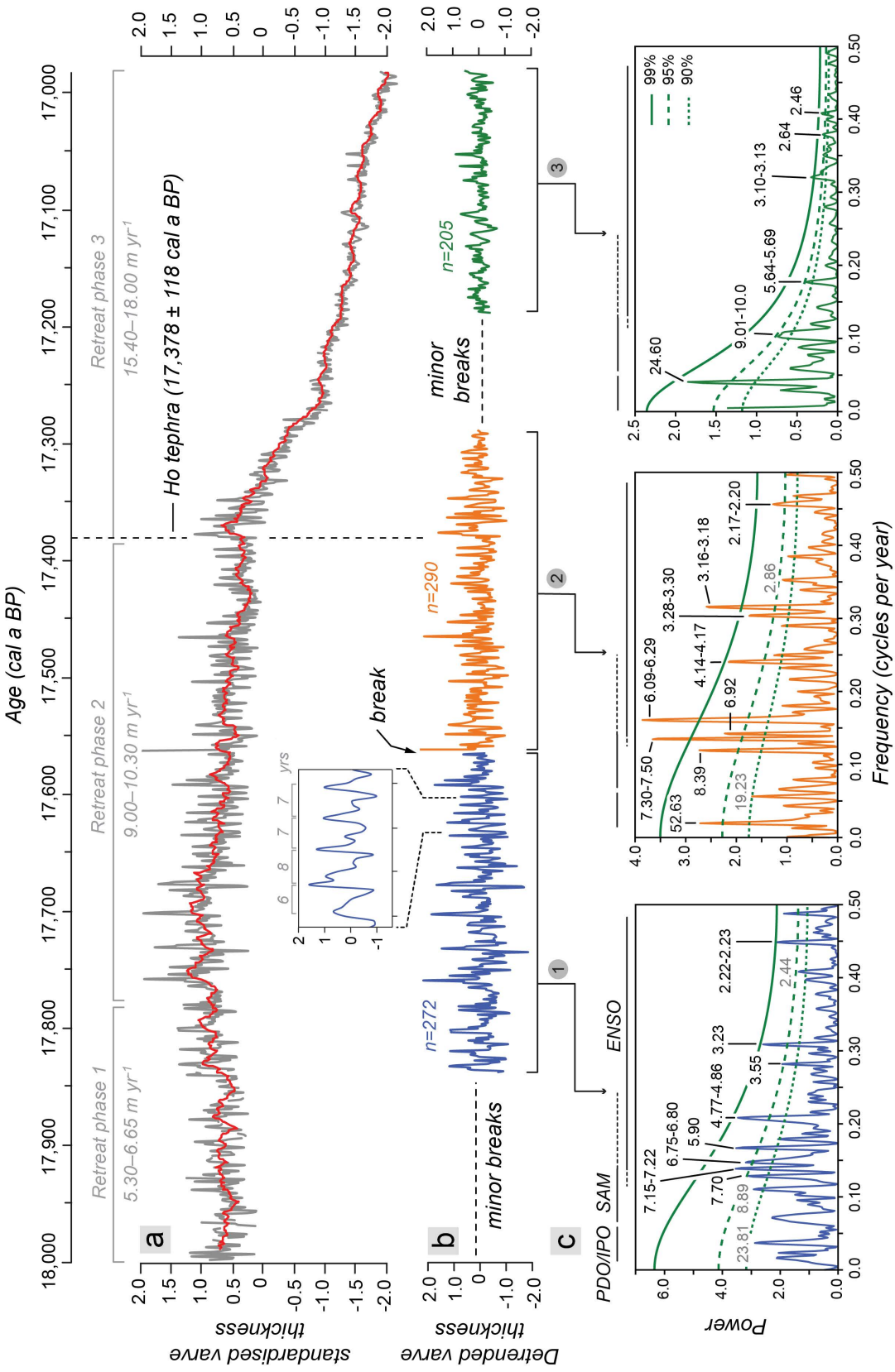

Figure 6.4. (a) Standardised (z-score) composite Fenix Chico Master Varve Chronology, with position and age of Ho tephra indicated. Average ice lobe retreat rates for retreat phases 1–3 (as shown in Figure 6.1), as defined in Chapter 5. (b) Detrended varve thickness intervals used for spectral analysis, and zones with breaks in thickness record that were omitted from analysis. Expanded graph shows common structure of inter-annual thickness variations, with interval in years between peaks indicated. (c) REDFIT power spectra (in years) for Intervals 1–3 against 90, 95 and 99% significance levels. Frequency bandwidths of modern ENSO, SAM and PDO/IPO variability are shown along upper axis.

6.4.2 Temporal variations in spectral periodicities

The wavelet analysis demonstrates variable behaviour of periodic features through time (Figure 6.5a). Inter-annual cycles with power concentrated in the 2–8-year wavelengths are strongly expressed in Intervals 1–2, between 17,835–17,273 cal a BP, with most power present at the 5–8-year wavelengths of this broader band (shown by black 95% confidence regions in Figure 6.5a). Nonetheless, temporal variations in both the amplitude and variance of 2–8-year periodicities exist, as evident in bandpass filtered varve series (Figure 6.5b). Zones of greatest amplitude and variance (Figure 6.5b) tend to coincide with the most significant expression of 2–8-year frequencies in the wavelet transforms (Figure 6.5a). Some of these high-amplitude thickness peaks exceed (interval-specific) 2σ limits (Figure 6.5b), and record episodes of particularly high sedimentation rate (thick varves). In Interval 3, between 17,186–16,982 cal a BP, the 6–8-year periodicities of the broader 2–8-year band disappear (Figure 6.5a). Shorter 2–5-year cycles remain, but vary in temporal expression. Significant 2–3 year cycles occur between 17,186–17,138 cal a BP, are absent over the next ~65 years, and then resume over a wider bandwidth (2–5 years) until the end of Interval 3. The 2–5-year cycles that characterise the final ~75 years exhibit the greatest amplitude and variance in bandpass filtered varve thickness data (Figure 6.5b).

Decadal cycles are expressed persistently over the investigated time-window, but vary in spectral power. The first ~80 years of Interval 1 exhibits significant power at ~20–30 and 30–50-year wavelengths, before the strong initiation of inter-annual cycles (Figure 6.5a). The bandpass filtered thickness series confirms this pattern, displaying decreased variance in the 2–7 year wavelengths, but greater variance and high-amplitude peaks at the 20–60 year wavelengths (Figure 6.5c). 20–30 and 30–50-year wavelengths extend over the next ~200 years, but are less significant (Figure 6.5a). Significant power at 30–50-year wavelengths exists throughout Interval 2, alongside the previously mentioned high-frequency cycles. Similarly, a persistent 20–30-year cycle exists through Interval 3, alongside temporarily significant regions at 10–20-year wavelengths (Figure 6.5a). For

both Intervals 2 and 3, the 20–60-year bandpass data demonstrate constant behaviour in decadal thickness amplitudes and variance (Figure 6.5c).

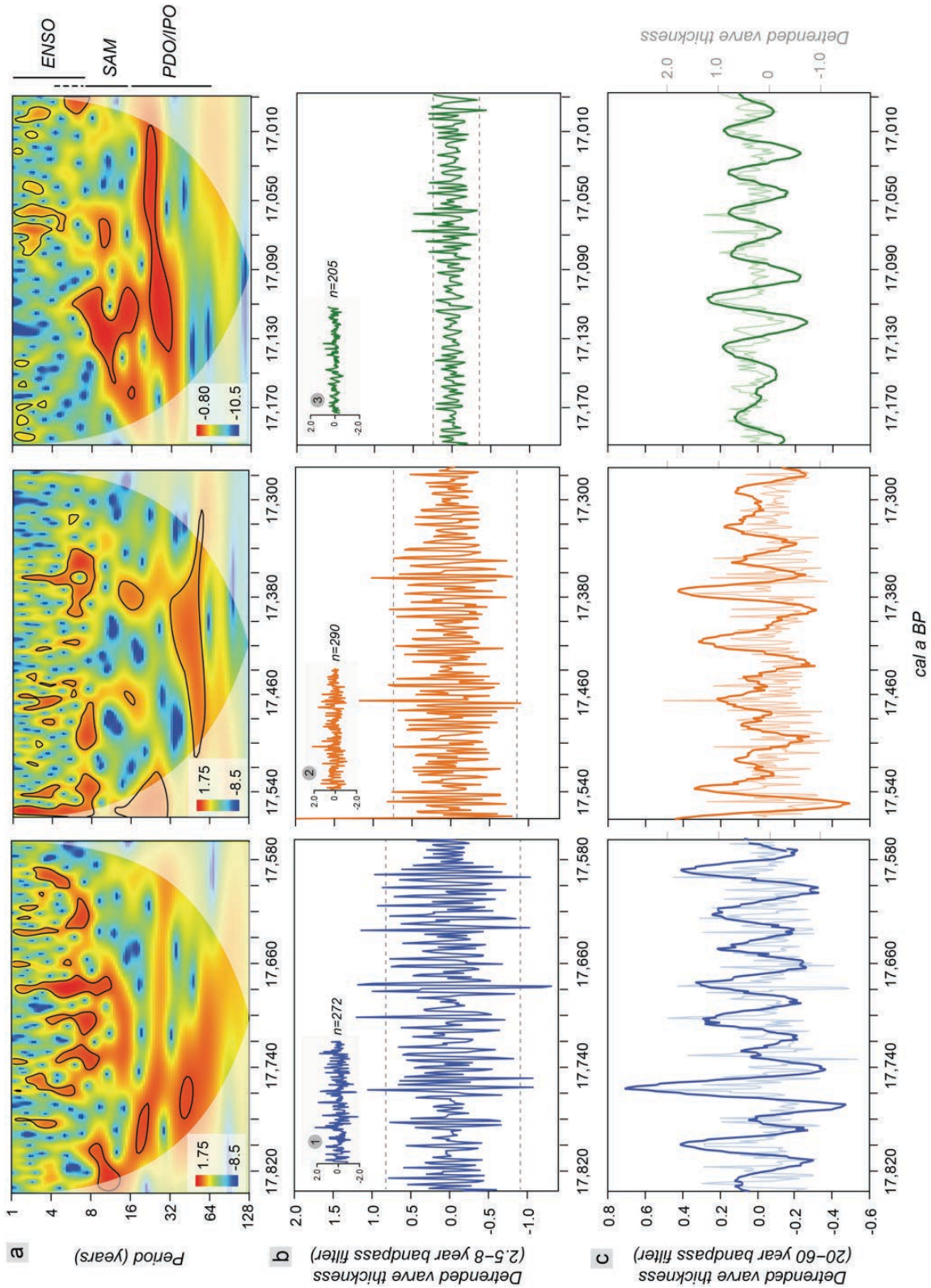

Figure 6.5. (a) Continuous wavelet transforms for Intervals 1 (left), 2 (centre) and 3 (right). The black contour is the 95% significance level using a red noise background spectrum, with lag-1 coefficients of 0.26, 0.21 and 0.32 defined using ARMA analysis. Shaded region represents cone of influence. (b) Gaussian bandpass filtered varve thickness series at 2.5–8 years, with 2 standard deviation limits shown (grey horizontal lines). (c) Gaussian bandpass filtered varve thickness series at 20–60 years, with unfiltered varve thickness beneath

6.5 Discussion

6.5.1 Comparing spectral periodicities to modes of climate variability

Previous work has documented both tropical and/or high-latitude influences on the climate of southern South America (Garreaud et al., 2009; Moy et al., 2009; Villalba, 2009), often through interactions with the moisture-bearing southern westerlies (e.g. Schneider and Gies, 2004). Potential climatic influences on LGC–BA varve thickness are explored through comparisons with periodic components of well-documented modes of contemporary climate variability (Table 6.2).

6.5.1.1 Inter-annual cycles

Significant inter-annual cycles at 2.00–2.20, 3.20–3.50, 4.10–4.90, 5.90, 6.00–6.80, and 7.10–7.70 years (Figure 6.4c) overlap the widely documented 2–8-year ENSO bandwidth (e.g. Mann and Park, 1994; D'Arrgio et al., 2005). The 2–8-year bandwidth comprises a quasi-biennial (2–3 years) component (Rasmusson et al., 1990) related to the duration of ENSO episodes, or the switch between El Niño and La Niña phases, and a low frequency (3–8 years) component related to the spacing of intense El Niños (Zebiak and Cane, 1987; Graham and White, 1988). Our dataset (Figure 6.4c) replicates this feature of contemporary ENSO variability (Figure S4 in Appendix). Note, however, that the 2.00–2.20-year periodicities are close to the Nyquist frequency (1/2 x sampling interval) of annual sampling, and should be viewed with caution. Despite close overlap with the spectral range of modern ENSO variance, Yuan and Yonekura (2011) recently detected inter-annual (3–7-year) periodicities in SAM indices and weather station datasets located between ~30–75°S, posing a problem for discriminating between ENSO- and SAM-like variability in LGC–BA varve thickness. This is important to consider given the overlapping spatial imprint of these modes at present (Garreaud et al., 2009). However, Yuan and Yonekura (2011) used just one terrestrial Patagonian weather station at Punta Arenas (53°S), located 6.5° south of LGC–BA (46.5°S) in a zone of stronger SAM than ENSO variability (Villalba, 2009). Moreover, REDFIT analyses of Niño3.4/SOI and SAM indices reveal close similarity between LGC–BA varve and modern ENSO cyclicity, and not SAM cyclicity (Figure S4 in Appendix). Support for a

dominant ENSO influence over inter-annual varve thickness fluctuations also comes from consideration of the ocean-atmosphere setting at the time of varve accumulation, as discussed in a subsequent section (section 6.5.3).

The 8.40-year periodicity in Interval 2 (95% confidence; plus an 8.90-year period at 90% confidence in Interval 1; Figure 6.4c) marginally exceeds the contemporary 2–8-year ENSO bandwidth, along with the 9.00–10.00-year periodicities in Interval 3 (Figure 6.4c). These cycles may relate to: (1) quasi-decadal ENSO oscillations that are documented at 9–13-year wavelengths and thought to arise from interactions of 2–3 (Quasi-Biennial Oscillation) and 3–8-year ENSO components (Allan, 2000), or decadal changes in tropical Pacific background mean state that modulate ENSO amplitude (Lohmann and Latif, 2005); (2) decadal variability in the SAM, which shows a dominant 8–16-year bandwidth (Yuan and Yonekura, 2011); or (3) interactions between ENSO and SAM-like variability, which cannot be ruled out given their coexistence in some observational records from the southeast Pacific (Yeo and Kim, 2015) and Southern Ocean (e.g. Simmonds and King, 2004; Fogt and Bromwich, 2006; Stammerjohn et al., 2008; Walker and Gardener, 2017) regions. Alternatively (4) the varve thickness signal may be affected by local processes during these periods (section 5.3).

6.5.1.2 Decadal cycles

The 24.60 and 52.60-year periodicities recorded in intervals 2–3 (95% confidence; and in interval 1 at 90% confidence) may relate to leading modes of Pacific Decadal Variability (PDV; Henley, 2017; Table 6.2). These include the Pacific Decadal Oscillation (PDO; Minobe, 1997; Mantua and Hare, 2002), Inter-decadal Pacific Oscillation (IPO; Power et al., 1999; Follan et al., 2002; Henley et al., 2015), and South Pacific Decadal Oscillation (SPDO; Shakun and Shaman, 2009; Chen and Wallace, 2015). These features modulate Pacific sea-surface temperature (SST) patterns in an ENSO-like fashion, demonstrating warm and cool phases (Henley, 2017). The PDO and SPDO are considered the north and south Pacific nodes of the Pacific-wide IPO (Henley et al., 2015). Frequency reconstructions demonstrate minimal PDV variance at <10-year bandwidths, but strong variance between 10–15, 20–50, and 50–70 year bandwidths (e.g. Biondi et al., 2001; D'Arrigo et al., 2001; Gedalof and Smith, 2001; Linsley et al., 2008; Table 6.2), and our data records power in these bandwidths. Contemporary PDV can modulate the strength of ENSO teleconnections (Wang et al., 2014; Henley et al., 2015) across South America (Andreoli and Kayano, 2005) and other south Pacific landmasses (e.g. Kiem et al., 2003; King et al., 2013). Moreover, PDV appears to be stimulated by tropical-extratropical climate interactions related to ENSO, alongside

stochastic atmospheric forcing (Newman et al., 2016; Henley, 2017), supporting the detection of ENSO-like periodicities, and suggesting their co-occurrence may have modulated LGC–BA varve thicknesses. However, note that the amplitude of ENSO can vary naturally over multi-decadal timescales, due to changes in oceanic mean state that influence modulating feedback processes (e.g. Li et al., 2011; Borlace et al., 2013; Boucharel et al., 2015). These studies report inter-decadal periodicities of ~50–70 years, compatible with the 52.60-year cycle recorded in interval 2.

Table 6.2. Summary of spectral peaks in Intervals 1–3 and their possible forcing mechanisms. PDV= Pacific Decadal Variability; IPO = Interdecadal Pacific Oscillation; PDO = Pacific Decadal Oscillation; ENSO = El Niño-Southern Oscillation; SAM = Southern Annular Mode.

Cycles (years)	Significance	Possible forcing	References
52.63	95%	PDV (IPO/PDO)	Minobe, 1997; Power et al., 1999; D'Arrigo et al., 2001; Gedalof and Smith, 2001; Mantua and Hare, 2002; Linsley et al., 2008; Henley et al., 2015
24.60	95%		
9.01–10.00	95%	ENSO(quasi-decadal)/SAM	Allen, 2000; Lohmann and Latif, 2005; Yuan and Yonekura, 2011
8.39	95%		
7.70	95%	ENSO	Zebiak and Cane, 1987; Graham and White, 1988; Mann and Park, 1994; D'Arrigo et al., 2005;
7.50–7.30	99%		
7.22–7.15	95%		
6.92	95%		
6.80–6.75	95%		
6.29–6.09	99%		
5.90	95%		
5.69–5.64	95%		
4.86–4.77	95%		
4.17–4.14	95%		
3.55	95%		
3.30–3.28	95%		
3.23	95%		
3.18–3.16	99%		
3.13–3.10	99%		
2.64	95%		
2.46	95%		
2.23–2.22	95%		
2.20–2.17	95%		

6.5.2 Influence of high-frequency climate variability on varve thickness

With no contemporaneous regional climate data at a sufficient temporal resolution to calibrate our varve thickness series, we evaluate possible mechanistic linkages between hypothesised climate influences, and processes that control varve sedimentation rates. In glaciolacustrine systems, sediment flux represents the integrated rate of sediment erosion and the capacity of the meltwater system to deliver stored erosion products to the lake (Larsen et al., 2011). Over inter-annual to decadal timescales, changes in the efficiency of the meltwater system are most important (Leonard, 1997; Loso et al., 2006; Ólafsdóttir et al., 2013), where increased (decreased) meltwater production leads to

increased (decreased) sediment transfer and the accumulation of thicker (thinner) varves. Meltwater production rates are likewise considered most important at LGC–BA. The LGC–BA proglacial lake system was likely dominated by sediment derived from directly glacier margins (Chapter 5). Moreover, sediment availability likely remained high throughout the studied time-window, due to the relative proximity of the ice-margin (Figure 6.1c) and the high glacier-to-lake volume ratio. As such, the capacity to mobilise and deliver sediments, rather than major changes in the volume of glacially-eroded materials, was likely most important.

Given this, potential climatic influences on meltwater production are considered. Previous work demonstrates that on inter-annual to decadal timescales, the climate during the melt season exerts strong control on meltwater production (Hodder et al., 2007). Significant correlations exist for comparisons of varve thickness and spring/summer air temperature (Leeman and Niessen, 1994; Ohlendorf et al., 1997; Moore et al., 2001; Hambley and Lamoureux, 2006; Loso et al., 2006; Bird et al., 2009; Cook et al., 2009; Thomas and Briner, 2011; Ólafsdóttir et al., 2013; Glur et al., 2015) and/or precipitation (Lamoureux, 2000; Cockburn and Lamoureux, 2008; Chutko and Lamoureux, 2008), with temperature correlations often being strongest, particularly in larger ice-dammed lake systems that are more analogous to palaeo-LGC–BA (Loso et al., 2006; Ólafsdóttir et al., 2013). Air temperatures tend to correlate positively with glacier ablation (Ohmura, 2001), and warmer conditions contribute towards the accumulation of thicker varves due to greater melting, run-off production, and consequent sediment transport (Loso et al., 2006). We hypothesise that systematic changes in melt season climate were the primary control on short-term variations in the thickness of LGC–BA varves. Melt season air temperatures, and possibly melt season duration (e.g. Ridge et al., 2012), likely represent the most important controls on annual meltwater production and sediment flux.

On the assumption that LGC–BA varve thickness offers a proxy for meltwater production and sediment transport (i.e. the efficiency of the glacial meltwater system), we consider the potential impacts of short-term climate variability on Patagonian Ice Sheet ablation (Figure S5–S9 in Appendix). In the inter-annual bands, spectral analyses suggest that ENSO, and possibly SAM-like variations, were most important (Figure 6.4c and Figure 6.5). NCEP/NCAR reanalyses data indicate that during El Niño (warm) episodes, which manifest most strongly in austral summer (DJF), the Intertropical Convergence Zone (ITCZ) weakens and/or migrates southwards, while SWW strength decreases south of 45°S (Schneider and Gies, 2004; Garreaud, 2007; Boucher et al., 2011; Figure S4–S5 in Appendix). Because the SWWs deliver cool, moist air to terrestrial Patagonia

(Schneider and Gies, 2004), weaker than average summer (DJF) westerlies instigate warmer surface air temperatures (Garreaud et al., 2009; 2013) and would have enhanced glacier surface ablation. Moreover, lower wind speeds are shown to limit the transfer of energy from (more efficient) melting to (less efficient) sublimation, whilst reduced cloud cover leads to increased incoming short-wave radiation and direct supraglacial melting (Francou et al., 2004). Correlations between instrumental time-series and the Southern Oscillation Index (SOI) depict a similar pattern to reanalyses data (Figure S6 in Appendix). Daniels and Veblen (2004) demonstrate that El Niño episodes over northern Patagonia coincide with warm, dry summers (DJF), and overall warmer annual conditions. Similarly, Villalba (2009) confirm a tendency for warm and dry summers in northwestern (39–44°S) Patagonia during El Niño episodes. In an earlier investigation, Villalba et al. (2003) showed that El Niño-related summer temperature anomalies were strongest on the Argentine steppe east of the Patagonian Andes, the zone occupied by the former LGC–BA ice lobe ablation zone. These data suggest that peaks (maxima) in varve thickness (Figure 6.4b) may record El Niño warming events that increased Patagonian Ice Sheet melting and, in turn, meltwater and sediment fluxes through the glacier. The lower amplitude thickness maxima sometimes observed 2–3 years after this initial peak (Figure 6.4b) may record (i) La Niña (cold) conditions that enhanced precipitation (Daniels and Veblen, 2004) and glacial surface run-off; or (ii) sediment recovery after extensive flushing of the glacial meltwater system 2–3 years earlier during an El Niño (warm) event. As these peaks always follow a high-amplitude swing from thickness maxima (year-1) to minima (year-2 or 3), we suggest that they represent sediment recovery 2-3 years after an El Niño event.

El Niño events may also have impacted melt season duration. Correlations of gridded temperature data with the Multivariate ENSO Index (MEI) demonstrate warmer than average conditions over central and northern Patagonia during austral summer (DJF) and autumn (MAM; Garreuad et al., 2009). Similarly, Yeo and Kim (2015) model positive SST anomalies (warming) in the southeast Pacific (40–70°S) lasting from austral summer (DJF) to autumn (MAM), under conventional eastern Pacific El Niño conditions. The length of the melt season, therefore, may have been an additional factor in increasing total annual sediment yields during El Niño episodes, by extending the period of ice sheet ablation, meltwater production, and sediment transfer.

The influence of potential PDO/IPO-like variations are similar in terms of expression (Figure S7 in Appendix), as well as intimately associated to ENSO variance (Power et al., 1999; Henley, 2017). The positive (warm) and negative (cool) phases of the IPO are associated with quasi-stable SST anomalies over decadal timescales, which show

strong correlations along the South American west coast and into the southeast Pacific sector (Henley et al., 2015). Moreover, these phases influence hemispheric air temperatures, with greater warming during positive phases (Meehl et al., 2013; England et al., 2014). Thus, PDO/IPO variations may have increased (decreased) the amplitude of ENSO warming (cooling) events (e.g. Wang et al., 2014), causing decadal periods of greater (lesser) ice sheet melting and sediment mobilisation.

The potential for SAM influences on ice sheet ablation cannot be completely disregarded based on spectral estimates (Figure 4c and 5). In mid-latitude South America, significant warming occurs during positive SAM phases (Thompson and Solomon, 2002; Gillett et al., 2006; Garreuad et al., 2009), especially in austral summer (DJF; Figure S8 in Appendix), due to a combination of enhanced horizontal advection, subsidence, and weaker westerlies that enhance solar radiation (Sen-Gupta and England, 2006). Consequently, it is not inconceivable that SAM-like variations, alongside tropical Pacific variations, may have influenced short-term fluctuations in glacier ablation and sediment discharges. Indeed, Villalba (2009) report significant correlations for comparisons of modern SAM indices and tree-ring growth anomalies for southern Patagonia, but note a gradual transition from tropical (ENSO) to high-latitude (SAM) climatic teleconnections between 40–47°S, with ENSO-related temperature anomalies dominant north of 47°S, and stronger SAM influences south of 47°S. However, comparison with regional climate proxy records (section 6.5.3 below) lend support to a dominant ENSO influence.

6.5.3 Comparison with records of deglacial climate variability

Cycles in LGC–BA varve thickness are indicative of possible teleconnections between the equatorial Pacific and mid-latitude South America between 18–17 ka, suggesting that ENSO variability may have provided an important element of hemispheric climate reorganisation at the onset of deglaciation. Currently, the exact state of ENSO activity during and after the gLGM remains controversial. During the gLGM, before the onset of deglaciation at LGC–BA, some studies argue for enhanced ENSO variability due to reduced east-west SST gradients across the equatorial Pacific (An et al., 2004; Koutavas and Joanides, 2012; Sadekov et al., 2013). Other studies, based on proxy data (Leduc et al., 2009; Wolff et al., 2011; Ford et al., 2015) and modelling investigations (Otto-Bliesner et al., 2006; Zhu et al., 2017), argue for reduced ENSO variability, possibly due to a deep mean thermocline in the eastern equatorial Pacific that inhibited upwelling of anomalous subsurface temperatures, and weakened dynamic feedbacks that enhance ENSO amplitude (Ford et al., 2015). One modelling simulation reveals active ENSO

variability in the tropics, but non-stationary teleconnections to the extratropics at the gLGM (Merkel et al., 2010).

The nature of ENSO variability during the last deglaciation, following the gLGM, also remains unclear because available palaeoclimatic proxy records are sparse or temporally poorly-resolved. However, a glaciolacustrine varve sequence from northeastern North America reveals 2–5-year varve thickness cycles, which are interpreted as evidence for ENSO activity between 17–13 ka (Rittenour et al., 2000). In South America, Rein et al. (2005) argue that ENSO activity increased at ~17 ka, based on the enhanced (millennial-scale) flux of continental sediments to the offshore Peruvian margin, interpreted to reflect more regular El Niño flood events. Other mid-latitude records are younger than the studied interval, and report both enhanced (Makou et al., 2010; Palmer et al., 2015) and reduced ENSO states (Pepper et al., 2004). Using their millennial resolution marine record, Rein et al. (2005) noted comparable timings for the onset of enhanced El Niño activity off Peru and Heinrich Stadial 1 (HS-1) cooling in the North Atlantic region, and suggested a possible link between these processes.

Both proxy (e.g. Wang et al., 2001; Placzek et al., 2006; Blard et al., 2011) and modelling (Timmermann et al., 2007) studies suggest that ITCZ migrated southwards in HS-1, in response to intense North Atlantic cooling and reorganisation of tropical climate (Denton et al., 2010). Southward migration of the ITCZ is thought to have propagated a poleward displacement of the mid-latitude westerlies (Anderson et al., 2009) and oceanic frontal systems (Barker et al., 2009; Sikes et al., 2009), leading to Southern Ocean upwelling and warming of the southeast (Kaiser et al., 2005; Lamy et al., 2007; Caniupán et al., 2011) and southwest (De Deckker et al., 2012) Pacific. Sikes et al. (2013) propose that the contraction of wind-driven oceanic fronts around Antarctica instigated a shift to persistent ENSO influences on New Zealand climate during deglaciation. Seasonally-resolved coral records from the south Pacific Ocean support this inference, suggesting that ENSO-related SST anomalies moved southwards at that time (Felis et al., 2012). Such changes are likely to have influenced central Patagonia, as southward migration of a coupled ocean-atmosphere frontal system (Lamy et al., 2007) would have delivered warmer subtropical waters to the mid-latitude Chilean margin. This supports a dominant equatorial Pacific (rather than high-latitude) influence on inter-annual variations of LGC–BA varve thickness and, in agreement with Sikes et al. (2013), suggests that ENSO-related climate variability accompanied large-scale meridional shifts at that time.

Hosing-experiments predict an intensification of ENSO variability under a slowdown of Atlantic meridional overturning circulation (AMOC; Timmermann et al., 2007; Merkel et

al., 2010; Liu et al., 2014), as would be expected during HS-1 (Ritz et al., 2013). In these simulations, southward displacement of the ITCZ causes weakening of the southeast trade winds, reduced Walker circulation, and expansion of the Western Pacific warm pool (WPWP). This weakens the east-west thermal gradient in the equatorial Pacific and amplifies ENSO through non-linear feedback mechanisms (Liu et al., 2014). Some models predict strong ENSO phase-locking during deglaciation, with the largest ENSO-related SST anomalies occurring during austral summer (DJF; Liu et al. (2014)), consistent with our suggestion that melt season ablation rates dominate high-frequency varve thickness variations. Southward migration of the coupled ocean-atmosphere frontal system (Lamy et al., 2007), and enhanced influence of low-latitude climate forcing, also account for PDO/IPO-like cycles in varve thickness, which at present manifest as ENSO-like changes in SST across the southeast Pacific (Henley, 2017). As previously stated, the influence of SAM-like variance on central Patagonian climate cannot be completely disregarded. While our analysis, supported by previous work, suggests strong ENSO influences in central Patagonia, annually-resolved records with the potential to detect SAM variability during the last deglaciation are sparse, and currently restricted to coastal Antarctica (Pike et al. 2013; Swann et al., 2013).

Annually-resolved changes in LGC–BA varve thickness provide the first strong evidence for ENSO influences on terrestrial southern South America during the earliest phases of deglaciation, consistent with some climate model simulations (Timmermann et al., 2007; Liu et al., 2014). This finding implies that ENSO was active by ~18 ka ago, ~1 ka earlier than reported previously in South (Rein et al., 2005) or North American (Rittenour et al., 2000) proxy records, and soon after a proposed episode of reduced ENSO activity during the gLGM (Otto-Bliesner et al., 2006; Wolff et al., 2011; Ford et al., 2015; Zhu et al., 2017).

6.5.4 Temporal influences on ice sheet melting

Having hypothesised connections between LGC–BA varve thickness and inter-annual (ENSO) to decadal (PDO/IPO) climate cycles, we consider their temporal evolution (Figure 6.5 and Figure 6.6). ENSO-like cyclicity, defined as variance within the 2–8-year bandwidths, was relatively weak before 17,756 cal a BP (Figure 6.6). The 20–50-year cycles that appear strongest before 17,756 cal a BP may record the dominance of PDO/IPO-like variations over this time. However, ENSO-like variance is strong in LGC–BA varve thickness after 17,756 cal a BP (Figure 6.6). This may suggest that either the glacial meltwater system was not as sensitive to inter-annual climate variability between 17,835–17,756 cal a BP, but became more sensitive after this time; or that ENSO

variability was initially supressed, but intensified significantly at 17,755 cal a BP. To place these changes into the longer-term context of glacier recession, between 17,835–17,766 cal a BP the ice-margin retreated slowly (Figure 6.4a), and stabilised temporarily at the Menucos moraine (Figure 6.1c; Chapter 5). Throughout this period, the pattern of varve thickness is stable, before gradually rising after ~17,850 cal a BP (Figure 6.4a), and interpreted to represent a gradual increase in the capacity of the glacial meltwater system to transport erosion products to the lake. The onset of decreasing varve thickness after 17,759 cal a BP, which coincides with the first strong expression of ENSO cyclicity, marks a switch to faster retreat rates (Figure 6.4a) and enhanced deglaciation (Chapter 5). Therefore, at present, and without any additional annually-resolved climate records in this region, we are unable to confidently discriminate whether the shift between dominant decadal cyclicity to strong inter-annual cyclicity records internal evolution (increasing sensitivity) of the glacial meltwater system, or a direct link between intensified ENSO activity and ice-margin destabilisation.

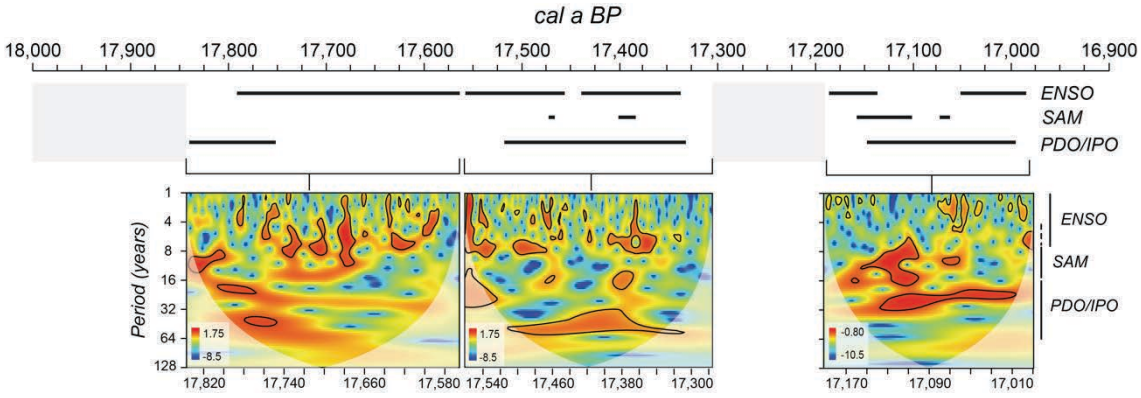

Figure 6.6. Temporal evolution of inter-annual and decadal climate influences in detrended varve thickness between 18–17 ka, based on continuous wavelet transforms.

After 17,759 cal a BP and until 17,273 cal a BP, wavelet analysis (Figure 6.5a) indicates persistent ENSO-like variability with strong controls on meltwater production and sediment transfer (Figure 6.6). Decadal-scale variations in the amplitude of ENSO-like cycles is evident in bandpass filtered data (Figure 6.5b) and might reflect modulation of South Pacific SSTs by PDO/IPO-like oscillations (Andreoli and Kayano, 2005), natural oscillations in ENSO behaviour (e.g. shifts in phase-locking), or changes in basic state that influence the strength of teleconnections to the extratropics (Allen, 2000; Cane, 2005). Such amplitude shifts are therefore consistent with contemporary features of the non-stationary ENSO system.

Between 17,272–17,187 cal a BP breaks in the varve sequence (Figure 6.4a) preclude assessment of high-frequency cyclicity. However, between 17,186–16,982 cal a BP,

persistent variance in the 20–30-year bandwidth suggests stable behaviour of PDO/IPO-like oscillations (Figure 6.6). In contrast, the disappearance of 6–8-year cycles from the broader 2–8-year ENSO band might reflect a shift in ENSO behaviour. In this period, ice-margin retreat rates increased (Figure 6.4a) and a calving margin was established ~12–15 km west of the varve sampling sites (Figure 6.1c; Chapter 5).

A more distal ice-margin during this interval is associated with lower annual sediment yields (relative to Interval 2–3; Figure 6.4a) and possible dampening of inter-annual variability due to fewer meltwater pulses reaching this sector of the basin. Moreover, meltwater processes may have altered in response to the establishment of a calving margin. Nonetheless, the existence of 2–5-year cycles leaves open the possibility that the average duration of ENSO cycles had reduced by 17,186 cal a BP. The SAM-like frequencies observed between ~17,129–17,098 cal a BP (Figure 6.6) coincide with an episode of significant ice-rafted debris (IRD) influx, and thus partially skewed thickness, so are not considered robust.

In summary, the LGC–BA varve record demonstrates that between 17,835–16,982 cal a BP, at the onset of deglaciation in central Patagonia, the cryospheric system was sensitive to inter-annual ocean-atmosphere climate variability operating at the hemispheric scale. The annual resolution of the record details, for the first time, the role of high-frequency climate variability on mid-latitude ice sheet ablation patterns, during a phase of large-scale climate reorganisation (e.g. Lamy et al., 2007; Timmermann, 2007). Such conclusions have not previously been possible using millennial-scale records.

6.6 Conclusions

- The LGC–BA varve record has provided the first opportunity to examine annual/decadal changes in southern mid-latitude palaeoclimate and ice sheet variability, at the onset of deglaciation (~18–17) in southern South America.
- The thickness of varves reflects fluctuations in meltwater and sediment fluxes to proglacial LGC–BA, owing to melt season climate conditions that influence ice sheet ablation and the efficiency of the glacial meltwater system. We hypothesise that spring/summer temperature was the most important control on sediment flux.
- Spectral analyses of detrended varve thickness series yield significant periodicities at 2–8, 8–10, 20–25, and ~50-year bandwidths. We infer that inter-annual cyclicity was dominated by ENSO, while the PDO/IPO and/or internal ENSO dynamics account for the multi-decadal cycles.
- The evidence for climate teleconnections between the tropics and the southern mid-latitudes during deglaciation is consistent with reconstructions of coupled

ocean-atmosphere frontal shifts at that time (Lamy et al., 2007; Barker et al., 2009; Sikes et al., 2013), and climate model simulations that predict enhanced ENSO variability during HS-1 (Timmermann, 2007). Assuming a state of reduced ENSO variability at the gLGM, these findings indicate that ENSO-related climate variance was reinvigorated by ~17,835 cal a BP, ~800 years earlier than previously demonstrated in Southern (Rein et al., 2005) and Northern American (Rittenour et al., 2000) proxy records.

- The annually-resolved varve thickness record provides direct empirical evidence suggesting that these factors may have played an important role in regional ice sheet deglaciation. Until now, however, the low-latitude tropical influences of ENSO and PDO/IPO have proven difficult to discern.
- Further work is now required to examine the spatial representativeness of these suggested changes across the southern mid- to high-latitudes. Annually-layered records offer great potential in this pursuit.

Chapter 7. Near-synchronous southern hemisphere warming and mid-latitude ice sheet response during Heinrich Stadial 1

Bendle, J.M., Palmer, A.P., Thorndycraft, V.R., Matthews, I.P. (in prep) Near-synchronous southern hemisphere warming and mid-latitude ice sheet response during Heinrich Stadial 1. *Nature Geoscience.*

The onset of deglaciation in the Southern Hemisphere mid-latitudes has been attributed to the southward transmission of climate anomalies in response to Northern Hemisphere freshwater forcing and slow-down of Atlantic meridional overturning circulation (AMOC) during Heinrich Stadial 1 (HS-1; 18–14.6 ka). Proxy records (Lamy et al., 2007; Barker et al., 2009) and climate models demonstrate the potential for abrupt warming and sub-centennial scale ocean-atmosphere reorganisation during HS-1 (Rind et al., 2001; Vellinga and Wood, 2002), but inferences on the timing and dynamics of ice-sheet response is limited by the relatively low, centennial-to-millennial, resolution of most mid-latitude glacial chronologies (e.g. Douglass et al., 2006; Hein et al., 2010; Boex et al., 2013; Shulmeister et al., 2010; Putnam et al., 2013a). Here we use a ~1000-year varve thickness record of Patagonian Ice Sheet (PIS) sediment fluxes during deglaciation at Lago General Carrera–Buenos Aires (LGC–BA), southern Argentina, to test the phasing of mid-latitude ice sheet response to ocean-atmosphere changes at sub-centennial timescales. The record is anchored to the calendar-year timescale by tephrochronology (Chapter 5) enabling a test of (a)synchronicity between mid-latitude ice sheet deglaciation and Southern Hemisphere ocean-atmosphere changes. Our results show, for the first time, that the onset of PIS deglaciation at 17,997 ± 144 cal a BP, and a subsequent acceleration in warming 229 ± 17 years later at ~17,768 ± 127 cal a BP, precisely coincide (within dating uncertainties) with patterns of atmospheric warming recorded in high-accumulation West Antarctic ice cores (WAIS Members, 2013; 2015; Cuffey et al., 2016), demonstrating rapid ice sheet response to near-synchronous intra-hemispheric warming at 18.0 ka. Our data provide the highest resolution terrestrial mid-latitude evidence in support of a Northern Hemisphere (HS-1) control on Southern Hemisphere deglaciation, through a chain of coupled ocean-atmosphere shifts (Denton et al., 2010; Putnam et al., 2013a) in response to North Atlantic freshwater forcing.

Constraining the precise timing of ice-sheet deglaciation from Last Glacial Maximum (LGM) limits is essential for understanding cryosphere sensitivity and climate system

drivers within major readjustments of Earth's ocean atmosphere circulation (Clark et al., 2009). To this end, the former mid-latitude ice masses of Patagonia (38–56°S; Glasser et al., 2008) and New Zealand (42–46°S; Barrell, 2011) are ideally located to investigate Southern Hemisphere cryosphere and climate dynamics during deglaciation (Darvill et al., 2016). This is because these regions are influenced by the southern westerlies (Sime et al., 2013) and Southern Ocean frontal systems (Sikes et al., 2009), as well as both tropical and extratropical (high-latitude) climate variability (Moy et al., 2009; Killan and Lamy, 2012). Studies on the timing of deglaciation in Patagonia (e.g. Denton et al., 1999a; Boex et al., 2013; Moreno et al., 2015) and New Zealand (e.g. Putnam et al., 2013a; 2013b), which use radiometric dating methods, provide chronologies at centennial-to-millennial temporal resolution and indicate broadly coincident timings for the onset of ice sheet retreat at ~18.0 ka. This has been interpreted to reflect synchronous warming and deglaciation of mid-latitude ice sheets at sub-millennial timescales (Schaefer et al., 2006; Putnam et al., 2013a; Moreno et al., 2015), driven by major reorganisation of the Southern Hemisphere ocean-atmosphere system coincident with records of cooling in Greenland and the North Atlantic in HS-1, during which the large iceberg rafting event, known as Heinrich event 1 occurred. HS-1 was associated with a strong reduction in North Atlantic overturning strength (McManus et al., 2004) that is thought to have instigated coeval Southern Hemisphere warming through the bipolar 'seesaw' mechanism. However, whether this seesaw operated through the oceans (Crowley, 1992; Broecker et al., 1998), atmosphere (Togweiller et al., 2006; Anderson et al., 2009), or through interlocked ocean-atmosphere changes (Denton et al., 2010), remains unclear.

Testing these hypotheses requires higher resolution chronologies than currently afforded. This is because cosmogenic nuclide exposure dating provides chronological uncertainties of mean moraine ages that overlap intervals of rapid climate transition, which can occur over centuries (WAIS Members, 2013, 2015) or decades (Rind et al., 2001; Vellinga and Wood, 2002; Markle et al., 2017). Incremental dating techniques, such as annual-layer counting of laminated (varved) lake sediment sequences, offer potential high-resolution palaeoclimate data (e.g. Brauer et al., 2008; Wolff et al., 2011) not yet routinely exploited in the Southern Hemisphere for testing the synchronicity of ice sheet response to inter-hemispheric climate changes during the last deglaciation. Varves allow the development of annually-resolved chronologies (Ojala et al., 2012) and are capable of recording changes in glacier terminus position and/or switches in glacial meltwater discharge at annual/decadal resolution (Palmer et al., 2010; Ridge et al., 2012; Chapter 5). Here, for the first time, we investigate the phasing of southern mid-latitude

cryosphere response to ocean-atmosphere changes at sub-decadal-to-centennial resolution using an annually-resolved glaciolacustrine varve record of PIS sediment fluxes. The archive spans the onset of HS-1 (~18–17 ka), and is anchored to the calendar-year timescale by the Ho tephra from Cerro Hudson (17,378 ± 118 cal a BP), which is preserved in the sedimentary varve sequence (Chapter 5; Figure S2 in Appendix).

The varve record, from the Río Fenix Chico valley in southern Argentina (46'34°S; 71'03°W;), lies at the eastern end of Lago General Carrera–Buenos Aires (LGC–BA; Figure 7.1; Figure S1 in Appendix), a major conduit of ice discharge in the central sector of the former PIS (Glasser and Jansson, 2005). The potential annual resolution of these laminated lake sediments was proposed in the early 20th Century (Caldenius, 1932), yet only recently confirmed using modern sedimentological techniques (Chapter 5). At this site, varves started to accumulate in an ice-marginal proglacial lake at 17,997 ± 144 cal a BP (hereafter 18.0 ± 0.14 cal ka; Chapter 5), following ice lobe retreat from its Last Glacial Maximum (LGM) limit (Kaplan et al., 2004; Douglass et al. 2006; Figure 7.1c). The varve sediments are composed of two primary sublayers. (1) A silt and/or fine sand sublayer (Figure 7.2) formed during the spring/summer melt season when sediment-laden meltwater was delivered to the lake and the coarsest sediments settled from suspension. (2) During the autumn/winter non-melt season, when meltwater supply was reduced and internal lake currents were at their minimum, clay particles were deposited to form distinct couplets representing one year of sedimentation (Ashley, 1975; Palmer et al., 2010; 2012; Ridge et al., 2012; Chapter 5). Annual/decadal varve thickness changes in this glacial system are a product of melt season climate conditions that control meltwater production and sediment fluxes (Chapter 5; section S2 in Appendix). Over multi-decadal to centennial timescales, varve thickness is modulated by glacial extent, where thicker (thinner) varves indicate a more proximal (distal) ice-margin. Using these glacier-varve relationships, and by linking discrete phases of varve sedimentation to specific ice-margin pinning points (Figure 7.1c), shifts in ice lobe retreat rates during the ~18–17 ka record can be inferred (Chapter 5). Time-series analysis of the varve thickness data has also revealed ENSO signatures in the annual record (Chapter 6), demonstrating the sensitivity of the former PIS to sub-decadal temperature variations.

A 3000-year window (19–16 ka) of Southern Hemisphere palaeoclimate is investigated to assess the phasing of mid-latitude ice sheet retreat to prevailing climate changes at the onset of deglaciation (Figure 7.3). The selected records (Appendix) offer the highest available temporal resolution from marine and terrestrial environments, and facilitate assessment of both oceanic and atmospheric changes on PIS deglaciation.

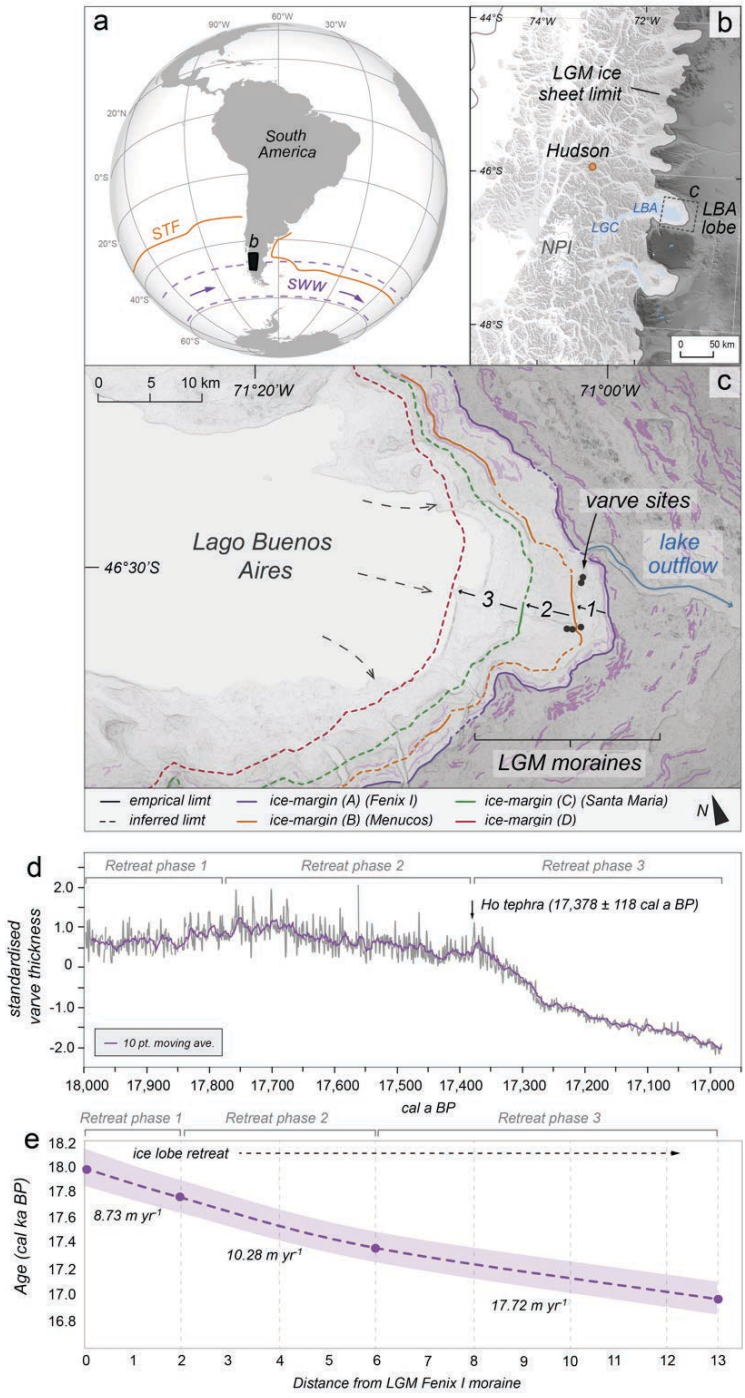

Figure 7.1. Study location and the LGC–BA varve record. (a) Location of LGC–BA in southern South America with contemporary position of the Sub-Tropical Front (STF; cf. Orsi et al., 1995; Carter et al., 2008) and southern westerly wind (SWW) system indicated. (b) LGM limit of the PIS in central Patagonia, showing former LGC–BA ice lobe (cf. Singer et al., 2004). (c) Ice lobe retreat phases and (empirical and inferred) ice-margin limits (Chapter 5). Varve sites are positioned between the Fenix I and Menucos moraines, and the Menucos moraine and the Santa Maria ice-proximal fan, enabling linkages between ice-margin retreat and varve sedimentation. (d) LGC–BA varve chronology and annual changes in sediment flux (standardised), with retreat phases 1–3 shown. (e) Time-distance path of LGC–BA terminus retreat estimated from varved sediment sequences. The varve chronology error is indicated with the purple envelope.

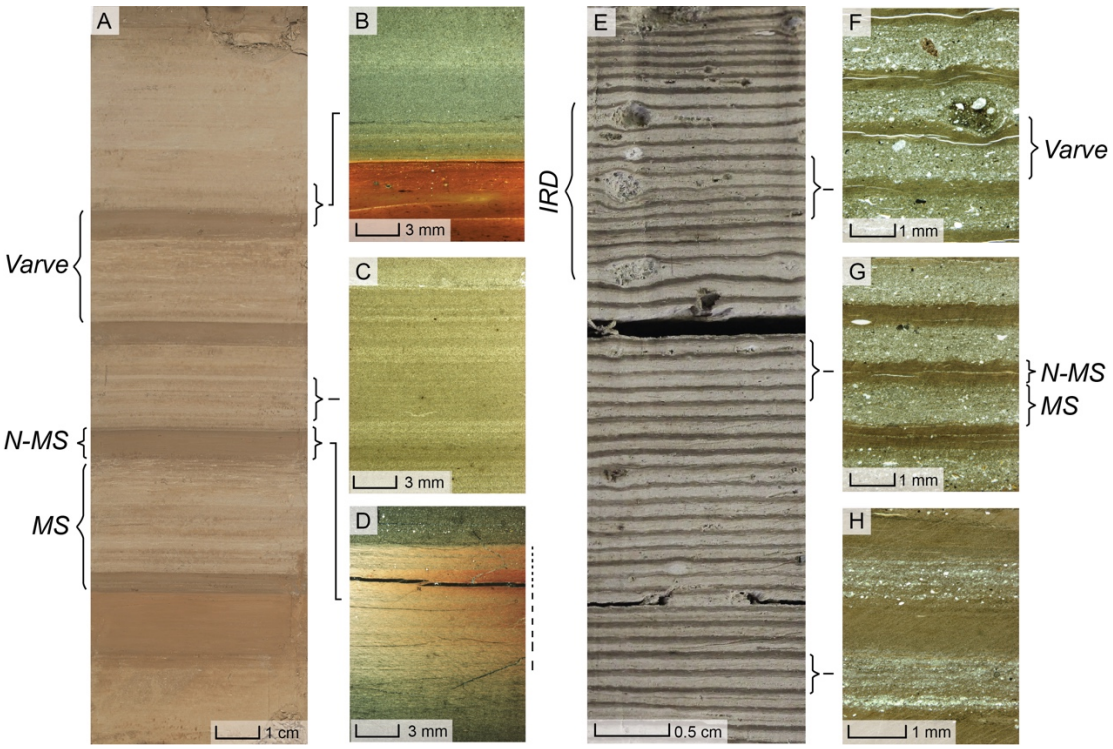

Figure 7.2. Examples of varved sediments. MS = melt season; N-MS = non-melt season. (a) Thick varves deposited during Retreat phase 2 (shown in Figure 7.1d), with thin-section photomicrographs showing internal sub-layer composition (b,c,d). (e) Thin varves deposited during Retreat phase 3, with thin-section photo-micrographs showing interval varve structure (f,g,h). Note the onset of ice-rafted debris deposition in (e).

At the start of this time-window, the West Antarctic Ice-Sheet Divide (WDC) ice-core record exhibits relatively stable temperatures between 19.0–18.0 ka ka (Figure 7.3b-c; WAIS Members, 2013, 2015) before rising by 2.5°C between 18.0–17.3 ka (Figure 7.3c; Cuffey et al., 2016). There are two phases to this warming: an increase of ~0.5°C between 18.0–17.8 ka followed by a phase of accelerated warming of ~2°C between 17.8–17.3 ka. Subsequently, temperatures increase by a further 2°C between 17.3–16.0 ka. A similar magnitude of increase is identified in the EDML (EPICA Members, 2006; Figure 7.3e) and EDC (Jouzel et al., 2007; Figure 7.3f) isotopic records from East Antarctica, although the increase is more constant. The WDC record also demonstrates increasing sea-ice volume and sea-salt sodium (ssNa) concentration up until 18.0 ka (Figure 7.3g), when an abrupt decrease in these proxies begins (WAIS Members, 2013). Marine sediment cores from the Chilean margin at 41°S (Figure 7.3h) and 53°S (Figure 7.3i) record sea surface temperature (SST) changes both north and south of LGC–BA. At 41°S (ODP-1233; Lamy et al., 2004, 2007), SSTs increase rapidly from ~7.5°C to ~10°C between 18.1–17.6 ka before more consistent temperatures are attained between ~10–12°C after 17.6 ka. At 53°S (MD07-3128; Caniupán et al., 2011), SSTs of ~5–6°C began to increase at 18.2 ka, and before a further 3–4°C of warming through the rest of the time-window. At site TN057-13 in the Southern Ocean (Figure 7.3j), opal fluxes rise

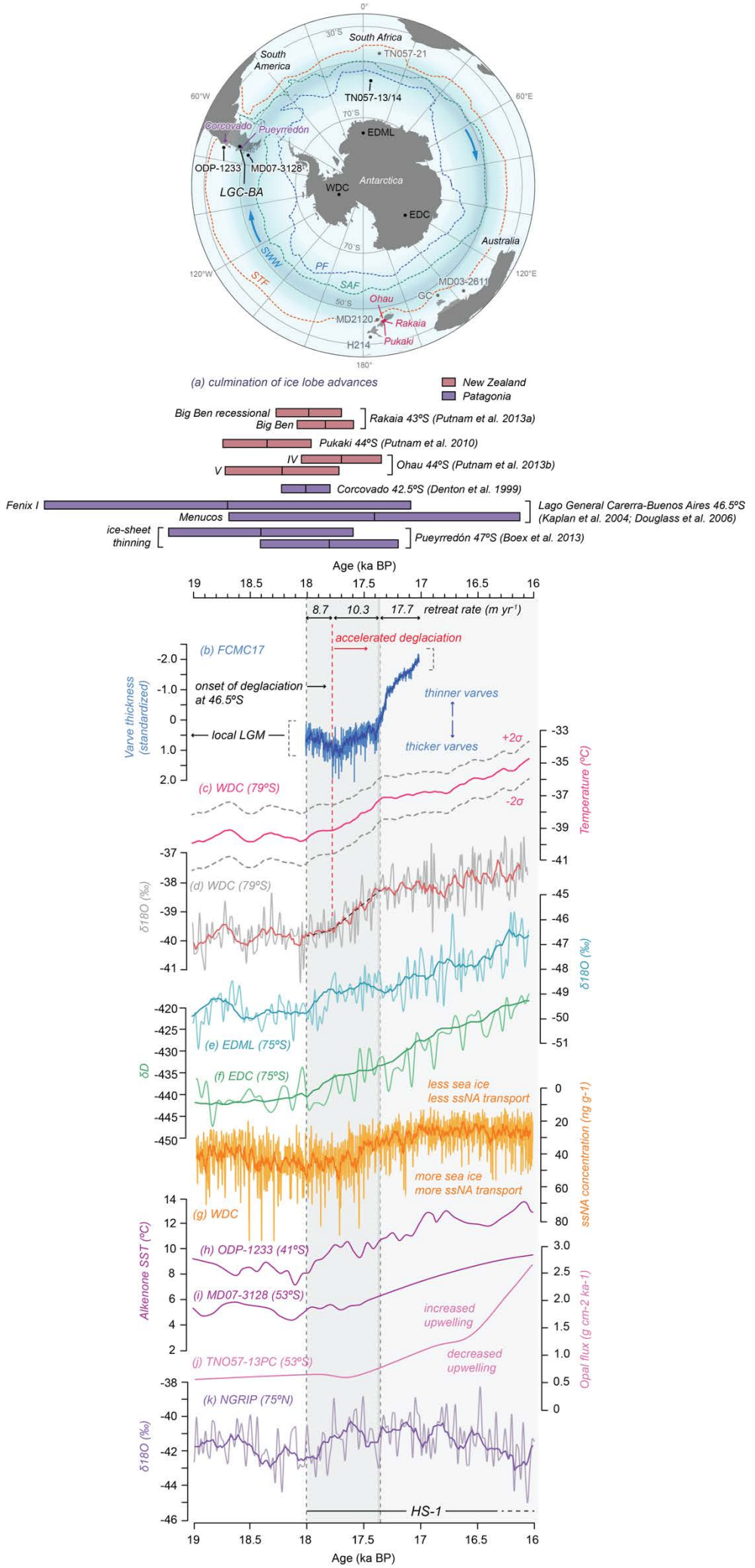
South America
South Africa
TN057-21
TN057-13/14
EDML
Antarctica
WDC
EDC
Australia
Corcovado
Pueyrredón
ODP-1233
MD07-3128
LGC-BA
MD03-2611
GC
Ohau
MD2120
Rakaia
Pukaki
H214
SWW
PF
SAF
STF
(a) culmination of ice lobe advances
New Zealand
Patagonia
Big Ben recessional
Big Ben
Rakaia 43ºS (Putnam et al. 2013a)
Pukaki 44ºS (Putnam et al. 2010)
IV
V
Ohau 44ºS (Putnam et al. 2013b)
Corcovado 42.5ºS (Denton et al. 1999)
Fenix I
Menucos
Lago General Carerra-Buenos Aires 46.5ºS (Kaplan et al. 2004; Douglass et al. 2006)
ice-sheet thinning
Pueyrredón 47ºS (Boex et al. 2013)
Age (ka BP)
8.7
10.3
17.7
retreat rate (m yr-1)
accelerated deglaciation
(b) FCMC17
onset of deglaciation at 46.5ºS
local LGM
thinner varves
thicker varves
Varve thickness (standardized)
+2σ
-2σ
(c) WDC (79ºS)
Temperature (ºC)
(d) WDC (79ºS)
δ18O (‰)
(e) EDML (75ºS)
(f) EDC (75ºS)
δD
less sea ice
less ssNA transport
more sea ice
more ssNA transport
ssNA concentration (ng g-1)
(g) WDC
(h) ODP-1233 (41ºS)
(i) MD07-3128 (53ºS)
Alkenone SST (ºC)
increased upwelling
decreased upwelling
(j) TNO57-13PC (53ºS)
Opal flux (g cm-2 ka-1)
(k) NGRIP (75ºN)
δ18O (‰)
HS-1
Age (ka BP)

Figure 7.3. LGC–BA deglacial sediment flux record compared with proxy records for ocean and atmosphere changes in the Southern Hemisphere mid- and high latitudes. (a) The timing of culmination of ice lobe advances (local moraine names indicated) from select sites in Patagonia (Denton et al., 1999; Boex et al., 2013; Kaplan et al., 2004; Douglass et al., 2006) and New Zealand (Putnam et al., 2010; 2013a, 2013b). (b) LGC–BA varve thickness and inferred ice lobe retreat rates. (c) West Antarctic temperature reconstruction from WDC ice-core (Cuffey et al., 2016). (d) West Antarctic $\delta^{18}O$ (temperature) record from WDC ice-core. WDC records shown on WD2014 timescale (Buizert et al., 2015). (e) East Antarctic $\delta^{18}O$ (temperature) record from the EDML ice-core (EPICA Members, 2006). (f) East Antarctic δD (temperature) record from the EDC ice-core (Jouzel et al., 2007). EDML and EDC shown on common Limeux-Dudon et al. (2010) timescale. (g) WDC ssNA record (WAIS Members, 2015). (h) Alkenone-derived SST reconstruction from ODP-1233 (Lamy et al., 2007). (i) Alkenone-derived SST from MD07-3128 (Caniupán et al., 2011). ODP-1233 and MD07-3128 use updated age models from Lamy et al. (2015). (j) Opal flux record from core TN057-13, a proxy for wind-driven upwelling in the South Atlantic (Anderson et al., 2009). (k) NGRIP $\delta^{18}O$ record (NGRIP Members, 2004) of Greenland temperature on GICC05 timescale (Rasmussen et al., 2006). Polar projection map shows location of palaeoclimate records and contemporary position of SWWs and ocean fronts (cf. Orsi et al., 1995; Carter et al., 2008). Records labeled in grey are referenced in the text, but not shown on Figure 7.3 (TN057-21: Barker et al., 2009; MD03-2611: Calvo et al., 2007; De Deckker et al., 2012; MD2120: Sikes et al., 2009; H214: Sikes et al., 2009; GC: comprises multiple cores from Sikes et al., 2013).

gradually from 19.0 ka, but increase markedly at 17.6 ka and again at 16.5 ka, suggesting enhanced Southern Ocean upwelling after 17.6 ka (Anderson et al., 2009). Within the time-window covered by climate fluctuations in Southern Hemisphere palaeorecords, cool and broadly consistent temperatures are evident in the North Atlantic NGRIP ice-core record (Figure 7.3k; NGRIP Members, 2004), and bracket the period associated with HS-1 (McManus et al., 2004).

Prior to the minimum estimate for the of onset of varve sedimentation at 18.0 ± 0.14 cal ka, the LGC–BA ice lobe was stable at the local LGM Fenix I moraine complex (Figure 7.1c; Kaplan et al., 2004; Douglass et al., 2006; Chapter 5), whilst the temperatures in Antarctica were at their lowest for the time-window (Figure 7.3c-f; EPICA Members, 2006; Jouzel et al., 2007; WAIS Members, 2013, 2015; Cuffey et al., 2016). In the marine records, there is evidence for warming of SST at 41°S at ~18.2–18.1 ka (Figure 7.3h-i), synchronous (within dating uncertainties) with abrupt atmospheric warming at 75–80°S (EPICA Members, 2006; Jouzel et al., 2007; WAIS Members, 2013, 2015; Figure 7.3c-f), and a gradual decrease in the sea-ice cover around West Antarctica (WAIS Members, 2015; Figure 7.3g) The onset of LGC–BA ice lobe retreat by 18.0 ± 0.14 cal ka is synchronous (within dating uncertainties) with these changes, and exhibits precise phasing with the abrupt atmospheric warming recorded in both the high-accumulation WDC ice-core (WAIS Members, 2015; Cuffey et al., 2016) and lower resolution East Antarctic records (EPICA Members, 2006; Jouzel et al., 2007). Over the next 229 ± 17 varve years (vyr), the thickness of annual layers in LGC–BA increase steadily (Figure

7.3b), reflecting greater meltwater production during retreat due to increased summer ablation and negative glacier mass balance (section S2 in Appendix), in phase with increasing Antarctic temperatures between ~18.0–17.8 ka (Figure 7.3c-f). The ice-margin retreated ~2 km west of the local LGM limit during this period (Figure 7.1c), yielding an average retreat rate of 8.73 m yr^{-1} (Figure 7.1e; Figure 7.3b).

A pronounced change in the varve thickness is recorded after 17,768 ± 127 cal a BP (hereafter 17.77 ± 0.13 cal ka; Figure 7.1d; Figure 7.3b). Initially, an abrupt 10-year increase in varve thickness demonstrates a rapid sediment flux response to enhanced ice sheet ablation and increased meltwater production. The subsequent decreasing trend in varve thickness records glacial retreat from the Menucos moraine (Figure 7.1c). The ice-margin contracted a minimum of ~4 km in 389 ± 9 vyrs until 17,378 ± 118 cal a BP (hereafter 17.38 ± 0.12 cal ka), yielding a modest increase in the glacier retreat rates to ~10.28 m yr^{-1}. This switch in glacier retreat rates is synchronous (within dating uncertainties) with an increase in the rate of atmospheric warming observed in the high-resolution WDC isotopic (Figure 7.3d; WAIS Members, 2013, 2015) and temperature reconstruction (Figure 7.3c-d; Cuffey et al., 2016).

The rate of Antarctic warming at WDC reduces after ~17.3 ka (Figure 7.3c-d), whilst the thickness of LGC–BA varves decreases rapidly over the same interval for the remaining 395 ± 9 years, until 16,982 ± 127 cal a BP (hereafter 16.98 ± 0.13 cal ka), covered by the record (Figure 7.3b). Ice-margin retreat rates increased to a minimum of ~17.72 m yr^{-1} (Figure 7.2), 58% faster than during the previous 389 ± 9 vyrs (Figure 7.1), and the fastest retreat rate observed in the ~18–17 ka time-window. The acceleration of glacial retreat can be explained by the development of a calving ice-margin, as the LGC–BA ice lobe contracted into progressively deeper lake waters, evidenced by an increase in the presence of ice-rafted debris in this part of the sequence (Chapter 5). Thus, it is likely that the pulse of high-latitude atmospheric warming between 17.8–17.3 ka (Figure 7.3c-d) also affected the mid-latitudes, and contributed to a change in glacial dynamics that sustained accelerated ice-sheet retreat rates after ~17.3 ka, even though the rate of Antarctic air temperature increase had slowed by then (Figure 7.3c-d). This suggests that internal glaciological controls played an increasingly important role in driving ice-lobe retreat after ~17.3 ka, in combination with continued atmospheric (Figure 7.3c-f) and oceanic (Figure 7.3h-i) warming.

The LGC–BA varve sequence provides the first record of sufficient temporal resolution to assess the phasing of mid-latitude cryospheric changes and high-resolution Southern Hemisphere temperature records (WAIS Members; 2013, 2015), during an interval of

abrupt climatic reorganisation (Figure 7.3). The onset (~18.0 ka) and acceleration (~17.8 ka) of LGC–BA ice lobe retreat (Figure 7.3b) displays a phase-locked relationship with stepped Antarctic temperature increases (Figure 7.3c-d), highlighting the potential synchronicity in atmospheric warming trends over 35° of latitude, between 46.5 and 80°S, coincident with the onset of mid-latitude deglaciation (Figure 7.3a-b). Recent model simulations provide a possible explanation for near-synchronous warming of the southern high- and mid-latitudes, which relates to Southern Ocean convection (upwelling) events (Pedro et al., 2016). Heat release associated with convection of Southern Ocean deep water around Antarctica can drive Antarctic temperature increases of up to 2°C in <100 years (Pedro et al., 2016), comparable to that observed in the WDC temperature reconstruction (Cuffey et al., 2016) for the interval of LGC–BA ice lobe retreat (Figure 7.3b-c). The simulated convection events produce an immediate (annual/decadal) increase in SST and surface air temperature increase south of the Antarctic Circumpolar Current (ACC; ~50°S), which is strongest in the Weddell Sea sector. As the convective state evolves through multi-decadal to century periods, the simulation shows significant mid-latitude warming forced by a poleward contraction of the ACC and Sub-Tropical Front (STF) due to a steeper meridional density gradient caused by buoyancy loss in the convection zone (Pedro et al., 2016). The mid-latitude warming in turn steepens the temperature gradient with Antarctica, inducing a poleward shift of the southern westerlies (Pedro et al., 2016) that enhances atmospheric heat flux southwards to Antarctica, likely through atmospheric eddies (Rind, 2000; Sen-Gupta and England, 2006). Our observation of phase-locking (within dating uncertainties) of LGC–BA glacial retreat and Antarctic temperatures (Figure 7.3c-d), provides the first empirical evidence at sufficient temporal resolution to support this simulation (Pedro et al., 2016), and highlights the possible critical role of Southern Ocean convective states in providing the oceanic and atmospheric heat to initiate synchronous mid-latitude deglaciation.

Our high-resolution deglacial record can be placed in the context of potential inter-hemispheric climate linkages, since the mid-latitude ice-sheet response to palaeoclimatic changes coincides (within dating uncertainties) with the onset of HS-1 at ~18.0 ka (McManus et al., 2004). Sea-surface cooling and stratification in the North Atlantic during HS-1 and subsequent AMOC reduction (McManus et al., 2004; Ritz et al., 2013) are hypothesised to have initiated mid-latitude deglaciation, on either side of the Pacific Ocean (Figure 7.3a; Putnam et al., 2013a; Moreno et al., 2015), due to a southward migration of the Intertropical Convergence Zone (ITCZ) that instigated poleward displacement of a coupled ocean-atmosphere system comprising the southern westerly winds (SWWs) and the Sub-Tropical (STF) and Subantarctic (SAF) fronts (Denton et al.,

2010). This reorganisation is recorded in equatorial precipitation records (Wang et al., 2001; Chiang et al., 2014; Montade et al., 2015) and marine archives of abrupt sea-surface warming in the south Atlantic (Barker et al., 2009), southeast Pacific (Lamy et al., 2007, 2015; Caniupán et al., 2011) and southwest Pacific (Barrows et al., 2007; Calvo et al., 2007; De Deckker et al., 2012).

The southward displacement of the ITCZ and SWWs, leading to decreased westerly airflow over Patagonia, is a persistent feature of modelling simulations of AMOC slow-down (Timmermann et al., 2005; 2007; Lee et al., 2011; Ceppi et al., 2013). Some simulations suggest that the transmission of AMOC-related climate anomalies can occur within several decades (Rind et al., 2001; Vellinga and Wood, 2002). This has led to the theory that migration of the Southern Hemisphere wind systems, played an important role in rapidly transmitting climatic anomalies between regions, and in driving Southern Hemisphere deglaciation (Toggweiler, 2009; Denton et al., 2010; Lee et al., 2011; Putnam et al., 2013a). The poleward displacement of the Southern Hemisphere surface wind fields provides a potential mechanism for the instigation of phase-locked hemispheric warming and mid-latitude ice-sheet deglaciation, as suggested by our comparison (Figure 7.3b-d), by enhancing Ekman-driven upwelling of intermediate-depth waters around coastal Antarctica and pushing the Southern Ocean into a convective (warming) state (Pedro et al., 2016). Southern Ocean marine sediment records exhibit enhanced overturning (Figure 7.3j; Anderson et al., 2009; Skinner et al., 2014) and a contemporaneous intensification of Drake Passage throughflow (Lamy et al., 2015) during HS-1, consistent with southward-shifted westerlies and stronger ACC circulation, and supporting a coupled ocean-atmosphere displacement (as advocated by Lamy et al., 2007; Denton et al., 2010; Putnam et al., 2013) as the primary driver of mid-latitude ice-sheet deglaciation.

Additional evidence from the LGC-BA varve record suggests that ENSO-related climate variability contributed to sub-decadal ice-sheet ablation events and periodic increases in melt-layer thickness (Chapter 6). This suggests that the influence of tropical Pacific changes affected climate as far south as 46.5°S, perhaps enhanced by southward migration of the coupled ocean-atmosphere frontal systems, which are thought to have contributed to greater low latitude influence on mid-latitude climate during deglaciation (Sikes et al., 2009, 2013). Enhanced ENSO variability is a feature of several models that simulate climate response to AMOC slow-down (Timmermann, 2007; Liu et al., 2014), lending support to this possibility. Therefore, overprinted on the multi-decadal-to-centennial changes in ice-lobe position (Figure 7.1d; Figure 7.3b), likely initiated by increasing atmospheric temperatures across the mid- to high-latitudes, are higher

frequency climatic oscillations. The temperature threshold that was surpassed at the initiation of PIS retreat could potentially have been enhanced by this tropical climate variability, but additional high-resolution palaeoclimate archives are required to further disentangle the relative influences of various climate systems on mid-latitude deglaciation.

We present the first annually-resolved terrestrial archive from the Southern Hemisphere with the capacity to test the precise intra- and inter-hemispheric phasing of mid-latitude ice sheet retreat and palaeoclimate, at the onset of the last deglaciation. Our results help to reconcile evidence for synchronous timing of southern mid-latitude deglaciation (Putnam et al., 2013a; Moreno et al., 2015), because the close synchronicity of LGC–BA varve thickness and Antarctic warming trends between ~18.0–17.3 ka, suggests a synchronous warming of the southern Pacific region, possibly driven by heat release via enhanced Southern Ocean convection (Pedro et al., 2016). This warming may have been triggered by events related to Northern Hemisphere cooling during HS-1, where Northern Atlantic freshwater influxes instigated a chain of coupled ocean-atmosphere shifts (Lamy et al., 2007; Denton et al., 2010) that kick-started Southern Ocean convection (Anderson et al., 2009. Our empirical evidence therefore highlights the sensitivity of Southern Hemisphere ice sheets to atmospheric warming, instigating LGC–BA ice lobe deglaciation at 18.0 ka, and contributing to accelerated retreat after 17.8 ka. Once established, deglaciation was partially sustained by internal glaciological controls. Our evidence for initial precise phasing of deglacial events demonstrates the need for additional high-resolution (annual/decadal) proxy records with the potential to clarify sub-centennial climate linkages during the last glacial-interglacial transition.

Methods

Production of varve chronology and thickness record. This study was carried out on a composite varve thickness record and chronology (FCMC17) derived from five individual site varve records in the Río Fenix Chico valley (Chapter 5). Varve counts and thickness measurements were generated from field (macroscopic) sediment sections (varves >1 cm thickness; 85.35% of composite) or microscopic analyses of petrographic thin sections (varves <1 cm thickness; 14.65% of composite). Site records were precisely correlated on a varve-to-varve basis using prominent marker layers as definitive tie-points between sequences, alongside distinctive trends in varve thickness. Varve count uncertainties were estimated through repeat measurements, although local disturbances

were often bridged by better preserved sequences during the correlation process. This process yielded a composite chronology of 994 ± 36 varve years (vyr).

Dating of composite varve record. A prominent time marker was established at vyr 605 ± 27 in the composite record, through geochemical fingerprinting of a visible tephra layer (Chapter 5; section S3 in Appendix). Samples from three sites were sieved at 125 μm and 15 μm, and an optimum glass fraction extracted using sodium polytungstate (SPT) at 2.55 g cm^{-3} density (Blockley et al., 2005). Glass shards were mounted in probe stubs, carbon coated, and major element analyses obtained for 195 individual glass shards (Appendix) using a Cameca-SX100 WDS-EPMA at the Tephra Analytical Unit, University of Edinburgh. Analyses were undertaken using a beam diameter of 5 µm and at 15 keV; a 2 nA beam current was employed for Na, Al, Si, Fe, K, Ca, Mg and a 80 nA beam current for Mn, Cl and Ti (Hayward, 2012). The uncertainty on this analysis is <1%, and international standards Lipari 1 (rhyolitic) and BCR2G (basaltic) were analysed frequently to monitor for instrument drift. In addition, five bulk tephra samples (~10–12 g) were prepared for trace element analyses (Appendix). Samples were sieved at 15 μm to remove the fine silt and clay fraction, and powdered in a tungsten carbide mill. Powered samples were pressed into pellets and analysed using a PANalytical Axios Sequential X-ray Fluorescence Spectrometer at Royal Holloway, University of London. Matrix corrections were applied using the major element chemical dataset obtained using the WDS-EMPA analysis, and Limits of Detection (LoD) were calculated using long-term data collected using the same equipment. Geochemical correlations with published tephrochronological datasets determined an origin as the Ho tephra from Cerro Hudson (Weller et al., 2014), and eight published radiocarbon determinations (Miranda et al., 2013) were remodeled in Oxcal v4.3 (Bronk Ramsey, 2009) to 17,378 ± 118 cal BP. This age was inserted at vyr 605 ± 27 and calendar years extrapolated for the remaining varves. Varve counting errors were propagated backwards and forwards from vyr 605 and summed with the uncertainty of the Ho tephra age.

Calculation of ice lobe retreat rates. The number of varves deposited between geomorphologically (i.e. moraines) or stratigraphically defined ice limits in the Río Fenix Chico valley, enabled calculation of average ice lobe retreat rates (m yr^{-1}) for three main recessional phases. These phases were also evident as prominent changes in the trend of varve thickness. The number of varves located between ice-margin limits was deduced from site varve records, which were positioned at different locations in the valley with respect to temporary ice lobe positions (section S4 in Appendix).

Chapter 8. Synthesis and future work

8.1 Synthesis

This thesis aimed to investigate the deglaciation of the Patagonian Ice Sheet in the Northern Patagonian Icefield (NPI) region, approximately 46–48°S, at a range of spatial and temporal scales. The specific aims were to: (1) reconstruct the deglacial evolution of proglacial lakes and their interactions with the retreating LGC–BA and LC–P ice lobes; (2) establish high-precision chronological control on the timing, rates and dynamics of initial ice lobe deglaciation; and (3) use this new chronology to examine possible climatic forcing of Patagonian Ice Sheet deglaciation. A high-resolution glacial geomorphological map for the region (Chapter 3) was produced to address Aim (1), and provided the foundation for a new reconstruction of proglacial lake evolution through the last deglacial cycle (Chapter 4). Aim (2) was addressed through sedimentological investigations of laminated glaciolacustrine sediments at LGC–BA, yielding the first annually-resolved and independently dated varve chronology and varve thickness record linked to Patagonian Ice Sheet retreat. This record has provided high-precision dating control for the timing of deglaciation at LGC–BA (Chapter 5). Aim (3) was addressed in two steps. First, sub-centennial variations in varve thickness were investigated to identify possible short-term climatic forcing of local meltwater production and sedimentation patterns, demonstrating the potential influence of tropical Pacific climate variability (ENSO) on Patagonian Ice Sheet ablation (Chapter 6). Second, the varve thickness record was compared with a compilation of hemispheric palaeoclimate records to investigate possible forcing mechanisms of mid-latitude ice-sheet deglaciation. The comparison identifies close phase-locking (within dating uncertainties) of ice lobe retreat dynamics and atmospheric warming in Antarctica, ~33.5° further south, and highlights the potential sensitivity of the Patagonian Ice Sheet to inter-hemispheric climate events during Heinrich Stadial 1 (HS-1).

8.1.1 Mapping of glacial geomorphology

Previous mapping at the ice lobe-scale has used relatively low-resolution (15–30 m) satellite imagery (Glasser and Jansson, 2008) and focused on dating of former glacial limits (Kaplan et al., 2004; Douglass et al., 2004), rather than the detailed nature of landform assemblages. More detailed mapping has been restricted to select valleys (Glasser et al., 2006; 2012; Nimick et al., 2016) or certain ice lobe margins (e.g. Turner et al., 2005; Hein et al., 2010; Glasser et al., 2012).

This thesis provided consistent, regional-scale mapping from high-resolution (<15 m) satellite images and localised field-checking (Chapter 3). In total, >35,000 landforms were mapped, and divided into fourteen main glacial landform types (hummocky terrain, continuous hummocky ridges, eskers, till eskers, iceberg wallow pits and craters, and ice-rafted moat lines). Other landforms, such as meltwater channels, were mapped in greater detail than in previous studies. The map reveals a difference in landform assemblages identified on former ice lobe forelands (maximum advances) and within topographically constrained valleys (deglaciation) west of the Patagonian mountain front. Former glacial forelands are dominated by nested latero-frontal moraine complexes and extensive meltwater related features (outwash plains and corridors, meltwater channels). The map also reveals areas of hummocky terrain, eskers, and possible till eskers inset behind larger latero-frontal moraines. Further west, raised deltas are common at the mouths of tributary valleys, while shorelines are mapped across the entire study area. Ice margins in the west of the study area are primarily recorded by ice-contact glaciofluvial features (fans, kame terraces), however, new moraine complexes have been identified in the western embayment of LGC–BA and in the Juncal valley west of LC–P.

Despite these advances, detailed geomorphological mapping was impossible in some areas, such as the area covered by the large transnational lakes of LGC–BA and LC–P, and the densely-vegetated terrain in the western sectors of the study area, close to the modern NPI. Because of this, certain zones lack detailed geomorphological constraints on ice-margin position, and thus the dynamics and rates of ice lobe retreat. In addition, the size of the study area prevented detailed examination of internal sedimentology of most mapped landforms, so this remains an underutilised line of evidence for discriminating landform origins and depositional processes.

8.1.2 Reconstruction of proglacial lake evolution

The evolution of proglacial lakes during the last deglaciation has proven contentious in earlier investigations, both in terms of the extent and levels of former lakes, and the timing and route of their drainage (Turner et al., 2005; Bell, 2008; Hein et al., 2010; Bourgois et al., 2016; Glasser et al., 2016; Martinod et al., 2016). In light of the new high-resolution geomorphological mapping (Chapter 3), proglacial lake evolution was reinvestigated through systematic regional analysis of shoreline elevation data, alongside targeted field mapping. The reconstruction of regional post-glacial isostasy enabled robust correlation of shoreline fragments between basins, and the identification of new lake levels and outflows. The isostatic dataset also enabled, for the first time, an

altitudinal-based assessment of published geochronological data that has previously proven contradictory (e.g. Douglass et al., 2005; Turner et al., 2005; Glasser et al., 2012, 2016; Villa-Martinez et al., 2012; Boex et al., 2013; Henríquez et al., 2017).

This work presents a new sequence of proglacial lake events, with several key differences from previous works. First, shoreline levels that exceed the elevation of the upper ~400 m asl (Deseado) and ~500 m asl (Caracoles) spillways at LGC–BA and LC–P are found to be only locally preserved in tributary valleys, and show no consistent regional pattern in their elevation. These levels are suggested to relate to lateral ice-dammed lakes formed when ice lobes occupied the main trunk valleys (in agreement with Martinod et al., 2016), and provide evidence against high regional lake levels that overtopped the LGM-aged Fenix and Río Blanco moraines (cf. Glasser et al., 2016).

Second, a previously unrecognised lake level at ~460 m asl was recorded in shoreline datasets from the LC–P and Chacabuco area, and a new drainage spillway identified through targeted field mapping. Shorelines and raised deltas at this level can be traced to the Soler ice dam that blocked the western embayment of LGC–BA, and suggest that a 'unified' lake at the upper Deseado level (~400–460 m asl) need not be inferred. Identification of a new drainage spillway at Río Barrancos, provides evidence for a first Atlantic–Pacific drainage reversal via the Río Baker, by at least 15.3–15.1 cal ka BP (based on Villa-Martinez, 2012 ages), in response to the separation of NPI outlet glaciers and Monte San Lorenzo ice.

Third, reconstructed post-glacial rebound data demonstrate that moraine boulders used to infer NPI advance at an equivalent time to the Northern Hemisphere Younger Dryas interval (Glasser et al., 2012) were likely submerged beneath the Bayo (~300–350 m asl) lake level, and therefore shielded from cosmogenic rays. Instead, these dates (alongside basal radiocarbon ages from infilled basins) likely constrain the drainage of the Bayo level to between ~13.0–10.0 ka and, by implication, suggest that glaciers retreated and/or thinned during this time, and were possibly stabilised during the ACR (as modelled by Hubbard et al., 2005). The drainage event was followed by a previously unrecognised moraine dammed lake phase that culminated in dam failure and high-magnitude GLOFs in the Cochrane and Río Baker valleys.

The reconstruction presented in this thesis (Chapter 4) allowed a coherent regional model that integrates new shoreline datasets with all available geochronological data. However, the reconstruction is limited by current DEM resolution (20 m vertical resolution), which prevents further separation of closely-spaced shorelines based on their elevation (as is possible using LiDAR datasets; e.g. Yang and Teller, 2012;

Breckenridge, 2013; Hickin et al., 2015). Thus, it is possible, and moreover likely, that a more complete lake-level history could be obtained. Furthermore, the approach used to model isostatic adjustment is based on a unidirectional (broadly east–west) rebound pattern; however, an additional axis (northeast–southwest) of uplift in the southern (LC–P) sector of the study area also likely exists. Finally, in many locations the regional lake reconstruction is not well supported by geochronological data targeted specifically at constraining lake level changes, and as such the exact timing of lake level events and drainage reversals remains uncertain.

8.1.3 Sedimentology of laminated glaciolacustrine deposits

Proglacial lakes provided large sinks for glaciolacustrine sediment during the last deglaciation (Caldenius, 1932), evidenced by thick laminated sediment sequences deposited at numerous locations across the study area (Chapter 3). Detailed macro- and micro-scale examination of these sediments, at five sites in the Río Fenix Chico valley from eastern LGC–BA, demonstrated characteristics typical of previously reported glaciolacustrine varves (e.g. Ashley, 1975; Ringberg and Erlström, 1999; Palmer et al., 2010; 2012; Ridge et al., 2012; Chapter 5). Most diagnostic are the regular alternations of texturally distinct coarse (melt season) and fine (non-melt season) sediment components with: (1) internally complex melt season layers composed of multiple silt and fine sand laminations; and (2) comparatively simple non-melt season layers that fine upwards from very fine silt to clay. A varve interpretation is supported by the lateral persistence of varve structures over several kilometres distance, and patterns of distal thinning. The structures within melt season layers suggest that sediment-laden meltwater plumes (underflows) sourced directly from ice lobe margins were responsible for the distribution of sediments across the former lake bed. Sedimentological examination also enabled discrimination of intercalated 'event' layers, such as coarser-grained sand layers in melt season laminations that likely record discrete high-discharge events, and were critical for the correlation of records between sites. Whilst this thesis used established sedimentological approaches (Ringberg and Erlström, 1999; Palmer et al., 2010; 2012; Ridge et al., 2012) to evaluate laminated sediment structures, which relies on current understanding of meltwater and sediment plumes in glacial lakes (e.g. Gustavson, 1975; Sugiyama et al., 2016), direct modern analogue studies are lacking, a persistent problem for investigations of palaeolake sequences.

8.1.4 High-precision dating of ice lobe deglaciation

The onset of deglaciation at LGC–BA has previously been inferred using cosmogenic nuclide exposure ages from boulders on late-LGM moraines (Kaplan et al., 2004;

Douglass et al., 2006) and luminescence dates of proglacial outwash sands (Smedley et al., 2016). To more precisely constrain the timing of regional deglaciation, a varve chronology was developed at Río Fenix Chico (Chapter 5). A composite record, termed the Fenix Chico Master Varve Chronology (FCMC17), was constructed through counts of the number of annual layers at five sites, which could be correlated across the former lake basin using prominent marker layers and varve thickness trends. The final FCMC17 covers 994 ± 36 vyrs. Precise inter-site correlations enabled local disturbances in site records to be bridged by more completely-preserved sequences, demonstrating the importance of a multi-site approach. The Ho tephra from Cerro Hudson (cf. Miranda et al., 2013; Weller et al., 2014), deposited at 605 ± 28 vyrs in the FCMC17, provided a tephrochronological anchor point for the floating varve chronology (17,378 ± 118 cal a BP), dating the sequence to between 17,997 ± 144 and 16,982 ± 127 cal a BP.

The FCMC17 provides the first annually-resolved chronology for ice sheet deglaciation in the southern mid-latitudes; and a record comparable in temporal resolution to those developed for the Laurentide (Antevs, 1922, 1928; Breckenridge, 2007; Ridge et al., 2012) and Scandinavian (De Geer, 1912, 1940; Wohlfarth et al., 1997) ice sheets. However, the FCMC17 is a relatively short record by comparison, covering ~1000 years of the initial deglaciation at LGC–BA. Currently, beyond 16,982 ± 127 cal a BP, the dating of ice lobe retreat relies upon comparatively low-resolution techniques (e.g. Glasser et al., 2012; 2016), and with few definitive ice-margin pinning points. Other issues that remain to be resolved include breaks of unknown duration in the FCMC17, which add a certain degree of unquantified uncertainty to the record. While these breaks are likely to be of short duration (Chapter 5) and, therefore, largely negligible in terms of the overall chronology, this remains to be confirmed. Finally, while firmly anchored in time using tephrochronology, the FCMC17 is currently lacking independent dating control at multiple depths in the composite varve sequence. In other records, such evidence provides tests of the interpretation of annual structure (e.g. Ridge et al., 2012).

8.1.5 Timing and dynamics of initial ice lobe deglaciation

The FCMC17 has constrained the initial deglaciation of the LGC–BA ice lobe precisely in time (Chapter 5). Within this time window, centennial-scale changes in the thickness of glaciolacustrine varves provide an indication of ice lobe proximity, and thus retreat behaviour. Discrete phases of ice lobe retreat were inferred from marked changes in composite varve thickness trends, the duration of which was defined by the FCMC17. These phases were related to the former ice lobe margin position through geomorphological and stratigraphic analysis, which identified a possible new stillstand

location at Estancia Santa Maria, west of the established Fenix I and Menucos moraine limits. Using a Bayesian age modelling approach, varve-dated retreat phases were integrated with published geochronology for moraine limits (Kaplan et al., 2004; Douglass et al., 2006) and glaciofluvial outwash sediments (Smedley et al., 2016), to refine the timing and sequence of glacial retreat dynamics (including moraine ages) and calculate average ice lobe retreat rates.

This analysis suggests that deglaciation of the Patagonian Ice Sheet at 46.5°S commenced at 18,086 ± 214 cal a BP, after remaining stable at the local LGM Fenix I moraine for ~700 years. The ice-margin stabilised at the Menucos moraine, ~2 km further west, at 17,710 ± 116 cal a BP, 376 modelled years after the onset of deglaciation, and yielded an average retreat rate of 5.30–6.65 m yr^{-1}. The dynamics of ice lobe retreat changed significantly after this temporary stillstand, accelerating progressively from 9.00–10.30 m yr^{-1} to 15.40–18.00 m yr^{-1} over the next ~750 years, with no evidence for prolonged ice-margin stabilisation (i.e. moraine construction) or readvance (e.g. overridden varves) during this period. Enhanced influx of ice-rafted debris (IRD) after 17,145 ± 122 cal a BP likely reflect a change in glaciological conditions in response to ice lobe retreat into deeper lake waters, and the establishment of a calving margin, which may have contributed to accelerated retreat rates. The ice lobe margin persisted in eastern LGC–BA for the next ~200 years, until at least 16,934 ± 116 cal a BP, but then retreated towards the Patagonian mountains.

Although limited by spanning a relatively short time-window of ice lobe deglaciation, varve and tephrochronological datasets have provided chronological refinement of existing retreat chronologies (Kaplan et al., 2004; Douglass et al., 2006; Smedley et al., 2016). Moreover, near continuous sediment records (with only minor breaks) have enabled detailed tracking of ice-margin position, and the identification of significant process changes (e.g. the onset of calving), adding new information on the dynamics of ice sheet deglaciation in central Patagonia, alongside firm chronological control.

8.1.6 Examining sub-centennial climatic influences on ice lobe deglaciation

A paucity of mid-latitude glacial records that are both securely-dated and provide sub-centennial temporal resolution has, until now, prevented investigations of potential short-term climatic forcing of Patagonian Ice Sheet deglaciation. This incorporates the potential influence of low-latitude climate systems, such as ENSO, which are globally-important modes of modern-day ocean-atmosphere variability, yet their impact on mid-latitude ice sheets has proven difficult to establish. To investigate the role of inter-annual to decadal climate variability on Patagonian Ice Sheet deglaciation, high-frequency

cycles in the FCMC17 varve thickness record were examined using spectral analysis methods, based on the assumption that varve thickness variability is a proxy for glacial meltwater production (ice sheet ablation) and sediment transport capacity.

This analysis identified significant variability of LGC–BA varve thickness at inter-annual (2–8 years) and decadal (20–30 and 40–50 years) timescales, with 2–8-year cycles the strongest and most pervasive between 17,835–17,273 cal a BP. The inter-annual cycles are most consistent with ENSO variability, while the decadal cycles are consistent with PDO and/or IPO-like oscillations. Inter-annual peaks in varve thickness likely reflect warmer surface air temperatures over central Patagonia during El Niño events, due to warming of the adjacent eastern Pacific Ocean, weaker SWWs, and greater atmospheric heat. This warming would have enhanced ice sheet ablation and meltwater production, and increased the evacuation of stored glacial erosion products to the former lake system. It is also possible that the duration of the melt season was increased during El Niño events, and contributed to greater annual sediment fluxes. This analysis provides the first potential identification of tropical Pacific climate influences on Patagonian Ice Sheet ablation patterns. This interpretation supports (i) numerical climate models that predict strong ENSO activity during the last deglaciation (Timmermann et al., 2007; Liu et al., 2014); and (ii) previous suggestions of increased low-latitude forcing of mid-latitude climatic variability during the last deglaciation because of southward migration of a coupled atmosphere-ocean frontal system (Sikes et al., 2013).

The influence of low-latitude climate systems on LGC–BA varve thickness represents a hypothesis for further testing because, at present, there is no contemporaneous temperature dataset sampled at comparable temporal resolution (e.g. annual) to calibrate the varve thickness record, and test the interpretation that ENSO variability influenced regional temperatures and ice sheet ablation patterns. Instead, our interpretations are based on understanding of the modern-day patterns of ENSO and PDV variability, for which monitoring data are limited (Garreaud et al., 2009). Furthermore, the influence of the SAM on inter-annual ablation patterns cannot be discounted based on the recorded spectral frequencies and, indeed, previous work shows that these low- and high-latitude modes of climatic variability may coexist and interact (Simmonds and King, 2004; Fogt and Bromwich, 2006; Stammerjohn et al., 2008; Yeo and Kim, 2015; Walker and Gardener, 2017). Finally, temporal changes in the expression of both inter-annual (ENSO) and decadal (PDO/IPO) varve thickness cycles are necessarily tentative at present because (i) not all of the FCMC17 could be analysed for periodic features owing to minor breaks in the varve sequence; and (ii) inter-annual ablation signals may be dampened when distance from the ice-front increases.

8.1.7 Examining possible climatic controls on southern mid-latitude deglaciation

The comparable timing of glacial retreat in valleys from Patagonia (Denton et al., 1999a; Moreno et al., 2015) and New Zealand (Putnam et al., 2013a, 2013b) has led to hypotheses of synchronous mid-latitude deglaciation driven by ocean-atmosphere reorganisation at the hemispheric scale. However, the sub-centennial phasing of ice sheet and palaeoclimate changes is typically blurred by the chronological precision of radiometric dating approaches. The annually-resolved and incremental FCMC17, however, provides an archive of sufficiently high temporal resolution for comparisons with other high-resolution palaeoclimate records.

To examine the possible climatic forcing factors responsible for ice lobe deglaciation in central Patagonia, a compilation of regional paleoclimate data was compared to ice lobe retreat patterns inferred from varve thickness trends. This shows that the onset of deglaciation at LGC–BA (17,997 ± 144 cal a BP) was coincident with warming of the South Pacific Ocean (e.g. Lamy et al., 2007; Caniupán et al., 2011), air temperature increase over Antarctica (WAIS Members, 2013, 2015; EPICA Members, 2006), and Southern Ocean sea-ice decline (WAIS Members, 2015). Most striking, however, is that both the onset (~18 ka), and a subsequent acceleration (~17.8 ka) of LGC–BA ice lobe retreat, displays a phase-locked relationship (within dating uncertainties) with changes in the rate of atmospheric warming over West Antarctica (WAIS Members, 2013, 2015), suggesting that the middle and high southern latitudes might have warmed synchronously (within dating uncertainties) at that time, and that a common forcing factor may be responsible.

A possible mechanism is inferred from recent modelling simulations, which suggest that Southern Ocean convection events may stimulate the release of excess oceanic heat, and cause approximately synchronous (<100 years) warming of the mid- and high-latitudes (Pedro et al., 2016). This inference can accommodate evidence for broadly coincident timings for the onset of deglaciation on either side of the South Pacific Ocean, and implies that mid-latitude glaciers were highly sensitive to atmospheric temperature changes (e.g. Putnam et al., 2013a). Moreover, this hypothesis is compatible with an established body of evidence for southward migration of a coupled ocean-atmosphere frontal system at ~18 ka, in response to North Atlantic cooling, AMOC reduction, and ITCZ displacement during HS-1 (Denton et al., 2010). Specifically, poleward contraction of the SWWs may have initiated Southern Ocean convection by enhancing oceanic upwelling around the Antarctic continent (e.g. Anderson et al., 2009). Whilst this work

highlights the potential of a varve-based approach, it is limited by the need for longer a temporal record, and other high-resolution studies from the southern mid-latitude region.

8.2 Future work

8.2.1 Geomorphological constraints on ice lobe and palaeolake history

High-resolution geomorphological mapping (Chapter 3) provided the foundation for a new reconstruction of ice lobe and palaeolake evolution for the NPI region (Chapter 4). However, further understanding of the distribution of glacial landforms is required to refine this model. The unmapped area beneath the LGC–BA and LC–P lakes remains key to tracking the westwards retreat of ice lobes, and can only feasibly be investigated with sub-lacustrine imaging datasets, which are currently unavailable for this region. Improved mapping in the densely-vegetated western sectors of the study area is critical to testing the hypothesis of early Atlantic–Pacific drainage reversal in response to separation of NPI and Monte San Lorenzo outlet glaciers (Chapter 4). Further targeted field mapping could build upon the regional-scale map developed in this thesis. Similarly, the acquisition of high-resolution (e.g. LiDAR; Roering et al., 2013) bare-earth elevation models would improve the ability to identify glacial limits, and enable refinements of palaeolake history through improved discrimination of numerous closely-spaced shoreline levels (Yang and Teller, 2012; Breckenridge, 2013, 2015), which cluster together when using lower resolution ASTER-GDEM data (Chapter 4).

8.2.2 Sedimentological work

Chapter 3 presented examples of previously unmapped landform assemblages (hummocky terrain, continuous hummocky ridges, eskers, till eskers, iceberg wallow pits and craters, and ice-rafted moat lines), but sedimentological data is required to test the geomorphological interpretations. Sedimentological data could also help to understand the processes that controlled the apparent zonation of landforms on former ice lobe forelands (i.e. hummocky terrain, till eskers and eskers inset behind latero-frontal moraines), and improve the understanding of former glacial dynamics and thermal regimes, as has been possible in southernmost Patagonia adopting a glacial landsystems approach (Darvill et al., 2016).

8.2.3 Dating of proglacial lake level changes

The proglacial lake reconstruction presented in Chapter 4 identified new lake levels, and proposed an alternative sequence of events. However, these interpretations are currently untested with geochronology. Additional dating is required to constrain the timing of lake level changes in both the LGC–BA and LC–P basins, as this could test

competing models of lake unification between these valleys (Chapter 4; Turner et al., 2005; Hein et al., 2010; Bourgois et al., 2016; Glasser et al., 2016). The potential of luminescence techniques for dating lake shoreline deposits has been demonstrated (Glasser et al., 2016), however, large dating uncertainties prevent sub-millennial events being resolved. Therefore, luminescence methods may not currently be sufficient to discriminate differences in the timing of lake level lowering between LGC–BA and LC–P.

Another possibility is radiocarbon dating. The new regional post-glacial isostatic adjustment curves allow strategic targeting of basins in relation to former proglacial lake levels. Recent studies indicate that vegetation existed around waning ice lobe margins in central Patagonia, and rapidly accumulated in isolated lake basins following glacial lake lowering (Villa-Martinez et al., 2012; Henríquez et al., 2017). Such basins could be used more systematically to constrain the timing of lake level regressions at centennial-scale resolution, through radiocarbon dating of basal organic remains. Basin stratigraphy could provide evidence for possible lake transgressions, which are difficult to discern from the geomorphological record. Coring of basins could also be used to establish the extent of ice-free and ice-covered terrain in areas where ice-marginal landforms are lacking, and thus better linkages between ice-margin positions and palaeolake levels.

8.2.4 Refining the FCMC17

As outlined in Chapter 5, the ~1000-year FCMC17 represents a minimum estimate for the duration of deglacial events in eastern LGC–BA, due to breaks in the composite sequence that could not be bridged by cross-dating. The examination of new sites in Río Fenix Chico valley is required to help close these gaps and refine the existing chronology. This work should first concentrate on sequences located between the Fenix I and Menucos moraines, where ~70% of chronology breaks occur. The acquisition of new site records is also required to test the accuracy of segments of the FCMC17 that are based on varve counts from a single site.

Coring is also required to obtain sediments from beneath the present-day valley bottom. Whilst the thickness of the lowest recorded varves would suggest they formed within decades of ice lobe retreat (e.g. Ridge et al., 2012), there is potential to more precisely constrain recessional ice margin positions, through the identification of basal varves at multiple sites. Finally, further analysis for (crypto)tephra layers (Lowe, 2011) could prove a beneficial test for the interpretation of varve structure based on sedimentology, through counts of the number of inferred annual layers between independently-dated isochronous marker horizons.

8.2.5 Extending the varve chronology for LGC–BA ice lobe deglaciation

Beyond the potential refinement of the FCMC17, outlined above, extending the varve chronology to cover a greater duration of the regional deglaciation cycle remains a clear target. Terrestrial glaciolacustrine deposits elsewhere in the study region were mapped in Chapter 3 and represent possible sites for further investigation. Chapter 5 demonstrated the potential of tephrochronology in linking and dating disparate sites, and this approach could allow westwards tracking of ice lobe retreat. Ultimately, coring of LGC–BA is likely to provide the longest and most complete records, but this aim is currently limited by incomplete understanding of lake bathymetry (Murdie et al., 1999). An extended varve chronology would help to elucidate the rates of ice lobe retreat beyond the ~18–17 ka interval reflected in the FCMC17. Hubbard et al. (2005) simulate rapid ice lobe collapse after ~16 ka, but this modelled scenario is untested with empirical data.

Furthermore, an extended varve record could facilitate further examination of mid-latitude palaeoclimate during the last deglaciation, and possible interactions with the Patagonian Ice Sheet. For example, Chapter 6 reported a shortening of varve thickness cycles (from 2–8 to 2–5 years) after 17.1 cal ka that could reflect a change in the ENSO teleconnection to central Patagonia at that time, but equally might reflect reduced sensitivity of the varve thickness proxy record because of greater ice lobe distality. Similarly, the comparison of varve thickness and Antarctic ice cores in Chapter 7 suggests that ice sheet retreat patterns initially followed high-latitude atmospheric temperature trends, but became partially decoupled after ~17.3 cal ka in response to internal glaciological controls (e.g. calving). A longer varve record could test this hypothesis, and provide a crucial mid-latitude record of equal temporal resolution to annually-resolved ice-core records (WAIS Members, 2013; 2015).

8.2.6 Younger Dryas vs. Antarctic Cold Reversal glacier advances

The timing of glacier re-advances, or stillstands, which interrupted the deglaciation of the Patagonian Ice Sheet, remain contentious in the NPI region. The new palaeolake reconstruction presented in Chapter 4 questions the hypothesis of glacier re-advance during the Northern Hemisphere Younger Dryas interval (Glasser et al., 2012) because the dated moraine boulders were likely submerged beneath glacial lakes and therefore shielded from cosmogenic rays until lake lowering. Dating of high-level moraines, i.e. those above former lake levels, could help to resolve this issue, and the new isostatic adjustment curves could be used to target sites of sufficient elevation. A potential dating target would be the previously unmapped Soler glacier moraines at Lago Bertrand, which

record a period of glacier readvance in the western embayment of LGC–BA, and are elevated above the upper reconstructed palaeolake level in LGC–BA. However, although successful in other mid-latitude glacial settings (Moreno et al., 2009, 2015; Putnam et al., 2010; García et al., 2014), the precision of cosmogenic nuclide exposure dating may prevent confident separation of potential YD or ACR re-advances. An extended varve chronology, as discussed above, could offer more precise dating of ice lobe re-advance phases (e.g. Ridge et al., 2012), and could also provide durations for such events.

8.2.7 Numerical modelling

The data presented in this thesis could contribute towards important empirical constraints for future modelling efforts. Ice lobe and proglacial lake reconstructions (Chapters 4 and 5) provide a target for ice-sheet modelling studies (e.g. Hulton et al., 2002; Hubbard et al., 2005), whereas regional palaeoclimate proxy (varve thickness) datasets (e.g. ENSO; Chapter 6) offer valuable numeric datasets that can help to refine the predictive capability of climate models (Power et al., 2017).

8.3 Conclusion

This thesis has examined the deglaciation of the Patagonian Ice Sheet in the region 46–48°S of southern South America. The contribution provides new insights into the timing and dynamics of ice lobe retreat and proglacial lake evolution, following the culmination of the local LGM. To improve the spatial and temporal constraints on Patagonian Ice Sheet deglaciation, this thesis focused on detailed mapping of glacial geomorphology, and analyses of laminated glaciolacustrine sediment sequences, which were originally proposed to be annually-laminated, or varved (cf. Caldenius, 1932), and confirmed in this study.

The major achievement of this study is the development of a 994 ± 36 vyr duration (3.62% error) varve chronology (the Fenix Chico Master Varve Chronology; FCMC17) that records the earliest phases of ice lobe retreat at LGC—BA. The chronology has been anchored to the calendar-year timescale through the identification of a regional tephra isochron (the Ho tephra: 17,378 ± 118 cal a BP), which fixes the varve record between 17,997 ± 144 and 16,982 ± 127 cal a BP. Varve thickness trends record steady, but accelerating, ice lobe retreat throughout this period, and suggest that ice persisted in eastern LGC–BA until at least 16,934 ± 116 cal a BP (modelled age; 16,982 ± 127 cal a BP = modelled age), consistent with numerical ice-sheet modelling simulations (Hubbard et al., 2005).

The annually-resolved, and time-anchored FCMC17 has provided new insights into South American palaeoclimate, through spectral analysis of varve thickness trends, and comparisons with Southern Hemisphere proxy records derived from marine and terrestrial (e.g. ice-core) settings. The spectral analysis provides the first evidence for tropical Pacific (ENSO) influences on PIS deglaciation, and demonstrates the sensitivity of Southern Hemisphere mid-latitude palaeo-ice sheets to inter-annual climate variability. Comparisons with regional proxy datasets reveal the onset of deglaciation at LGC—BA to be in-phase (within dating uncertainties) with atmospheric warming trends recorded in West Antarctic ice cores, implying a rapid ice-sheet response to near-synchronous atmospheric warming of the mid- and high southern latitudes. The record also contributes to a growing body of evidence in support of a southward shift of a coupled ocean-atmosphere frontal system during HS-1, in response to North Atlantic freshwater forcing and ITCZ migration (Lamy et al., 2007; Denton et al., 2010; Putnam et al., 2013a). The Southern Ocean provides a possible link between the southern mid- and high latitudes in response to poleward frontal migration, through enhanced wind-driven convection around the Antarctic continent, and the rapid redistribution of oceanic and atmospheric heat.

References

Allan, R.J. 2000. ENSO and climatic variability in the past 150 years. In: Diaz, H., and Markgraf, V. (Eds.) El Niño and the Southern Oscillation – Multiscale Variability and Global and Regional Impacts. Cambridge University Press. pp. 3–56.

Alloway, B.V., Moreno, P.I., Pearce, N.J., Pol-Holz, D., Henríquez, W.I., Pesce, O.H., Sagredo, E., Villarosa, G. & Outes, V. 2017. Stratigraphy, age and correlation of Lepué Tephra: a widespread c. 11 000 cal a BP marker horizon sourced from the Chaitén Sector of southern Chile. Journal of Quaternary Science, 32, 795–829.

An, S.I., Timmermann, A., Bejarano, L., Jin, F.F., Justino, F., Liu, Z. & Tudhope, A.W. 2004. Modeling evidence for enhanced El Niño–Southern Oscillation amplitude during the last glacial maximum. Paleoceanography, 19. PA4009.

Anderson, R.F., Ali, S., Bradtmiller, L.I., Nielsen, S.H.H., Fleisher, M.Q., Anderson, B.E. & Burckle, L.H. 2009. Wind-driven upwelling in the Southern Ocean and the deglacial rise in atmospheric CO_2. Science, 323, 1443–1448.

Andreoli, R.V. & Kayano, M.T. 2005. ENSO-related rainfall anomalies in South America and associated circulation features during warm and cold Pacific decadal oscillation regimes. International Journal of Climatology, 25, 2017–2030.

Antevs, E. 1922. On the late-glacial and post-glacial history of the Baltic. American Geographical Society, 12, 602–612.

Antevs, E. 1928. The last glaciation, with special reference to the ice sheet in northeastern North America: American Geographical Society Research Series 17, 292 p.

Ariztegui, D., Bösch, P. & Davaud, E. 2007. Dominant ENSO frequencies during the Little Ice Age in Northern Patagonia: the varved record of proglacial Lago Frías, Argentina. Quaternary International, 161, 46–55.

Ashley, G.M. 1975. Rhythmic sedimentation in Glacial Lake Hitchcock, Massachusetts-Connecticut, in: Jopling, A.V., McDonald, B.C. (Eds.) Society of Economic Paleontologists and Mineralogists Special Publication, 23, pp. 304–320.

Ashley, G.M., Southard, J.B., Boothroyd, J.C., 1982. Deposition of climbing-ripple beds: a flume simulation. Sedimentology.

ASTER GDEM Validation Team. 2011. ASTER Global Digital Elevation Model Version 2 – Summary of Validation Results. NASA Land Processes Distributed Active Archive Center and the Joint Japan-US ASTER Science Team report.

Baker, V.R. 2009. The Channelled Scablands: A retrospective. Annual Review of Earth and Planetary Sciences, 37, 393–411.

Balco, G. 2011. Contributions and unrealized potential contributions of cosmogenic-nuclide exposure dating to glacier chronology, 1990–2010. Quaternary Science Reviews, 30, 3–27.

Balco, G., Stone, J.O., Lifton, N.A. & Dunai, T.J. 2008. A complete and easily accessible means of calculating surface exposure ages or erosion rates from ^{10}Be and ^{26}Al measurements. Quaternary Geochronology, 3, 174–195.

Bard, E. & Rickaby, R.E. 2009. Migration of the subtropical front as a modulator of glacial climate. Nature, 460, 380–384.

Barker, S., Diz, P., Vautravers, M.J., Pike, J., Knorr, G., Hall, I.R. & Broecker, W.S. 2009. Interhemispheric Atlantic seesaw response during the last deglaciation. Nature, 457, 1097–1102.

Barr, I.D. & Lovell, H., 2014. A review of topographic controls on moraine distribution. Geomorphology, 226, 44–64.

Barrell, D.J.A., 2011. Quaternary glaciers of New Zealand. In: Ehlers, J., Gibbard, P.L., Hughes, P.D. (Eds.) Developments in Quaternary Sciences, 15. Elsevier. pp. 1047–1064.

Barrows, T.T., Juggins, S., De Deckker, P., Calvo, E. & Pelejero, C. 2007. Long-term sea surface temperature and climate change in the Australian–New Zealand region. Paleoceanography, 22, PA2215.

Bell, C.M. 2008. Punctuated drainage of an ice-dammed Quaternary lake in Southern South America. Geografiska Annaler: Series A Physical Geography, 90, 1–17.

Bell, C.M. 2009. Quaternary lacustrine braid deltas on Lake General Carrera in southern Chile. Andean Geology, 36, 51–65.

Bendle, J.M., Palmer, A.P., Thorndycraft, V.R. & Matthews, I.P., 2017. High-resolution chronology for deglaciation of the Patagonian Ice Sheet at Lago Buenos Aires (46.5°S) revealed through varve chronology and Bayesian age modelling. Quaternary Science Reviews, 177, 314–339.

Bendle, J.M., Palmer, A.P., Thorndycraft, V.R. & Matthews, I.P. in prep. Sensitivity of the Patagonian Ice Sheet to sub-decadal tropical climate variability between 18–17 ka revealed by a glaciolacustrine varve thickness record at Lago Buenos Aires, Argentina. Earth and Planetary Science Letters.

Bendle, J.M., Thorndycraft, V.T. & Palmer, A.P., 2017. The glacial geomorphology of the Lago Buenos Aires and Lago Pueyrredón ice lobes of central Patagonia. Journal of Maps, 13, 654–673.

Benn, D.I. 1996. Subglacial and subaqueous processes near a glacier grounding line: sedimentological evidence from a former ice-dammed lake, Achnasheen Scotland. Boreas, 25, 23–36.

Benn, D.I., Warren, C.R. & Mottram, R.H. 2007. Calving processes and the dynamics of calving glaciers. Earth-Science Reviews, 82, 143–179.

Bennett, G.L., Evans, D.J.A., Carbonneau, P. & Twigg, D.R. 2010. Evolution of a debris-charged glacier landsystem, Kviárjökull, Iceland. Journal of Maps, 6, 40–67.

Bennett, M. R., Huddart, D. & Waller, R.I. 2000. Glaciofluvial crevasse and conduit fills as indicators of supraglacial dewatering during a surge, Skeiðarárjoökull, Iceland. Journal of Glaciology, 46, 25–34.

Bennett, M.R., Huddart, D. & Thomas, G.S. 2002. Facies architecture within a regional glaciolacustrine basin: Copper River, Alaska. Quaternary Science Reviews, 21, 2237–2279.

Bentley, M.J., Sugden, D.E., Hulton, N.R.J. & McCulloch, R.D. 2005. The landforms and pattern of deglaciation in the Strait of Magellan and Bahía Inútil, southernmost South America. Geografiska Annaler: Series A Physical Geography, 87, 313–333.

Biondi, F., Gershunov, A. & Cayan, D.R. 2001. North Pacific decadal climate variability since 1661. Journal of Climate, 14, 5–10.

Bird, B.W., Abbott, M.B., Finney, B.P. & Kutchko, B. 2009. A 2000 year varve-based climate record from the central Brooks Range, Alaska. Journal of Paleolimnology, 41, 25–41.

Blard, P.H., Sylvestre, F., Tripati, A.K., Claude, C., Causse, C., Coudrain, A., Condom, T., Seidel, J.L., Vimeux, F., Moreau, C. & Dumoulin, J.P. 2011. Lake highstands on the Altiplano (Tropical Andes) contemporaneous with Heinrich 1 and the

Younger Dryas: new insights from 14 C, U–Th dating and $\delta^{18}O$ of carbonates. Quaternary Science Reviews, 30, 3973–3989.

Blockley, S.P.E., Pyne-O'Donnell, S.D.F., Lowe, J.J., Matthews, I.P., Stone, A., Pollard, A.M., Turney, C.S.M. & Molyneux, E.G. 2005. A new and less destructive laboratory procedure for the physical separation of distal glass tephra shards from sediments. Quaternary Science Reviews, 24, 1952–1960.

Blunier, T., Chappellaz, J., Schwander, J., Dällenbach, A., Stauffer, B., Stocker, T.F., Raynaud, D., Jouzel, J., Clausen, H.L., Hammer, C.U. & Johnsen, S.J. 1998. Asynchrony of Antarctic and Greenland climate change during the last glacial period. Nature, 394, 739—743.

Boës, X. & Fagel, N. 2008. Relationships between southern Chilean varved lake sediments, precipitation and ENSO for the last 600 years. Journal of Paleolimnology 39, 237–252.

Boex, J.P. 2011. From ice sheet to icefield: a 3D reconstruction of the Patagonian ice mass at 47°S. PhD Thesis. Exeter University.

Boex, J., Fogwill, C., Harrison, S., Glasser, N., Hein, A., Schnabel, C. & Xu, S. 2013. Rapid thinning of the Late Pleistocene Patagonian Ice Sheet followed migration of the Southern Westerlies. Scientific Reports 3, 2118.

Boone, S. J. & Eyles, N. 2001. Geotechnical model for great plains hummocky moraine formed by till deformation below stagnant ice. Geomorphology, 38, 109–124.

Borlace, S., Cai, W. & Santoso, A. 2013. Multidecadal ENSO amplitude variability in a 1000-yr simulation of a coupled global climate model: Implications for observed ENSO variability. Journal of Climate, 26, 9399–9407.

Boucharel, J., Timmermann, A., Santoso, A., England, M.H., Jin, F.F. & Balmaseda, M.A. 2015. A surface layer variance heat budget for ENSO. Geophysical Research Letters, 42, 3529–3537.

Boucher, É., Guiot, J. & Chapron, E. 2011. A millennial multi-proxy reconstruction of summer PDSI for southern South America. Climate of the Past, 7, 957–974.

Boulton, G.S. & Eyles, N. 1979. Sedimentation by valley glaciers: a model and genetic classification. In: Schuchter, C. (Ed.) Moraines and Varves. Balkema. pp. 11–23.

Bourgois, J., Cisternas, M.E., Braucher, R., Bourlès, D. & Frutos, J. 2016. Geomorphic records along the General Carrera (Chile)–Buenos Aires (Argentina) glacial lake (46°–48°S), climate inferences, and glacial rebound for the past 7–9 ka. The Journal of Geology, 124, 27—53.

Boyce, E.S., Motyka, R.J. & Truffer, M. 2007. Flotation and retreat of a lake-calving terminus, Mendenhall Glacier, southeast Alaska, USA. Journal of Glaciology, 53, 211–224.

Brauer, A. 2004. Annually laminated lake sediments and their palaeoclimatic relevance. In: Fischer, H., Kumke, T., Lohmann, G., Negendank, J. (Eds.) The Climate in Historical Times. Springer. pp. 109–127.

Brauer, A., Endres, C., Günter, C., Litt, T., Stebich, M. & Negendank, J.F. 1999. High resolution sediment and vegetation responses to Younger Dryas climate change in varved lake sediments from Meerfelder Maar, Germany. Quaternary Science Reviews, 18, 321–329.

Brauer, A., Haug, G.H., Dulski, P., Sigman, D.M. & Negendank, J.F. 2008. An abrupt wind shift in western Europe at the onset of the Younger Dryas cold period. Nature Geoscience, 1, 520–523.

Breckenridge, A. 2007. The Lake Superior varve stratigraphy and implications for

eastern Lake Agassiz outflow from 10,700 to 8900 cal ybp (9.5–8.0 14 C ka). Palaeogeography, Palaeoclimatology, Palaeoecology, 246, 45–61.

Breckenridge, A. 2013. An analysis of the late glacial lake levels within the western Lake Superior basin based on digital elevation models. Quaternary Research, 80, 383–395.

Breckenridge, A. 2015. The Tintah-Campbell gap and implications for glacial Lake Agassiz drainage during the Younger Dryas cold interval. Quaternary Science Reviews, 117, 124–134.

Breckenridge, A., Lowell, T., Stroup, J. & Evans, G. 2012. A review and analysis of varve thickness records from glacial Lake Ojibway (Ontario and Quebec, Canada). Quaternary International, 260, 43–54.

Broecker, W.S. 1998. Paleocean circulation during the last deglaciation: a bipolar seesaw?. Paleoceanography, 13, 119–121.

Bronk Ramsey, C. 2008. Deposition models for chronological records. Quaternary Science Reviews, 27, 42–60.

Bronk Ramsey, C. 2009a. Bayesian analysis of radiocarbon dates. Radiocarbon, 51, 337–360.

Bronk Ramsey, C. 2009b. Dealing with outliers and offsets in radiocarbon dating. Radiocarbon, 51, 1023–1045.

Caldenius, C.C. 1932. Las glaciaciones cuaternarios en la Patagonia y Tierra del Fuego. Geografiska Annaler, 14, 1–164.

Calvo, E., Pelejero, C., De Deckker, P. & Logan, G.A. 2007. Antarctic deglacial pattern in a 30 kyr record of sea surface temperature offshore South Australia. Geophysical Research Letters, 34, L13707.

Cane, M.A. 2005. The evolution of El Niño, past and future. Earth and Planetary Science Letters, 230, 227–240.

Caniupán, M., Lamy, F., Lange, C.B., Kaiser, J., Kilian, R., Arz, H.W., León, T., Mollenhauer, G., Sandoval, S., De Pol-Holz, R. & Pantoja, S. 2014. Holocene sea-surface temperature variability in the Chilean fjord region. Quaternary Research, 82, 342–353.

Carel, M., Siani, G. & Delpech, G. 2011. Tephrostratigraphy of a deep-sea sediment sequence off the south Chilean margin: New insight into the Hudson volcanic activity since the last glacial period. Journal of Volcanology and Geothermal Research, 208, 99–111.

Carling, P.A. 2013. Freshwater megaflood sedimentation: what can we learn about generic processes? Earth Science Reviews, 125 87–113.

Carrivick, J.L. & Tweed, F.S. 2013. Proglacial lakes: character, behaviour and geological importance. Quaternary Science Reviews, 78, 34–52.

Cembrano, J. and Lara, L., 2009. The link between volcanism and tectonics in the southern volcanic zone of the Chilean Andes: a review. Tectonophysics, 471, 96-113.

Cembrano, J., Hervé, F. & Lavenu, A. 1996. The Liquiñe Ofqui fault zone: a long-lived intra-arc fault system in southern Chile. Tectonophysics, 259, 55–66.

Ceppi, P., Hwang, Y.T., Liu, X., Frierson, D.M. & Hartmann, D.L. 2013. The relationship between the ITCZ and the Southern Hemispheric eddy-driven jet. Journal of Geophysical Research: Atmospheres, 118, 5136–5146.

Cheel, R.J. & Rust, B.R. 1986. A sequence of soft-sediment deformation (dewatering) structures in Late Quaternary subaqueous outwash near Ottawa,

Canada. Sedimentary Geology, 47, 77–93.
Chen, X. & Wallace, J.M. 2015. ENSO-like variability: 1900–2013. Journal of Climate, 28, 9623–9641.
Chiang, J.C., Lee, S.Y., Putnam, A.E. & Wang, X. 2014. South Pacific Split Jet, ITCZ shifts, and atmospheric North–South linkages during abrupt climate changes of the last glacial period. Earth and Planetary Science Letters, 406, 233–246.
Chiverrell, R.C., Thrasher, I.M., Thomas, G.S., Lang, A., Scourse, J.D., van Landeghem, K.J., Mccarroll, D., Clark, C.D., Cofaigh, C.Ó., Evans, D.J.A. & Ballantyne, C.K. 2013. Bayesian modelling the retreat of the Irish Sea Ice Stream. Journal of Quaternary Science, 28, 200–209.
Christoffersen, P., Piotrowski, J. A. & Larsen, N. K. 2005. Basal processes beneath an Arctic glacier and their geomorphic imprint after a surge, Elisebreen, Svalbard. Quaternary Research, 64, 125–137.
Chutko, K.J. & Lamoureux, S.F. 2008. Identification of coherent links between interannual sedimentary structures and daily meteorological observations in Arctic proglacial lacustrine varves: potentials and limitations. Canadian Journal of Earth Sciences, 45, 1–13.
Clapperton, C. M. 1993. Quaternary geology and geomorphology of South America. Elsevier, Amsterdam.
Clark, C.D., Evans, D.J., Khatwa, A., Bradwell, T., Jordan, C.J., Marsh, S.H., Mitchell, W.A. & Bateman, M.D. 2004. Map and GIS database of glacial landforms and features related to the last British Ice Sheet. Boreas, 33, 359–375.
Clark, C.D., Hughes, A.L.C., Greenwood, S.L., Jordan, C. & Sejrup, H.P. 2012. Pattern and timing of retreat of the last Birtish-Irish Ice Sheet. Quaternary Science Reviews,44 ,112–146.
Clark, P.U., Dyke, A.S., Shakun, J.D., Carlson, A.E., Clark, J., Wohlfarth, B., Mitrovica, J.X., Hostetler, S.W. & McCabe, A.M. 2009. The last glacial maximum. Science, 325, 710–714.
Cockburn, J.M. & Lamoureux, S.F. 2008. Inflow and lake controls on short-term mass accumulation and sedimentary particle size in a High Arctic lake: implications for interpreting varved lacustrine sedimentary records. Journal of Paleolimnology, 40, 923–942.
Condron, A. & Winsor, P. 2012. Meltwater routing and the Younger Dryas. Proceedings of the National Academy of Sciences, 909, 19928–19933.
Cook, T.L., Bradley, R.S., Stoner, J.S. & Francus, P. 2009. Five thousand years of sediment transfer in a high arctic watershed recorded in annually laminated sediments from Lower Murray Lake, Ellesmere Island, Nunavut, Canada. Journal of Paleolimnology, 41, 77–94.
Coronato, A. & Rabassa, J. 2011. Pleistocene glaciations in Southern Patagonia and Tierra del Fuego. In Ehlers, L., Gibbard, P.L., Hughes, P.D. (Eds.) Developments in Quaternary Sciences, 15, Elsevier. pp. 715–727.
Coronato, A., Martínez, O. & Rabassa, J. 2004. Glaciations in Argentine Patagonia, southern South America. Ehlers, J., Gibbard, P.L. (Eds.) Developments in Quaternary Sciences. Elsevier.
Crowley, T.J. 1992. North Atlantic deep water cools the Southern Hemisphere. Paleoceanography, 7, 489–497.
Cuffey, K.M., Clow, G.D., Steig, E.J., Buizert, C., Fudge, T.J., Koutnik, M., Waddington, E.D., Alley, R.B. & Severinghaus, J.P. 2016. Deglacial temperature history of

West Antarctica. Proceedings of the National Academy of Sciences*, 113,* 14249–14254.

Czymzik, M., Brauer, A., Dulski, P., Plessen, B., Naumann, R., von Grafenstein, U. & Scheffler, R. 2013. Orbital and solar forcing of shifts in Mid-to Late Holocene flood intensity from varved sediments of pre-alpine Lake Ammersee (southern Germany). Quaternary Science Reviews, 61, 96–110.

D'Arrigo, R., Cook, E.R., Wilson, R.J., Allan, R. & Mann, M.E. 2005. On the variability of ENSO over the past six centuries. Geophysical Research Letters, 32, L03711.

D'Arrigo, R., Villalba, R. & Wiles, G. 2001. Tree-ring estimates of Pacific decadal climate variability. Climate Dynamics, 18, 219–224.

D'Orazio, M., Innocenti, F., Manetti, P., Tamponi, M., Tonarini, S., González-Ferrán, O., Lahsen, A. & Omarini, R. 2003. The Quaternary calc-alkaline volcanism of the Patagonian Andes close to the Chile triple junction: geochemistry and petrogenesis of volcanic rocks from the Cay and Maca volcanoes (~45°S, Chile). Journal of South American Earth Sciences, 16, 219–242.

Daniels, L.D. & Veblen, T.T. 2004. Spatiotemporal influences of climate on altitudinal treeline in northern Patagonia. Ecology, 85, 1284–1296.

Darvill, C.M., Bentley, M.J., Stokes, C.R., Hein, A.S. & Rodés, Á. 2015. Extensive MIS 3 glaciation in southernmost Patagonia revealed by cosmogenic nuclide dating of outwash sediments. Earth and Planetary Science Letters, 429, 157–169.

Darvill, C.M., Stokes, C.M., Bentley, M.J., Evans, D.J.A. & Lovell, H. 2016. Dynamics of former ice lobes of the southernmost Patagonian Ice Sheet based on a glacial landsystems approach. Journal of Quaternary Science, 32, 857–876.

Darvill, C.M., Stokes, C.R., Bentley, M.J. & Lovell, H. 2014. A glacial geomorphological map of the southernmost ice lobes of Patagonia: the Bahía Inútil–San Sebastián, Magellan, Otway, Skyring and Río Gallegos lobes. Journal of Maps, 10, 500–520.

Davies, B.J. & Glasser, N.F. 2012. Accelerating shrinkage of Patagonian glaciers from the Little Ice Age (~AD 1870) to 2011. Journal of Glaciology, 58, 1063–1084.

De Deckker, P., Moros, M., Perner, K. & Jansen, E. 2012. Influence of the tropics and southern westerlies on glacial interhemispheric asymmetry. Nature Geoscience, 5, 266–269.

De Geer, G. 1912. Geochronologie der letzten 12000 Jahre. Geologische Rundschau III, 457–471.

De Geer, G. 1940, Geochronologia Suecica principles: Kungl. Svenska Vetenskapsakademiens Handlingar, Tredje Series, Band 18, no. 6, 357 p.

Denton, G.H., Anderson, R.F., Toggweiler, J.R., Edwards, R.L., Schaefer, J.M. & Putnam, A.E. 2010. The last glacial termination. Science, 328, 1652–1656.

Denton, G.H., Heusser, C.J., Lowel, T.V., Moreno, P.I., Andersen, B.G., Heusser, L.E., Schlühter, C. & Marchant, D.R. 1999a. Interhemispheric linkage of paleoclimate during the last glaciation. Geografiska Annaler: Series A Physical Geography, 81, 107–153.

Denton, G.H., Lowell, T.V., Heusser, C.J., Schluchter, C., Andersen, B.G., Heusser, L.E., Moreno, P.I. & Marchant, D.R. 1999b. Geomorphology, stratigraphy, and radiocarbon chronology of Llanquihue drift in the area of the southern Lake District, Seno Reloncavi, and Isla Grande de Chiloe, Chile. Geografiska Annaler: Series A Physical Geography, 81, 167–229.

Desloges, J.R. & Gilbert, R. 1994. Sediment source and hydroclimatic inferences from glacial lake sediments: the postglacial sedimentary record of Lillooet Lake, British

Columbia. Journal of Hydrology, 159, 375–393.
Devine, R.M. & Palmer, A.P. 2017. A new varve thickness record from Allt Bhraic Achaidh Fan, middle Glen Roy, Lochaber: implications for understanding the Loch Lomond Stadial glaciolacustrine varve sedimentation trends. Proceedings of the Geologists' Association, 128, 136–145.
Douglass, D.C., Singer, B.S., Kaplan, M.R., Ackert, R.P., Mickelson, D.M. & Caffee, M.W. 2005. Evidence of early Holocene glacial advances in southern South America from cosmogenic surface-exposure dating. Geology, 33, 237–240.
Douglass, D.C., Singer, B.S., Kaplan, M.R., Mickelson, D.M. & Caffee, M.W. 2006. Cosmogenic nuclide surface exposure dating of boulders on last-glacial and late-glacial moraines, Lago Buenos Aires, Argentina: interpretive strategies and paleoclimate implications. Quaternary Geochronology, 1, 43–58.
Dussaillant, A.J., Buytaert, W., Meier, C. & Espinoza, F. 2012. Hydrological regime of remote catchments with extreme gradients under accelerated change: the Baker basin in Patagonia. Hydrological Sciences Journal, 57, 530–1542
Dutrieux, P., De Rydt, J., Jenkins, A., Holland, P.R., Ha, H.K., Lee, S.H., Steig, E.J., Ding, Q., Abrahamsen, E.P. & Schröder, M. 2014. Strong sensitivity of Pine Island ice-shelf melting to climatic variability. Science, 343, 174–178.
England, M.H., McGregor, S., Spence, P., Meehl, G.A., Timmermann, A., Cai, W., Gupta, A.S., McPhaden, M.J., Purich, A. & Santoso, A. 2014. Recent intensification of wind-driven circulation in the Pacific and the ongoing warming hiatus. Nature Climate Change, 4, 222–227.
EPICA Project Members. 2006. One-to-one coupling of glacial climate variability in Greenland and Antarctica. Nature, 444, 195–198.
Evans, D. J.A., Ewertowski, M. & Orton, C. 2016. Fláajökull (north lobe), Iceland: active temperate piedmont lobe glacial landsystem. Journal of Maps, 12, 777–789.
Evans, D.J.A. & Benn, D.I, 2004. A practical guide to the study of glacial sediments. Routledge.
Evans, D.J.A. & Orton, C. 2015. Heinabergsjökull and Skalafellsjökull, Iceland: active temperate piedmont lobe and outwash head glacial landsystem. Journal of Maps, 11, 415–431.
Evans, D.J.A. & Twigg, D.R. 2002. The active temperate glacial landsystem: a model based on Breiðamerkurjökull and Fjallsjökull, Iceland. Quaternary Science Reviews, 21, 2143–2177.
Evans, D.J.A. 2003. Glacial Landsystems. Hodder-Arnold.
Evans, D.J.A. 2009. Controlled moraines: origins, characteristics and palaeoglaciological implications. Quaternary Science Reviews, 28, 183–208.
Evans, D.J.A. 2013a. Tills. In: Elias, S.A. (Ed). Encyclopedia of Quaternary Science, 62–75.
Evans, D.J.A. 2013b. Moraine forms and genesis. In: In: Elias, S.A. (Ed). Encyclopedia of Quaternary Science, 769-779.
Evans, D.J.A., Hiemstra, J.F. & Cofaigh, C.Ó. 2012. Stratigraphic architecture and sedimentology of a Late Pleistocene subaqueous moraine complex, southwest Ireland. Journal of Quaternary Science, 27, 51–63.
Evans, D.J.A., Nelson, C.D. & Webb, C. 2010. An assessment of fluting and “till esker” formation on the foreland of Sandfellsjökull, Iceland. Geomorphology, 114, 453—465.
Evans, D.J.A., Phillips, E.R., Hiemstra, J.F. & Auton, C.A. 2006. Subglacial till:

formation, sedimentary characteristics and classification. Earth-Science Reviews, 78, 115–176.

Evans, D.J.A., Rother, H., Hyatt, O.M. and Shulmeister, J. 2013. The glacial sedimentology and geomorphological evolution of an outwash head/moraine-dammed lake, South Island, New Zealand. Sedimentary Geology, 284, 45–75.

Eyles, N., Boyce, J.I. & Barendregt, R.W. 1999. Hummocky moraine: sedimentary record of stagnant Laurentide Ice Sheet lobes resting on soft beds. Sedimentary Geology, 123, 163–174.

Fagel, N., Boës, X. & Loutre, M.F. 2008. Climate oscillations evidenced by spectral analysis of Southern Chilean lacustrine sediments: the assessment of ENSO over the last 600 years. Journal of Paleolimnology, 39, 253–266.

Farr, T.G., Rosen, P.A., Caro, E., Crippen, R., Duren, R., Hensley, S., Kobrick, M., Paller, M., Rodriguez, E., Roth, L. & Seal, D. 2007. The shuttle radar topography mission. Reviews of Geophysics, 45, RG2004.

Felis, T., Merkel, U., Asami, R., Deschamps, P., Hathorne, E.C., Kölling, M., Bard, E., Cabioch, G., Durand, N., Prange, M. & Schulz, M. 2012. Pronounced interannual variability in tropical South Pacific temperatures during Heinrich Stadial 1. Nature Communications, 3, 965.

Feruglio, E. 1950. Descripción geológica de la Patagonia. Dirección General de Yacimientos Petroliferos Fiscales, Tomo, III 1–342. Buenos Aires.

Fidalgo, F. & Riggi, J. 1965. Los rodados patagónicos de la Maesta de Guenguel y airededores (Santa Cruz). Revista de la Asociación Geológica Argentina, 20, 273–325.

Fogt, R.L. & Bromwich, D.H. 2006. Decadal variability of the ENSO teleconnection to the high-latitude South Pacific governed by coupling with the southern annular mode. Journal of Climate, 19, 979–997.

Folland, C.K., Renwick, J.A., Salinger, M.J. & Mullan, A.B. 2002. Relative influences of the interdecadal Pacific oscillation and ENSO on the South Pacific convergence zone. Geophysical Research Letters, 29, 2002.

Fontijn, K., Lachowycz, S.M., Rawson, H., Pyle, D.M., Mather, T.A., Naranjo, J.A. & Moreno-Roa, H. 2014. Late Quaternary tephrostratigraphy of southern Chile and Argentina. Quaternary Science Reviews, 89, 70–84.

Fontijn, K., Rawson, H., Van Daele, M., Moernaut, J., Abarzúa, A.M., Heirman, K., Bertrand, S., Pyle, D.M., Mather, T.A., De Batist, M. & Naranjo, J.A. 2016. Synchronisation of sedimentary records using tephra: A postglacial tephrochronological model for the Chilean Lake District. Quaternary Science Reviews, 137, 234–254.

Ford, H.L., Ravelo, A.C. & Polissar, P.J. 2015. Reduced El Niño–Southern Oscillation during the Last Glacial Maximum. Science, 347, 255–258.

Francou, B., Vuille, M., Favier, V. & Cáceres, B. 2004. New evidence for an ENSO impact on low-latitude glaciers: Antizana 15, Andes of Ecuador, 0°28'S. Journal of Geophysical Research: Atmospheres, 109, D18106.

Fraser, G.S., Thompson, T.A., Kvale, E.P., Carlson, C.P., Fishbaugh, D.A., Graver, B.L., Holbrook, J., Kairo, S., Kohler, C.S., Malone, A.E. & Moore, C.H. 1991. Sediments and sedimentary structures of a barred, nontidal coastline, southern shore of Lake Michigan. Journal of Coastal Research, 7, 1113–1124.

Galbraith, R.F., Roberts, R.G., Laslett, G.M., Yoshida, H. & Olley, J.M. 1999. Optical Dating of Single and Multiple Grains of Quartz from Jinmium Rock Shelter,

Northern Australia: Part I, Experimental Design and Statistical Models. Archaeometry, 41, 339–364

García, J.L., Hall, B.L., Kaplan, M.R., Vega, R.M. & Strelin, J.A. 2014. Glacial geomorphology of the Torres del Paine region (southern Patagonia): Implications for glaciation, deglaciation and paleolake history. Geomorphology, 204, 599–616.

García, J.L., Kaplan, M.R., Hall, B.L., Schaefer, J.M., Vega, R.M., Schwartz, R. & Finkel, R. 2012. Glacier expansion in southern Patagonia throughout the Antarctic Cold Reversal. Geology, 40, 859–862.

Garreaud, R. 2007. Precipitation and circulation covariability in the extratropics. Journal of Climate, 20, 4789–4797.

Garreaud, R., Lopez, P., Minvielle, M. & Rojas, M. 2013. Large-scale control on the Patagonian climate. Journal of Climate, 26, 215–230.

Garreaud, R.D., Vuille, M., Compagnucci, R. & Marengo, J. 2009. Present-day South American climate. Palaeogeography, Palaeoclimatology, Palaeoecology, 281, 180–195.

Gedalof, Z.E. & Smith, D.J. 2001. Interdecadal climate variability and regime-scale shifts in Pacific North America. Geophysical Research Letters, 28, 1515–1518.

Gersonde, R., Crosta, X., Abelmann, A. & Armand, L. 2005. Sea-surface temperature and sea ice distribution of the Southern Ocean at the EPILOG Last Glacial Maximum—a circum-Antarctic view based on siliceous microfossil records. Quaternary Science Reviews, 24, 869–896.

Gillett, N.P., Kell, T.D. & Jones, P.D. 2006. Regional climate impacts of the Southern Annular Mode. Geophysical Research Letters, 33. L23704.

Glasser, N.F. & Ghiglione, M.C. 2009. Structural, tectonic and glaciological controls on the evolution of fjord landscapes. Geomorphology, 105, 291–302.

Glasser, N.F. & Jansson, K. 2008. The glacial map of southern South America. Journal of Maps, 4, 175–196.

Glasser, N.F. & Jansson, K.N. 2005. Fast-flowing outlet glaciers of the last glacial maximum Patagonian Icefield. Quaternary Research, 63, 206–211.

Glasser, N.F., Harrison, S. & Jansson, K.N. 2009. Topographic controls on glacier sediment–landform associations around the temperate North Patagonian Icefield. Quaternary Science Reviews, 28, 2817–2832.

Glasser, N.F., Harrison, S., Ivy-Ochs, S., Duller, G.A. & Kubik, P.W. 2006. Evidence from the Rio Bayo valley on the extent of the North Patagonian Icefield during the Late Pleistocene-Holocene transition. Quaternary Research, 65, 70–77.

Glasser, N.F., Harrison, S., Schnabel, C., Fabel, D. & Jansson, K.N. 2012. Younger Dryas and early Holocene age glacier advances in Patagonia. Quaternary Science Reviews, 58, 7–17.

Glasser, N.F., Jansson, K.N., Duller, G.A., Singarayer, J., Holloway, M. & Harrison, S. 2016. Glacial lake drainage in Patagonia (13-8 kyr) and response of the adjacent Pacific Ocean. Scientific Reports, 6. 21064.

Glasser, N.F., Jansson, K.N., Goodfellow, B.W., de Angelis, H., Rodnight, H. & Rood, D.H. 2011. Cosmogenic nuclide exposure ages for moraines in the Lago san Martin valley, Argentina. Quaternary Research, 75, 636–646.

Glasser, N.F., Jansson, K.N., Harrison, S. & Kleman, J. 2008. The glacial geomorphology and Pleistocene history of South America between 38°S and 56°S. Quaternary Science Reviews, 27, 365–390.

Glasser, N.F., Jansson, K.N., Harrison, S. & Rivera, A. 2005. Geomorphological evidence for variations of the North Patagonian Icefield during the Holocene. Geomorphology, 71, 263—277.

Glur, L., Stalder, N.F., Wirth, S.B., Gilli, A. & Anselmetti, F.S. 2015. Alpine lacustrine varved record reveals summer temperature as main control of glacier fluctuations over the past 2250 years. The Holocene, 25, 280–287.

Golyandina, N. & Korobeynikov, A. 2014. Basic singular spectrum analysis and forecasting with R. Computational Statistics & Data Analysis, 71, 934–954.

Golyandina, N. & Zhigljavsky, A. 2013. Singular Spectrum Analysis for Time Series. Springer.

Gorring, M., Singer, B., Gowers, J. & Kay, S.M. 2003. Plio-Pleistocene basalts from the Meseta del Lago Buenos Aires, Argentina: evidence for asthenosphe-lithosphere interactions during slab window magmatism. Chemical Geology, 193, 215–235.

Graham, N. & White, W. 1988. The El Nino cycle: A natural oscillator of the Pacific Ocean- Atmosphere system. Science, 240, 1293–1302.

Guillaume B., Gautheron, C., Simon-Labric, T., Martinod, J., Roddaz, M., and Douville, E., 2013, Dynamic topography control on Patagonian relief evolution as inferred from low temperature thermochronology: Earth and Planetary Science Letters, 364, 157–167.

Guivel, C., Morata, D., Pelleter, E., Espinoza, F., Maury, R.C., Lagabrielle, Y., Polvé, M., Bellon, H., Cotten, J., Benoit, M. & Suárez, M. 2006. Miocene to Late Quaternary Patagonian basalts (46–47 S): geochronometric and geochemical evidence for slab tearing due to active spreading ridge subduction. Journal of Volcanology and Geothermal Research, 149, 346–370.

Gupta, S.A. & England, M.H. 2006. Coupled ocean–atmosphere–ice response to variations in the Southern Annular Mode. Journal of Climate, 19, 4457–4486.

Gustavson, T.C. 1975. Bathymetry and sediment distribution in proglacial Malaspina Lake, Alaska. Journal of Sedimentary Petrology, 45, 450–461.

Gutiérrez, F., Gioncada, A., Ferran, O.G., Lahsen, A. & Mazzuoli, R. 2005. The Hudson Volcano and surrounding monogenetic centres (Chilean Patagonia): an example of volcanism associated with ridge–trench collision environment. Journal of Volcanology and Geothermal Research, 145, 207-233.

Haberle, S.G. & Lumley, S.H. 1998. Age and origin of tephras recorded in postglacial lake sediments to the west of the southern Andes, 44°S to 47°S. Journal of Volcanology and Geothermal Research, 84, 239–256.

Hall, B.L., Hendy, C.H. & Denton, G.H. 2006. Lake-ice conveyor deposits: Geomorphology, sedimentology, and importance in reconstructing the glacial history of the Dry Valleys. Geomorphology, 75, 143–156.

Hall, B.L., Porter, C.T., Denton, G.H., Lowell, T.V. & Bromley, G.R. 2013. Extensive recession of Cordillera Darwin glaciers in southernmost South America during Heinrich Stadial 1. Quaternary Science Reviews, 62, 49–55.

Hambley, G.W. & Lamoureux, S.F. 2006. Recent summer climate recorded in complex varved sediments, Nicolay Lake, Cornwall Island, Nunavut, Canada. Journal of Paleolimnology, 35, 629–640.

Hammer, Ø., Harper, D.A.T. & Ryan, P.D. 2001. PAST: Paleontological Statistics Software Package for Education and Data Analysis. Palaeontologia Electronica 4, 9 p.

Hang, T. 2003. A local clay varve chronology and proglacial sedimentary environment

in glacial Lake Peipsi, eastern Estonia. Boreas, 32, 416–426.
Harrison, S., Glasser, N.F., Winchester, V., Haresign, E., Warren, C.R., Duller, G.A.T., Bailey, R., Ivy-Ochs, S., Jansson, K. & Kubik, P. 2008. Glaciar León, Chilean Patagonia: late Holocene chronology and geomorphology. The Holocene, 18, 643–652.
Harrison, S., Glasser, N.F., Winchester, V., Haresign, E., Warren, C.R. & Jansson, K.N. 2006. A glacial lake outburst food associated with recent mountain glacier retreat, Patagonian Andes. The Holocene, 16, 611–620.
Hayward, C. 2012. High spatial resolution electron probe microanalysis of tephras and melt inclusions without beam-induced chemical modification. The Holocene, 22, 119–125.
Heideman, M., Menounos, B. & Clague, J.J. 2015. An 825-year long varve record from Lillooet Lake, British Columbia, and its potential as a flood proxy. Quaternary Science Reviews, 126, 158–174.
Heideman, M., Menounos, B. & Clague, J.J. 2015. An 825-year long varve record from Lillooet Lake, British Columbia, and its potential as a flood proxy. Quaternary Science Reviews, 126, 158–174.
Hein, A.S. 2009. Quaternary glaciations in the Lago Pueyrredon valley, Argentina. PhD Thesis, Edinburgh University.
Hein, A.S, Hulton, N.R.J., Dunai, T.J., Schnabel, C., Kaplan, M.R, Naylor, M. & Xu, S. 2009. Middle Pleistocene glaciation in Patagonia dated by cosmogenic-nuclide measurements on outwash gravels. Earth and Planetary Science Letters, 286, 184–197.
Hein, A.S, Hulton, N.R.J., Dunai, T.J., Sugden, D.E., Kaplan, M.R. & Xu, S. 2010. The chronology of the Last Glacial Maximum and deglacial events in central Argentine Patagonia. Quaternary Science Reviews, 29, 1212–1227.
Hein, A.S., Cogez, A., Darvill, C.M., Mendelova, M., Kaplan, M.R., Herman, F., Dunai, T.J., Norton, K., Xu, S., Christl, M. & Rodés, Á. 2017. Regional mid-Pleistocene glaciation in central Patagonia. Quaternary Science Reviews, 164, 77–94.
Hein, A.S., Dunai, T.J., Hulton, N.R. & Xu, S. 2011. Exposure dating outwash gravels to determine the age of the greatest Patagonian glaciations. Geology, 39, 103–106.
Hein, A.S., Hulton, N.R., Dunai, T.J., Sugden, D.E., Kaplan, M.R. & Xu, S. 2010. The chronology of the Last Glacial Maximum and deglacial events in central Argentine Patagonia. Quaternary Science Reviews, 29, 1212–1227.
Henley, B.J. 2017. Pacific decadal climate variability: Indices, patterns and tropical-extratropical interactions. Global and Planetary Change, 155, 42–55.
Henley, B.J., Gergis, J., Karoly, D.J., Power, S., Kennedy, J. & Folland, C.K. 2015. A tripole index for the Interdecadal Pacific Oscillation. Climate Dynamics, 45, 3077–3090.
Henríquez, W.I., Villa-Martínez, R., Vilanova, I., De Pol-Holz, R. & Moreno, P.I. 2017. The last glacial termination on the eastern flank of the central Patagonian Andes (47°S). Climate of the Past, 13, 879–895.
Hodder, K.R., Gilbert, R. & Desloges, J.R. 2007. Glaciolacustrine varved sediment as an alpine hydroclimatic proxy. Journal of Paleolimnology, 38, 365–394.
Hogg, A.G., Hua, Q., Blackwell, P.G., Niu, M., Buck, C.E., Guilderson, T.P., Heaton, T.J., Palmer, J.G., Reimer, P.J., Reimer, R.W. & Turney, C.S. 2013. SHCal13 Southern Hemisphere calibration, 0–50,000 years cal BP. Radiocarbon, 55, 1–15.

Hubbard, A., Hein, A.S., Kaplan, M.R., Hulton, N.R. & Glasser, N. 2005. A modelling reconstruction of the last glacial maximum ice sheet and its deglaciation in the vicinity of the Northern Patagonian Icefield, South America. Geografiska Annaler: Series A Physical Geography 87, 375–391.

Hudson, P.F., Middelkoop, H. & Stouthamer, E. 2008. Flood management along the Lower Mississippi and Rhine Rivers (The Netherlands) and the continuum of geomorphic adjustment. Geomorphology, 101, 209–236.

Hughes, A.L., Clark, C.D. & Jordan, C.J. 2010. Subglacial bedforms of the last British Ice Sheet. Journal of Maps, 6, 543–563.

Hulton, N., Sugden, D., Payne, A. & Clapperton, C. 1994. Glacier modeling and the climate of Patagonia during the last glacial maximum. Quaternary Research, 42, 1–19.

Hulton, N.R., Purves, R.S., McCulloch, R.D., Sugden, D.E. & Bentley, M.J. 2002. The last glacial maximum and deglaciation in southern South America. Quaternary Science Reviews, 21, 233–241.

Hyttinen, O., Salonen, V.-P. & Kaakinen, A. 2011. Depositional evidence of water-level changes of the Baltic Ice Lake in southern Finland during the Younger Dryas/Holocene transition. Gff, 133, 77–88.

Jouzel, J., Masson-Delmotte, V., Cattani, O., Dreyfus, G., Falourd, S., Hoffmann, G., Minster, B., Nouet, J., Barnola, J.M., Chappellaz, J. & Fischer, H. 2007. Orbital and millennial Antarctic climate variability over the past 800,000 years. Science, 317, 793–796.

Kaiser, J., Lamy, F. & Hebbeln, D., 2005. A 70-kyr sea surface temperature record off southern Chile (Ocean Drilling Program Site 1233). Paleoceanography, 20, PA4009.

Kaplan, M.R., Ackert, R.P., Singer, B.S., Douglass, D.C. & Kurz, M.D. 2004. Cosmogenic nuclide chronology of millennial-scale glacial advances during O-isotope stage 2 in Patagonia. Geological Society of America Bulletin, 116, 308–321.

Kaplan, M.R., Douglass, D.C., Singer, B.S., Ackert, R.P. & Caffee, M.W. 2005. Cosmogenic nuclide chronology of pre-last glacial maximum moraines at Lago Buenos Aires, 46°S, Argentina. Quaternary Research, 63, 301–315.

Kaplan, M.R., Fogwill, C.J., Sugden, D.E., Hulton, N.R.J., Kubik, P.W. & Freeman, S.P.H.T. 2008. Southern Patagonian glacial chronology for the Last Glacial period and implications for Southern Ocean climate. Quaternary Science Reviews, 27, 284–294.

Kaplan, M.R., Hein, A.S., Hubbard, A. & Lax, S.M. 2009. Can glacial erosion limit the extent of glaciation? Geomorphology, 103, 172–179.

Kaplan, M.R., Strelin, J.A., Schaefer, J.M., Denton, G.H., Finkel, R.C., Schwartz, R., Putnam, A.E., Vandergoes, M.J., Goehring, B.M. & Travis, S.G. 2011. In-situ cosmogenic ^{10}Be production rate at Lago Argentino, Patagonia: implications for late-glacial climate chronology. Earth and Planetary Science Letters, 309, 21–32.

Kiem, A.S., Franks, S.W. & Kuczera, G. 2003. Multi-decadal variability of flood risk. Geophysical Research Letters, 30, 1035.

Kilian, R. & Lamy, F. 2012. A review of Glacial and Holocene paleoclimate records from southernmost Patagonia (49–55°S). Quaternary Science Reviews, 53, 1–23.

King, A.D., Alexander, L.V. & Donat, M.G. 2013. Asymmetry in the response of eastern Australia extreme rainfall to low-frequency Pacific variability. Geophysical Research Letters, 40, 2271–2277.

Kirkbride, M.P. & Dugmore, A.J. 2003. Glaciological response to distal tephra fallout from the 1947 eruption of Hekla, south Iceland. Journal of Glaciology, 49, 420–428.

Kirkbride, M.P. 2000. Ice marginal geomorphology and Holocene expansion of debris-covered Tasman Glacier, New Zealand. In: Nakawo, M., Raymond, C., Fountain, A. (Eds.) Debris-covered glaciers. IAHS Publication, 264. pp. 211–217.

Kleman, J. & Borgström, I. 1996. Reconstruction of palaeo-ice sheets: the use of geomorphological data. Earth Surface Processes and Landforms, 21, 893–909.

Kleman, J., Hättestrand, C., Stroeven, A.P., Jansson, K., De Angelis, H. & Borgström, I. 2006. Reconstruction of palaeo-ice sheets – inversion of their glacial geomorphological record. In Knight, P. (Ed.) Glaciology and Earth's Changing Environment. Blackwell. pp. 192–198.

Kohfeld, K.E., Graham, R.M., De Boer, A.M., Sime, L.C., Wolff, E.W., Le Quéré, C. & Bopp, L. 2013. Southern Hemisphere westerly wind changes during the Last Glacial Maximum: paleo-data synthesis. Quaternary Science Reviews, 68, 76–95.

Koutavas, A. & Joanides, S. 2012. El Niño–Southern Oscillation extrema in the Holocene and Last Glacial Maximum. Paleoceanography, 27. PA4208.

Kratzmann, D.J., Carey, S., Scasso, R. & Naranjo, J.A. 2009. Compositional variations and magma mixing in the 1991 eruptions of Hudson volcano, Chile. Bulletin of Volcanology, 71, 419.

Lal, D. 1991. Cosmic ray labeling of erosion surfaces: in situ nuclide production rates and erosion models. Earth and Planetary Science Letters, 104, 424-439.

Lamoureux, S. 2000. Five centuries of interannual sediment yield and rainfall-induced erosion in the Canadian High Arctic recorded in lacustrine varves. Water Resources Research, 36, 309–318.

Lamoureux, S.F. & Bradley, R.S. 1996. A late Holocene varved sediment record of environmental change from northern Ellesmere Island, Canada. Journal of Paleolimnology, 2, 239–255.

Lamoureux, S.F. & Gilbert, R. 2004. A 750-yr record of autumn snowfall and temperature variability and winter storminess recorded in the varved sediments of Bear Lake, Devon Island, Arctic Canada. Quaternary Research, 61, 134–147.

Lamoureux, S.F. 2001. Varve chronology techniques. Kluwer Academic Publishers. pp. 247–258.

Lamy, F., Arz, H.W., Kilian, R., Lange, C.B., Lembke-Jene, L., Wengler, M., Kaiser, J., Baeza-Urrea, O., Hall, I.R., Harada, N. & Tiedemann, R. 2015. Glacial reduction and millennial-scale variations in Drake Passage throughflow. Proceedings of the National Academy of Sciences, 112, 13496–13501.

Lamy, F., Kaiser, J., Arz, H.W., Hebbeln, D., Ninnemann, U., Timm, O., Timmermann, A. & Toggweiler, J.R. 2007. Modulation of the bipolar seesaw in the Southeast Pacific during Termination 1. Earth and Planetary Science Letters, 259, 400–413.

Lane, C.S., Brauer, A., Blockley, S.P.E. & Dulski, P. 2013. Volcanic ash reveals time-transgressive abrupt climate change during the Younger Dryas. Geology, 41, 1251–1254.

Lane, T.P., Roberts, D.H., Rea, B.R., Cofaigh, C.Ó., Vieli, A. & Rodés, A. 2014. Controls upon the last glacial maximum deglaciation of the northern Uummannaq ice stream system, west Greenland. Quaternary Science Reviews, 92, 324–344.

Larsen, D.J., Geirsdóttir, Á. & Miller, G.H. 2015. Precise chronology of Little Ice Age expansion and repetitive surges of Langjökull, central Iceland. Geology, 43, 167-170.

Larsen, D.J., Miller, G.H., Geirsdóttir, Á. & Thordarson, T. 2011. A 3000-year varved record of glacier activity and climate change from the proglacial lake Hvítárvatn, Iceland. Quaternary Science Reviews, 30, 2715–2731.

Larsen, N.K., Piotrowski, J.A., Christoffersen, P. & Menzies, J. 2006. Formation and deformation of basal till during a glacier surge; Elisebreen, Svalbard. Geomorphology, 81, 217—234.

Le Bas, M., Maitre, R.L., Streckeisen, A. & Zanettin, B. 1986. A chemical classification of volcanic rocks based on the total alkali-silica diagram. Journal of Petrology, 27, 745–750.

Leduc, G., Vidal, L., Cartapanis, O. & Bard, E. 2009. Modes of eastern equatorial Pacific thermocline variability: Implications for ENSO dynamics over the last glacial period. Paleoceanography, 24, PA3202.

Lee, S.Y., Chiang, J.C., Matsumoto, K. & Tokos, K.S., 2011. Southern Ocean wind response to North Atlantic cooling and the rise in atmospheric CO2: Modeling perspective and paleoceanographic implications. Paleoceanography, 26, PA1214.

Leeman, A. & Niessen, F. 1994. Varve formation and the climatic record in and Alpine proglacial lake: calibrating annually laminated sediments against hydrological and meteorological data. The Holocene, 4, 1–8.

Lemieux-Dudon, B., Blayo, E., Petit, J.R., Waelbroeck, C., Svensson, A., Ritz, C., Barnola, J.M., Narcisi, B.M. & Parrenin, F. 2010. Consistent dating for Antarctic and Greenland ice cores. Quaternary Science Reviews, 29, 8–20.

Leonard, E.M. 1997. The relationship between glacial activity and sediment production: evidence from a 4450 year varve record of neoglacial sedimentation in Hector Lake, Alberta, Canada. Journal of Palaeolimnology, 17, 319–330.

Lewis, T., Gilbert, R. & Lamoureux, S.F. 2002. Spatial and temporal changes in sedimentary processes at proglacial Bear Lake, Devon Island, Nunavut, Canada. Arctic, Antarctic, and Alpine Research 34, 119–129.

Li, J., Xie, S.P., Cook, E.R., Huang, G., D'arrigo, R., Liu, F., Ma, J. & Zheng, X.T. 2011. Interdecadal modulation of El Niño amplitude during the past millennium. Nature Climate Change, 1, 114–118.

Linsley, B.K., Zhang, P., Kaplan, A., Howe, S.S. & Wellington, G.M. 2008. Interdecadal-decadal climate variability from multicoral oxygen isotope records in the South Pacific Convergence Zone region since 1650 AD. Paleoceanography, 23. PA2219.

Liu, Z., Lu, Z., Wen, X., Otto-Bliesner, B.L., Timmermann, A. & Cobb, K.M. 2014. Evolution and forcing mechanisms of El Niño over the past 21,000 years. Nature, 515, 550–553.

Livingstone, S.J., Cofaigh, C.Ó.. Evans, D.J.A. & Palmer, A.P. 2010. Sedimentary evidence for a major glacial oscillation and proglacial lake formation in the Solway Lowlands (Cumbria, UK) during Late Devensian deglaciation. Boreas, 39, 505–527.

Lohmann, K. & Latif, M. 2005. Tropical Pacific decadal variability and the subtropical–tropical cells. Journal of Climate, 18, 5163–5178.

Lomb, N.R. 1976. Least-squares frequency analysis of unequally spaced data. Astrophysics and Space Science, 39, 447–462.

López-Escobar, L., Kilian, R., Kempton, P.D. & Tagiri, M. 1993. Petrography and geochemistry of Quaternary rocks from the Southern Volcanic Zone of the Andes between 41°30' and 46°00'S, Chile. Revista Geológica de Chile, 20, 33–55.

Loso, M.G., Anderson, R.S., Anderson, S.P. & Reimer, P.J. 2006. A 1500-year record of temperature and glacial response inferred from varved Iceberg Lake, southcentral Alaska. Quaternary Research, 66, 12–24.

Lovell, H., Stokes, C.R. & Bentley, M.J. 2011. A glacial geomorphological map of the Seno Skyring-Seno Otway-Strait of Magellan region, southernmost Patagonia. Journal of Maps, 7, 318–339.

Lovell, H., Stokes, C.R., Bentley, M.J. & Benn, D.I. 2012. Evidence for rapid ice flow and proglacial lake evolution around the central Strait of Magellan region, southernmost Patagonia. Journal of Quaternary Science, 27, 625–638.

Lowe, D.J. 2011. Tephrochronology and its application: a review. Quaternary Geochronology, 6, 107–153.

Lukas, S. 2005. A test of the englacial thrusting hypothesis of 'hummocky' moraine formation: case studies from the northwest Highlands, Scotland. Boreas, 34, 287—307.

MacLeod, A, Brunnberg, L, Wastegård, S., Hang, T. & Matthews, I.P. 2014. Lateglacial cryptotephra detected within clay varves in Östergötland, south east Sweden. Journal of Quaternary Science, 29, 605–609.

MacLeod, A., Matthews, I.P., Lowe, J.J. & Palmer, A.P. 2015. A second tephra isochron for the Younger Dryas period in Northern Europe: the Abernethy Tephra. Quaternary Geochronology, 28, 1–11.

MacLeod, A., Palmer, A., Lowe, J., Rose, J., Bryant, C. & Merritt, J. 2011. Timing of glacier response to Younger Dryas climatic cooling in Scotland. Global and Planetary Change, 79, 264–274.

Makou, M.C., Eglinton, T.I., Oppo, D.W. & Hughen, K.A. 2010. Postglacial changes in El Niño and La Niña behavior. Geology, 38, 43–46.

Mangili, C., Brauer, A., Moscariello, A. & Naumann, R. 2005. Microfacies of detrital event layers deposited in Quaternary varved lake sediments of the Piànico-Sèllere Basin (northern Italy). Sedimentology, 52, 927–943.

Mann, M.E. & Park, J. 1994. Global-scale modes of surface temperature variability on interannual to century timescales. Journal of Geophysical Research: Atmospheres, 99, 25819–25833.

Mantua, N.J. & Hare, S.R. 2002. The Pacific decadal oscillation. Journal of Oceanography, 58, 35–44.

Marcott, S.A., Bauska, T.K., Buizert, C., Steig, E.J., Rosen, J.L., Cuffey, K.M., Fudge, T.J., Severinghaus, J.P., Ahn, J., Kalk, M.L. & McConnell, J.R. 2014. Centennial-scale changes in the global carbon cycle during the last deglaciation. Nature, 514, 616–619.

Markle, B.R., Steig, E.J., Buizert, C., Schoenemann, S.W., Bitz, C.M., Fudge, T.J., Pedro, J.B., Ding, Q., Jones, T.R., White, J.W. & Sowers, T. 2017. Global atmospheric teleconnections during Dansgaard-Oeschger events. Nature Geoscience, 10, 36–40.

Marshall, G.J. 2003. Trends in the Southern Annular Mode from observations and reanalyses. Journal of Climate, 16, 4134–4143.

Martinod, J., Pouyaud, B., Carretier, S., Guillaume, B. & Hérail, G. 2016. Geomorphic Records along the General Carrera (Chile)–Buenos Aires (Argentina) Glacial Lake (46°–48°S), Climate Inferences, and Glacial Rebound for the Past 7–9 ka: A Discussion. The Journal of Geology, 124, 631-635.

McCulloch, R.D., Bentley, M.J., Tipping, R.M. & Clapperton, C.M., 2005. Evidence for late glacial ice dammed lakes in the central Strait of Magellan and Bahía Inútil, southernmost South America. Geografiska Annaler: Series A Physical Geography 87, 335–362.

McManus, J.F., Francois, R., Gherardi, J.M., Keigwin, L.D. & Brown-Leger, S. 2004. Collapse and rapid resumption of Atlantic meridional circulation linked to deglacial climate changes. Nature, 428, 834–838.

Meehl, G.A., Hu, A., Arblaster, J.M., Fasullo, J. & Trenberth, K.E. 2013. Externally forced and internally generated decadal climate variability associated with the Interdecadal Pacific Oscillation. Journal of Climate, 26, 7298–7310.

Melard, G. 1984. Algorithm AS 197: A fast algorithm for the exact likelihood of autoregressive-moving average models. Journal of the Royal Statistical Society. Series C (Applied Statistics), 33, 104–114.

Mendelova, M., Hein, A.S., McCulloch, R. & Davies, B. 2017. The Last Glacial Maximum and deglaciation in central Patagonia, 44°S–49°S. Cuadernos de Investigacíon Geográfica.

Mercer, J.H. 1976. Glacial History of Southernmost South-America. Quaternary Research, 6, 125–166.

Merkel, U., Prange, M. & Schulz, M. 2010. ENSO variability and teleconnections during glacial climates. Quaternary Science Reviews, 29, 86–100.

Minobe, S. 1997. A 50–70 year climatic oscillation over the North Pacific and North America. Geophysical Research Letters, 24, 683–686.

Miranda, C.G., Moreno, P.I., Vilanova, I. & Villa-Martinez, R.P. 2013. Glacial fluctuations in the Coyhaique-Balmaceda sector of central Patagonia (45°S-46°S) during the last glacial termination. Bollettino Geofisica Teorica Applicata, 54, 268–271.

Moernaut, J., Daele, M.V., Heirman, K., Fontijn, K., Strasser, M., Pino, M., Urrutia, R. & De Batist, M. 2014. Lacustrine turbidites as a tool for quantitative earthquake reconstruction: New evidence for a variable rupture mode in south central Chile. Journal of Geophysical Research: Solid Earth, 119, 1607–1633.

Monecke, K., Anselmetti, F.S., Becker, A., Sturm, M. & Giardini, D. 2004. The record of historic earthquakes in lake sediments of Central Switzerland. Tectonophysics, 394, 21–40.

Montade, V., Kageyama, M., Combourieu-Nebout, N., Ledru, M.P., Michel, E., Siani, G. & Kissel, C. 2015. Teleconnection between the Intertropical Convergence Zone and southern westerly winds throughout the last deglaciation. Geology, 43, 735–738.

Moore, J.J., Hughen, K.A., Miller, G.H. & Overpeck, J.T. 2001. Little Ice Age recorded in summer temperature reconstruction from vavred sediments of Donard Lake, Baffin Island, Canada. Journal of Paleolimnology, 25, 503–517.

Moreno, P.I., Denton, G.H., Moreno, H., Lowell, T.V., Putnam, A.E. & Kaplan, M.R. 2015. Radiocarbon chronology of the last glacial maximum and its termination in northwestern Patagonia. Quaternary Science Reviews, 122, 233–249.

Moreno, P.I., Kaplan, M.R., Francois, J.P., Villa-Martinez, R., Moy, C.M., Stern, C.R. & Kubik, P.W. 2009. Renewed glacial activity during the Antarctic Cold Reversal and persistence of cold conditions until 11.5 ka in southwestern Patagonia. Geology, 37, 375–378.

Mörner, N-A. 1985. Paleoseismicity and geodynamics in Sweden. Tectonophysics, 117, 139–153.

Mörner, N. & Sylwan, C. 1987. Revised terminal moraine chronology at Lago Buenos Aires, Patagonia, Argentina. International Project on Paleolimnology and Late Cenozoic Climate, 4, 15–16.

Mörner, N. & Sylwan, C. 1989. Magnetostratigraphy of the Patagonian moraine sequences at Lago Buenos Aires. Journal of South American Earth Sciences, 2, 385–389.

Mörner, N.A. 1996. Liquefaction and varve deformation as evidence of paleoseismic events and tsunamis. The autumn 10,430 BP case in Sweden. Quaternary Science Reviews, 15, 939–948.

Moy, C.M., Moreno, P.I., Dunbar, R.B., Kaplan, M.R., Francois, J.P., Villalba, R. & Haberzettl, T. 2009. Climate change in southern South America during the last two millennia. In: Vimeux, F., Sylvestre, F., Khodri, M. (Eds.) Past climate variability in South America and surrounding regions. Springer. pp. 353–393.

Mudelsee, M. 2010. Climate Time Series Analysis: Classical Statistical and Bootstrap Methods. Springer.

Mudelsee, M. 2013. Climate Time Series Analysis. Springer.

Mulder, T., & Alexander, J. 2001. The physical character of subaqueous sedimentary density flows and their deposits. Sedimentology, 48, 269–299.

Murdie, R.E., Pugh, D.T. & Styles, P. 1999. A lightweight, portable, digital probe for measuring the thermal gradient in shallow water sediments, with examples from Patagonia. Geo-Marine Letters, 18, 315–320.

Murray, D.S., Carlson, A.E., Singer, B.S., Anslow, F.S., He, F., Caffee, M., Marcott, S.A., Liu, Z. & Otto- Bliesner, B.L. 2012. Northern Hemisphere forcing of the last deglaciation in southern Patagonia. Geology, 40, 631–334.

Naranjo, J.A. & Stern, C.R. 1998. Holocene explosive activity of Hudson Volcano, southern Andes. Bulletin of Volcanology, 59, 291-306.

Naranjo, J.A. & Stern, C.R. 2004. Holocene tephrochronology of the southernmost part (42°30'–45°S) of the Andean Southern Volcanic Zone. Revista Geológica de Chile, 31, 224-240.

Neugebauer, I., Brauer, A., Dräger, N., Dulski, P., Wulf, S., Plessen, B., Mingram, J., Herzschuh, U. & Brande, A. 2012. A Younger Dryas varve chronology from the Rehwiese palaeolake record in NE-Germany. Quaternary Science Reviews, 36, 91–102.

Newman, M., Alexander, M.A., Ault, T.R., Cobb, K.M., Deser, C., Di Lorenzo, E., Mantua, N.J., Miller, A.J., Minobe, S., Nakamura, H. & Schneider, N. 2016. The Pacific decadal oscillation, revisited. Journal of Climate, 29, 4399–4427.

Nimick, D.A., McGrath, D., Mahan, S.A., Friesen, B.A. & Leidich, J. (2016). Latest Pleistocene and Holocene glacial events in the Colonia valley, Northern Patagonia Icefield, southern Chile. Journal of Quaternary Science, 31, 551–564.

O'Neel, S., Pfeffer, W.T., Krimmel, R. & Meier, M. 2005. Evolving force balance at Columbia Glacier, Alaska, during its rapid retreat. Journal of Geophysical Research: Earth Surface, 110, F03012.

Ohlendorf, C., Niessen, F. & Weissert, H. 1997. Glacial varve thickness and 127 years of instrumental climate data: a comparison. Climate Change, 36, 391– 411.

Ohmura, A. 2001. Physical basis for the temperature-based melt-index method. Journal of Applied Meteorology, 40, 753–761.

Ojala, A.E.K., Francus, P., Zolitschka, B., Besonen, M. & Lamoureux, S.F. 2012. Characteristics of sedimentary varve chronologies – A review. Quaternary Science Reviews, 43, 45–60.

Ojala, A.E.K., Launonen, I., Holmström, L. & Tiljander, M. 2015. Effects of solar forcing and North Atlantic oscillation on the climate of continental Scandinavia during the Holocene. Quaternary Science Reviews, 112, 153–171.

Ólafsdóttir, K.B., Geirsdóttir, Á., Miller, G.H. & Larsen, D.J. 2013. Evolution of NAO and AMO strength and cyclicity derived from a 3-ka varve-thickness record from Iceland. Quaternary Science Reviews, 69, 142–154.

Otto-Bliesner, B.L., Brady, E.C., Clauzet, G., Tomas, R., Levis, S. & Kothavala, Z. 2006. Last glacial maximum and Holocene climate in CCSM3. Journal of Climate, 19, 2526–2544.

Ovenshine, A.T. 1970. Observations on iceberg rafting in Glacier Bay, Alaska and the identification of ice-rafted deposits: Geological Society of America Bulletin, 81, 891–894.

Palmer, A. & Lowe, J.J. 2017. Dynamic landscape changes in Glen Roy and vicinity, west Highland Scotland, during the Younger Dryas and earyl Holocene: a synthesis. Proceedings of the Geologists' Association, 128, 2-25.

Palmer, A.P., Carr, S.J. & Lee, A.J. 2008b. Revised Laboratory Procedures for the Preparation of Thin Sections from Unconsolodated Material. Unpublished Internal Report. University of London, Royal Holloway.

Palmer, A.P., Lowe, J.J., Rose, J. & Walker, M.J.C. 2008a. Annually laminated Late Pleistocene sediments from Llangorse Lake, South Wales, UK: a chronology for the pattern of ice wastage. Proceedings of the Geologists Association, 119, 245–258.

Palmer, A.P., Rose, J. & Rasmussen, S.O. 2012. Evidence for phase-locked changes in climate between Scotland and Greenland during GS-1 (Younger Dryas) using micromorphology of glaciolacustrine varves from Glen Roy. Quaternary Science Reviews, 36, 114–123.

Palmer, A.P., Rose, J., Lowe, J.J. & MacLeod, A. 2010. Annually resolved events of Younger Dryas glaciation in Lochaber (Glen Roy and Glen Spean), western Scottish Highlands. Journal of Quaternary Science, 25, 581–596.

Palmer, J.G., Turney, C.S., Cook, E.R., Fenwick, P., Thomas, Z., Helle, G., Jones, R., Clement, A., Hogg, A., Southon, J. & Ramsey, C.B. 2016. Changes in El Niño–Southern Oscillation (ENSO) conditions during the Greenland Stadial 1 (GS-1) chronozone revealed by New Zealand tree-rings. Quaternary Science Reviews, 153, 139–155.

Parrenin, F., Masson-Delmotte, V., Köhler, P., Raynaud, D., Paillard, D., Schwander, J., Barbante, C., Landais, A., Wegner, A. & Jouzel, J. 2013. Synchronous change of atmospheric CO 2 and Antarctic temperature during the last deglacial warming. Science, 339, 1060–1063.

Pedersen, V.K., Huismans, R.S., Hermen, F. & Egholm, D.L. 2014 Controls of initial topography on temporal and spatial patterns of erosion. Geomorphology, 223, 96-116.

Pedro, J.B., Martin, T., Steig, E.J., Jochum, M., Park, W. & Rasmussen, S.O. 2016. Southern Ocean deep convection as a driver of Antarctic warming events. Geophysical Research Letters, 43, 2192–2199.

Pepper, A.C., Shulmeister, J., Nobes, D.C. & Augustinus, P.A. 2004. Possible ENSO signals prior to the Last Glacial Maximum, during the last deglaciation and the early Holocene, from New Zealand. Geophysical Research Letters, 31, L15206.

Petit, J.R., Jouzel, J., Raynaud, D., Barkov, N.I., Barnola, J.M., Basile, I., Bender, M., Chappellaz, J., Davis, M., Delaygue, G. & Delmotte, M. 1999. Climate and atmospheric history of the past 420,000 years from the Vostok ice core, Antarctica. Nature, 399, 429–436.

Pfeffer, W.T., Arendt, A.A., Bliss, A., Bolch, T., Cogley, J.G., Gardner, A.S., Hagen, J.O., Hock, R., Kaser, G., Kienholz, C. & Miles, E.S. 2014. The Randolph Glacier Inventory: a globally complete inventory of glaciers. Journal of Glaciology, 60, 537–552.

Pike, J., Swann, G.E., Leng, M.J. & Snelling, A.M. 2013. Glacial discharge along the west Antarctic Peninsula during the Holocene. Nature Geoscience, 6, 199–202.

Placzek, C., Quade, J. & Patchett, P.J. 2006. Geochronology and stratigraphy of late Pleistocene lake cycles on the southern Bolivian Altiplano: implications for causes of tropical climate change. Geological Society of America Bulletin, 118, 515–532.

Pollard, D., DeConto, R.M., & Alley, R.B. 2015. Potential Antarctic Ice Sheet retreat driven by hydrofracturing and ice cliff failure. Earth and Planetary Science Letters, 412, 112–121.

Porter, S.C., Clapperton, C.M. & Sugden, D.E. 1992. Chronology and dynamics of deglaciation along and near the Strait of Magellan, southernmost South America. SGU Series Research Paper, 81, 233–239.

Powell, R.D., Dawber, M., McInnes, J.N. & Pyne, A.R. 1996. Observations of the grounding-line area at a floating glacier terminus. Annals of Glaciology, 22, 217–223.

Power, S., Casey, T., Folland, C., Colman, A. & Mehta, V. 1999. Inter-decadal modulation of the impact of ENSO on Australia. Climate Dynamics, 15, 319–324.

Power, S., Saurral, R., Chung, C., Colman, R., Kharin, V., Boer, G., Gergis, J., Henley, B., McGregor, S., Arblaster, J., Holbrook, N. & Liguori, G. 2017. Towards the prediction of multi-year to decadal climate variability in the Southern Hemisphere. PAGES News Letter, 25, 32–40.

Putnam, A.E., Denton, G.H., Schaefer, J.M., Barrell, D.J., Andersen, B.G., Finkel, R.C., Schwartz, R., Doughty, A.M., Kaplan, M.R. & Schlüchter, C. 2010a. Glacier advance in southern middle-latitudes during the Antarctic Cold Reversal. Nature Geoscience, 3, 700–704.

Putnam, A.E., Schaefer, J.M., Barrell, D.J.A., Vandergoes, M., Denton, G.H., Kaplan, M.R., Finkel, R.C., Schwartz, R., Goehring, B.M. & Kelley, S.E. 2010b. In situ cosmogenic ^{10}Be production-rate calibration from the Southern Alps, New Zealand. Quaternary Geochronology, 5, 392–409.

Putnam, A.E., Schaefer, J.M., Denton, G.H., Barrell, D.J., Andersen, B.G., Koffman, T.N., Rowan, A.V., Finkel, R.C., Rood, D.H., Schwartz, R. & Vandergoes, M.J. 2013a. Warming and glacier recession in the Rakaia valley, Southern Alps of New Zealand, during Heinrich Stadial 1. Earth and Planetary Science Letters, 382, 98–110.

Putnam, A.E., Schaefer, J.M., Denton, G.H., Barrell, D.J., Birkel, S.D., Andersen, B.G., Kaplan, M.R., Finkel, R.C., Schwartz, R. & Doughty, A.M. 2013b. The last glacial maximum at 44°S documented by a ^{10}Be moraine chronology at Lake Ohau, Southern Alps of New Zealand. Quaternary Science Reviews, 62, 114–141.

Rabassa, J. & Clapperton, C.M., 1990. Quaternary glaciations of the southern Andes Quaternary Science Reviews, 9, 153–174.

Rabassa, J. 2008. Late Cenozoic Glaciations in Patagonia and Tierra del Fuego. In: Rabassa, J. (Ed.) Developments in Quaternary Sciences. Elsevier, Amsterdam, Netherlands.

Rabassa, J., Coronato, A. & Martinez, O., 2011. Late Cenozoic glaciations in Patagonia and Tierra del Fuego: an updated review. Biological Journal of the Linnean Society, 103, 316–335.

Rach, O., Brauer, A., Wilkes, H. & Sachse, D. 2014. Delayed hydrological response to Greenland cooling at the onset of the Younger Dryas in western Europe. Nature Geoscience 7, 109–111.

Rasmusson, E.M., Wang, X. & Ropelewski, C.F. 1990. The biennial component of ENSO variability. Journal of Marine Systems, 1, 71–96.

Reimnitz, E. & Kempema, E.W. 1982. Dynamic ice-wallow relief on northern Alaska's nearshore. Journal of Sedimentary Petrology, 52, 451–461.

Rein, B., Lückge, A., Reinhardt, L., Sirocko, F., Wolf, A. & Dullo, W.C. 2005. El Niño variability off Peru during the last 20,000 years. Paleoceanography, 20. PA4003.

Ridge, J.C., Balco, G., Bayless, R.L, Beck, C.C, Carter, L..B, Dean, J.L, Voytek, E.B & Wei, J.H., 2012. The new North American Varve Chronology: A precise record of southeastern Laurentide Ice Sheet deglaciation and climate, 18.2-12.5 kyr BP, and correlations with Greenland ice core records. American Journal of Science, 312, 685–722.

Rind, D. 2000. Relating paleoclimate data and past temperature gradients: Some suggestive rules. Quaternary Science Reviews, 19, 381–390.

Rind, D.G., Russell, G., Schmidt, G., Sheth, S., Collins, D., De-Menocal, P. & Teller, J. 2001. Effects of glacial meltwater in the GISS Coupled Atmosphere-Ocean model: Part II. A bipolar seesaw in deep water production. Journal Geophysical Research, 106, 27355–27365.

Ringberg, B. & Erlström, M. 1999. Micromorphology and petrography of Late Weichselian glaciolacustrine varves in southeastern Sweden. Catena 35, 147–177.

Ringberg, B., Björck, J. & Hang, T. 2003. Correlation of stadial and interstadial events in the south Swedish glacial varves with the GRIP oxygen isotope record. Boreas, 32, 427–435.

Rittenour, T.M., Brigham-Grette, J. & Mann, M.E. 2000. El Nino-like climate teleconnections in New England during the late Pleistocene. Science, 288, 1039–1042.

Ritz, S.P., Stocker, T.F., Grimalt, J.O., Menviel, L. & Timmermann, A. 2013. Estimated strength of the Atlantic overturning circulation during the last deglaciation. Nature Geoscience, 6, 208–212.

Ritz, S.P., Stocker, T.F., Grimalt, J.O., Menviel, L. & Timmermann, A. 2013. Estimated strength of the Atlantic overturning circulation during the last deglaciation. Nature Geoscience, 6, 208–211.

Rodbell, D.T., Smith, J.A. & Mark, B.G. 2009. Glaciation in the Andes during the Lateglacial and Holocene. Quaternary Science Reviews, 28, 2165–2212.

Roering, J.J., Mackey, B.H., Marshall, J.A., Sweeney, K.E., Deligne, N.I., Booth, A.M., Handwerger, A.L. & Cerovski-Darriau, C. 2013. 'You are HERE': Connecting the dots with airborne lidar for geomorphic fieldwork. Geomorphology, 200, 172–183.

Rust, B.R. & Romanelli, R. 1975. Late Quaternary subaqueous outwash deposits near Ottawa, Canada. In: Jopling, A.V., McDonald, B.C. (Eds.) Glaciofluvial and Glaciolacustrine Sedimentation: Society of Economic Paleontologists and Mineralogists Special Publication, 23, Tulsa, Oklahama, pp. 177–192.

Sadekov, A.Y., Ganeshram, R., Pichevin, L., Berdin, R., McClymont, E., Elderfield, H. & Tudhope, A.W. 2013. Palaeoclimate reconstructions reveal a strong link between El Nino-Southern Oscillation and Tropical Pacific mean state. Nature Communications, 4, 2692–2697.

Sagredo, E.A., Moreno, P.I., Villa-Martínez, R., Kaplan, M.R., Kubik, P.W. & Stern, C.R., 2011. Fluctuations of the Última Esperanza ice lobe (52°S), Chilean Patagonia, during the last glacial maximum and termination 1. Geomorphology, 125, 92–108.

Scalabrino, B., Lagabrielle, Y., Malavieille, J., Dominguez, S., Melnick, D., Espinoza, F., Suarez, M. & Rossello, E. 2010. A morphotectonic analysis of central Patagonian Cordillera: Negative inversion of the Andean belt over a buried spreading center? Tectonics, 29, TC2010.

Scargle, J.D. 1982. Studies in astronomical time series analysis. II-Statistical aspects of spectral analysis of unevenly spaced data. The Astrophysical Journal, 263, 835–853.

Schaefer, J.M., Denton, G.H., Barrell, D.J., Ivy-Ochs, S., Kubik, P.W., Andersen, B.G., Phillips, F.M., Lowell, T.V. & Schlüchter, C. 2006. Near-synchronous interhemispheric termination of the last glacial maximum in mid-latitudes. Science, 312, 1510–1513.

Schlolaut, G., Marshall, M.H., Brauer, A., Nakagawa, T., Lamb, H.F., Staff, R.A., Ramsey, C.B., Bryant, C.L., Brock, F., Kossler, A. & Tarasov, P.E. 2012. An automated method for varve interpolation and its application to the Late Glacial chronology from Lake Suigetsu, Japan. Quaternary Geochronology, 13, 52–69.

Schneider, C. & Gies, D. 2004. Effects of El Niño–southern oscillation on southernmost South America precipitation at 53°S revealed from NCEP–NCAR reanalyses and weather station data. International Journal of Climatology, 24, 1057–1076.

Schulz, M. & Mudelsee, M. 2002. REDFIT: estimating red-noise spectra directly from unevenly spaced paleoclimatic time series. Computers & Geosciences, 28, 421–426.

Sen Gupta, A. & England, M.H. 2006. Coupled ocean–atmosphere–ice response to variations in the Southern Annular Mode. Journal of Climate, 19, 4457–4486.

Shakun, J.D. & Shaman, J. 2009. Tropical origins of North and South Pacific decadal variability. Geophysical Research Letters, 36, L19711.

Shaw, J. & Archer, J. 1978. Winter turbidity current deposits in Late Pleistocene glaciolacustrine varves, Okanagan Valley, British Columbia, Canada. Boreas, 7, 123-130.

Shulmeister, J., Fink, D., Hyatt, O.M., Thackray, G.D. & Rother, H. 2010. Cosmogenic ^{10}Be and 26 Al exposure ages of moraines in the Rakaia Valley, New Zealand and the nature of the last termination in New Zealand glacial systems. Earth and Planetary Science Letters, *297*, 558–566.

Sikes, E.L., Howard, W.R., Samson, C.R., Mahan, T.S., Robertson, L.G. & Volkman, J.K. 2009. Southern Ocean seasonal temperature and Subtropical Front movement on the South Tasman Rise in the late Quaternary. Paleoceanography, 24, PA2201.

Sikes, E.L., Medeiros, P.M., Augustinus, P., Wilmshurst, J.M. & Freeman, K.R. 2013. Seasonal variations in aridity and temperature characterize changing climate during the last deglaciation in New Zealand. Quaternary Science Reviews, 74, 245–256.

Silvestri, G.E. & Vera, C.S. 2003. Antarctic Oscillation signal on precipitation anomalies over southeastern South America. Geophysical Research Letters, 30, 2115.

Sime, L.C., Kohfeld, K.E., Le Quéré, C., Wolff, E.W., de Boer, A.M., Graham, R.M. & Bopp, L. 2013. Southern Hemisphere westerly wind changes during the Last Glacial Maximum: model-data comparison. Quaternary Science Reviews, 64, 104–120.

Simmonds, I. & King, J.C. 2004. Global and hemispheric climate variations affecting the Southern Ocean. Antarctic Science, 16, 401–413.

Singer, B.S. & Pringle, M.S. 1996. Age and duration of the Matuyama-Brunhes geomagnetic polarity reversal from $^{40}Ar^{39}Ar$ incremental heating analyses of lavas. Earth and Planetary Science Letters, 139, 47–61.

Singer, B.S., Ackert, R.P. & Guillou, H. 2004. $^{40}Ar/^{39}Ar$ and K-Ar chronology of Pleistocene glaciations in Patagonia. Geological Society of America Bulletin, 116, 434–450.

Singer, B.S., Ackert, R.P. and Guillou, H., 2004. $^{40}Ar/^{39}Ar$ and K-Ar chronology of Pleistocene glaciations in Patagonia. Geological Society of America Bulletin 116, 434-450.

Skinner, L.C., Waelbroeck, C., Scrivner, A.E. & Fallon, S.J. 2014. Radiocarbon evidence for alternating northern and southern sources of ventilation of the deep Atlantic carbon pool during the last deglaciation. Proceedings of the National Academy of Sciences, 111, 5480–5484.

Smedley, R.K., Glasser, N.F. & Duller, G.A.T. 2016. Luminescence dating of glacial advances at Lago Buenos Aires (~46ºS), Patagonia. Quaternary Science Reviews, 134, 59—73.

Smith, M.J. & Clark, C.D. 2005. Methods for the visualization of digital elevation models for landform mapping. Earth Surface Processes and Landforms, 30, 885–900.

Smith, M.J. & Wise, S.M. 2007. Problems of bias in mapping linear landforms from satellite imagery. International Journal of Applied Earth Observation and Geoinformation, 9, 65–78.

Smith, M.J., Rose, J. & Booth, S. 2006. Geomorphological mapping of glacial landforms from remotely sensed data: An evaluation of the principal data sources and an assessment of their quality. Geomorphology 76, 148–165.

Smith, N.D. & Ashley, G.M., 1985. Proglacial lacustrine environment. In Glacial Sedimentary Environments, Ashley G.M., Shaw J., Smith, N.D. (Eds) Society of Palaeontologists and Mineralogists: Tulsa, OK, 135–212.

Spedding, N. & Evans, D.J.A. 2002. Sediments and landforms at Kvıárjökull, southeast Iceland: a reappraisal of the glaciated valley landsystem. Sedimentary Geology, 149, 21-42.

Stammerjohn, S.E., Martinson, D.G., Smith, R.C., Yuan, X. & Rind, D. 2008. Trends in Antarctic annual sea ice retreat and advance and their relation to El Niño–

Southern Oscillation and Southern Annular Mode variability. Journal of Geophysical Research: Oceans, 113, C03S90.

Steig, E.J., Ding, Q., Battisti, D.S. & Jenkins, A. 2012. Tropical forcing of Circumpolar Deep Water inflow and outlet glacier thinning in the Amundsen Sea Embayment, West Antarctica. Annals of Glaciology, 53, 19–28.

Stern, C., Porras, M. & Maldonado, A. 2015. Tephrochronology of the upper Río Cisnes valley (44°S), southern Chile. Andean Geology, 42, 173–189.

Stern, C.R. & Weller, D. 2012. A revised age of 7430 ± 250 ^{14}C yrs BP for the very large mid-Holocene explosive H1 eruption of the Hudson volcano, southern Chile. 13th Chilean Geologic Congress, Antofagasta, Chile, 2 p..

Stern, C.R. 2008. Holocene tephrochronology record of large explosive eruptions in the southernmost Patagonian Andes. Bulletin of Volcanology, 70, 435-454.

Stern, C.R., Moreno, P.I., Henríquez, W.I., Villa Martínez, R., Sagredo, E., Aravena, J.C. & Pol-Holz, R.D. 2016. Holocene tephrochronology around Cochrane (~47°S), southern Chile. Adean Geology, 43, 1–19.

Stern, C.R., Moreno, P.I., Villa-Martínez, R., Sagredo, E.A., Prieto, A. & Labarca, R. 2011. Evolution of ice-dammed proglacial lakes in Última Esperanza, Chile: implications from the late-glacial R1 eruption of Reclús volcano, Andean Austral Volcanic Zone. Andean Geology, 38, 82–97.

Stokes, C.R. & Clark, C.D. 2003. The Dubawnt Lake palaeo-ice stream: evidence for dynamic ice sheet behaviour on the Canadian Shield and insights regarding the controls on ice-stream location and vigour. Boreas, 32, 263–279.

Stone, J.O. 2000. Air pressure and cosmogenic isotope production. Journal of Geophysical Research: Solid Earth, 105, 23753–23759.

Storrar, R. D., Evans, D. J., Stokes, C. R. & Ewertowski, M. 2015. Controls on the location, morphology and evolution of complex esker systems at decadal timescales, Breiðamerkurjökull, southeast Iceland. Earth Surface Processes and Landforms, 40, 1421–1438.

Stott, L., Timmermann, A. & Thunell, R. 2007. Southern hemisphere and deep-sea warming led deglacial atmospheric CO2 rise and tropical warming. Science, 318, 435–438.

Strelin, J.A., Denton, G.H., Vandergoes, M.J., Ninnemann, U.S. & Putnam, A.E. 2011. Radiocarbon chronology of the late-glacial Puerto Bandera moraines, southern Patagonian Icefield, Argentina. Quaternary Science Reviews, 30, 2551–2569.

Stromberg, B. 1989. Late Weichselian deglaciation and clay varve chronology in east-central Sweden. Sveriges Geologiska Undersökning, 73, 70 p.

Sturm, M. & Matter, A. 1978. Turbidites and varves in Lake Brienz (Switzerland): deposition of clastic detritus by density currents. In: Matter, A., Tucker, M.E. (Eds.) Modern and Ancient Sediments. Blackwell, Oxford, pp. 147–168.

Sugden, D.E., Bentley, M.J., Fogwill, C.J., Hulton, N.R.J., McCulloch, R.D. & Purves, R.S. 2005. Late-glacial glacier events in southernmost South America: a blend of 'Northern' and 'Southern' hemispheric climatic signals? Geografiska Annaler: Series A Physical Geography, 87, 273–288.

Sugiyama, S., Minowa, M., Sakakibara, D., Skvarca, P., Sawagaki, T., Ohashi, Y., Naito, N. & Chikita, K. 2016. Thermal structure of proglacial lakes in Patagonia. Journal of Geophysical Research: Earth Surface, 121, 2270–2286.

Sugiyama, S., Skvarca, P., Naito, N., Enomoto, H., Tsutaki, S., Tone, K., Marinsek, S. & Aniya, M. 2011. Ice speed of a calving glacier modulated by small fluctuations in basal water pressure. Nature Geoscience, 4, 597–600.

Swann, G.E., Pike, J., Snelling, A.M., Leng, M.J. & Williams, M.C. 2013. Seasonally resolved diatom δ 18 O records from the West Antarctic Peninsula over the last deglaciation. Earth and Planetary Science Letters, 364, 12–23.

Sylwan, C., Beraza, L. & Casteli, A. 1991. Magnetostratigrafía de la secuencia morénica en la Valle del Lago Pueyrredón, Provincia de Santa Cruz. Revista de la Asociación Geológica Argentina, 54, 333–352.

Sylwan, C.A. 1989. Paleomagnetism, paleoclimate, and chronology of Late Cenozoic deposits in southern Argentina [Ph.D. thesis]: Sweden, Stockholm University, 110 p.

Talling, P.J., Masson, D.G., Sumner, E.J. & Malgesini, G. 2012. Subaqueous sediment density flows: depositional processes and deposit types. Sedimentology, 59, 1937–2003.

Teller, J., Leverington, D. & Mann, J. 2002. Freshwater outbursts to the oceans from glacial Lake Agassiz and their role in climate change during the last deglaciation. Quaternary Science Reviews, 21, 879-887.

Thomas, E.K. & Briner, J.P., 2009. Climate of the past millennium inferred from varved proglacial lake sediments on northeast Baffin Island, Arctic Canada. Journal of Paleolimnology, 41, 209–224.

Thomas, G.S.P. & Connell, R.J. 1985. Iceberg drop, dump and grounding structures from Pleistocene glaciolacustrine sediments, Scotland. Journal of Sedimentary Research, 55, 243–249.

Thompson, D.W. & Solomon, S. 2002. Interpretation of recent Southern Hemisphere climate change. Science, 296, 895–899.

Thompson, D.W. & Wallace, J.M. 2000. Annular modes in the extratropical circulation. Part I: Month-to-month variability. Journal of Climate, 13, 1000–1016.

Thompson, T.A. & Baedke, S.J. 1997. Strand-plain evidence for late Holocene lake-level variations in Lake Michigan. Geological Society of America Bulletin, 109, 66–682.

Thomson, D.J. 1982. Spectrum estimation and harmonic analysis. Proceedings of the IEEE, 70, 1055–1096.

Timmermann, A., Krebs, U., Justino, F., Goosse, H. & Ivanochko, T. 2005. Mechanisms for millennial-scale global synchronization during the last glacial period. Paleoceanography, 22, PA4008.

Timmermann, A., Krebs, U., Justino, F., Goosse, H. & Ivanochko, T. 2005. Mechanisms for millennial-scale global synchronization during the last glacial period. *Paleoceanography*, *20*, PA4008.

Timmermann, A., Okumura, Y., An, S.I., Clement, A., Dong, B., Guilyardi, E., Hu, A., Jungclaus, J.H., Renold, M., Stocker, T.F. & Stouffer, R.J. 2007. The influence of a weakening of the Atlantic meridional overturning circulation on ENSO. Journal of Climate, 20, 4899–4919.

Timmermann, A., Okumura, Y., An, S.I., Clement, A., Dong, B., Guilyardi, E., Hu, A., Jungclaus, J.H., Renold, M., Stocker, T.F. & Stouffer, R.J. 2007. The influence of a weakening of the Atlantic meridional overturning circulation on ENSO. Journal of Climate, 20, 4899–4919.

Toggweiler, J.R., 2009. Shifting westerlies. Science, 323, 1434–1435.

Toggweiler, J.R., Russell, J.L. & Carson, S.R., 2006. Midlatitude westerlies, atmospheric CO_2, and climate change during the ice ages. Paleoceanography, 21, PA2005.

Ton-That, T., Singer, B., Mörner, N.A., & Rabassa, J. 1999. Datacion por el metodo $^{40}Ar/^{39}Ar$ de lavas basalticas y geologia del Cenozoico superior en la region del Lago Buenos Aires, provincia de Santa Cruz, Argentina. Asociacion Geologica Argentina, Revista, 54, 333–352.

Torrence, C. & Compo, G.P. 1998. A practical guide to wavelet analysis. Bulletin of the American Meteorological Society, 79, 61–78.

Tröften, P.E. & Mörner, N-A. 1997. Varved clay chronology as a means of recording paleoseismic events in southern Sweden. Journal of Geodynamics, 24, 249–258.

Turner, K.J., Fogwill, C.J., McCulloch, R.D. & Sugden, D.E. 2005. Deglaciation of the eastern flank of the north patagonian icefield and associated continental-scale lake diversions. Geografiska Annaler: Series A Physical Geography, 87, 363–374.

Van Daele, M., Bertrand, S., Meyer, I., Moernaut, J., Vandoorne, W., Siani, G., Tanghe, N., Ghazoui, Z., Pino, M., Urrutia, R. & De Batist, M. 2016. Late Quaternary evolution of Lago Castor (Chile, 45.6°S): Timing of the deglaciation in northern Patagonia and evolution of the southern westerlies during the last 17 kyr. Quaternary Science Reviews, 133, 130–146.

Vautard, R. & Ghil, M. 1989. Singular spectrum analysis in nonlinear dynamics, with applications to paleoclimatic time series. Physica D: Nonlinear Phenomena, 35, 395–424.

Vellinga, M. & Wood, R.A. 2002. Global climatic impacts of a collapse of the Atlantic thermohaline circulation. *Climatic change*, *54*, 251–267.

Villa-Martínez, R., Moreno, P.I., & Valenzuela, M.A. 2012. Deglacial and postglacial vegetation changes on the eastern slopes of the central Patagonian Andes (47°S). Quaternary Science Reviews, 32, 86–99.

Villalba, R. 2009. Tree-ring evidence for tropical-extratropical influences on climate variability along the Andes in South America. PAGES News, 15, 23–25.

Villalba, R., Lara, A., Boninsegna, J.A., Masiokas, M., Delgado, S., Aravena, J.C., Roig, F.A., Schmelter, A., Wolodarsky, A. & Ripalta, A. 2003. Large-scale temperature changes across the southern Andes: 20th-century variations in the context of the past 400 years. Climatic Change, 59, 177–232.

Villalba, R., Lara, A., Masiokas, M.H., Urrutia, R., Luckman, B.H., Marshall, G.J., Mundo, I.A., Christie, D.A., Cook, E.R., Neukom, R. & Allen, K., 2012. Unusual Southern Hemisphere tree growth patterns induced by changes in the Southern Annular Mode. Nature Geoscience, 5, 793–797.

WAIS Divide Project Members. 2013. Onset of deglacial warming in West Antarctica driven by local orbital forcing. Nature, 500, 440–443.

WAIS Divide Project Members. 2015. Precise interpolar phasing of abrupt climate change during the last ice age. Nature, 520, 661–665.

Walker, C.C. & Gardner, A.S., 2017. Rapid drawdown of Antarctica's Wordie Ice Shelf glaciers in response to ENSO/Southern Annular Mode-driven warming in the Southern Ocean. Earth and Planetary Science Letters, 476 100–110.

Wang, S., Huang, J., He, Y. & Guan, Y. 2014. Combined effects of the Pacific Decadal Oscillation and El Niño–Southern Oscillation on global land dry–wet changes. Scientific Reports, 4:6651.

Wang, Y.J., Cheng, H., Edwards, R.L., An, Z.S., Wu, J.Y., Shen, C.C. & Dorale, J.A. 2001. A high-resolution absolute-dated late Pleistocene monsoon record from Hulu Cave, China. Science, 294, 2345–2348.
Wang, Y.J., Cheng, H., Edwards, R.L., An, Z.S., Wu, J.Y., Shen, C.C. & Dorale, J.A. 2001. A high-resolution absolute-dated late Pleistocene monsoon record from Hulu Cave, China. Science, 294, 2345–2348.
Warren, C. & Aniya, M., 1999. The calving glaciers of southern South America. Global and Planetary Change, 22, 59–77.

Warren, C.R., Greene, D.R., Glasser, N.F., 1995. Glaciar Upsala, Patagonia: rapid calving retreat in fresh water. Annals of Glaciology, 21, 311–316.

Wastegård, S., Veres, D., Kliem, P., Hahn, A., Ohlendorf, C., Zolitschka, B. & Team, T.P.S. 2013. Towards a late Quaternary tephrochronological framework for the southernmost part of South America–the Laguna Potrok Aike tephra record. Quaternary Science Reviews, 71, 81–90.

Weller, D., Miranda, C.G., Moreno, P.I., Villa-Martínez, R. & Stern, C.R. 2014. The large late-glacial Ho eruption of the Hudson volcano, southern Chile. Bulletin of Volcanology, 76, 831.

Weller, D.J., Miranda, C.G., Moreno, P.I., Villa-Martínez, R. & Stern, C.R. 2015. Tephrochronology of the southernmost Andean southern volcanic zone, Chile. Bulletin of Volcanology, 77, 107.

Winsemann, J., Asprion, U. & Meyer, T. 2004. Sequence analysis of early Saalian glacial lake deposits (NW Germany): evidence of local ice margin retreat and associated calving processes. Sedimentary Geology, 165, 223–251.

Winsemann, J., Asprion, U., Meyer, T. & Schramm, C. 2007. Facies characteristics of Middle Pleistocene (Saalian) ice-margin subaqueous fan and delta deposits, glacial Lake Leine, NW Germany. Sedimentary Geology, 193, 105-129.

Wohlfarth, B., Björck, S., Cato, I. & Possnert, G. 1997. A new middle Holocene varve diagram from the River Ångermanälvan, northern Sweden: indications for a possible error in the Holocene varve chronology. Boreas, 26, 347–353.

Wolff, C., Haug, G.H., Timmermann, A., Damsté, J.S.S., Brauer, A., Sigman, D.M., Cane, M.A. & Verschuren, D. 2011. Reduced interannual rainfall variability in East Africa during the last ice age. Science, 333, 743–747.

Wolff, E.W., Fischer, H. & Röthlisberger, R. 2009. Glacial terminations as southern warmings without northern control. Nature Geoscience, 2, 206–210.

Wulf, S., Keller, J., Paterne, M., Mingram, J., Lauterbach, S., Opitz, S., Sottili, G., Giaccio, B., Albert, P.G., Satow, C. &Tomlinson, E.L. 2012. The 100–133 ka record of Italian explosive volcanism and revised tephrochronology of Lago Grande di Monticchio. Quaternary Science Reviews, 58, 104–123.

Wulf, S., Ott, F., Słowiński, M., Noryśkiewicz, A.M., Dräger, N., Martin-Puertas, C., Czymzik, M., Neugebauer, I., Dulski, P., Bourne, A.J. & Błaszkiewicz, M. 2013. Tracing the Laacher See Tephra in the varved sediment record of the Trzechowskie palaeolake in central Northern Poland. Quaternary Science Reviews, 76, 129–139.

Yang, Z. & Teller, J.T. 2012. Using LiDAR Digital Elevation Model data to map Lake Agassiz beaches, measure their isostatically-induced gradients, and estimate their ages. Quaternary International, 260, 32–42.

Yeo, S.R. & Kim, K.Y. 2015. Decadal changes in the Southern Hemisphere sea surface temperature in association with El Niño–Southern Oscillation and Southern Annular Mode. Climate Dynamics, 45, 3227–3242.

Yokoyama, Y., Lambeck, K., De Deckker, P., Johnston, P. & Fifield, I. K. 2001. Timing of the Last Glacial Maximum from observed sea-level minima. Nature, 412, 99–99.

Yuan, X. & Yonekura, E. 2011. Decadal variability in the Southern Hemisphere. Journal of Geophysical Research: Atmospheres, 116. D19115.

Zebiak, S.E. & Cane, M.A. 1987. A Model El Niño–Southern Oscillation. Monthly Weather Review, 115, 2262–2278.

Zhu, J., Liu, Z., Brady, E., Otto-Bliesner, B., Zhang, J., Noone, D., Tomas, R., Nusbaumer, J., Wong, T., Jahn, A. & Tabor, C. 2016. Reduced ENSO Variability at the LGM Revealed by an Isotope-enabled Earth System Model. Geophysical Research Letters, 44, 6984–6992.